AD-A175 487   PHOTOTHERMAL IMAGING OF DEFECTS IN METALS AND CERAMICS   1/3
(U) JOHNS HOPKINS UNIV LAUREL MD APPLIED PHYSICS LAB
J C MURPHY ET AL OCT 86 JHU/APL/RC-TPS-012
UNCLASSIFIED ARO-210661 11-MS N00024-85-C-5301   F/G 11/6   NL

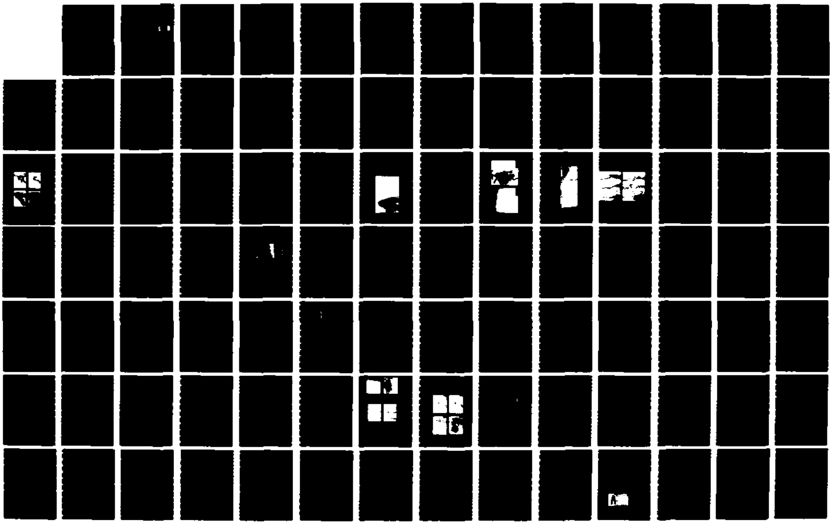

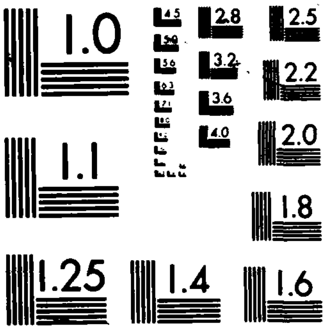

CROCOPY RESOLUTION TEST CHART

ARO 21066.11-MS

RC-TPS-012 ②

PHOTOTHERMAL IMAGING OF DEFECTS IN METALS AND CERAMICS

FINAL REPORT

J. C. MURPHY and L. C. AAMODT

SEPTEMBER 1, 1983 - AUGUST 31,1986

U. S. ARMY RESEARCH OFFICE

ARO IDENTIFICATION NUMBER 21066-MS
NAVAL SEA SYSTEMS COMMAND CONTRACT N00024-85-C-5301

THE JOHNS HOPKINS UNIVERSITY
APPLIED PHYSICS LABORATORY
LAUREL, MD 20707

APPROVED FOR PUBLIC RELEASE;
DISTRIBUTION UNLIMITED.

RC-TPS-012

PHOTOTHERMAL IMAGING OF DEFECTS IN METALS AND CERAMICS

FINAL REPORT

J. C. MURPHY and L. C. AAMODT

SEPTEMBER 1, 1983 - AUGUST 31,1986

U. S. ARMY RESEARCH OFFICE

ARO IDENTIFICATION NUMBER 21066-MS
NAVAL SEA SYSTEMS COMMAND CONTRACT N00024-85-C-5301

THE JOHNS HOPKINS UNIVERSITY
APPLIED PHYSICS LABORATORY
LAUREL, MD 20707

MASTER COPY - FOR REPRODUCTION PURPOSES

UNCLASSIFIED

SECURITY CLASSIFICATION OF THIS PAGE (When Data Entered)

REPORT DOCUMENTATION PAGE		READ INSTRUCTIONS BEFORE COMPLETING FORM
1. REPORT NUMBER ARO 21066.11-MS	2. GOVT ACCESSION NO. N/A	3. RECIPIENT'S CATALOG NUMBER N/A
4. TITLE (and Subtitle) PHOTOTHERMAL IMAGING OF DEFECTS IN METALS AND CERAMICS		5. TYPE OF REPORT & PERIOD COVERED Final Report 9/1/83 - 8/31/86
		6. PERFORMING ORG. REPORT NUMBER
7. AUTHOR(s) J. C. Murphy and L. C. Aamodt		8. CONTRACT OR GRANT NUMBER(s) N00024-85-C-5301 21066-MS
9. PERFORMING ORGANIZATION NAME AND ADDRESS The Johns Hopkins University Applied Physics Laboratory Laurel, MD 20707		10. PROGRAM ELEMENT, PROJECT, TASK AREA & WORK UNIT NUMBERS
11. CONTROLLING OFFICE NAME AND ADDRESS U. S. Army Research Office Post Office Box 12211 Research Triangle Park, NC 27709		12. REPORT DATE October 1986
		13. NUMBER OF PAGES 230
14. MONITORING AGENCY NAME & ADDRESS (if different from Controlling Office)		15. SECURITY CLASS. (of this report) Unclassified
		15a. DECLASSIFICATION/DOWNGRADING SCHEDULE

16. DISTRIBUTION STATEMENT (of this Report)

Approved for public release; distribution unlimited.

17. DISTRIBUTION STATEMENT (of the abstract entered in Block 20, if different from Report)

NA

18. SUPPLEMENTARY NOTES

The view, opinions, and/or findings contained in this report are those of the author(s) and should not be construed as an official Department of the Army position, policy, or decision, unless so designated by other documentation.

19. KEY WORDS (Continue on reverse side if necessary and identify by block number)

Nondestructive evaluation
Image contrast mechanisms
Grain boundaries in metals
Defect structures in metals

20. ABSTRACT (Continue on reverse side if necessary and identify by block number)

Photothermal - or Thermal-Wave - Imaging is a new technique for the characterization and nondestructive evaluation of materials. This report describes developments in the method, theory, and application of thermal-wave imaging techniques. Contrast mechanisms have been a subject of dominant interest and several distinct mechanisms have been shown to contribute to the images obtained. These mechanisms enocmpass the range of physical processes that create the thermal image. An intimate knowledge of these mechanisms is needed for thermal-wave imaging to become a quantitative tool for material characteri-

DD FORM 1 JAN 73 1473 EDITION OF 1 NOV 65 IS OBSOLETE

UNCLASSIFIED

SECURITY CLASSIFICATION OF THIS PAGE (When Data Entered) zation.

A theory of multilayer films has been developed which has shown that both thermal (and for optical sources) optical-boundary-condition reflections contribute to the temperature field within the specimen and hence affect the ability of thermal-wave imaging methods to determine the depth (or thickness) of buried flaws (or layers).

In addition, an analysis has been made which shows that thermal barriers affecting heat flow in a heterogeneous material are of two types, one type depending exclusively on thermal properties and the other type depending on both thermal and optical properties.

Applications of thermal-wave imaging have included grain-boundary studies in metals, studies of void location and sizing, and closed crack visualization using both thermal and thermoelastic methods.

Summarizing major items, we have shown a) that thermal-wave imaging is a pervasive technique for nondestructive evaluation, encompassing a variety of experimental configurations, each supplying different physical information; b) that three different types of processes are effective in creating thermal images; c) that this technique is suitable for studying the microstructure of a variety of materials; d) that thermoelastic mechanisms are operative in thermal-wave imaging; and e) that momentum processes are ineffective in producing thermal images using particle beam sources. We have also developed a new thermal wave imaging technique using an ion-beam as the excitation source.

FINAL REPORT

PHOTOTHERMAL IMAGING OF DEFECTS IN METALS AND CERAMICS

Sept. 1, 1983 - August 31,1986

ARO Identification Nbr. 21066-MS

Naval Sea Systems Command Contract N00024-85-C-5301

Photothermal (Thermal Wave) Imaging is a family of imaging methods with important applications for materials characterization and for the non-destructive evaluation of materials. These methods have contributed to an understanding of the properties of electronic materials and structural materials including metals, ceramics, composites, polymers and related organic systems, and to the location and characterization of defects in materials and electronic devices.

The work conducted under this program contributed to the development of an understanding and application of thermal wave imaging in a wide range of topics. This work has been partially described in publications in technical journals and talks at professional meetings. Additional information is contained in several other papers that have been accepted for publication, but have not yet been published.

The complete list includes:

1. L. C. Aamodt and J. C. Murphy, "A Thermal Wave Approach for Heterogeneous Materials with Continuously Varying Thermal and Optical Properties in One Dimension," 4th International Topical Meeting on Photoacoustic, Thermal, and Related Sciences, Ville d'Esterel, Quebec, Aug. 4-8, 1985.

2. L. C. Aamodt and J. C. Murphy, "Thermal Effects in Photothermal Spectroscopy and Photothermal Imaging," J. Appl. Phys., Vol. 54, No. 2, p. 581, 1983.
3. J. W. Maclachlan, J. C. Murphy, R. B. Givens, and F. G. Satkiewicz, "Linear Thermal Wave Imaging," 11th World Conference on Nondestructive Testing, Nov. 3-8, 1985, Las Vegas, Dallas: Taylor Publishing Co., p. 441, 1985.
4. F. G. Satkiewicz, J. C. Murphy, L. C. Aamodt, and J. W. Maclachlan, "Ion-acoustic Imaging of Subsurface Flaws in Aluminum," 4th International Topical Meeting on Photoacoustic, Thermal, and Related Sciences, Ville d'Esterel, Quebec, Aug. 4-8, 1985.
5. F. G. Satkiewicz, J. C. Murphy, L. C. Aamodt, and J. W. Maclachlan, "Ion-acoustic Imaging of Subsurface Flaws in Aluminum," Williamsburg, VA, June 23-28, 1985, Review of Progress in Quantitative NDE, Plenum Press, 1986.
6. J. C. Murphy, J. W. Maclachlan, R. B. Givens, F. G. Satkiewicz, and L. C. Aamodt, "The Generation of Ultrasound by Laser, Electron and Ion Probes and Its Application to the Characterization of Materials," Proceedings of Ultrasonics International 1985, London: Butterworth Scientific, 1985.
7. J. W. Maclachlan, R. B. Givens, J. C. Murphy, and L. C. Aamodt, "Contrast Mechanisms in Scanning Electron Acoustic Imaging of Grain Boundaries," 4th International Topical Meeting on Photoacoustic, Thermal, and Related Sciences, Ville d'Esterel, Quebec, Aug. 4-8, 1985.
8. Grover C. Wetsel, Jr., "Photothermal Generation of Thermoelastic Waves in a Composite Media", IEEE Transactions on Ultrasonics, Ferroelectrics, and Frequency Control, Vol. 33, No. 5, pp. 450-461, 1986.

9. G. C. Wetsel, Jr., J. B. Spicer, J. W. Maclachlan, and J. C. Murphy, "Comparison of Photoacoustic and Photothermal Optical Beam Deflection Imaging of Subsurface Structure in Solids," 1985 IEEE Ultrasonics Symposium Proceedings, San Francisco, October 1985.
10. J. W. Maclachlan and J. C. Murphy, "Thermal Wave Imaging for Materials Characterizations," Proceedings of 2nd International Symposium on the Non-Destructive Characterization of Materials, Montreal, July 1986, Plenum Press, 1986.
11. G. C. Wetsel, Jr., J. W. Maclachlan, J. B. Spicer, and J. C. Murphy, "NonDestructive Evaluation and Materials Characterization Using Photothermal-Optical-Beam-Deflection Imaging," Review of Progress in Qunatitative NonDestructive Evaluation, Edited by D. O. Thompson and D.E. Chimenti (Plenum Pub. Co), Vol. 5A, p. 713 (1986).
12. J. C. Murphy, L. C. Aamodt, F. G. Satkiewicz, R. B. Givens, and P. R. Zarriello, "Materials and Microstructure," Johns Hopkins APL Technical Digest, Vol. 7, pp. 187-199 (1986).
13. L. C. Aamodt and J. C. Murphy, "Thermal Effects in Materials with Continuously Varying Optical and Thermal Properties in One Dimension," Can. J. Phys. to be published.
14. G. C. Wetsel, Jr., J. C. Murphy, and L. C. Aamodt, "Non-Destructive Characterization of Coatings on Metal Alloys", Review of Progress in Quantitative NDE, to be published.
15. J. C. Murphy, L.C. Aamodt, and G. C. Wetsel, Jr., "Coating Thickness Determination Using Time Dependent Surface Temperature Measurements," Review of Progress in Quantitative NDE, to be published.

16. J. C. Murphy, J. W. Maclachlan, and L. C. Aamodt, "Image Contrast Processes in Thermal and Thermoelastic Imaging", IEEE Transactions on Ultrasonics, Ferroelectrics and Frequency Control, Vol.33, No. 5, pp. 529-541, 1986.

Copies of these publications are attached to this report. The last of these publications is a review article which surveys the field of contrast mechanisms in thermal wave imaging, including our work and the work of others.

In addition to these publications, Jane W. Maclachlan, a graduate student at The Johns Hopkins University, has completed work toward a doctorate degree in Materials Science based upon work that she has done supporting the experimental work performed under this contract. Dr. Grover C. Wetsel, Jr., a visiting professor from Southern Methodist University, has contributed to some of the results reported here.

The work summarized in this report extended over many aspects of thermal wave imaging. This brief report describes our general approach and highlights our major results. Details of the work done is contained in the sixteen papers listed above which should be considered to be an integral part of this report.

In carrying out the work done in this program, an effort was made to pursue basic issues related to thermal wave imaging. Special attention was given to contrast mechanisms operative in thermal wave imaging - i.e., those processes that produce the image. These studies have been applied to both natural and fabricated interfaces in sample materials, including grain boundaries and artificially created cracks in metals.

To provide a background for the analytic and experimental results described below, we begin with a brief description of thermal wave imaging.

THERMAL WAVE IMAGING: Theory and Techniques.

Thermal Wave Imaging is characterized by use of a modulated excitation source to heat a sample specimen in a controlled manner [1-3]. Imaging methods are distinguished by the type of excitation source used and by the method of detecting a temperature change in the specimen. Image contrast depends upon spatial variations in specimen properties and upon how these variations are converted into a measureable detected signal.

A. Survey of Thermal Wave Imaging Techniques

Figure 1 is a composite sketch representing most of the major thermal wave imaging methods. The sample shown in this figure is opaque to the incident beam, but thermal wave imaging techniques can also be used with transparent specimens [4]. The modulated excitation beam shown in Fig. 1 is vertically incident on the specimen. This beam is typically a laser or particle (e.g. electron or ion) beam, but it could also be a microwave [5,6] or a sound beam [7]. Other modulated heating methods that have also been used include a resistively-heated source [8] attached to the sample and rf induction heating [9]. In all cases the excitation heats the specimen directly, by some relaxation process particular to the specimen being studied, and heats it indirectly, via thermal or mass diffusion within the specimen.

Several detection methods are shown in Fig. 1. Optical beam deflection (OBD) or "mirage" detection (Method 1) [10-12] is represented by the surface skimming probe ray traveling through a gas or liquid in thermal contact with the surface of the sample. This ray is deflected by the "thermal lens" created by time-dependent refractive index variations in the fluid caused by

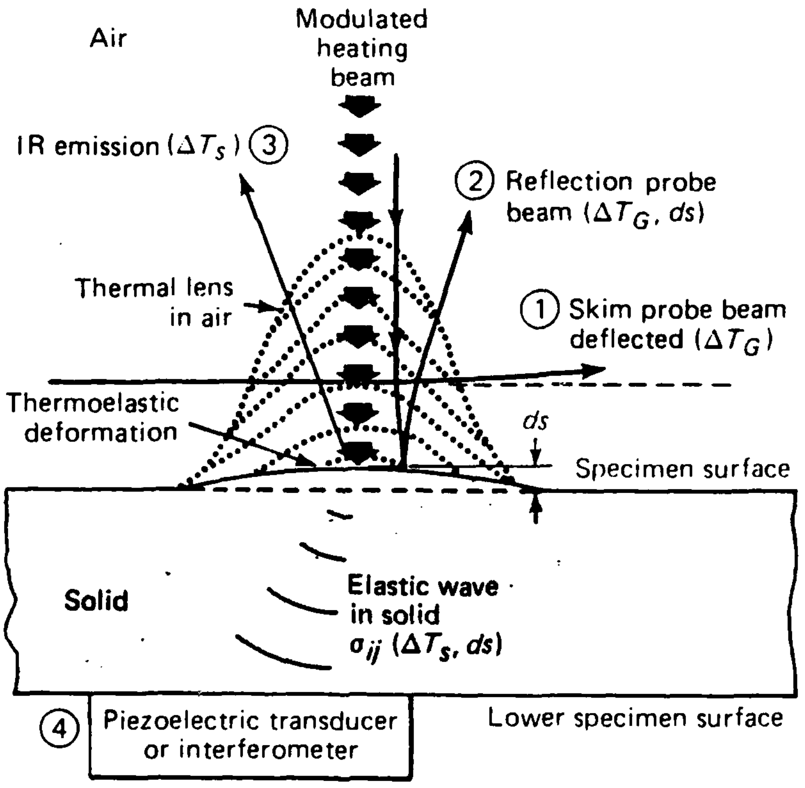

Fig. 1 Composite sketch summarizing several thermal wave imaging methods (1) Optical Beam Deflection, (2) Reflective Optical Beam Deflection, (3) IR radiometric, (4) Thermoelastic (transducer or interferometric).

heat transfer from the specimen, and the deflection is measured by a position sensitive optical detector, either a sectored quadrant detector, a lateral detector or a conventional optical detector apertured by a knife edge.

The geometry of the OBD process is shown in further detail in Fig. 2. The deflection, $\vec{\phi}$, [12] is a vector quantity measured relative to the undeflected probe beam path and the normal to the sample surface. This deflection can be decomposed into a deflection in the plane defined by the probe ray and the normal to the specimen surface (normal component), and a deflection in the plane orthogonal to that plane (transverse component) [12,13]. Each of these components has a special physical significance and a simple relationship to the sample surface temperature. The normal deflection of the probe beam is proportional to the average surface temperature along the projection of the probe beam path on the sample surface, while the transverse component is sensitive to the average surface temperature gradient orthogonal to the probe ray along this same path. Both of these relationships are implicit in the vectorial expression for the beam deflection,

$$\vec{\phi} = - \int_p dn/ndT_g \, \nabla T_g \times d\vec{\ell} \qquad (1)$$

Here n and $T_g(x,y,z)$ are the thermally dependent index of refraction, and temperature, respectively, of the fluid above the sample surface, $d\vec{\ell}$ is an incremental length along the probe beam path, and p is probe beam path along which the line integral is integrated. [See Refs. 12, 13 for details. These references derive the dependence of the deflection on the distance of the probe beam above the sample surface (normal offset) and the dependence on the separation of probe and excitation beam axes (transverse offset). They also

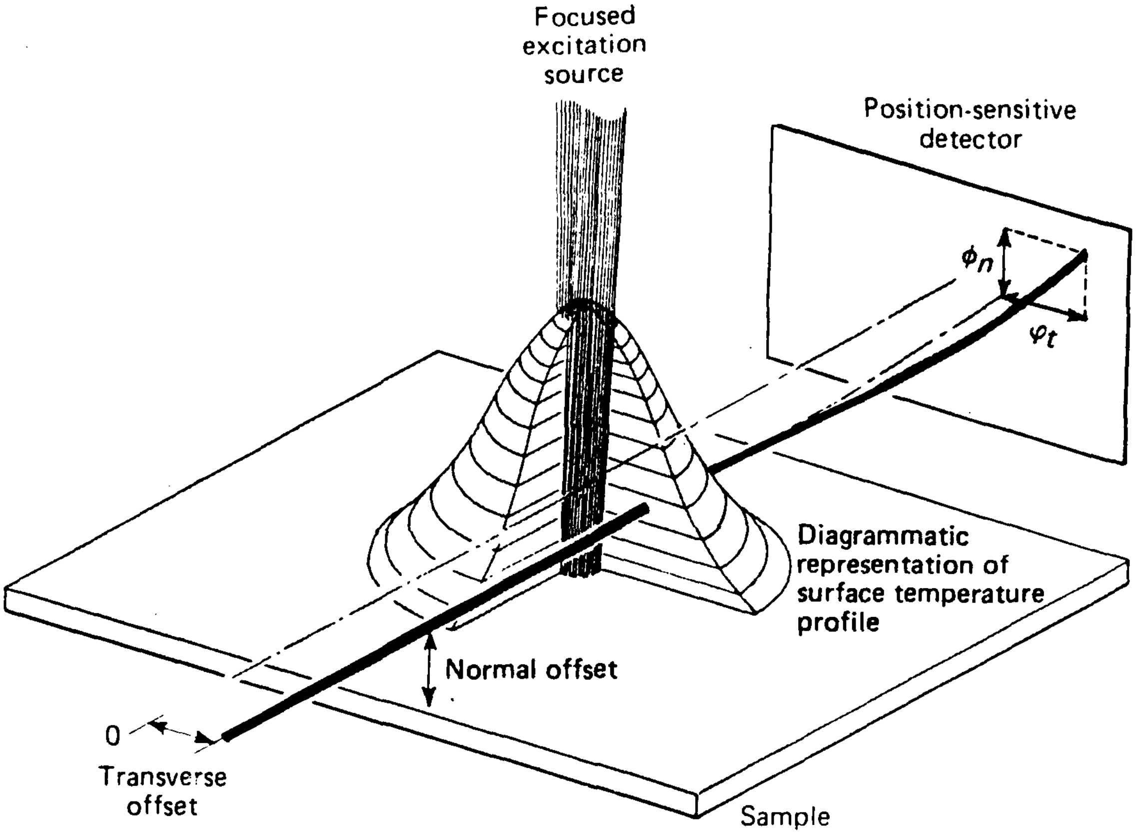

Fig. 2 Schematic of the Optical Beam Deflection Imaging Method showing the two deflection components mentioned in the text.

describe the surface temperature pattern produced by a Gaussian excitation beam on a homogeneous sample.]

For a radially symmetric beam and for isotropic specimens, the amplitude of the transverse signal is zero when the two beam axes intersect. In this configuration, the transverse component is a sensitive monitor of thermal anisotropy in the specimen. Measurement with two probe beams angularly displaced, in principle, permits the reconstruction of the specimen surface temperature distribution by a method somewhat resembling x-ray tomography.

In Fig. 1, Reflective Optical Beam Deflection (Method 2) [14,15] is represented by the vertically-oriented probe ray. This ray is approximately parallel to the excitation beam. It passes through the thermal lens region discussed above and is detected by a position sensitive optical detector after reflection from the specimen surface. In reflected OBD detection, the reflected beam is affected by a thermally induced deformation of the specimen produced locally near the heated region as well as by the thermal lens in the fluid above the sample surface. Image formation may also involve thermal modulation of specimen reflectivity (thermo-reflectance) [16].

Method 3 in Fig. 1 is optical interferometry [17,18]. This method monitors the vertical component of sample surface displacement produced by thermally generated elastic waves in the sample. It is complementary to the reflective optical beam deflection imaging in that interferometry detects the vertical displacement of the surface deformation of the specimen while the optical beam deflection detects the angular tilt of the surface.

Photothermal radiometry (PTR) (Method 3) [19-21] is based on the enhanced IR emission of a heated object. Figure 3a shows the spectral distribution of IR emission for a heated black body at several selected temperatures while

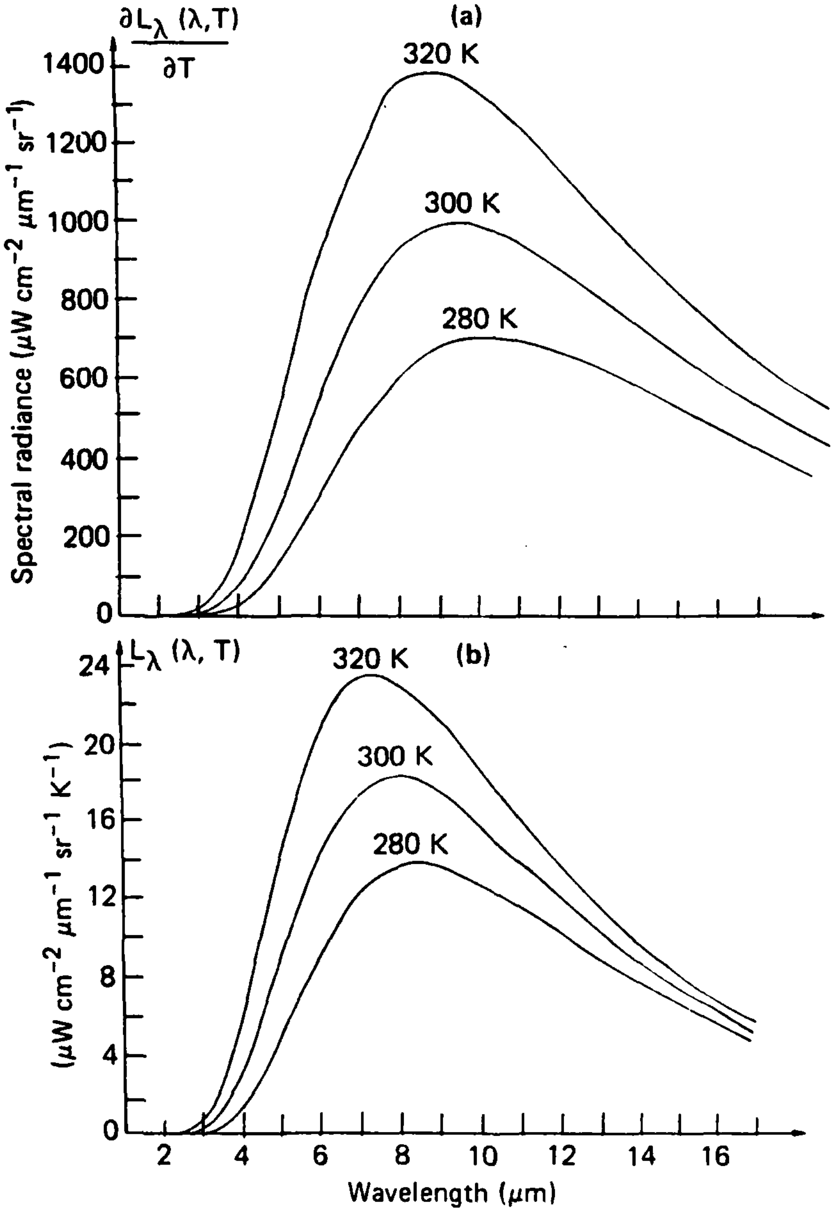

Fig. 3 (a) The spectral distribution of IR emission for a heated black body at several selected temperatures; (b) The spectral distribution of the incremental emission assuming a 1° K change in sample temperature.

Fig. 3b shows the spectral distribution of the incremental emission assuming a 1^0 K change in sample temperature. For actual specimens, these black body curves must be multiplied by the wave length dependent specimens emissivity to yield curves that can be compared with experiment.

This method is non-contacting and is capable of parallel acquisition of the spatially-resolved surface temperature by using devices such as detector arrays or pyrovidicons. Photothermal radiometry has been applied to a range of applications including measurement of thin film thickness on a variety of substrates and to studies of thermal transport in layered materials. PTR can provide image contrast through spatial variations in emissivity.

The last method shown in Fig. 1 (Method 4) detects thermoelastic stress using an attached transducer [22-25] or an optical interferometer [26,27] placed at a point of the sample removed from the point of heating. The detector position shown in the figure is on the side of the sample opposite to that illuminated by the exciting beam, but other geometries are possible and may offer some advantages in specific applications. Method 4 involves both the temperature field in the sample and the elastic and thermoelastic response of the sample in the signal formation process and is termed a thermoelastic(TE) method in this report.

B. Theoretical Background

Detection methods for thermal wave imaging can be classified as being either THERMAL or THERMOELASTIC. THERMAL detection is a local, scalar process in which image data depends upon the temperature pattern developed on the sample surface by local heating. The image may also depend upon which temperature dependent physical parameter is being measured. (This analysis assumes that the only important transport process is thermal diffusion. For semiconductor samples or for certain luminescent or porous solids where mass or excitation transport can occur, the equations must be modified to incorporate these effects. The present analysis is adequate for the samples discussed in this report.) THERMOELASTIC detection, on the other hand, is a nonlocal process which depends upon both the thermal and mechanical properties of the sample via the thermoelastic effect. Elastic waves are created by expansion of the sample during localized heating, and as a result the detection signal depends upon both the surface and bulk temperature of the sample.

The basic relationship between these two types of imaging is expressed by the two coupled thermoelastic equations [28-30]:

$$\nabla^2 T - \alpha^{-1} \partial T/\partial t = -H(r,t)/\kappa + (T\ \beta_t B/\kappa)\ \nabla\ \partial\vec{u}/\partial t \qquad (2)$$

$$\nabla^2 \vec{u} + (1+\lambda/\mu)\nabla(\nabla\ \vec{u}) - (\rho/\mu)\ \partial^2\vec{u}/\partial t^2 = (\beta_t B/\mu)\ \nabla T \qquad (3)$$

where $T(x,y,z)$ is the temperature throughout the sample volume, $\vec{u}(x,y,z)$ is the elastic displacement vector, κ is the thermal conductivity, α is the thermal diffusivity, β_t is the volume thermal expansion coefficient, λ and μ are the Lame´ constants, ρ is the density, B is the bulk modulus, and $H(x,y,z,t)$ is the heat source, developed as the incident radiation in the excitation beam is converted to heat. H is the source function for Eq. 2, directly, and Eq. 3, indirectly. In general, it extends throughout the specimen volume although for strongly absorbing specimens it may be significant only near the specimen surface.

The right hand term in Eq. 2 represents heat produced by particle displacements associated with an elastic wave. This term is usually small. When it can be ignored, the two equations are partially decoupled, and the temperature pattern in the sample is produced by the 3 dimensional thermal diffusion equation:

$$\nabla^2 T - \alpha^{-1} \partial T/\partial t = - H(r,t)/\kappa, \qquad (4)$$

subject to thermal boundary conditions. This pattern exclusively determines the thermal wave image when THERMAL detection methods are used.

In THERMOELASTIC thermal wave imaging, the displacement, $\vec{u}$, is measured. $\vec{u}$ depends upon the elastic properties of the specimen via Eq. 3, and upon elastic boundary conditions in the sample (in the near field limit). Since the source term for Eq. 3 is the temperature obtained from the solution of Eq. 2, $\vec{u}$ also depends upon the sample's thermal properties and thermal boundary conditions.

The sample temperature determined from the thermal diffusion equation may be solved for $T_s(x,y)$ and $T_b(x,y,z)$, the surface and bulk specimen temperatures, respectively. This analysis leads to a determination of T_b and T_s as functions of position and time, or, for CW modulation, as a function of ω, the angular modulation frequency [13,31,32].

For opaque solids most THERMAL thermal wave imaging techniques depend directly on T_s. In OBD imaging, for example, there is heat transfer from the specimen surface to the adjacent fluid and the specimen parameters are reflected in the image through changes in T_s. This dependence on T_s makes thermal diffusion an integral part of the imaging process, and consequently intrinsically restricts it to long observation times or low modulation frequencies when sub-surface details of the specimen are of interest or depth profiling is important.

For opaque solids where only surface heatings exists, THERMOELASTIC thermal wave imaging depends on an integral over the specimen volume that is affected by thermal diffusion. Thus, T_b contributes to the image directly, not indirectly, through its effect on T_s. This result provides the basis for the observation that subsurface features can be detected at greater depths in THERMOELASTIC imaging than in thermal imaging. Since temperature changes in the specimen directly generate stress which is detectable by the transducer, the role of thermal diffusion in the signal generation process is reduced. Some increase in modulation frequency and hence scanning rate may be made. These findings are summarized in greater detail below.

Some of the characteristics of bulk and surface temperature is evident in an analysis of heat flow in thin films [33], which was made in order to provide a theoretical basis for our experiments [34] characterizing thin film samples, specifically determining their thickness and the quality of their bonding.

For a thermally thick planer sample with a thin coating on its surface, the surface temperature is given by the expression,

$$
\begin{aligned}
T_{surf}(\vec{\rho},t) = {} & (2\pi)^{-3} \iiint_0^{\zeta} \tilde{H}_{\rho t}(\vec{\lambda},\omega)\ (1-\Gamma_0)\ H_z(u)\ (D/2\kappa) \\
& \times \left[\exp(-u/D)+\sum_{\ell=1}^{\infty} \Gamma_1^{\ell}\ \exp(-2\zeta\ell/D)\ (\exp(-u/D)-\exp(u/D)/\Gamma_0)\right] \\
& \times \exp(j(\vec{\lambda}\cdot\vec{\rho}+\omega t))\ d\vec{\lambda}\ d\omega\ du\ . \qquad (5)
\end{aligned}
$$

if the coating is sufficiently opaque so that heat generation occurs in the coating only. The bulk temperature in the coating is given by the expression,

$$T_{bulk}(\vec{\rho},z,t) = (2\pi)^{-3} \iiint \tilde{H}_{\rho t}(\vec{\lambda},\omega)\ (D/2\kappa)[\int_0^z H_z(u)\ \{\exp(-(z-u)/D)$$

$$- \exp((z-u)/D)]\ du + \{\exp(z/d)-\Gamma_0\exp(-z/d)\} \int_0^\zeta H_z(u)\ \{\exp(-u/D)$$

$$+ \sum_{\ell=1}^{\infty} \Gamma_1^\ell \exp(-2\ell\zeta/D)\ (\exp(u/D) - \Gamma_0 \exp(-u/D)/\Gamma_0)\}\ du\ ]$$

$$\times \exp(j(\vec{\lambda}\ \vec{\rho}+\omega t))\ d\vec{\lambda}\ d\omega \qquad (6)$$

The integral limits not specified are from $-\infty$ to ∞. $\tilde{H}_{\rho t}(\vec{\lambda},\omega)$ is the Fourier transform of the excitation beam spatial distribution on the sample surface, $H_z(u)$ is the spatial dependence of heat generation in the sample with depth (z), D is the effective complex thermal diffusion length for the $\vec{\lambda}$ spatial harmonic ($D= \surd[\lambda^2+ j\omega/\alpha]$), α is the thermal diffusivity of the sample coating, κ is the thermal conductivity of the coating, ζ is the coating thickness, $\vec{\rho}$ is the position coordinates in the transverse plane, z is the depth in the sample, Γ and Γ_0 are the thermal match at the substrate-coating and the air-coating interfaces, respectively, and $\Gamma_1= \Gamma\ \Gamma_0$. [The thermal match is a measure of the thermal discontinuity at an interface of two layers having different thermal properties. In general, $\Gamma_{12}= [(D/\kappa)_1- (D/\kappa)_2] /[(D/\kappa)_1 + (D/\kappa)_2]$ at the interface of any two adjacent layers, 1 and 2.]

The summation in Eqs. 5 and 6 represents successive reflections of the thermal wave at the coating-substrate interface. The factor $2\ell\zeta$ is the total distance travelled in the ℓth order reflection.

Equations 5 and 6 simplify for two experimentally interesting cases. These are for an opaque sample with spatially uniform excitation and either a pulsed or harmonic excitation source.

For a harmonic source,

$$T_{surf}(\omega,t) = (\delta/\kappa)\ [1 + 2\sum_{\ell=1}^{\infty}(-\Gamma)^{\ell}\exp(-2\ell\zeta/\delta)]\ \exp(j\omega t) \tag{7}$$

and

$$T_{bulk}(z,\omega,t) = (\delta/\kappa)\exp(-z/\delta)[1 + \sum_{\ell=1}^{\infty}(-\Gamma)^{\ell}\{\exp(-2\ell\zeta/\delta)$$

$$+ \exp((z-2\ell\zeta)/\delta)\}]\ \exp(j\omega t) \tag{8}$$

where δ is the complex thermal diffusion length.

As expected, the bulk temperature is attenuated through the multiplicative factor, $\exp(-z/\delta)$, which is typical for heat diffusion from the sample surface. The terms in the summation, however, indicate that the thermal interaction with the reflecting interface is different for the surface and bulk temperatures.

This result is mirrored in the time regime where

$$T_{surf}(t) = (\pi\kappa C)^{-1/2}\int_{0}^{\infty} H_t(t-u)\ [1 + 2\sum_{\ell=1}^{\infty}(-\Gamma)^{\ell}\exp(-\ell^2\zeta^2/\alpha u)]\ du/\sqrt{u} \tag{9}$$

and

$$T_{bulk}(z,t) = (\pi\kappa C)\int_{0}^{\infty} H_t(t-u)\ \exp(-z^2/4\alpha u)\ [1 + \sum_{\ell=1}^{\infty}(-\Gamma)^{\ell}\exp(\ell^2\zeta^2/\alpha u)$$

$$\times \{\exp(\ell\zeta z/\alpha u) + \exp(\ell\zeta z/\alpha u)\}]\, du/\sqrt{u} \qquad (10)$$

where $H_t(t)$ is the temporal excitation pulse shape.

INSTRUMENTATION

To provide the capability of using particle as well as laser sources for imaging, a Scanning Electron Microscope (SEM) and a Secondary Ion Spectrometer (SIM) were modified to create, respectively, a Scanning Electron Acoustic Microscope (SEAM) and a Scanning Ion Acoustic Microscope (SIAM).

The SEM that was modified was an ETEC Autoscan Secondary Electron Microscope equipped with a 200 litre/second ion pump. It's beam blanking system was magnetic and much too slow for acoustic imaging. The magnetic blanking coil was replaced with an electrostatic blanking system of our own design. By grounding one plate and reducing stray coupling between the beam blanking system and the detection system to a minimum, a 125 volt square wave blanking pulse was obtained with a rise time of 20 ns. We typically use the same 200μ beam aperatures for both acoustic and SEM imaging. We have used a variety of PZT transducers and peripheral electronic equipment. An important aspect of the electronic system is the use of a high (1μHz) resolution synthesizer as the system clock. This has allowed for greater control than has been previously reported by others.

The basic SIMS modified for thermoacoustic imaging was a GCA IMS-101B with a high voltage capability of 12 Kv at 15 μA designed to generate secondary ions by ion-sputtering. Again an electrostatic beam blanking system was developed and installed for beam modulation, and a PZT detection was added within the vacuum chamber.

Figure 4 shows a block diagram of the electron or ion acoustic sytem capable of simultaneously detecting specimen current and the acoustic (PZT) signal. Provisions were made for spectrum analysis in certain experiments.

Figure 5 shows the block diagram for a photothermal imaging system that can simultaneously monitor surface temperature through mirage detection and through PZT detection. The specific need for this capability is discussed below in the section reporting on thermoelastic contrast mechanisms.

IMAGE CONTRAST MECHANISMS

The structure (i.e., contrast features) of a thermal wave image is affected by many factors. A number of potential contrast mechanisms have been identified, and some controversy has existed over their relative importance. This issue is further complicated by a mechanism involved in visual processing in the brain (the Craik-O'Brien effect) [35]. This mechanism induces an apparent contrast between areas on either side of a visible boundary, a contrast that is not observed in numerical processing of the image data. We have observed this effect in SEAM (Secondary Electron Acoustic Microscope) images of grain structure in aluminum, and it is presumably a common feature of other images. When viewing thermal wave images with strong boundary contrast, care must be taken to ensure that this effect does not influence the interpretation of the image.

A thermal wave image is initiated by a beam of energy (radiant or particle) impinging upon the surface of a sample specimen. The contrast features

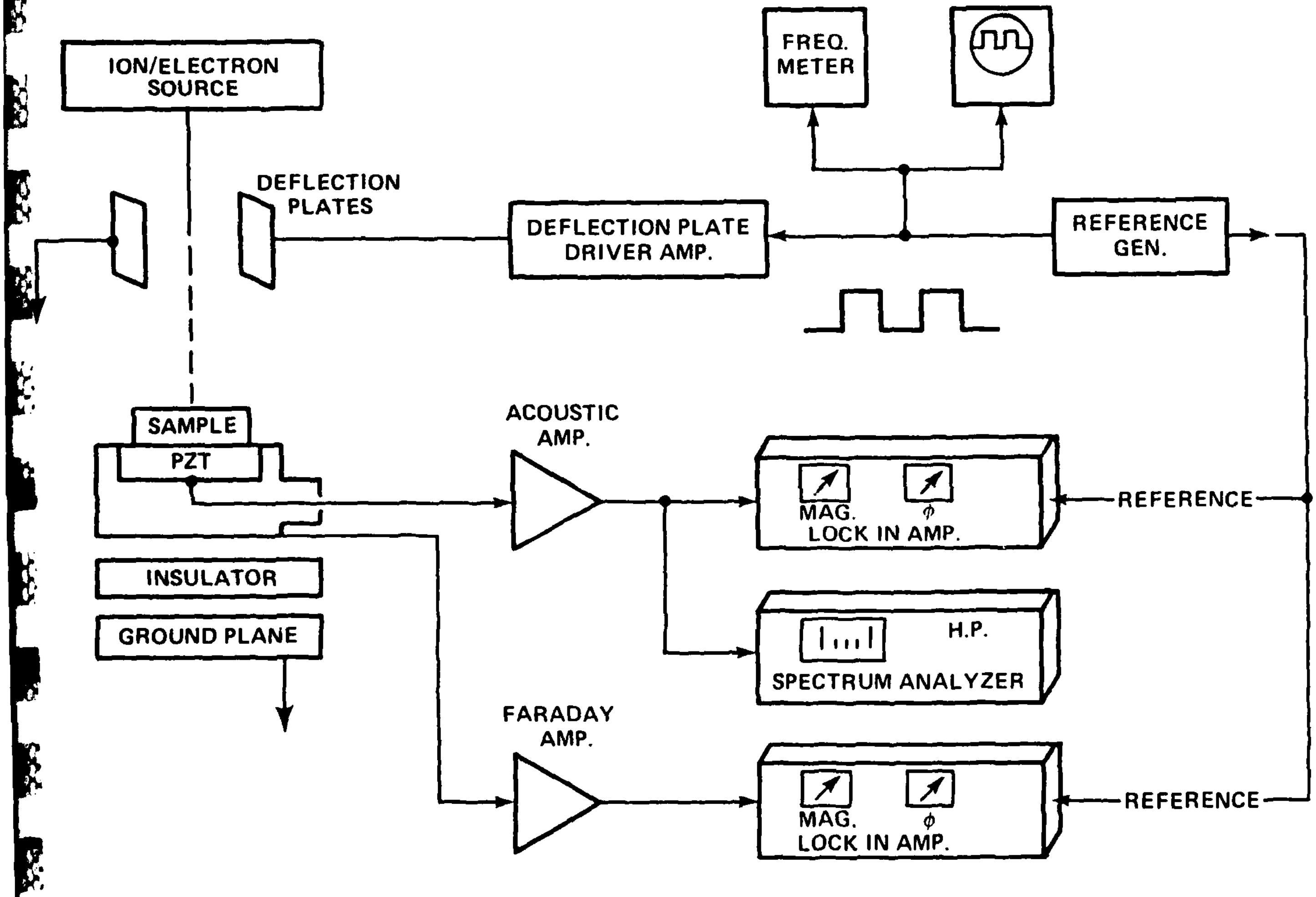

Fig. 4 Block diagram of electron or ion acoustic detection system showing simultaneous detection of specimen current.

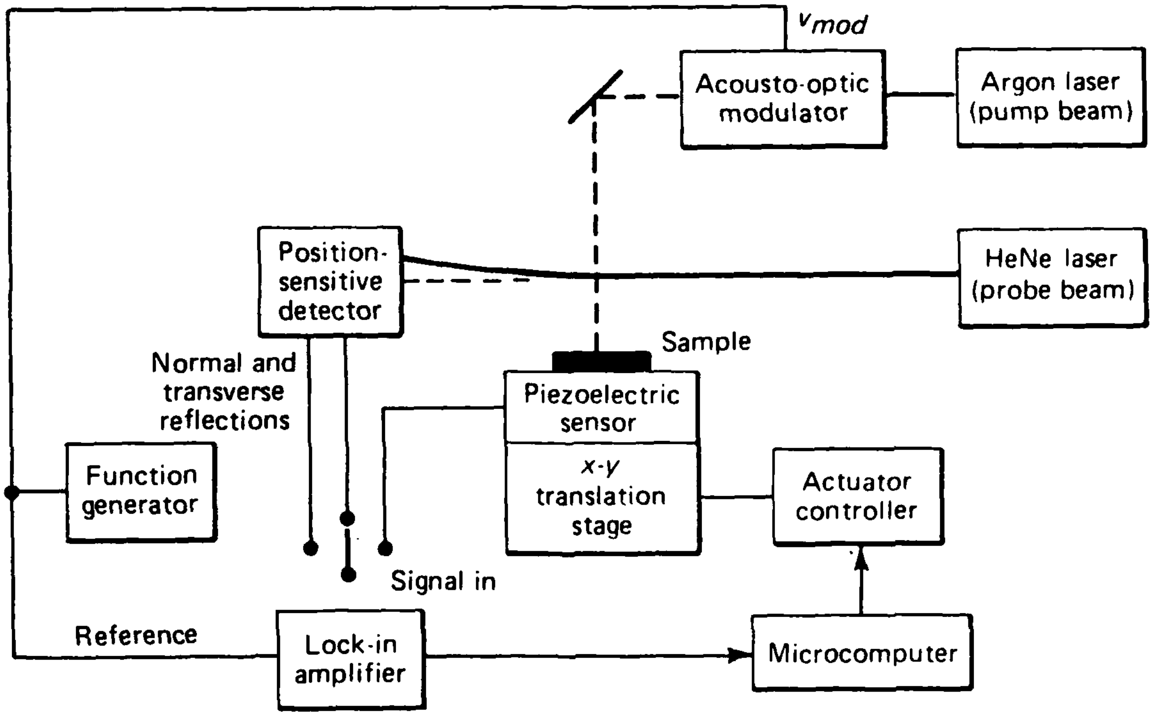

Fig. 5 Block diagram of laser source optical beam deflection and acoustic imaging system.

in the final thermal image results from a variety of contrast mechanisms operative between the initial conversion of the input beam energy into heat and the final detection of changes in the thermally dependent properties of the material.

These contrast mechanisms are not well understood, and it has been one objective of this research to identify potential contrast mechanisms, to determine their relative importance, and to apply this information to help thermal wave imaging become a tool for quantitative characterization of materials. The results of this investigation indicates that these mechanisms differ in significance depending upon the sample, upon the method of illumination, upon the method of detection, and upon experimental operating parameters as below.

Contrast mechanisms can be separated into three categories:

1. Beam Specimen Mechanisms - These are related to the method of heat formation within the sample and depend upon the nature of the beam and manner of illumination as well as upon the sample itself.
2. Thermal Contrast Mechanisms - These are related to heat flow within the sample and consequently they are affected by sample thermal inhomogeneities and thermal barriers produced by impurities and major defects in the sample material.
3. Thermoelastic Contrast Mechanisms - These are related to the interaction between the thermal and mechanical systems in the sample and upon acoustic transmission and mechanical boundary conditions in the sample medium.

Each of these contrast mechanisms will be discussed separately.

1. Beam-Specimen Contrast

Beam-specimen interactions are manifest in a variety of ways. For optical sources, a spatial dependence of the optical absorption or the reflectivity occurs, either of which may be wavelength dependent. For specimens which show photochemical or photocatalytic activity including semiconductors or phosphorescent materials, spatial variations in the rate of conversion of light to heat contribute to the image as does carrier or excitation migration/diffusion.

For electron sources, spatial variations in the fraction of beam energy absorbed and the spatial distribution of the absorbed energy are sources of beam-specimen contrast. The volume over which the beam is absorbed is related to the energy distribution of both secondary and backscattered electrons. The secondary electron yield is of prime importance to SEM microscopy, however, it is the rate of heat deposited in the specimen and its spatial distribution that plays the primary role in thermal wave imaging. Measurement of the specimen, secondary electron and backscattered electron currents alone does not adequately specify the thermal signal generation process.

To investigate electron beam-specimen contrast, several silicon IC's were thermally imaged. Figure 6 shows and compares secondary electron (SEM) and scanning electron acoustic microscope (SEAM) images of a silicon IC for two beam voltages (5 keV and 30 keV) [36]. A NBS conical transducer was used to detect the acoustic signals. At the lower beam voltage where the interaction depth is of the order of 0.5μ, both SEM and SEAM images show similar structure. At the higher beam voltage (interaction depth about 9μ), the SEAM image shows buried structure not observed in the SEM image. In other

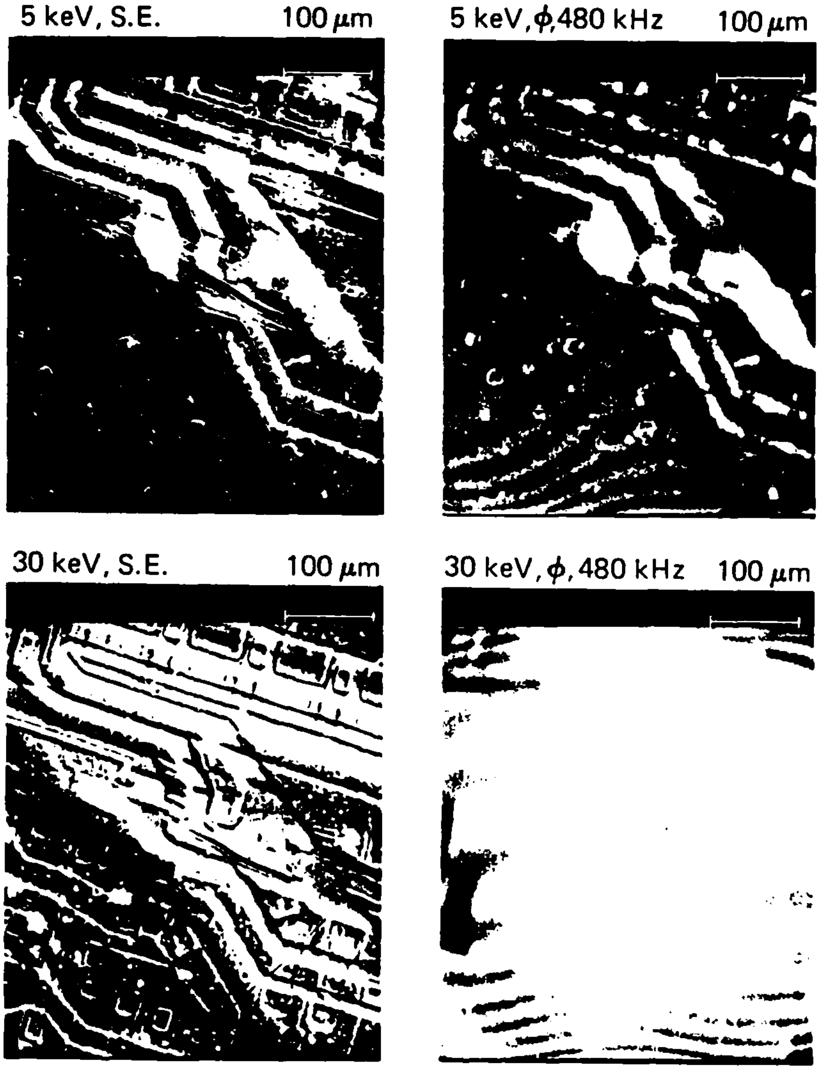

5 keV, S.E. 100 μm

5 keV, ϕ, 480 kHz 100 μm

30 keV, S.E. 100 μm

30 keV, ϕ, 480 kHz 100 μm

Fig. 6 Secondary electron and electron-acoustic images at two primary beam voltages showing beam-specimen contrast.

experiments it was found that one origin of the contrast observed in the SEAM images was spatial changes associated with impurity doping. Thermal spreading of the details of the image is observed at lower modulation frequencies.

Ion specimen interactions have been widely studied and ion bombardment has become an important tool for semiconductor processing and surface treatment of materials [37,38]. In addition, ion beams have been used as analytical tools in sputtering. We have shown that ion beams can also act as sources for thermal wave imaging. In general, the details of the interactions are complex and depend upon the ions used for bombardment, on the composition of the target and on the incident ion energy and total dose, among other parameters, all of which are topics of current interest. A common characteristic of ion sources is the existence of a "range" which defines a depth in the specimen at which a substantial fraction of the energy in the incident beam is selectively deposited. This raises the prospect that ions might be depth-selective probes for materials studies in imaging applications.

In light of the high ion mass (relative to electron mass) and the prospect of ion-specimen interactions specific to some beam-specimen combinations, the question of the role thermal and non-thermal beam-specimen interactions play in ion-acoustic imaging becomes important. One potential mechanism, which has been identified, is acoustic wave generation caused by ion impact and the related momentum transfer.

Momentum transfer is thought to be responsible for fast-ion beam recrystallization of silicon [39], where thermal contributions have been shown to be relatively unimportant. Secondary ion mass spectroscopy (SIMS) techniques based on ion sputtering mechanisms are thought to be dominated by momentum transfer to the specimen [40].

To investigate the relative importance of momentum and thermal mechanisms in ion-acoustic signal generation, an experimental study was made of beam voltage dependence. Figures 7a, b show the dependence of the acoustic signal in an aluminum specimen as a function of beam current and voltage, respectively. The relative importance of momentum and thermal processes in acoustic generation should vary with beam voltage V_B since the beam momentum rate, $P_B = \dot{N}_I(2M_I q V_B)^{1/2}$ where $\dot{N}_I$ is the ion fluence, q the specific ion charge, M_I the ion mass, and V_B the beam voltage. The resulting total acoustic signal S_T has both momentum and thermal terms:

$$S_T = S_{mom} + S_{TH} = K_1(1 + \frac{K_2}{V_B^{1/2}}) V_B$$

where K_1 and K_2 are constants. For a momentum-only process the slope in Fig. 7b would be 0.5 based on this relation. A thermal process would ideally have a slope of 1.0. In Fig. 7a the slope of acoustic signal is linear in beam current (slope ≈ 1). However, in Fig.7b, the slope of acoustic signal with beam voltage V_B is approximately equal to 0.8. This could be considered as suggesting that a strong thermal contribution is present along with a momentum contribution. This presumed thermal contribution far exceeds that expected based on the relative importance of momentum and thermal processes in the accepted theories of sputtering.

The dominant role of the thermal contribution to ion-acoustic imaging under specific experimental conditions is supported by line scan and image data comparing ion, electron and laser sources [41]. We have shown that all three sources give equivalent scanned images over a range of frequencies. The specimen studied was a 1 cm diameter aluminum disk 3 mm thick containing a

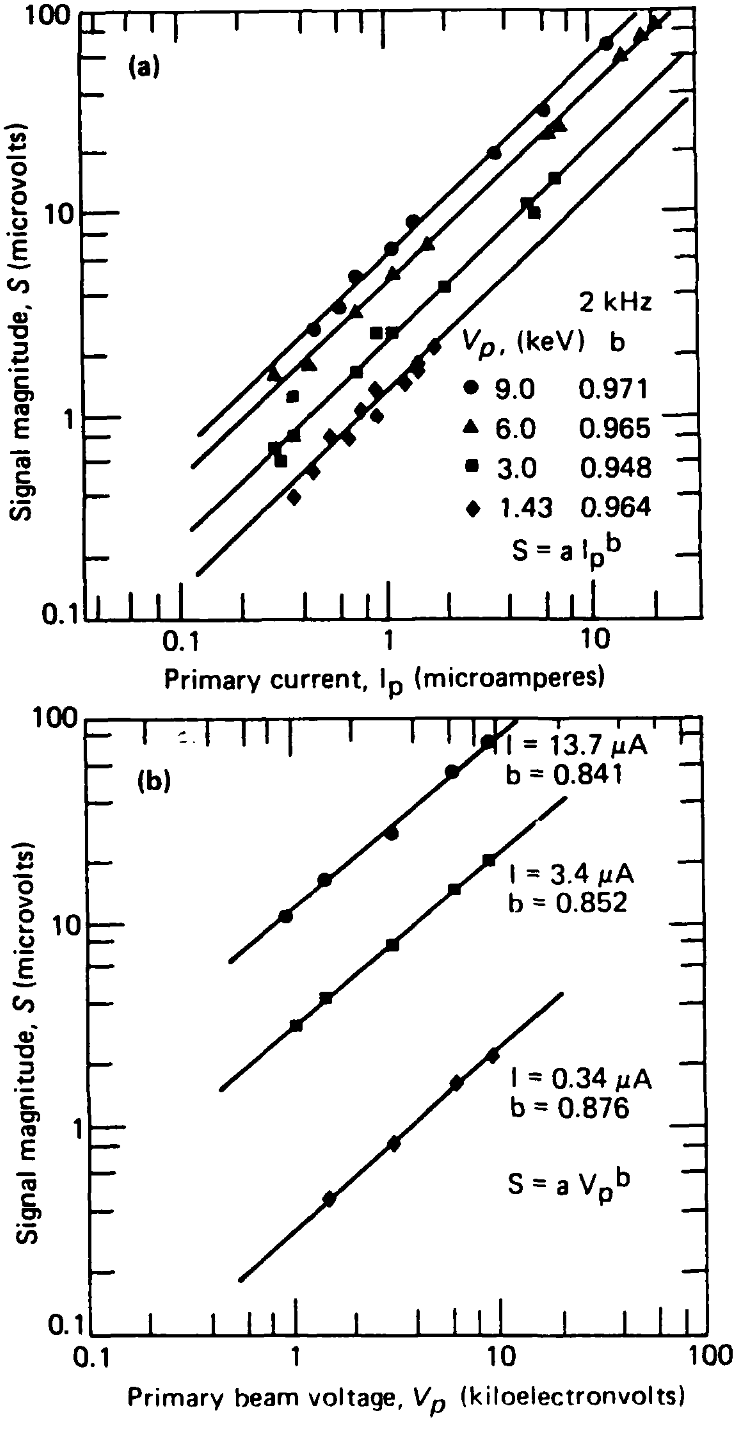

Fig. 7 Ion-acoustic signal dependence on beam current (a) and beam voltage (b). A slope of 1.0 is expected for the voltage dependence if thermal effects dominate and 0.5 if momentum processes dominate.

1 mm slant subsurface hole. Figure 8 shows ion line scans at constant slant hole depth for several frequencies. Figure 9 shows image and line scan data for the same sample using electron and laser sources at higher frequency and for a series of slant hole depths. In all three cases, the signal increases over the hole for $D/\delta_{TH} < 1$ where D is the depth of the slant hole at the scan location and $\delta_{TH} = [2\alpha/\omega]^{1/2}$ is the thermal diffusion length, with $\alpha = \kappa/\rho C$ and $\omega = 2\pi f$ the angular modulation frequency. As the ratio of D/δ_{TH} increases (either by increasing the depth of the hole or decreasing δ by increasing the frequency), the signal over the hole decreases and two lobes develop adjacent to the hole position. The specifics of these particular signal shapes are discussed in the Thermoelastic Contrast section of this report, but for the purposes of the present discussion on beam-specimen contrast mechanisms, it is important to note that these signal shapes are independent of excitation beam type, indicating a common thermal signal generation mechanism for all sources. This suggests that momentum transfer does not play a significant role in ion-acoustic imaging contrast under the conditions of these experiments. An additional test of the momentum mechanism was made by us using Ne, Ar, and Xe ions as the exciting source. At constant beam energy, the momentum increases through the series by 6 times, however, no change in acoustic signal was seen suggesting a minimal momentum term.

2. THERMAL Contrast

Thermal contrast mechanisms are widely observed in thermal wave imaging. They play a major role in current applications of thermal wave imaging to materials characterization and non-destructive evaluation of materials. In many of these studies the questions of interest are the visualization of

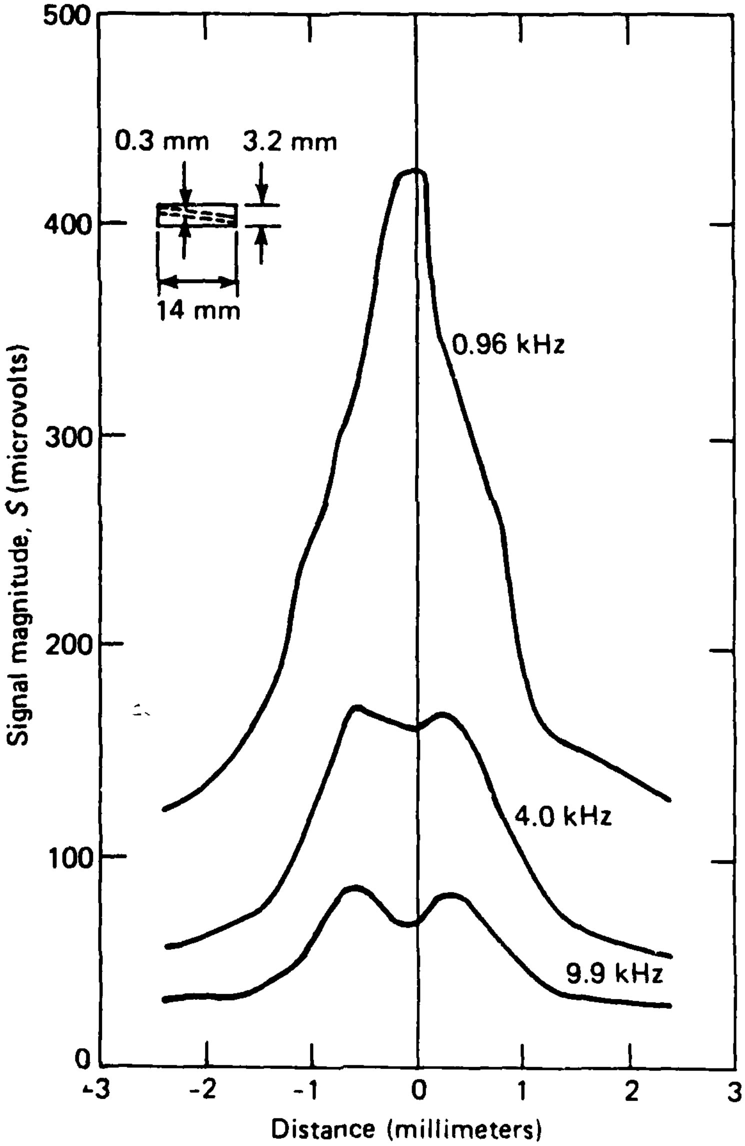

Fig. 8 Ion-acoustic profiles for a sample containing a subsurface slant hole. At low frequencies thermal interaction with the hole causes a signal increase. At high frequencies the signal generation process is still thermal but the contrast interaction is non-thermal.

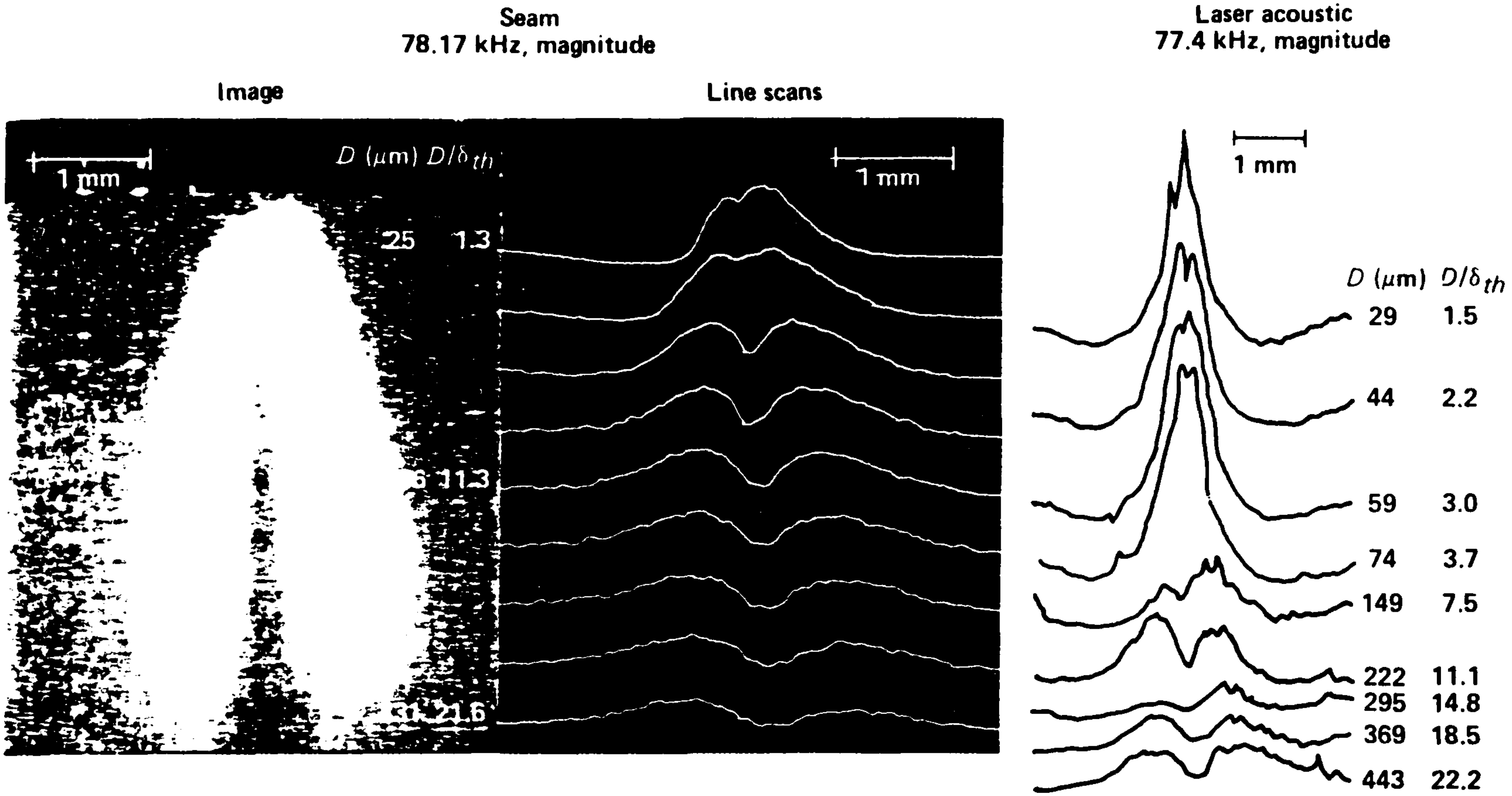

Fig. 9 Electron-acoustic image and line scans of sample of Fig. 8. Laser acoustic line scans are also seen. While the modulation frequency is much higher than that of Fig. 8, the information is similar. Particle and laser excitation yield similar specimen response.

specimen microstructure, location and sizing of buried defects in opaque solids, including cracks and voids, and the determination of the characteristics of films on a variety of substrates including the question of film thickness and bonding.

The importance of thermal contrast mechanisms in thermoelastic thermal wave imaging has been controversial. Some [2] have suggested that thermal contrast mechanisms are the important mechanisms responsible for imaging of microstructure in SEAM applications while others [42,43] have suggested that elastic anisotropy and other non-thermal contrast mechanisms are dominant, partly due to the importance of elastic contrast in acoustic microscopy.

To resolve these different conjectures, we obtained high contrast SEM and SEAM images of grain boundaries and specimen microstructure features. Figure 10 is an example of SEAM imaging of microstructure obtained on a specimen of polycrystalline aluminum. Contrast between grain interiors and contrast at the grain boundaries are both clearly observed. The dependence of the grain boundary width observed by SEAM on modulation frequency is shown in Fig. 11 [44]. The $\omega^{-0.5}$ suggests a thermal origin of the image.

Figure 12 shows SEM image with superimposed SEAM line scans measured on an aluminum bicrystal where the grain boundary is normal to the plane of the image. The precise position of the grain boundary is identifiable in the secondary electron image (on which the electron-acoustic line scans are superimposed) because of a preferential attack of the grain boundary by the chemical polishing procedure used. The physical extent of this attack was much smaller than a thermal diffusion length over the frequency range studied and did not influence the SEAM images. Data of this type were used to construct the dependence of boundary width on modulation frequency and the

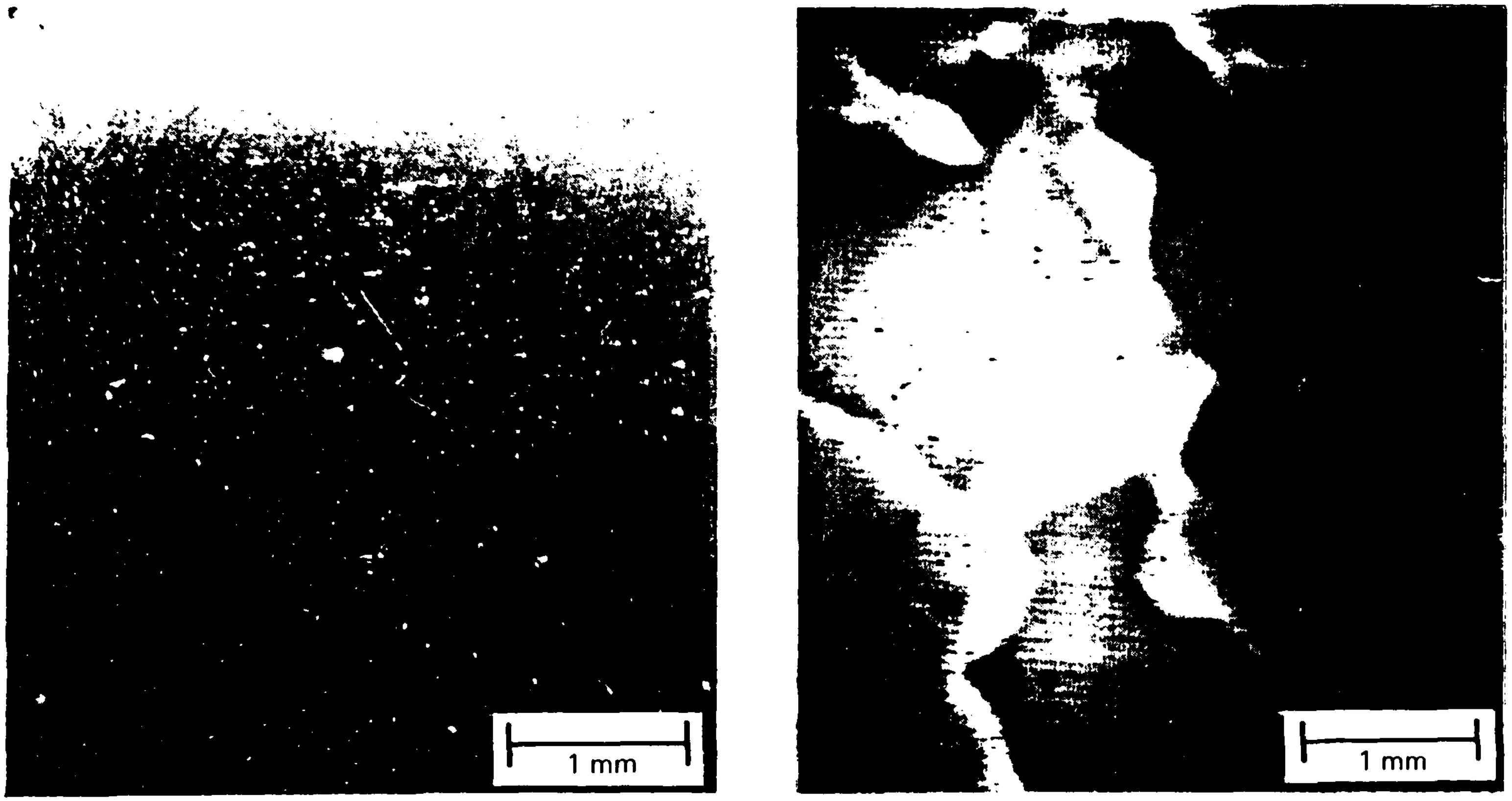

Secondary electron image Acoustic magnitude image

Fig. 10 Electron-acoustic image of grains in high purity aluminum. Note the presence of contrast at the grain boundaries and between the interiors of grains. Some of the interior contrast is due to the Craik-O'Brien effect.

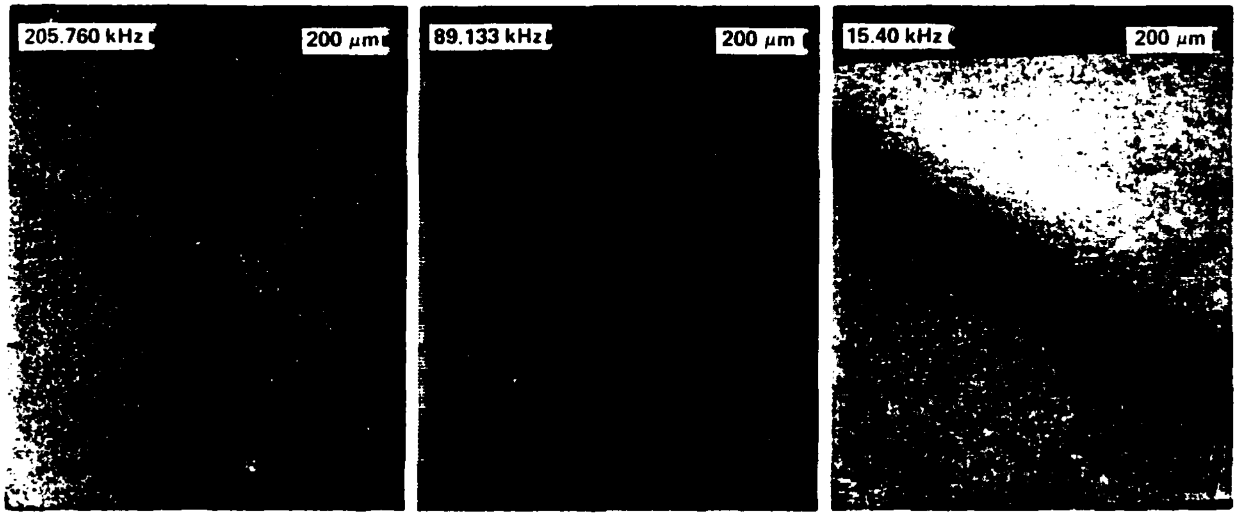

REVERSE
CALLOUTS

Fig. 11 Grain-boundary images of aluminum grains as a function of modulation frequency. The width varies as $\omega^{-0.5}$.

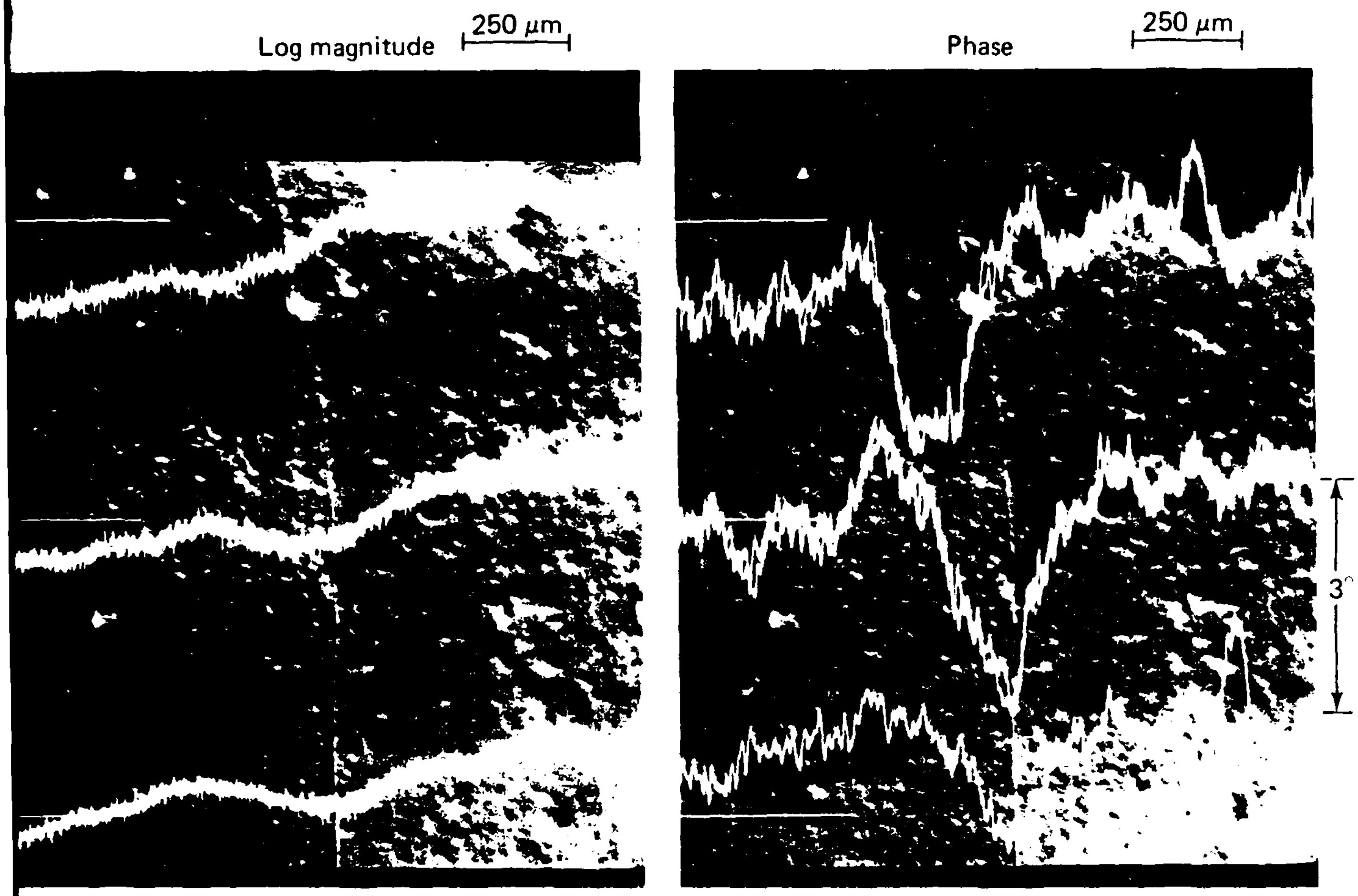

Fig. 12 Secondary electron image with an overlay of electron-acoustic line scans taken on a large bicrystal of aluminum. The crystal was over-etched to show the boundary. The position of the scans is indicated by the horizontal lines in the figure. Data for Fig. 12 used the response on the right hand side of the boundary because of the interfering subsurface structure seen on the left hand side.

results are shown in Fig. 13. The solid line indicates the thermal diffusion length in pure aluminum as a function of $\omega^{-0.5}$. The data points indicate the half-width-half-maximum (HWHM) value for the phase signal on the right hand side of the boundary for the middle line scan of Fig. 12 for a series of 5 different frequencies. This indicates a definite thermal component to the boundary contrast observed in SEAM images of grain structure. Elastic contrast mechanisms are not excluded from a role in microstructural contrast, however.

Thermal contrast depends upon spatial variations in the thermal properties of the specimen, κ and ρC and through them, upon temperature, composition, and doping (in the case of semiconductors and many other materials). For homogeneous specimens these parameters may be determined by using modulated temperature methods through the temporal or frequency response of the specimen temperature. The degree of homogeneity required [32] depends on the thermal detection method selected, on the pump beam diameter, and on the frequency dependent complex thermal diffusion length ($\delta = [\frac{j2K}{\omega C}]^{1/2}$) and complex thermal admittance ($Y = [j2\omega Kc]^{1/2}$) . The potential spatial resolution of the imaging of the thermal parameters is limited by considerations of heterogeneity.

Thermal contrast also depends on changes in the specimen temperature distribution caused by thermal boundaries [31]. These boundaries inhibit thermal flow in the specimen and lead to localized increases in specimen temperature [32]. For many metal and ceramic specimens, the macroscopic thermal parameters depend on the microstructure and hence on the processing history of the material. Thermal wave imaging may be able to help determine the relative contribution of the intrinsic thermal property values and the extrinsic

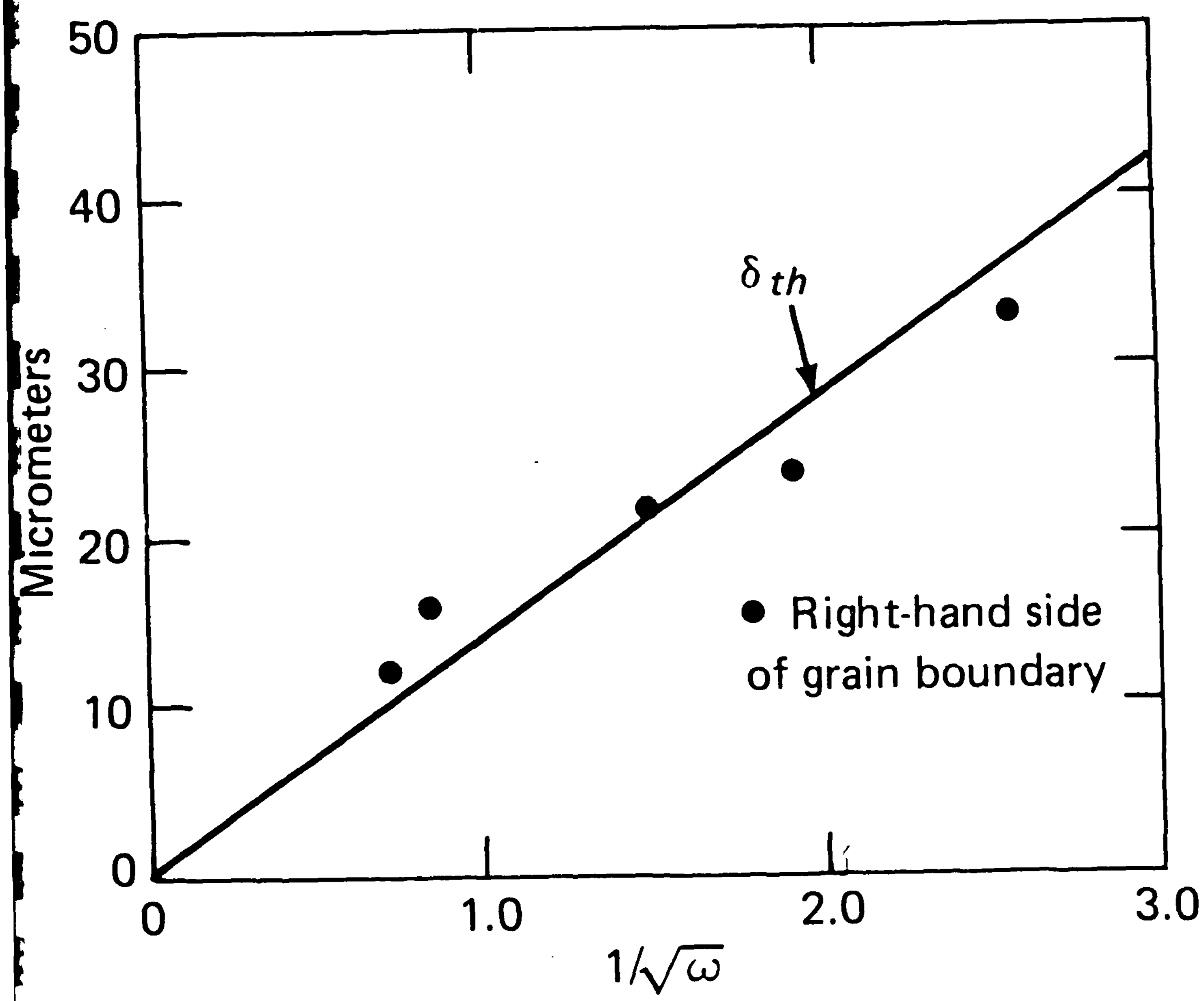

Fig. 13 Plot of grain boundary width vs. $\omega^{-0.5}$. The solid line is the thermal diffusion length of aluminum calculated using a diffusivity $\alpha = 1.0\ \text{cm}^2\ \text{sec}^{-1}$.

thermal boundary impedance to the macroscopic parameter values. However, relating image features to intrinsic and boundary thermal contrast mechanisms is difficult.

To further determine the effect of heterogeneities on thermal wave imaging, a theoretical investigation was made of the effects of spatially varying thermal and optical parameters on sample surface temperature. The particular case of one-dimensional heterogeneity varying with depth was considered. This case was amenable to a closed form analytical solution and was directly applicable to all layered, and many composite, materials.

The results indicate that both thermal and optical heterogeneities produce thermal barriers in the sample that impede heat flow. These barriers can be separated into two groups identified as pure-thermal barriers and opto-thermal (or photothermal) barriers [45]. The first type of barrier is produced by spatial variations in the thermal effusivity, $\varepsilon(x,y,z)$, while the second is created by spatial variations in the ratio $[R(x,y,z)]$ of the optical absorption length to the thermal diffusion length.

The magnitude of these thermal barriers is expressible in terms of a barrier density that is proportional to the logarithmic derivative of ε or R, respectively, with depth in the sample. Specifically,

$$M_{\text{thermal}} = (2\varepsilon)^{-1}\partial\varepsilon/\partial z, \text{ and}$$

$$M_{\text{opto-thermal}} = (2R)^{-1}\partial R/\partial z\ . \quad [45]$$

These results indicate that when thermal and optical properties vary rapidly (spatially) within a sample, these heterogeneities can be seen in a thermal image just as sample defects or impurity inclusions can.

The analysis also indicates that spatial variations in thermal capacity and thermal conductivity may affect the thermal image differently. In areas of the sample where there is optical saturation (i.e., where the thermal diffusion length is large compared with the reciprocal optical absorption length, [R>>1]), the simple homogeneous temperature pattern that would exist in the absence of heterogeneities is distorted by spatial variations in the optical absorption coefficient and thermal conductivity, but not by spatial variations in thermal capacity. By contrast, in areas of the sample where it is optically unsaturated [R<<1], thermal waves are reflected by spatial variations in optical absorption and thermal capacity but not by spatial variations in thermal conductivity. Since optical saturation is frequency dependent, the variation of the modulation frequency can be used experimentally to alter the thermal dependence in the thermal image. (Heterogeneous thermal effects is discussed in more detail in Paper #13 in the appendix of this report.)

3. THERMOELASTIC Contrast

Thermoelastic contrast mechanisms encompass the coupling of potentially anisotropic elastic parameters with the temperature field through the thermal expansion tensor, subject to thermal and elastic boundary conditions. Although the complexity of this coupling in practical applications makes an analytical solution difficult to obtain except for selected special cases, substantial progress has been made in acoustic microscopy in interpreting images in terms of elastic parameters [46-48]. Scanning acoustic microscopy clearly shows the presence of microstructure such as grains and grain boundaries in metals. Briggs [42] has noted the similarity of acoustic images and electron-acoustic images and has suggested that elastic contrast may play a role in SEAM imaging.

To explore the role of elastic contrast mechanisms in THERMOELASTIC thermal wave imaging, we conducted two series of experiments, one series imaging a fabricated vertical crack in a metal (aluminum) sample, and the other simultaneously imaging a buried hole in an aluminum sample using both THERMAL thermal wave detection and THERMOELASTIC thermal wave detection.

The presence of elastic contrast mechanisms in thermal wave imaging was established [41] using an attached transducer in an experiment employing simultaneous optical beam and piezoelectric detection in SEAM imaging. Laser acoustic and normal deflection component OBD line scans of an aluminum sample containing a buried slant hole are shown in Fig. 14. The acoustic detection method senses the hole to greater depths than the purely thermal method. This result is consistent with our previous discussion of the role T_b and T_s play in the two detection methods.

The importance of non-thermal contrast mechanisms in thermoelastic imaging is also shown in Fig. 9 where a second type of signal shape develops as the hole depth increases. In this figure the hole is observable down to depths reaching to $D/\delta_{TH} > 23$ where D is the depth and δ_{TH} is the thermal diffusion length. (Ringermacher [49] has made similar observations.) Neither T_b or T_s are affected by the presence of the hole at such large values of D/δ_{TH}. Hence, the contrast mechanism must be non-thermal.

A speculative explanation of these observations is that the angular distribution of the specimen stress response is a cone of approximately 40 degree cone angle peaked on epicenter. If this cone is interrupted by the hole at varied depth, the image of Fig. 9 is produced. The existence of a finite extent to the stress distribution is supported by observations using localized detectors. In our experiments an increase in signal is observed

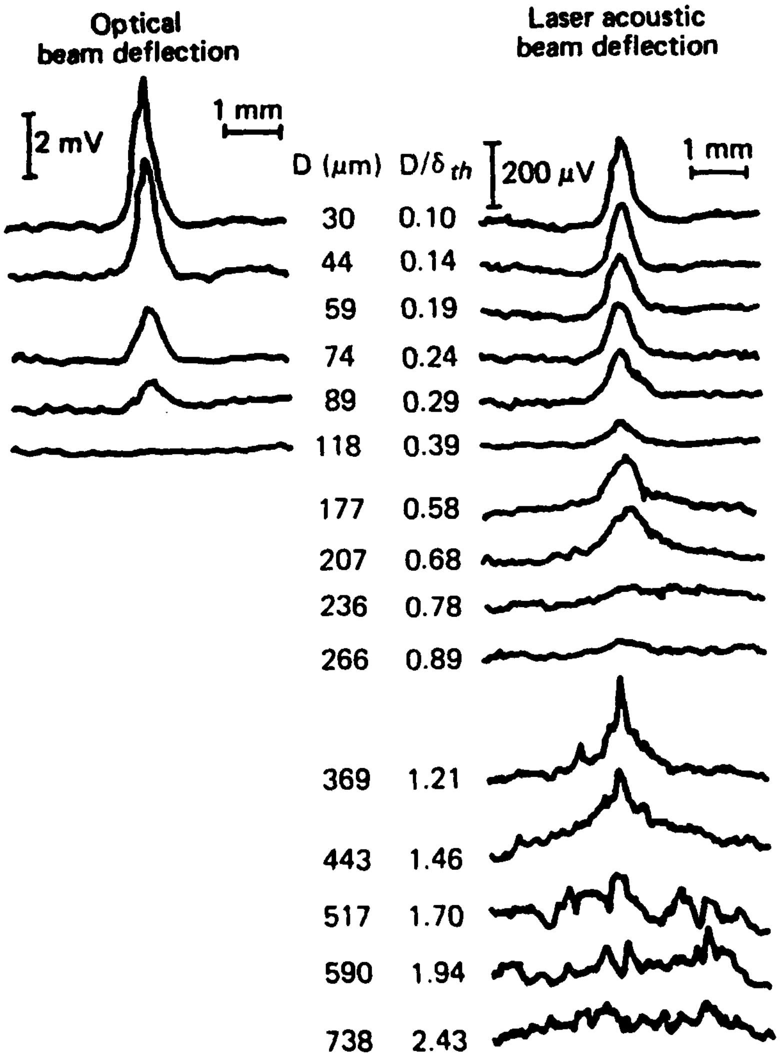

Fig.14 Laser source normal OBD and PZT line scans of a slant hole specimen. Thermal interaction with the buried hole is observed at greater depths with attached transducer detection than with OBD detection.

when an excitation beam passes over the region of the specimen directly above the NBS conical transducer. (Kubota and Marai [50] conducted laser acoustic experiments with a monolithic detector array on a PZT substrate and have found a very strong maximum in PZT signal when the exciting beam was directly above the active detector. Our ion-acoustic studies of other slant hole and partial hole specimens are consistent with this proposal.)

Our experiments with vertical boundaries indicate that both thermal and thermoacoustic contrast mechanisms contribute to thermoelastic imaging of these boundaries [51]. Figure 15 shows magnitude and phase images at 1.1 kHz of a portion of a sample containing a fabricated vertical crack for transverse OBD and PZT detection respectively and excitation with an Ar^+ laser source. Registration of the figures is possible using the features labeled (A) in each figure. The local features seen are probably iron and manganese inclusions in the 2024 aluminum alloy.

The interface is not visible in normal deflection magnitude and phase images but is present in the transverse magnitude and phase images. Transverse phase images shows a 180 degree phase reversal at the boundary and no signal related to inclusions. The PZT image closely resembled the normal deflection image and gave no indication of the interface.

The measurements were repeated using the electron source with the same specimen-detector combination without disrupting the bond. The frequency dependence observed for the electrons fits an ω^{-1} dependence at low frequencies and shows a frequency corner around 8 KHz. No interface contrast is seen below 4.5 KHz but strong contrast is present above 7 KHz with a transition region between. The absence of interface contrast in the laser source images at 1.1 KHz is consistent with the absence of contrast at low frequencies using

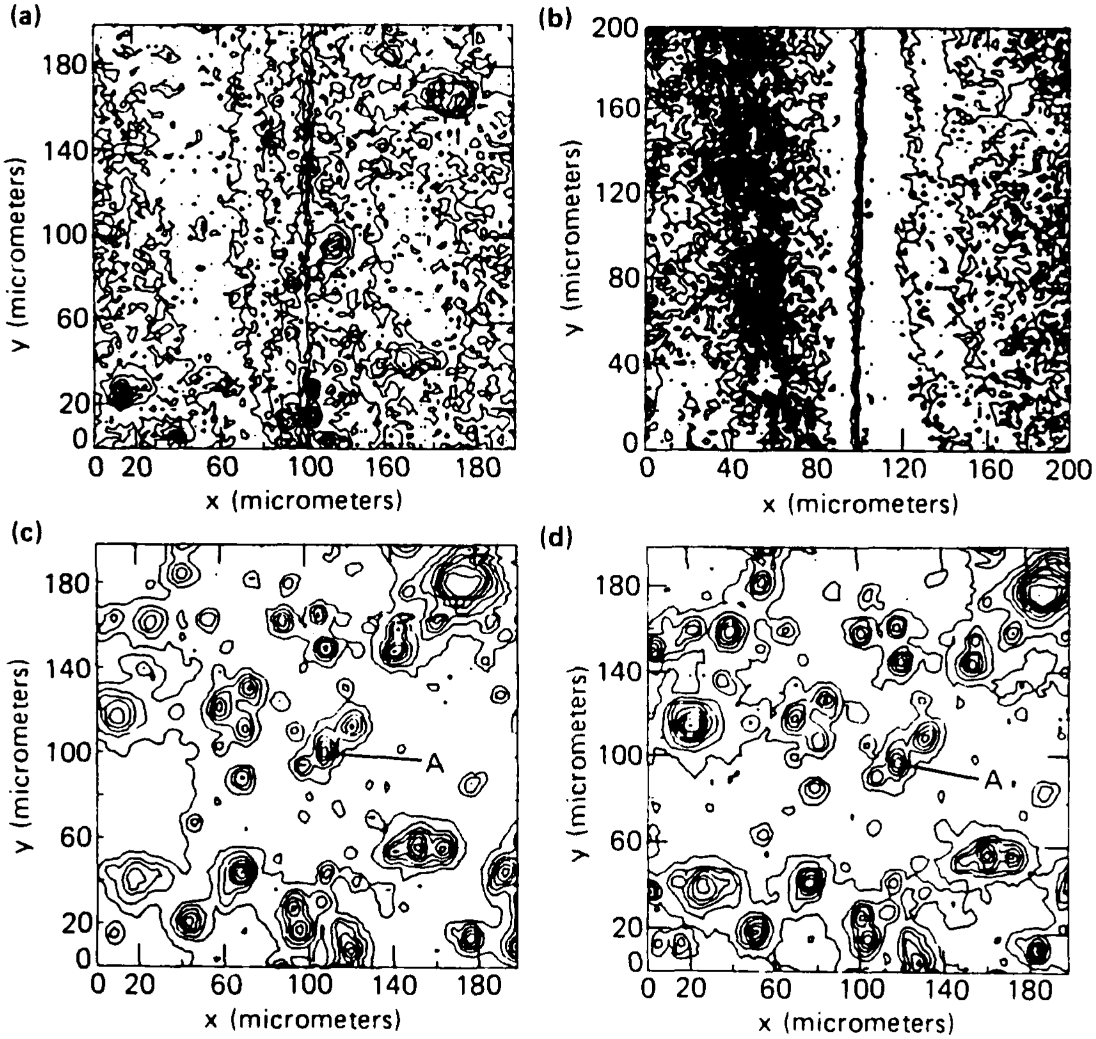

Fig.15 Transverse deflection component Optical Beam Deflection contour image showing a narrow vertical boundary (a). Attached transducer image (PZT) of the same region (b). Points labeled A allow registration. The 2024 aluminum sample consisted of two sections lapped, polished and clamped together with other faces then polished.

the electron beam. The ω^{-1} dependence suggests a thermal signal generation process in this low frequency regime. The visibility of the interface above 8 kHz, however, suggests that a non-thermal mechanism contributes to the image contrast in this case. This conclusion is further supported by the absence of any frequency dependence of the width of the boundary region (~ 200 microns). This width should be compared with the SEM determined width of the interface of 3 microns and with the thermal diffusion length of 70 microns at 7 KHz. The conclusion is that thermal contrast is not important in this case possibly because the width of the apparent boundary (200 μm) is large relative to the thermal diffusion length. Elastic contrast may be important at higher frequencies. No model of these phenomena is presently available.

SUMMARY AND CONCLUSIONS

Thermal Wave Imaging was first developed in the early 1980's. Since then it has expanded greatly and has become an important tool for locating and characterizing defects in structural materials and electronic devices and for studying and monitoring the microstructure of materials. Some of the materials that have been studied include metals, ceramics, composites, polymers, and related organic systems, as well as semiconductors and luminescent phosphors.

A variety of thermal wave imaging techniques exist. Each has different experimental requirements, and each provides different information about the material being studied. Many of these techniques are non-invasive and non-contacting making them ideally suited for the non-destructive evaluation and characterization of materials.

The experimental and analytical results obtained in this research project have ranged over a wide spectrum of topics as indicated by the range of subject matter and number of the publications appended to this report. Our objective has been to address fundamental issues related to thermal wave imaging using physical systems of scientific and industrial interest to investigate these issues. We have found that thermal wave imaging is especially suitable for studying many of the new structural and electronic materials that are presently being created.

In particular we have been concerned with contrast mechanisms in thermal wave imaging since these are the processes that form the thermal image and consequently are fundamental to all aspects of thermal wave imaging. From our work it has become evident that the initial concept of purely thermal image contrast, which was widely held when this work began, must now be expanded to include beam-specimen and elastic contrast mechanisms. We have also shown that while thermal wave imaging is useful in locating defects, which was the initial motivation for using it, it is a far more pervasive tool for the non-destructive evaluation of materials. In particular, we have show it to be useful in investigating the microstructure of materials and studying interactions between the exciting radiation and the sample.

Some major results of this project can be listed. We initiated the development of a new thermal wave technique using an ion-beam source, and using this method showed that a momentum contrast mechanism plays a minor role role in thermal wave imaging. Recently we have shown that ion-acoustic specimen interactions are surface sensitive and may be another tool for surface analysis, playing a role in ion implantation and in ion milling. We have also shown that mechanical as well as thermal contrast mechanisms are effective in creating thermal wave images and have obtained images of subsurface defects in aluminum specimens at depths greater than 23 thermal diffussion lengths. In addition, we have shown that it is possible to do depth probing in electronic devices utilizing the electron beam-specimen interaction characteristics of electron beam excitation.

Analytically, we have investigated heat flow in heterogeneous materials with continuously varying thermal and optical properties in one dimension and have shown that two different type of thermal barriers are created by spatial variations in optical and thermal properties.

Additional results and details of the experiments and analysis summarized in this report are contained in the sixteen publications attached to this report as an appendix.

REFERENCES

[1] G. Busse, "Imaging with optically generated thermal waves," IEEE Trans. Son. Ultrason., Vol. SU-32, No. 2, p. 355, 1985.

[2] A. Rosencwaig, "Thermal-wave imaging in a scanning electron microscope," Ann. Rev. Mater. Sci., Vol. 15, p. 103, 1985.

[3] G. Birnbaum and G. S. White in Research Techniques in Nondestructive Testing, "Laser Techniques in NDE," R. S. Sharpe, ed., Vol. 7, p. 259, New York: Academic Press, 1984.

[4] W. B. Jackson, N. Amer, A. C. Boccara, and D. Fournier, "Photothermal deflection spectroscopy and detection," Appl. Opt., Vol. 20, p. 1333, 1981.

[5] A. L. Tronconi, M. A. Amato, P. C. Morais and K. S. Neto, "Simple model for measurements of the photoacoustic signal by a piezoelectric detector in the microwave region," J. Appl. Phys., Vol. 56, No. 5, p. 1462, 1984.

[6] R. L. Nasoni, G. A. Evanoff, Jr., P. G. Halverson, and T. Bowen, "Thermoacoustic emission by deeply penetrating microwave radiation," Proc. IEEE Ultrason. Symp., 1981, p. 633.

[7] J.-P. Monchalin, J. F. Bussiere, and L. Bertrand, "Measurement of ultrasonic absorption in a polycrystalline metal by a photoacoustic-like technique," 4th International Topical Meeting on Photoacoustic, Thermal and Related Sciences, Ville d'Esterel, Quebec, Aug. 4-8, 1985.

[8] D. R. Green, "Thermal surface impedance method for NDT," Mater. Eval., Vol. 10, p. 231, Oct. 1967.

[9] J. Saniie, M. Luukkala, A. Lehto, and R. Rajala, "Thermal wave imaging through radio-frequency induction heating," Electron. Lett., Vol. 18, p. 651, 1982.

[10] A. C. Boccara, D. Fournier, and J. Badoz, "Thermo-optical spectroscopy: Detection by the mirage effect," Appl. Phys. Lett., Vol. 36, p. 136, 1980.

[11] D. Fournier and A. C. Boccara, "The mirage effect in photothermal imaging," in Scanned Image Microscopy, E. A. Ash, Ed. London: Academic, 1980, p. 347.

[12] J. C. Murphy and L. C. Aamodt, "Optically detected photothermal imaging," Appl. Phys. Lett., Vol. 38, p. 196, 1981.

[13] L. C. Aamodt and J. C. Murphy, "Photothermal measurements using a localized excitation source," J. Appl. Phys., Vol. 52, p. 4903, 1981.

[14] M. A. Olmstead, N. M. Amer, S. Kohn, D. Fournier, and A. C. Boccara, "Photothermal displacement spectroscopy: A new optical probe for solids and surfaces," Appl. Phys. A, Vol. 32, p. 141, 1983.

[15] J. C. Murphy and L. C. Aamodt, "Reflective photothermal imaging," J. Physique, Colloque C6, p. 513, 1983.

[16] A. Rosencwaig, J. Opsal, W. L. Smith, and D. L. Willenborg, "Detection of thermal waves through optical reflectance," Appl. Phys. Lett., Vol. 46, No. 11, p. 1013, 1985.

[17] S. Ameri, E. A. Ash, V. Neuman, and C. R. Petts, "Photodisplacement imaging," Electron Lett., Vol. 17, p. 337, 1981.

[18] C. R. Petts and H. K. Wickramasinghe, "Photothermal spectroscopy on a microscopy scale," in Proc. IEEE Ultrason. Symp., 1981, p. 832.

[19] P. E. Nordal and S. O. Kanstad, "Photothermal radiometry," Physica Scripta, Vol. 20, p. 659, 1979.

[20] G. Busse, "Photothermal transmission probing of a metal," Infrared Phys., Vol. 20, p. 419, 1980.

[21] P.-E. Nordal and S. O. Kanstad, "New developments in photothermal radiometry," Infrared Phys., Vol. 25, No. 1/2, p. 295, 1985.

[22] A. Hordvik and H. Schlossberg, "Photoacoustic technique for determining optical absorption coefficients in solids," Appl. Opt., Vol. 16, No. 1, p. 101, 1977.

[23] A. C. Tam and C. K. N. Patel, "High-resolution optoacoustic spectroscopy of rare-earth oxide powders," Appl. Phys. Lett., Vol. 35, p. 843, 1979.

[24] G. Busse and A. Rosencwaig, "Subsurface imaging with photoacoustics," Appl. Phys. Lett., Vol. 36, p. 815, 1980.

[25] G. S. Cargill, "Electron-acoustic microscopy," Scanned Image Microscopy, ed. E. A. Ash, London: Academic Press, p. 319, 1980.

[26] Y. Martin and E. A. Ash, "Imaging of micro-cracks by photo-displacement microscopy," Proc. IEEE Ultrason. Symp., 1984, p. 647.

[27] P. Cielo, F. Nadeau, and M. Lamontagne, "Laser generation of convergent acoustic waves for materials inspection," Ultrasonics, March 1985, p. 53.

[28] R. M. White, "Generation of elastic waves by transient surface heating," J. Appl. Phys., Vol. 34, No. 12, p. 3559, 1963.

[29] H. S. Carslaw and J. C. Jeager, Conduction of Heat in Solids, 2nd ed., Oxford: Clarendon, 1959.

[30] W. Nowacki, Thermoelasticity, London: Addison-Wesley, 1962.

[31] L. C. Aamodt and J. C. Murphy, "Effect of 3-D heat flow near edges in photothermal measurements," Appl. Opt., Vol. 21, No. 1, p. 111, 1982.

[32] L. C. Aamodt and J. C. Murphy, "Thermal Effects in Photothermal Spectroscopy and Photothermal Imaging," J. Appl. Phys., Vol. 54, No. 2, p. 581, 1983.

[33] J. C. Murphy, L.C. Aamodt, and G. C. Wetsel, Jr., "Coating Thickness Determination Using Time Dependent Surface Temperature Measurements," Review of Progress in Quantitative NDE, to be published.

[34] G. C. Wetsel, Jr., J. C. Murphy, and L. C. Aamodt, "Non-Destructive Characterization of Coatings on Metal Alloys", Review of Progress in Quantitative NDE, to be published.

[35] F. Ratliff, "Contour and contrast," Sci. Am., June 1972.

[36] J. W. Maclachlan, J. C. Murphy, R. B. Givens, and F. G. Satkiewicz, "Linear Thermal Wave Imaging," 11th World Conference on Nondestructive Testing, Nov. 3-8, 1985, Las Vegas, Dallas: Taylor Publishing Co., p. 441, 1985.

[37] F. G. Satkiewicz, J. C. Murphy, L. C. Aamodt, and J. W. Maclachlan, "Ion-acoustic Imaging of Subsurface Flaws in Aluminum," Williamsburg, VA, June 23-28, 1985, Review of Progress in Quantitative NDE, Plenum Press, 1986.

[38] D. N. Rose, H. R. Turner, and K. O. Legg, "Scanning ion acoustic microscopy," 4th International Topical Meeting on Photoacoustic, Thermal and Related Sciences, Ville d'Esterel, Quebec, Aug. 4-8, 1985.

[39] B. Svensson, J. Linros, and G. Holmen, "Ion-beam induced annealing of radiation damage in silicon on sapphire," Nucl. Instr. Meth., Vol. 209, p. 755, 1983.

[40] P. Sigmund, "Sputtering by ion bombardment: Theoretical concepts," in Topics in Applied Physics, vol. 47, Sputtering by Particle Bombardment I, ed. R. Behrisch, Berlin: Springer-Verlag, 1981.

[41] J. C. Murphy, J. W. Maclachlan, R. B. Givens, F. G. Satkiewicz, and L. C. Aamodt, "The Generation of Ultrasound by Laser, Electron and Ion Probes and Its Application to the Characterization of Materials," Ultrasonics International '85 -- Conference Proceedings, London: Butterworth Scientific, 1985, p. 30-36.

[42] G. A. D. Briggs, "Scanning electron acoustic microscopy and scanning acoustic microscopy: a favorable comparison," Scan. Elec. Microscopy, III, p. 1041, 1984.

[43] M. G. Sommekh, G. A. D. Briggs, and C. Ilett, "The effect of elastic anisotropy on contrast in the scanning acoustic microscope," Phil. Mag. A, Vol. 49, No. 2, p. 179, 1984.

[44] J. W. Maclachlan, R. B. Givens, J. C. Murphy, and L. C. Aamodt, "Contrast Mechanisms in Scanning Electron Acoustic Imaging of Grain Boundaries," 4th International Topical Meeting on Photoacoustic, Thermal, and Related Sciences, Ville d'Esterel, Quebec, Aug. 4-8, 1985.

[45] L. C. Aamodt and J. C. Murphy, "Thermal Effects in Materials with Continuously Varying Optical and Thermal Properties in One Dimension," Can. J. Phys. (to be published).

[46] Grover C. Wetsel,Jr, "Photothermal Generation of Thermoelastic Waves in a Composite Media", IEEE Transactions on Ultrasonics, Ferroelectrics, and Frequency Control, Vol. 33, No. 5, pp. 450-461, 1986.

[47] H. K. Wickramasinghe, "Contrast and imaging performance in the scanning acoustic microscope," J. Appl. Phys., Vol. 50, No. 2, p. 664, 1979.

[48] C. Ilett, M. G. Somekh, and G. A. D. Briggs, "Acoustic microscopy of elastic discontinuities," Proc. R. Soc. Lond. A, Vol. 393, p. 171, 1984.

[49] H. I. Ringermacher and L. Jackman, "Deep thermoacoustic imaging using scanning electron acoustic microscopy (SEAM)," Williamsburg, VA, June 23-28, 1985, to be published in Review of Progress in Quantitative NDE, Plenum Press, 1986.

[50] K. Kubota and H. Murai, "Photoacoustic spectroscopy of semiconductor heterostructures by piezoelectric transducers II. Space-resolved detection of photoacoustic modes," J. Appl. Phys., Vol. 56, No. 3, p. 835, 1984.

[51] G. C. Wetsel,Jr., J. B. Spicer, J. W. Maclachlan, and J. C. Murphy, "Comparison of Photoacoustic and Photothermal Optical Beam Deflection Imaging of Subsurface Structure in Solids," 1985 IEEE Ultrasonics Symposium Proceedings, San Francisco, October 1985 (to be published)

APPENDIX

PHOTOTHERMAL IMAGING OF DEFECTS IN METALS AND CERAMICS

1. L. C. Aamodt and J. C. Murphy, "A Thermal Wave Approach for Heterogeneous Materials with Continuously Varying Thermal and Optical Properties in One Dimension," 4th International Topical Meeting on Photoacoustic, Thermal, and Relate [illegible] ences, Ville d'Esterel, Quebec, Aug. 4-8, 1985.

A Thermal Wave Approach For Heterogeneous Materials With Continuously Varying Thermal And Optical Properties In One Dimension*

Leonard C. Aamodt and John C. Murphy
Applied Physics Laboratory
Johns Hopkins University
Johns Hopkins Road,
Laurel, Md. 20707 U.S.A.

The physical existence of thermal waves has been the subject of controversy, but their use as a mathematical tool in analyzing photothermal processes has provided easy, natural, and productive solutions for many problems. In addition, the conceptual framework based on thermal waves has provided a useful guide for intuitive thinking about these problems. In this paper, a simple thermal wave approach is used to describe the complicated heat flow, and temperature, patterns in heterogeneous materials with continuously varying thermal and optical properties in one dimension. Such materials are abstractions, but they are approximated by planer layered and composite materials, some thin film samples, and materials with impurities whose presence is predominantly dependent upon depth within the sample. Conceptual, rather than computational, aspects are emphasized. We consider the broad beam case where heat flow is predominately in one dimension. This result, although restricted, has many features in common with general heat flow.

If instead of using thermal capacitance (C), thermal conductivity (κ), and optical absorption(β) as the basic thermal and optical parameters, the complex thermal diffusion length [$\delta = \kappa/j\omega C$], the thermal admittance [$y = \delta/\kappa$], and the ratio of the thermal diffusion length to the optical absorption length (β^{-1}), [$\varepsilon = \beta\delta$] are used, a simple notation results and this choice provides a natural way to characterize heat obstructions within the sample. These obstructions can be classified as: heat-source-spatial-fluctuations (which have received insufficient attention), which develop at locations in the sample where the "effectiveness" of a heat source in establishing a temperature pattern in the sample changes, and thermal barriers, which are created by spatial variations in the sample's thermal properties. The first type of obstruction depends upon both the optical and thermal properties of the sample while the latter depends on thermal properties only.

New thermal waves are created at heat-source-spatial-fluctuation levels as well as at thermal barriers and propagate through the sample. The surface temperature (i.e., the complex summation of these waves at the sample surface) can be decomposed into two components, one similar to that which would be obtained for a homogeneous sample with the weight-averaged properties of the heterogeneous sample and a second component containing terms depending exclusively on the heterogeneous character of the sample. The heterogeneous component can be expressed in terms of a continuum of thermal barriers and heat-source-fluctuations.

An alternate formulation, allows the heterogeneous component to be expanded in terms of basis functions obtained from simple homogeneous thermal wave solutions, and which, when expressed in terms of κ and C, describe how the surface temperature depends upon the degree of optical saturation at each depth in the sample.

In the approach used, a formal solution of the heat equation is obtained before a knowledge of the spatial patterns of thermal and optical properties in the sample are required. These patterns are then used to evaluate the spatial integrals that comprise the formal solution. The generalized solution that is obtained expresses the surface temperature in terms of surface and bulk heat obstructions in the sample and shows that the logarithmic derivative of the thermal admittance describes a continuum of thermal barriers within the sample bulk.

Two types of thermal waves are distinquished in this solution: reflected waves which are created by both optical and thermal discontinuities in the sample and whose propagation characteristics depend exclusively on the sample's thermal properties, and fundamental (or heat-source-waves) that are created by spatial variations in both optical and thermal properties and whose propagation characteristics depend only on the optical properties of the sample.

While frequency dependance in heterogeneous samples is complicated, it is possible to subdivide this dependence into various frequency-dependence patterns and to assign a particular pattern to each wave. This allows a determination of the relative contribution of each wave to the total frequency dependence of the sample.

* This work has been supported by the Office of Naval Research, the U.S. Army Research Office and the U.S. Naval Sea Command under Contract No. N00024-85-C-5301.

APPENDIX

PHOTOTHERMAL IMAGING OF DEFECTS IN METALS AND CERAMICS

2. L. C. Aamodt and J. C. Murphy, "Thermal Effects in Photothermal Spectroscopy and Photothermal Imaging," J. Appl. Phys., Vol. 54, No. 2, p. 581, 1983.

Thermal effects in photothermal spectroscopy and photothermal imaging

L. C. Aamodt and J. C. Murphy
The Johns Hopkins University, Applied Physics Laboratory, Laurel, Maryland 20707

(Received 22 March 1982; accepted for publication 7 October 1982)

The effect of thermal parameters on photothermal spectroscopy and photothermal imaging for certain types of spatially heterogeneous samples has been studied. Results have been obtained for both photoacoustic and photothermal deflection modes of detection. Specific attention has been paid to optical saturation in samples whose properties exhibit gradual spatial changes and to the dependence of the photothermal signal on the individual thermal parameters. Most photothermal spectroscopy has been done using thermally homogeneous samples, and most photothermal imaging using optically saturated samples. In this paper, these limitations are relaxed, and the photothermal signal is assumed to depend simultaneously on gradual spatial variations in the optical absorption coefficient, thermal conductivity, and thermal capacity of the sample.

PACS numbers: 44.50. + f, 78.20.Nv, 07.60.Pb

I. INTRODUCTION

Photoacoustic (PA), or more generally, photothermal spectroscopy has the ability to measure optical absorption properties of opaque or highly scattering solids. This ability is associated with the nature of the detection process which measures temperature changes in a sample or at its surface.[1-4] Because the signal generated is defined by an intimate association of optical and thermal properties, photothermal methods have also been used to measure sample thermal properties.[5] In addition, nonradiative transition rates and processes present in luminescent or in photochemically active solids[6] can be measured.

In most spectroscopic studies a spatially uniform, temporally modulated light source heats a spatially homogeneous sample. Under these conditions, heat flow in the sample is normal to the sample surface, and one-dimensional diffusion theory adequately describes the temperature in the sample volume and on the sample surface. In a heterogeneous sample, however, optical and thermal properties vary spatially so that each point on the sample surface contributes differently to the photothermal signal. Consequently, when broad-beam excitation is used, the photothermal signal is an average over the sample surface. When the optical spectrum at a specific point on the surface of a heterogeneous sample is wanted, localized excitation must be used and three-dimensional heat flow must be considered in interpreting the results obtained. In this case, relative spectral amplitudes can be quantitatively compared only when the sample is unsaturated and the spectra have been obtained at the same point on the sample surface.

Imaging studies of defects in metals[7,8] in thin films[9] and in integrated circuits[10] have also been made using localized excitation. Most of these studies have used photothermally saturated samples. In this paper, we consider a broader class of conditions where the sample is not photothermally saturated and where both optical and thermal properties (and their spatial variations) affect the observed photothermal signal. We consider only heterogeneous samples whose thermal and optical properties vary slowly relative to a sample thermal diffusion length. The results we obtain, however, show features that must be present in an analysis of general heterogeneity.

Before discussing these topics, we briefly review a new method of photothermal detection which is especially suited to the study of heterogeneous materials because of its use of localized detection.

II. OBD DETECTION

Recently a new method of photothermal imaging[11,12] has been developed based on optical beam deflection (OBD) spectroscopy.[13,14] Figure 1 illustrates the basic principles of OBD detection when applied to a spatially homogeneous solid under localized heating.[15] An amplitude-modulated, focused laser beam heats the sample at the point $x_0, y_0, 0$ causing a temporal and spatial variation in the temperature $T(x,y,z)$ within the sample, the temperature $T_s(x,y)$ on the sample surface, and the temperature $T_f(x,y,z)$ in the fluid (liquid or gas) immediately above the sample surface. This figure shows the temperature profile of $T_s(x,y)$ at an arbitrary time t. Thermal diffusion in the sample causes the profile of T_s to differ from that of the incident light distribution $I_0(x,y)$.

When I_0 is radially symmetric, the fluid temperature and sample surface temperature are[15]

$$
\begin{aligned}
T_s(r) &= \int_0^\infty t(\mu)\, h(\mu)\, J_0(\mu r)\, d\mu \\
&= \int_0^\infty \bar{T}_s(\mu)\, \mu\, J_0(\mu r)\, d\mu, \qquad (1) \\
T_f(r,z) &= \int_0^\infty \bar{T}_s(\mu)\, \mu\, J_0(\mu r) \exp(-b_f z)\, d\mu,
\end{aligned}
$$

where r is the radial distance from the beam axis, J_0 is the zero-order Bessel function of the first kind, $b_i^2 = \mu^2 + 2j/\delta_i^2$, $\delta_i = (2\kappa_i/\omega C_i)^{1/2}$ is the *real* diffusion length, and κ_i and C_i are the thermal conductivity and thermal capacity, respectively, in media i. (For simplicity we drop the subscript s when referring to sample thermal parameters.) $\omega = 2\pi f$, where f is the modulation frequency. $\mu/2\pi$ is the spatial frequency. $t(\mu)$ contains the dependence of the surface temperature on the sample optical and thermal parameters. $h(\mu) = \{ I_0 R^2/2 \} \exp(-\mu^2 R^2/4)$ contains the dependence on the heat source (which we assume to be a Gaussian excitation beam of intensity I_0 and radius R), and $\bar{T}_s(\mu)$ is the

0021-8979/83/020581-11$02.40

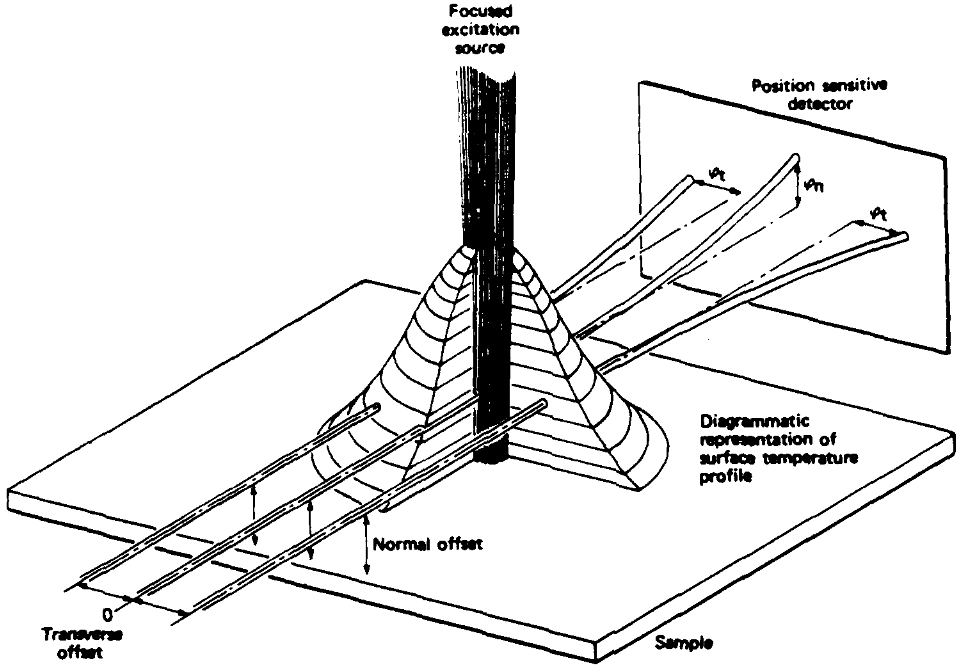

FIG. 1. A diagramatic representation of the surface-temperature profile showing optical beam deflection trajectories for various probe-beam transverse offsets when localized excitation is used. When the transverse offset $\neq 0$, the deflection has both a normal and transverse component. (For clarity, only the transverse component is shown.) When the transverse offset $= 0$, the transverse component is absent.

Hankel transform of $T_s(r)$. If $I_0(x,y)$ is radially symmetric, $T_s(x,y)$ is also radially symmetric in a homogeneous sample.

It is convenient to express μ in units of $2/R$, thus we let $\mu = 2\nu/R$. Then,

$$T_f(r,z) = 4/R^2 \int_0^\infty \bar{T}(\nu)\, \nu\, J_0(2\nu r/R) \times \exp(-b_f(\nu) z)\, d\nu\,, \tag{2}$$

where $b_i^2 = 2j/\delta_i^2(1 - 2j\nu^2\delta_i^2/R^2)$.

For fluids whose optical index of refraction varies with temperature, a time varying thermal lens is created which deflects a small-diameter probe beam (moving parallel to the sample surface) through an angle whose magnitude and direction depend on the index of refraction gradient integrated along the probe-beam path.

Several special cases are shown in Fig. 1. If the probe beam passes through the center of the temperature profile, only a z-directed (normal) deflection is present. For rays on either side of the center of the profile, a reduced-amplitude normal deflection component and a transverse deflection component (i.e., a deflection parallel to the plane of the sample and normal to the probe ray) are observed. The direction of the transverse component is reversed for the two rays. Analytically, the deflections $\phi_{n,t}$ for a narrow probe beam are[15]

$$\begin{aligned} \phi_n &= 4/R \int_0^\infty T_0^{-1}\, \bar{T}_s(\nu)\, b_f(\nu) \times \exp(-b_f z) \cos(2\nu y/R)\, d\nu\,, \\ \phi_t &= 8/R^2 \int_0^\infty T_0^{-1}\, \bar{T}_s(\nu)\, \nu \times \exp(-b_f z) \sin(2\nu y/R)\, d\nu\,, \end{aligned} \tag{3}$$

where n is the index of refraction in the fluid, $T_0^{-1} = -n^{-1}\, dn/dT_f$, y is the transverse offset of the probe beam (see Fig. 1), and the subscripts n and t denote the normal and transverse deflection components, respectively. If the variation in fluid temperature is small, T_0^{-1} is essentially constant and can be taken out of the integral. Experimental confirmation of these dependencies is shown in Fig. 2. When the sample surface is uniformly illuminated, the normal component in Eq. (3) reduces to the one-dimensional result, which depends only on the spatial frequency $\nu = 0$, and the transverse component vanishes. Because ϕ_t is an odd function of the transverse offset (coordinate) y, it is useful in studying sample inhomogeneities.

For the common experimental case where the distance from the sample to the detector is large compared with the excitation-beam radius, the photothermal signal is proportional to the probe-beam deflection, and

$$\begin{aligned} S_n(y,z) &= 4M/R \int_0^\infty \bar{T}_s(\nu)\, b_f(\nu) \times \exp(-b_f z) \cos(2\nu y/R)\, d\nu\,, \\ S_t(y,z) &= 8M/R^2 \int_0^\infty \bar{T}_s(\nu)\, \nu \times \exp(-b_f z) \sin(2\nu y/R)\, d\nu\,, \end{aligned} \tag{4}$$

where T_0^{-1} and other multiplicative constants such as instrumental gain have been included in the factor M. The corresponding equation for PA detection can be written in terms of the spatial frequency as[15]

$$S_{pa} = M'\omega^{-1/2} \int_0^\infty \bar{T}_s(\nu)\, \delta(\nu,0)\, d\nu\,, \tag{5}$$

where $\delta(\nu,0)$ is the Dirac delta function, and M' is independent of frequency but does depend upon the thermal properties of the gas.

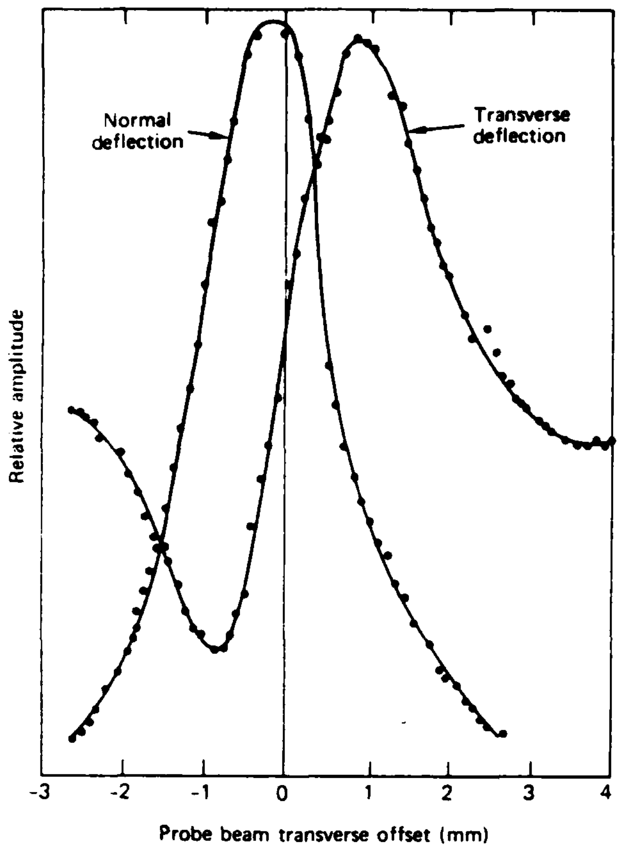

FIG. 2. Experimentally determined normal and transverse optical beam deflection profiles plotted vs probe-beam transverse offset. The sample used was a thin silicon wafer.

S_n, S_t, and S_{pa} each measure different features of the surface-temperature profile. S_{pa} is proportional to the modulated sample-surface temperature integrated over the complete sample surface, while S_n and S_t monitor the modulated sample-surface temperature along $\mathbf{P}_s$, the projection of the probe-beam path on the sample surface. When the probe beam just skims the sample surface ($z \simeq 0$), S_n is proportional to the mean temperature along $\mathbf{P}_s$, and S_t is proportional to the mean value of $\partial T/\partial y$ along $\mathbf{P}_s$.[15]

Photoacoustic detection is not localized. S_n and S_t, however, depend upon the probe-beam position through the transverse offset y. Thus, in principle, spatial derivatives (and integrals) of S_n and S_t (such as $\partial S_t/\partial y$, $\partial S_n/\partial z$, and $\int S_n\, dy$) can be measured experimentally. Note that each of these quantities is sensitive to specific features of the surface-temperature profile. For example, $(\partial S_t/\partial y)_{y,z=0}$ is proportional to the mean value of $\partial^2 T_s(x,y)/\partial y^2$ along $\mathbf{P}_s$ while $(\partial S_n/\partial z)_{y,z=0}$ is proportional to the mean normal derivative of the temperature in the fluid along $\mathbf{P}_s$. As a consequence, each measurement is sensitive to, and reveals, a different aspect of the heat-flow pattern in the sample. OBD detection, for example, is sensitive to transverse flow while photoacoustic detection is not.

For reference Eqs. 6–11 summarize some spatial functions of S_t and S_n of interest in terms of the surface-temperature spatial-frequency spectrum.

$$S_{pa} = M'\omega^{-1/2} \int_0^\infty \bar{T}_s(\nu)\, [\delta(\nu,0)]\, d\nu\,, \tag{6}$$

$$S_n(y; z=0) = 4M/R \int_0^\infty \bar{T}_s(\nu) \times [b_f \cos(2\nu y/R)]\, d\nu\,, \tag{7}$$

$$(\partial S_n/\partial z)_{y,z=0} = 4M/R \int_0^\infty \bar{T}_s(\nu)\, [b_f^2]\, d\nu\,, \tag{8}$$

$$S_n(y=0, z=0) = 4M/R \int_0^\infty \bar{T}_s(\nu)\, [b_f]\, d\nu\,, \tag{9}$$

$$S_t(y; z=0) = 8M/R^2 \int_0^\infty \bar{T}_s(\nu) \times [\nu \sin(2\nu y/R)]\, d\nu\,, \tag{10}$$

$$(\partial S_t/\partial y)_{y,z=0} = 8M/R^2 \int_0^\infty \bar{T}_s(\nu) \times [2\nu^2/R]\, d\nu\,. \tag{11}$$

Each of these quantities represents a different weighted average of the spatial spectrum $\mathbf{T}_s(\nu)$, with the weighting factor appearing in the bracket [ ], and each has a different dependence on the optical/thermal properties of the sample. These functions provide a variety of experimental measurements which reveal different features of the temperature profile. In this paper we consider two types of photothermal measurements: gas/microphone photothermal detection [Eq. (6)], and the transverse slope of S_t [Eq. (11)]. (This is the slope of S_t at the cross-over point, $y = 0$, in Fig. 2.) Experimental arrangements for measurements of this type are shown in Fig. 3. Figure 3(a) illustrates a method where the probe-beam transverse offset varies harmonically [i.e., $y = \Delta y \cos(\omega_0 t)$]. If $z \simeq 0$,

$$S_t(\Delta y, z=0) = 8M/R^2 \int_0^\infty \bar{T}_s(\nu)\, \nu \sin(2\nu\, \Delta y \cos(\omega_0 t))\, d\nu$$

and, if Δy is small, sin can be replaced by its argument, and

$$S_t(\Delta y, z=0) = \{16M/R^3\} \left\{ \int_0^\infty \bar{T}_s(\nu)\, \nu^2\, d\nu \right\} \Delta y \cos(\omega_0 t)$$

$$= \Delta y (\partial S_t/\partial y)_{y,z=0} \cos(\omega_0 t)\,.$$

After demodulation at frequency ω_0, $S_t(\Delta y, z=0) = \Delta y (\partial S_t/\partial y)_{y,z=0}$.

Figure 3(b), illustrates a second method using two probe beams having transverse offsets $y = \pm \Delta y/2$. If Δy is small, the difference of the two photothermal signals is also proportional to $(\partial S_t/\partial y)_{y,z=0}$.

III. LOCAL HOMOGENEITY

Consider a special case where the optical and thermal properties of the sample vary slowly (spatially) so that they can be considered to be spatially constant in a local region although they may vary significantly over the whole sample. Under these conditions, the photothermal signal at each point on the sample can be computed using local optical/thermal parameters and Eq. (4), provided three-dimensional heat flow is properly considered.

For this case, $S = S(\beta, \kappa, C, \omega, R, I_0)$. However, ω, R, I_0 are experimental parameters, hence $S = S(\beta, \kappa, C)$. The related pair of functions $\delta = (2\kappa/\omega C)^{1/2}$, the thermal diffu-

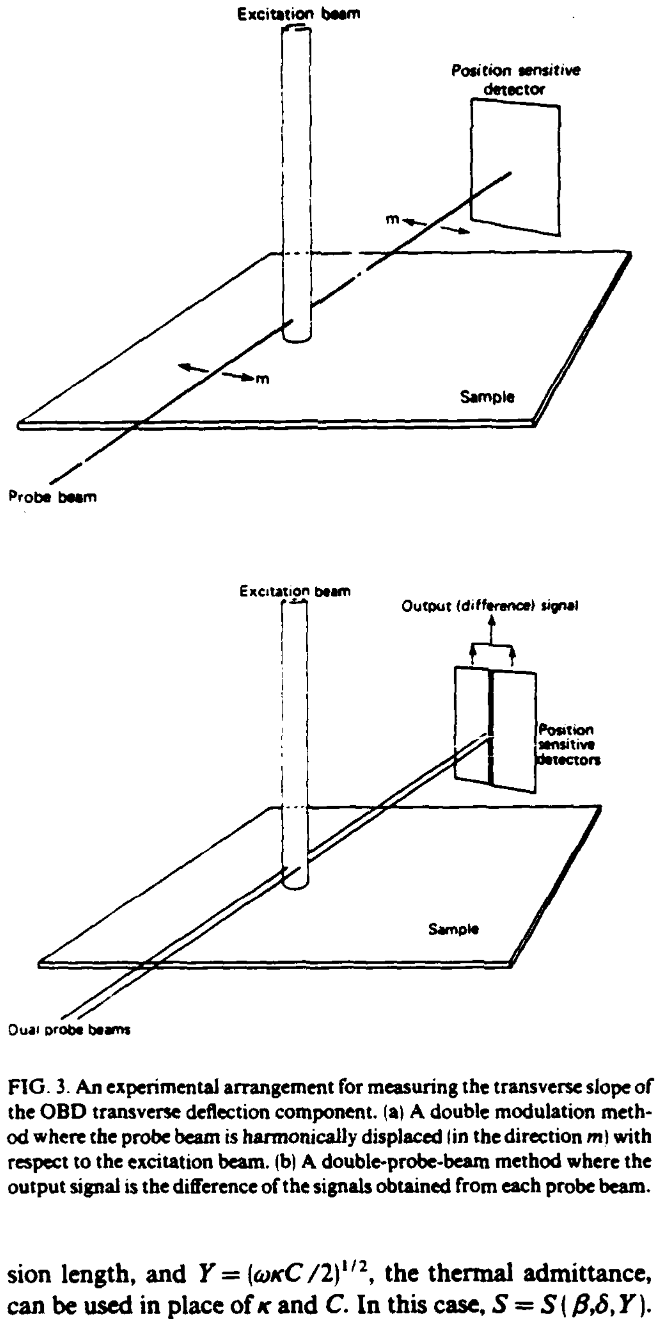

FIG. 3. An experimental arrangement for measuring the transverse slope of the OBD transverse deflection component. (a) A double modulation method where the probe beam is harmonically displaced (in the direction m) with respect to the excitation beam. (b) A double-probe-beam method where the output signal is the difference of the signals obtained from each probe beam.

sion length, and $Y = (\omega\kappa C/2)^{1/2}$, the thermal admittance, can be used in place of κ and C. In this case, $S = S(\beta,\delta,Y)$. (Note that the thermal diffusion length δ alone does not properly represent the thermal response of the sample.)

In principle it is possible to invert S to obtain the dependence on individual parameters since spatial variation in β, κ, C, jointly determine the sample's surface-temperature pattern. In practice inversion is difficult except for those cases where the sample temperature (or a feature of the temperature profile) is related to a single thermal or optical parameter. Consequently, it is useful to determine the dependence of the photothermal signal on each of the optical/thermal parameters to determine whether conditions exist where it might be possible to invert S to obtain this variable.

To this end, we introduce two functions, $\sigma(x,y) = 1 - (\beta/S)(\partial S/\partial\beta)$, *the degree of photothermal saturation* and $TC(x,y) = -(\kappa/S)(\partial S/\partial\kappa)$, the *"thermal character"* which describe, respectively, the sensitivity of S to variations in the optical parameter β and to variations in the thermal parameters at the point x,y. In Secs. V and VI we discuss the relationship of TC and σ in detail. Here we note that $\sigma = 1$ corresponds to a photothermally saturated sample and $\sigma = 0$ an unsaturated sample, while $TC = 0$ indicates that S depends exclusively on C, $TC = 1$, exclusively on κ, and $TC = 1/2$, exclusively on Y (i.e., the product κC). Other values of TC correspond to various intermediate cases. σ and TC both depend parametrically on the modulation frequency and the excitation-beam radius.

IV. THE DEPENDENCE OF THE PHOTOTHERMAL SIGNAL ON THE THERMAL VARIABLES IN SATURATED AND UNSATURATED SAMPLES

For photoacoustic detection [Eq. (6)],

$$S_p = S_{pa} = \{ I_0 M' R^2/2\sqrt{\omega} \} \, t(\beta,\kappa,C,\nu = 0), \tag{12}$$

and for optical detection using the experimental arrangement shown in Fig. 3 [Eq. (11)],

$$\begin{aligned} S_0 &= (\partial S_t/\partial y)_{y,z=0} \\ &= 4MI_0/R \int_0^\infty t(\beta,\kappa,C,\nu) \exp(-\nu^2)\, d\nu. \end{aligned} \tag{13}$$

The excitation spectrum has been explicitly included in these equations.

From Ref. 15, the photothermal response $t(\nu)$ is

$$t(\nu) = \kappa^{-1}(b_s + b_s^2/\beta)^{-1}$$

$$\text{(For thermally thick samples; } s = \text{sample.)} \tag{14}$$

and

$$t(\nu) = \beta l/[\kappa_b(b_b + (\kappa l/\kappa_b) b^2]$$

$$\text{(For thermally optically thin samples; } b = \text{backing.)} \tag{15}$$

We consider only the thermally thick case. The thermally optically thin case can be handled using a similar approach.

For an unsaturated sample (β small so $\beta b_s \ll b_s^2$),

$$|S_0| = 8I_0 M\beta/R\omega C \times \left| \int_0^\infty \nu^2 \exp(-\nu^2)/[1 - 2j\nu^2\delta^2/R^2]\, d\nu \right|, \tag{16}$$

$$|S_p| = I_0 M' R^2 \beta/(2C\omega^{3/2}); \tag{17}$$

and for a saturated sample ($\beta \to \infty; \beta b_s \gg b_s^2$),

$$|S_0| = 8M\sqrt{2}\, I_0/[R(\omega\kappa C)^{1/2}] \times \left| \int_0^\infty \nu^2 \exp(-\nu^2)/[A(+) + jA(-)]\, d\nu \right|, \tag{18}$$

where $A(\pm) = [(1 + 4\nu^4\delta^4/R^4)^{1/2} \pm 2\nu^2\delta^2/R^2]^{1/2}$,

$$|S_p| = M' I_0 R^2/[2\omega(\kappa C)^{1/2}] = M' I_0 R^2/[2Y(2\omega)^{1/2}]. \tag{19}$$

S_p depends (thermally) on C when the sample is unsaturated and on Y [i.e., $\sqrt{(\kappa C)}$] when the sample is saturated. It does not depend exclusively on κ under any condition. When OBD detection is used, the photothermal signal is affected by the size of the excitation beam (or more specifically by the ratio δ/R) as well as by the degree of saturation. When $\delta/R \ll 1$, $\nu^2\delta^2/R^2 \ll 1$ for all values of ν where the integrals in Eqs. (16) and (18) are not effectively terminated by the exponential. Thus for an unsaturated sample, $|S_0|$

$= 8MI_0\beta/R\omega C\int_0^\infty \nu^2\exp(-\nu^2)\,d\nu \propto 1/C, [TC = 0]$, while for a saturated sample, $|S_0| \propto 1/\surd(\kappa C)[TC = 1/2]$. These results are identical with PA detection. On the other hand, when $\delta/R \gg 1$, $\nu^2\delta^2/R^2 \gg 1$ for most spatial frequencies, and, for an unsaturated sample,

$$|S_0| = \{4MI_0\beta R^2/[\omega CR]\}\{R^2/\delta^2\} \times \int_0^\infty \exp(-\nu^2)\,d\nu \propto 1/\kappa \tag{20}$$

$[TC = 1]$. A similar result is obtained for a saturated sample. Thus when δ/R is large, S_0 depends exclusively in κ regardless of the degree of optical saturation.

These results can be made more quantitative by dividing the range of the integrals in Eqs. (16) and (20) into two parts, $\nu = 0 \rightarrow R/\delta$, where we assume $\nu\delta/R$ can be ignored with 1 and $\nu = R/\delta \rightarrow \infty$, where we assume 1 can be ignored compared with $\nu\delta/R$. Using this approximation,

$$|S_0| = I_0[\{2/j\omega\kappa C)^{1/2}/R\}\operatorname{erf}(R/\delta) + 8/\kappa\exp(-R^2/\delta^2)] \tag{21}$$

for a saturated sample, and,

$$|S_0| = I_0\beta R[\{2\pi^{1/2}/R^2\omega C\}\operatorname{erf}(R/\delta) - \{8/R\surd(2\omega\kappa C)\}\exp(-R^2/\delta^2) + j\pi^{1/2}/\kappa\operatorname{erfc}(R/\delta)] \tag{22}$$

for an unsaturated sample. The nature of the error function, complementary error function, and exponential indicate that the terms dependent on $1/C$ are dominant when δ/R is small, and those dependent on $1/\kappa$ are dominant when δ/R is large in agreement with the somewhat coarser approximation above.

To summarize: if δ/R is small the parametric dependence on thermal parameters is the same for both PA and OBD detection and ranges from an exclusive dependence on C (for an unsaturated sample) to a dependence on the product κC (for a saturated sample). If δ/R is large, PA thermal dependence is unchanged, but the OBD signal depends exclusively on κ regardless of the degree of saturation.

The results obtained thus far apply only to fully saturated or fully unsaturated samples. In Sec. V we quantify the term partial saturation, and, in Sec. VI, determine the thermal character of partially saturated samples.

V. PARTIAL SATURATION

Figure 4(a) shows the usual saturation curve for photoacoustic detection (S vs β). For small β, the sample is unsaturated ($S \propto \beta^1$), and the curve has a slope of one. For large β, the sample is saturated ($S \propto \beta^0$), and the curve has a slope of zero. Between these limits the slope varies between 0 and 1, and the sample is partially saturated. We relate the degree of partial saturation to the slope of the saturation curve by defining $\sigma = 1 - [\partial\log(S)/\partial\log(\beta)]_\delta = 1 - \beta/S(\partial S/\partial\beta)_\delta$ (i.e., one minus the slope of the saturation curve plotted using a log-log scale). Using this definition, $\sigma = 1$ when the sample is saturated, and $\sigma = 0$ when the sample is unsaturated. Fractional values of σ indicate partial saturation. Although derived specifically for PA detection, this definition can be extended to OBD, and other photothermal measurements, as a general definition of partial saturation.

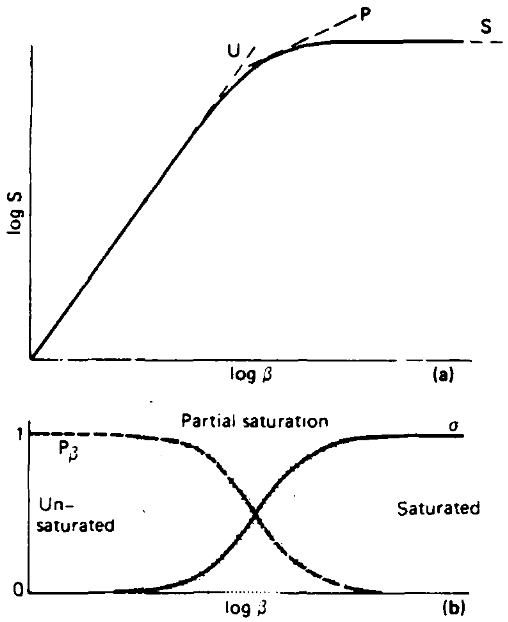

FIG. 4. (a) Photothermal saturation curve for PA detection. The tangents U and S show the slope of the curve under unsaturated and saturated conditions, respectively. The tangent P shows the slope at an arbitrary point where the sample is partially saturated. (b) The slope of the saturation curve P_β and the degree of saturation σ plotted vs $\log\beta$.

The local dependence of S on β in the vicinity of an arbitrary point β_0 on the saturation curve can be determined by expanding $\log S$ in a Taylor series. If Y and δ are fixed parameters, $\log S = \log S(Y,\delta,\beta_0) + (\partial\log S/\partial\log\beta)(\beta_0) \times \log(\beta/\beta_0) + \ldots$. When β is restricted to values close to β_0, $\log(\beta/\beta_0)$ is small and only the first two terms in the expansion need be retained. Since $\partial\log S/\partial\log\beta = 1 - \sigma$, $\log S = \log S(Y,\delta,\beta_0) + \log(\beta/\beta_0)^{1-\sigma}$, so $S = S(Y,\delta,\beta_0) \times (\beta/\beta_0)^{1-\sigma}$.

Y, δ, and β_0 vary with position so σ and S are also functions of position. The value of the photothermal signal at a particular point on the sample surface is obtained by calculating S (using the local values of Y, δ, and β at that point) and the sensitivity of S to variations in β is then given by the value of σ at that point.

A similar approach can be used in defining thermal character. If the explicit value of b_s is inserted in Eq. (14), and δ and Y are used as the thermal variables, S can be written in the form $S = \bar{S}(\beta,\delta)/Y$, where $\bar{S}$ is independent of Y. If $\log\bar{S}$ is plotted versus $\log\delta$, and we restrict δ to a small range near δ_0, we can expand $\log\bar{S}$ in a Taylor series and write $\bar{S} = \bar{S}(\beta,\delta_0)(\delta/\delta_0)^n$, where $n = \delta/\bar{S}(\partial\bar{S}/\partial\delta)_{\beta,Y}(\delta_0) = \delta/S(\partial S/\partial\delta)_{\beta,Y}(\delta_0)$. Thus $S = B(\beta,Y,\delta_0)\delta^n/Y$, where B is independent of δ. We define $n = 1 - 2TC$. When $TC = 0$, $S \propto 1/C$, when $TC = 1/2$, $S \propto 1/Y$, and when $TC = 1$, $S \propto 1/\kappa$. These special cases are listed in Table I. Other values of TC form intermediate cases. Since κ is a more convenient variable to use than δ, we note that $\delta/S(\partial S/\partial\delta)_{\beta,Y} = 1 + 2\kappa/S(\delta S/\partial\kappa)_{\beta,C}$ and obtain the definition given in Sec. III.

TABLE I. Thermal and frequency characteristics of three special values of thermal character.

TC	S is proportional to	Frequency dependence OBD	PA	Exclusive thermal dependence on
0	$(Y\delta)^{-1} = \kappa^{-1}$	$f^0 = 1$		Thermal conductivity
$\frac{1}{2}$	Y^{-1}	$f^{-1/2}$	f^{-1}	Thermal admittance
1	$\delta / Y = (fC)^{-1}$	f^{-1}	$f^{-3/2}$	Thermal capacity

As the sample is scanned, the photothermal signal S varies with the values of β, κ and C at the instantaneous point of illumination and parametrically with ω and R. When these changes are small,

$$\begin{aligned}\Delta S = {} & [(\partial S / \partial \kappa)(d\kappa / dx) + (\partial S / \partial \beta)(\partial \beta / \partial x) \\ & + (\partial S / \partial C)(dC / dx)]\, \Delta x \\ & + [(\partial S / \partial \beta)(\partial \beta / \partial \lambda)]\, \Delta \lambda \\ & + (\partial S / \partial \omega)\, \Delta \omega + (\partial S / \partial R)\, \Delta R\,. \end{aligned} \tag{23}$$

Here λ is the wavelength of the exciting light and x is an incremental distance along the scan. In terms of fractional changes,

$$\begin{aligned}\Delta S / S = {} & [\, P_\kappa\, d\kappa / \kappa dx + P_\beta\, \partial \beta / \beta \partial x + P_C\, dC / C dx \,]\, \Delta x \\ & + [\, P_\beta\, \partial \beta / \beta \partial \lambda \,]\, \Delta \lambda + P_\omega\, \Delta \omega / \omega + P_R\, \Delta R / R, \end{aligned} \tag{24}$$

where $P_\epsilon = \epsilon / S (\partial S / \partial \epsilon)$.

The P_ϵ are related through Eqs. 16–19 and are related to σ and TC through the definitions: $\sigma = 1 - P_\beta$ and $TC = -P_\kappa$. These relationships are shown in Table II. Several are of interest. Note that σ and TC are proportional to each other for PA detection but not for OBD detection. Also note that TC-1 measures the sensitivity of S to changes in C just as TC measures the sensitivity of S to κ. Table II shows that P_κ, P_C, and TC can be written as a function of P_ω only. This relationship is of practical importance since it indicates that the thermal character at any point on the sample surface can be determined by experimentally measuring P_ω at that point.

VI. THE EFFECT OF β, δ, AND R ON THERMAL CHARACTER AND PHOTOTHERMAL SATURATION OF PARTIALLY SATURATED SAMPLES

By numerically integrating Eq. (13) with respect to v and differentiating with respect to κ and β, TC and σ can be determined for all degrees of photothermal saturation. Figures 5 and 6 show contours of equal thermal character and equal photothermal saturation mapped over the βR, δ/R plane. Each axis is the ratio of two lengths, δ/R (abscissa) and R/μ (ordinate), where $\mu = \beta^{-1}$ is the optical-absorption length. When $\delta < R < \mu$ (R/μ and δ/R small), heat is generated in a circular cylinder (of length μ and radius R) that is longer than it is wide, and both dimensions are longer than a thermal-diffusion length. Under these circumstances, transverse heat flow (measured by the ratio δ/R) and normal heat flow (measured by the ratio $\delta/\mu = \beta\delta$) are both small and only heat generated close to the sample surface affects the surface temperature. In this case, heat flow is unimportant, and S depends exclusively on thermal capacity for both PA and OBD detection. This corresponds to the region where $TC = 0$ in Fig. 5.

When $\delta < \mu < R$ ($\delta/R < 1$ and $R/\mu > 1$), heat is generated in a short cylinder where the diffusion length, though still small, is comparable to μ. Under these circumstances, the sample is partially saturated, and S depends on both κ and C.

Increased transverse heat flow ($\delta/R > 1$) has no effect on the photoacoustic signal (Figs. 5 and 6), but the OBD signal is changed markedly. When $R < \mu < \delta$ ($R/\mu < 1$ and $\delta/R > 1$), competition exists between transverse and normal heat flow. For a sufficiently large ratio, δ/R, S depends exclusively on κ. In this case, the saturation criterion becomes $\beta R > 1$ rather than $\beta\delta > 1$. The crossover occurs when transverse heat flow and normal heat flow are equally important, i.e., when $R/\mu = R/\delta$ or $\beta\delta = 1$.

Figures 7–9 show these effects through standard optical saturation curves. In each figure, the solid curve is plotted with $\delta = \delta_{\min}$. In curve a both κ and C vary randomly within the range $\kappa/\kappa_{\min} = C/C_{\min} = 3$. In curve b, κ is constant and C varies randomly while in curve c, C is constant and κ varies randomly. The scatter in S produced by random variations in κ and C is shown by the dot-scatter pattern. (Curves b and c have been displaced slightly for clarity.)

As expected, when δ/R is small S depends on C when the sample is unsaturated, and on both κ and C when the sample is saturated (Figs. 7, 8). When $\delta/R > 1$, PA dependence remains the same, but OBD thermal dependence

TABLE II. The relationship between P_κ, P_β, P_C, P_ω, P_R,[a] σ, and TC.

	OBD	PA
P_κ	$-(1 + P_\omega) = -TC = -(\sigma + P_R')/2$	$-(3/2 + P_\omega) = -TC = -\sigma/2$
P_β	$-2P_\omega + P_R = 1 - 2TC + P_R' = 1 - \sigma$	$-2 - 2P_\omega = 1 - 2TC = 1 - \sigma$
P_C	$P_\omega = TC - 1 = (\sigma + P_R' - 2)/2$	$1/2 + P_\omega = TC - 1 = (\sigma - 2)/2$
TC	$1 + P_\omega = TC = (\sigma + P_R')/2$	$3/2 + P_\omega = TC = \sigma/2$
σ	$P_R - 2P_\omega = 2TC - P_R' = \sigma$	$3 + 2P_\omega = 2TC = \sigma$

[a] Where $P_R' = 1 \pm P_R$

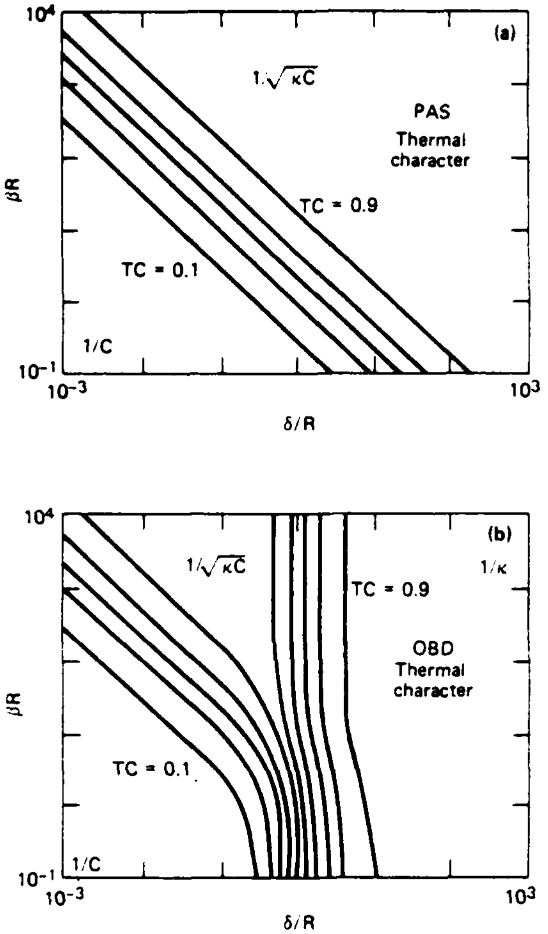

FIG. 5. Topographical map of thermal character for a thermally thick sample. Constant-*TC* contour lines separate areas where the photothermal signal is essentially controlled by a single thermal variable.

ranges from a dependence on C (for an unsaturated sample), a dependence on κ and C (for a partially saturated sample), and a dependence exclusively on κ (for a saturated sample) (Fig. 9).

VII. THERMALLY INDUCED PHOTOTHERMAL SATURATION

In a thermally homogeneous sample, when ω is fixed, δ is constant, and photothermal saturation depends upon the value of β alone. In a heterogeneous sample, where δ varies with position, saturation can result from either an increase in δ or a decrease in μ. This is illustrated in Fig. 6(a) for photoacoustic detection, where saturation can occur along either a vertical line (δ constant, β varying) or a horizontal line (β constant, δ varying). (We term this latter type of saturation *thermally induced optical saturation*.) For PA detection, the photothermal signal can saturate optically, regardless of the value of δ, and saturate thermally, regardless of the value of β.

For OBD detection, two distinct regimes exist [Fig. 6(b)]. When $\delta/R < 1$, OBD detection has the same saturation characteristics as PA detection, but when $\delta/R \gg 1$, all saturation contour lines become horizontal (Fig. 6), indicating that saturation is independent of the diffusion length δ, and the

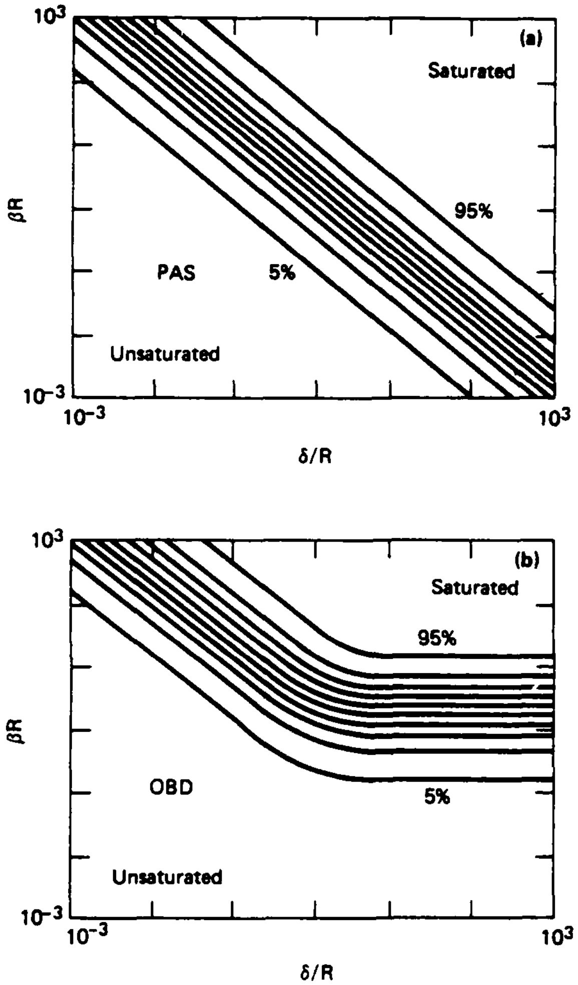

FIG. 6. Topographical map of σ, the degree of photothermal saturation, for a thermally thick sample. Constant-σ lines separate saturated from unsaturated regions.

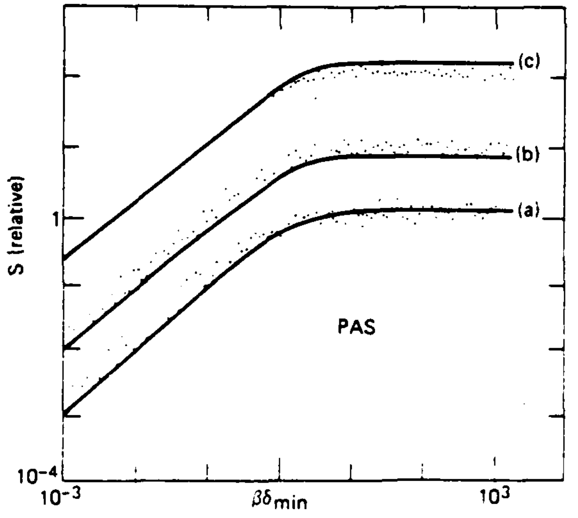

FIG. 7. Saturation curve for PA detection. (Curves *b* and *c* are offset for clarity.) β is plotted in units of δ_{min}^{-1}, and S values are relative. κ and C are constant for the solid curve while the scattered points are obtained by letting κ and C vary randomly within the bounds: $\kappa_{max}/\kappa_{min} = 3, 1, 3$ (for curves *a*, *b*, and *c*, respectively); $C_{max}/C_{min} = 3, 3, 1$ (for curves *a*, *b*, and *c*, respectively). Curves *b* and *c* show the independent effects of κ and C, respectively. (Figures 7–12 are plotted using log-log scales.)

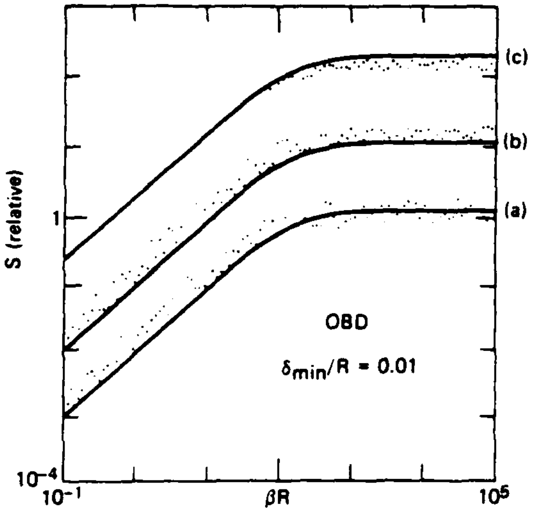

FIG. 8. Saturation curve (corresponding to Fig. 7) for OBD detection when $\delta/R = 0.01$. β is plotted in units of R^{-1}.

criterion for saturation becomes $\beta R > 1$.

To explain this situation, we again use the simplified picture where heat is generated in the sample within a circular cylinder of radius, R and length μ, and flows from this cylinder either normal or parallel to the sample surface. When $\delta \gg R$, heat spreads radially well beyond the cylinder walls. Only heat generated within a depth $\mu \simeq R$ reaches the sample surface before it flows (transversely) out of the volume in which it was generated. When $\mu > R$, the amount of heat reaching the surface near the excitation-beam axis (the region monitored by OBD detection) is unaffected by small changes in μ, and thus the photothermal signal is saturated.

When $\mu < R$, the amount of heat flowing to the sample surface in the vicinity of the excition beam is determined by the ratio of transverse to normal heat flow, i.e., by the ratio $(\delta/\mu)/(\delta/R) = R/\mu = \beta R$. Saturation is independent of δ as long as δ/R remains sufficiently large.

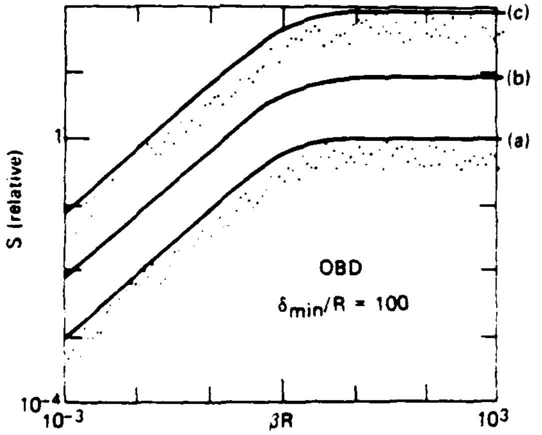

FIG. 9. Saturation curve (corresponding to Fig. 7) for OBD detection when $\delta/R = 100$. β is plotted in units of R^{-1}.

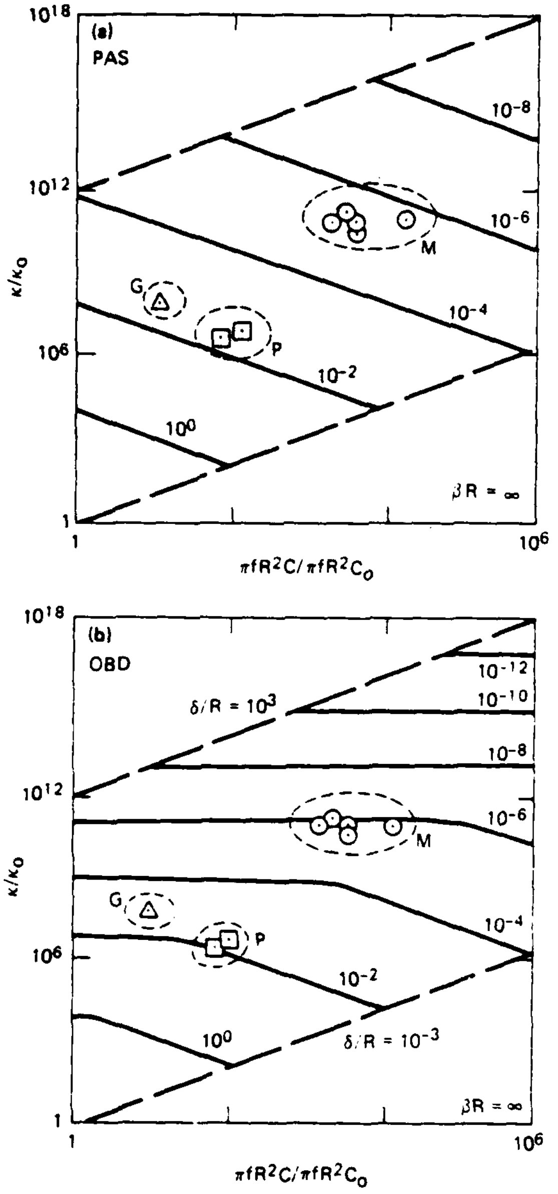

FIG. 10. Topographical map of the photothermal signal over the κC plane under saturated conditions ($\beta \rightarrow \infty$). (Thermally thick sample; localized excitation.) S values are relative. The point clusters illustrate the thermal dependence of selected M (metals), G (glass), and P (polymers) (see text). Position of clusters is for $f = 100$ Hz and $R = 100\ \mu$.

VIII. THE DEPENDENCE OF THE PHOTOTHERMAL SIGNAL ON INDIVIDUAL THERMAL VARIABLES

In Secs. VI and VII and Figs. 5–9, the dependence of S on κ and C was discussed in terms of the thermal ratio, κ/C (i.e., δ). To display the effect of κ and C separately, we view cross sections of $S\beta\kappa C$ space where β is constant. These results are applicable to photothermal imaging of optically saturated samples or any sample where β is spatially relatively uniform.

Figure 10 is a contour map of the cross section of $S\beta\kappa C$ space where $\beta \rightarrow \infty$. To make the figure universal, $\omega R^2 C/2$ has been used as the abscissa rather than C. If ω and R are constant, $\omega R^2/2$ is merely a scaling factor. The scale factors

κ_0 and C_0 (where $\kappa_0 = 10^{-6}\omega R^2 C_0/2$) permit a wide range of thermal parameters to be plotted. Using these axes makes the value of S relative, so absolute comparisons cannot be made. In Fig. 10, the thermal parameters of 5 metals, 2 polymers, and 1 glass are plotted for a particular value of κ_0 for $f = 100$ Hz and $R = 100$ microns. A different choice of κ_0 would shift each point and change the absolute value of S, but would not affect the relative positions of the various materials or their local dependence on S.

The purpose of Fig. 10 is to show the relative sensitivity of each material to changes in κ and C for a given value of ω and R. In OBD detection, the metals are seen to be insensitive to small variations in C and to depend only on κ, while the polymers depend on variations in both κ and C. For PA detection, all materials are equally sensitive to variations in both κ and C. Figure 11 presents similar information for $\beta = 0.1/R$ for $f = 100$ Hz and $R = 10$ microns. In this case, the polymers are affected only by C while the metals are still affected mainly by κ but show some dependence on C when OBD detection is used. In PA detection, all materials depend only on variations in C.

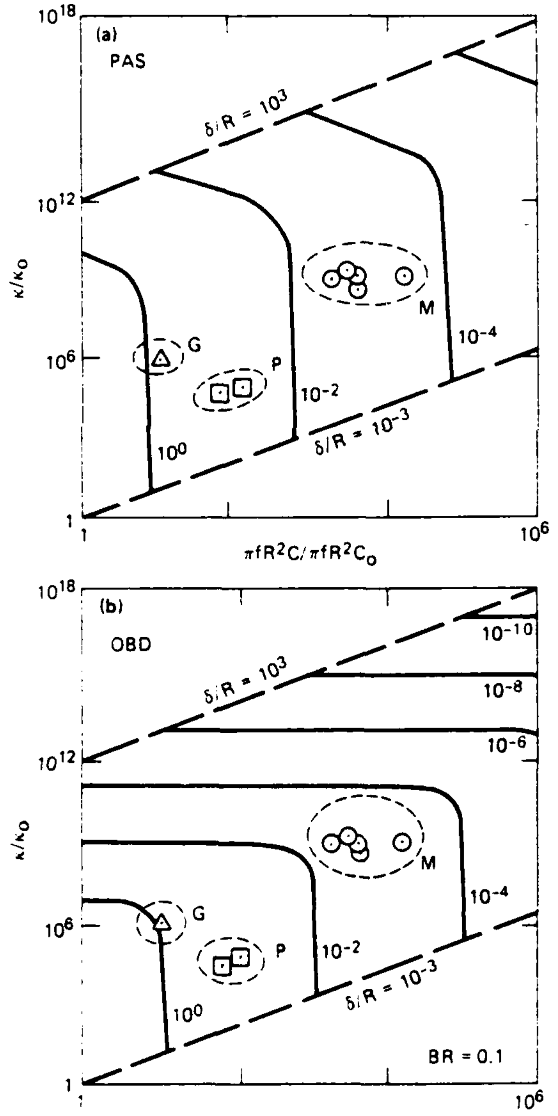

FIG. 11. Topographical map of the photothermal signal corresponding to Fig. 10 under unsaturated conditions when $\beta = 0.1/R$. S values are relative. The location of the clusters are for the parameters, $f = 100$ Hz and $R = 10$ μ.

In general, in a heterogeneous sample, the local thermal parameters vary over the sample surface and thus are represented by different points on the κC plane. As the sample is scanned, a corresponding curve is traced out in the κC plane (the "thermal trajectory" of the scan). Figure 12 illustrates this situation. The circled point in this figure is the value of κ, C assumed at the start of the scan. The arbitrary, dashed curve starting at this point represents a possible trajectory for some scan. At each point on the trajectory, the photothermal signal has different sensitivities to variations in the thermal parameters. The four vectors shown in Fig. 12 are thermal trajectories for the special conditions where the thermal-diffusion length, thermal admittance, thermal capacity, and thermal conductivity, respectively, are constant over the scan. The sensitivity of S to changes in C, Y, δ, and κ are indicated by the magnitude of the parameter change needed along each trajectory (from starting point to vector tip) to produce a fixed change in the photothermal signal.

IX. SUMMARY AND CONCLUSIONS

As long as homogeneous samples are used in photothermal spectroscopy and saturated samples in photothermal imaging, the pertinent analysis is reasonably straightforward. However, when heterogeneous and unsaturated samples, respectively, are used, a variety of additional complications arise. In studying such samples, optical beam deflection methods are especially useful since they are highly sensitive to transverse heat flow, and hence are helpful in

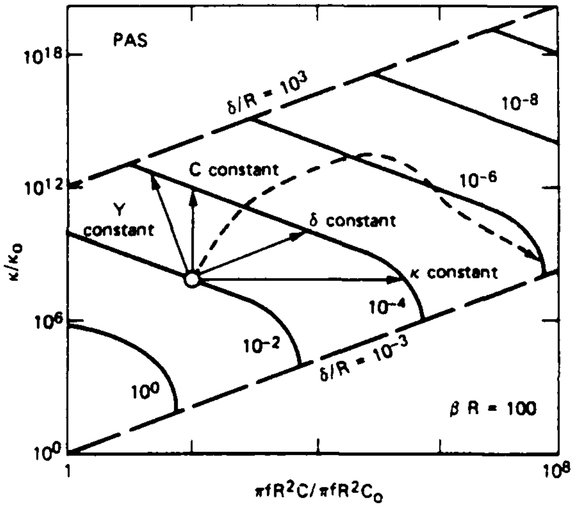

FIG. 12. A topographical map of the photothermal (OBD) signal over the κC plane for a thermally thick heterogeneous sample when $\beta = 100/R$. S values are relative. The dashed curve shows a possible thermal trajectory. Note the varying sensitivities to κ and C along the trajectory (scan). The four vectors shown are thermal trajectories corresponding to special scans where the thermal capacity, thermal conductivity, thermal admittance, and thermal-diffusion length, respectively, are constant over the scan.

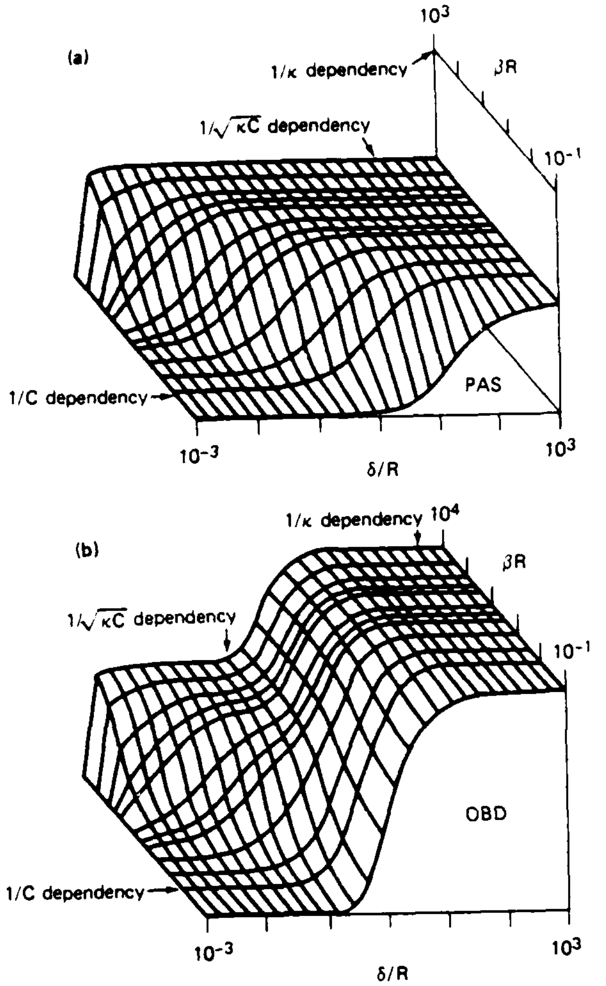

FIG. 13. The thermal-character-surface mapped over the $\beta\delta$ plane for a thermally thick sample. (See Fig. 5.) ($x/y/z$ axes: log/log/linear.)

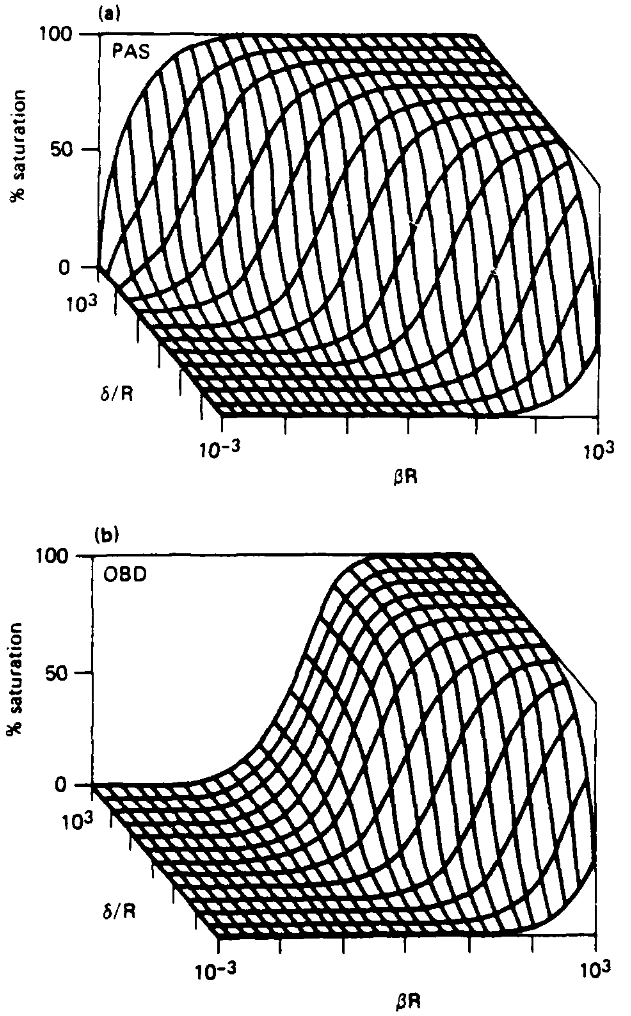

FIG. 14. The degree of photothermal-saturation surface mapped over the $\beta\delta$ plane for a thermally thick sample. (See Fig. 6.) ($x/y/z$ axes: log/log/linear.)

separating optical and thermal effects. This is especially true for the transverse component of the optical beam deflection. This component is capable of distinguishing homogeneous and inhomogeneous thermal effects. This method of detection also has the advantage of requiring no enclosed cell (which restricts sample size) and is relatively insensitive to environmental factors. These advantages have made it useful in studying optical and thermal defects in metals and ceramics.

This paper has considered the dependence of two types of photothermal signals on sample optical and thermal parameters. The analysis is specifically applicable to scanning studies of samples with spatially varying photothermal parameters that change gradually so that the sample can be considered homogeneous on the scale of several thermal-diffusion lengths.

It is found that the parametric dependence of the photothermal signal depends upon the detection method used. For a specific variant of the Optical Beam Deflection method of spectroscopy/imaging which is sensitive to local thermal transport, it is shown that by choice of the parameters under the control of the experimenter, the signal may be caused to depend on the thermal conductivity κ or the heat capacity C separately. This feature has potential application in studies which seek to invert the photothermal signal data to obtain the local values of κ and C. Such information could be important in use of photothermal imaging to study defects in solids. The more familiar photoacoustic detection method does not exhibit this type of parametric dependence and is potentially less convenient in imaging applications.

It is also found that the concept of photothermal saturation must be broadened when localized detection methods are used. For OBD detection, a new saturation regime exists which is defined by the product βR (β = optical absorption coefficient, R = excitation-beam radius), not the product $\beta\delta$ (δ = thermal-diffusion length) familiar from earlier formulations of photoacoustic saturation.

Based on these concepts, the concept of a thermal trajectory is introduced which is applicable to scanning imaging applications. As part of this development, it is shown that the photothermal expressions based on κ and C may be recast in terms of thermal admittance Y and thermal diffusion length δ. From this development, it is clear that prior photothermal treatments based on a consideration of δ only are special cases of a more general analysis.

ACKNOWLEDGMENT

This work has been supported by the U. S. Naval Sea Systems Command under Contract No. N00024-81-C-5301.

APPENDIX

Some of the data represented in the text by topographical maps are more easily (but less quantiatively) visualized via three-dimensional cross sections of $S\beta\kappa C$ space. Two of these cross sections are shown in Figs. 13 and 14. Each is referenced to the figure in the text to which it corresponds.

[1] A. Rosencwaig and A. Gersho, J. Appl. Phys. **47**, 64 (1976).

[2] L. C. Aamodt, J. C. Murphy, and J. G. Parker, J. Appl. Phys. **48**, 927 (1977).

[3] F. A. McDonald and G. C. Wetsel, Jr., J. Appl. Phys. **49**, 2313 (1978).

[4] L. C. Aamodt and J. C. Murphy, J. Appl. Phys. **49**, 3036 (1978).

[5] J. C. Murphy and L. C. Aamodt, J. Appl. Phys. **51**, 4580 (1980).

[6] J. C. Murphy and L. C. Aamodt, J. Appl. Phys. **48**, 3502 (1977).

[7] Y. L. Wong, R. L. Thomas, and G. F. Hawkins, Appl. Phys. Lett. **32**, 538 (1978).

[8] M. Lukkala and S. G. Askerov, Electron Lett. **16**, 84 (1980).

[9] R. J. Freese, Ph.D. thesis, University of Rochester, 1979.

[10] G. Busse and A. Ograboch, J. Appl. Phys. **51**, 3576 (1980).

[11] J. C. Murphy and L. C. Aamodt, Appl. Phys. Lett. **38**, 196 (1981).

[12] D. Fournier and A. C. Boccara, in *Scanned Image Microscopy*, edited by E. A. Ash (Academic, New York, 1980).

[13] A. C. Boccara, D. Fournier, and J. Badoz, Appl. Phys. Lett. **36**, 130 (1980).

[14] W. B. Jackson, N. M. Amer, A. C. Boccara, and D. Fournier, Appl. Opt. **20**, 1333 (1981).

[15] L. C. Aamodt and J. C. Murphy, J. Appl. Phys. **52**, 4903 (1981).

APPENDIX

PHOTOTHERMAL IMAGING OF DEFECTS IN METALS AND CERAMICS

3. J. W. Maclachlan, J. C. Murphy, R. B. Givens, and F. G. Satkiewicz, "Linear Thermal Wave Imaging," 11th World Conference on Nondestructive Testing, Nov. 3-8, 1985, Las Vegas, Dallas: Taylor Publishing Co., p. 441, 1985.

LINEAR THERMAL WAVE IMAGING

Jane W. Maclachlan, John C. Murphy, R. Ben Givens and Frank G. Satkiewicz

Center for Nondestructive Evaluation
Applied Physics Laboratory
The Johns Hopkins University, Laurel, MD

INTRODUCTION

Thermal wave imaging is a new technique for NDE which has been used to study a wide range of materials systems, from insulators to metals, and has proven to be a valuable tool for the nondestructive evaluation of both flaws and microstructure. There are a wide variety of techniques grouped under the term "thermal wave imaging", each with inherent advantages and disadvantages. Figure 1 summarizes the basic

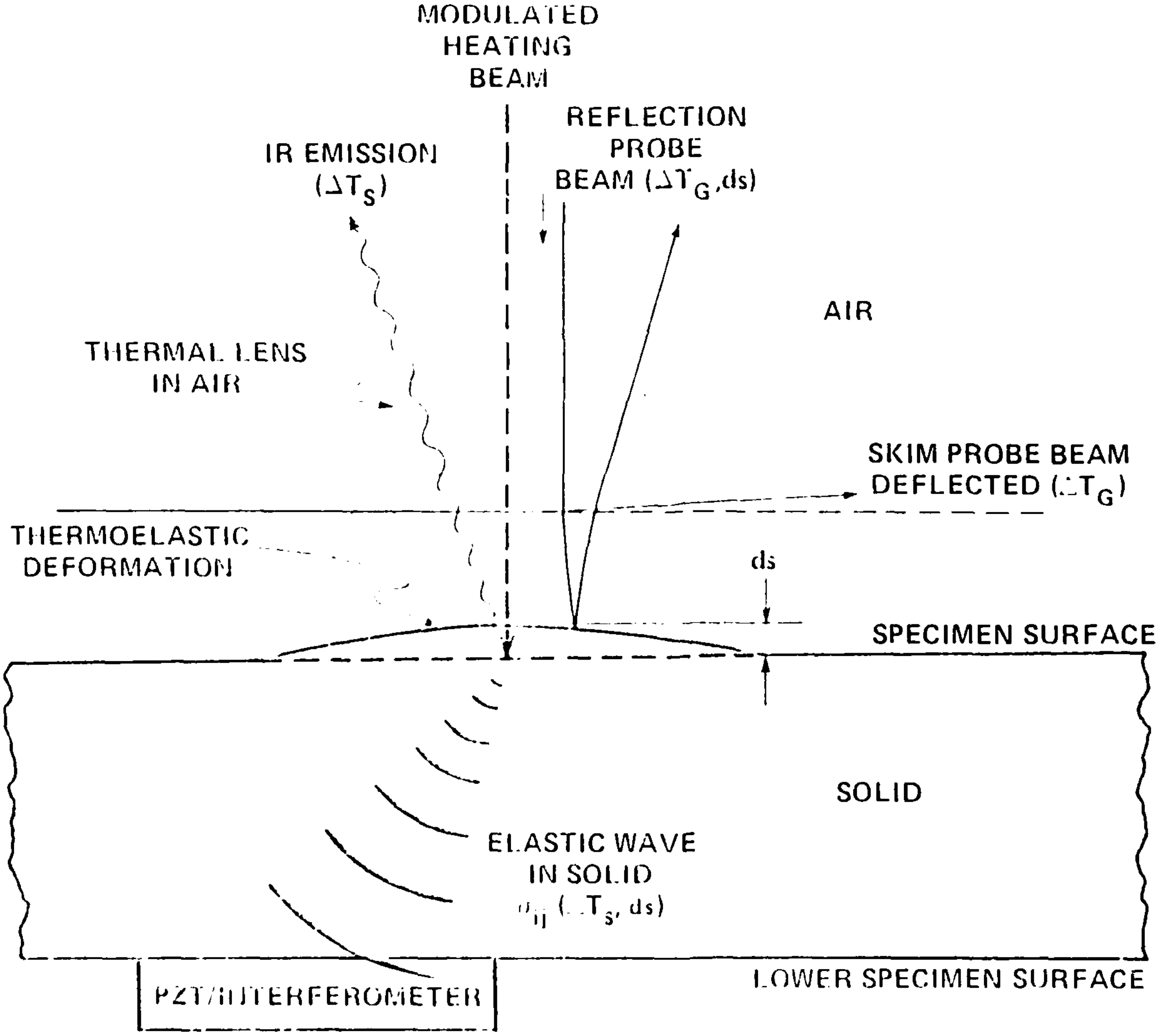

Fig. 1 Physical Mechanisms Involved in Thermal Wave Imaging

physical processes involved in a number of these techniques. In all cases heat is locally introduced into a sample using a periodic heating source such as a modulated laser beam, electron beam or ion beam. This pump beam produces a periodic change in the local temperature distribution of the sample and it is convenient to think of this temperature distribution in terms of the propagation of "thermal waves". These waves decay exponentially with distance and both the thermal wavelength and the exponential decay rate are dependent on a parameter known as the thermal diffusion length. The thermal diffusion length is given by:

$$\delta = \left(\frac{\kappa}{2\rho C\omega}\right)^{1/2}$$

where κ is the thermal conductivity, C is the heat capacity, ρ is the density and ω is the modulation frequency of the pump beam. The propagation of the thermal waves is therefore sensitive to local variations in the thermal properties of the material via the thermal diffusion length and an image of the variation in thermal properties can be produced. The resolution of this image depends on a number of parameters including geometrical considerations such as the pump beam diameter. As a rule of thumb, however, one can consider the thermal diffusion length in the material to be a good estimate of the resolution obtainable in a thermal wave image.

Information about the propagation of the thermal waves can be collected in a variety of ways as shown in Fig. 1. The spatial temperature distribution in the material can be measured by either optical beam deflection[1,2] or radiometry[3]. In optical beam deflection techniques there are two possible geometries for the probe beam as shown in the figure. In the skimming orientation the probe beam is directed parallel to the sample surface and is sensitive to temperature gradients in the gas layer above the sample, a phenomenon termed the mirage effect. In the reflective orientation, the probe beam is reflected at the sample surface and the deflections of the beam are a combination of the mirage effect and thermoelastic displacements of the sample surface. Alternatively, the elastic waves generated at the heating beam modulation frequency by local thermal expansion can be monitored using a piezoelectric detector[4]. In Fig. 1 such a detector is shown mounted on the bottom surface of the sample. It is also possible to monitor the elastic waves using laser interferometric detection schemes.

The nature of the thermal wave images produced depends to a large extent on the type of detection process used. When the temperature distribution in the material is the measured parameter (e.g. optical beam deflection, radiometry), the contrast mechanisms depend solely on thermal properties of the material. A combination of thermal, thermoelastic and elastic properties determine the contrast mechanisms when the elastic waves are detected. The geometry of the detection process is also important. Radiometry and piezoelectric detection give a signal which has been integrated over a large area. Optical beam deflection and laser interferometric schemes allow localization of the detection process. Contrast mechanisms in thermal wave imaging also depend on the nature of the excitation process. Specific characteristics of the specimen-beam interactions for photons, electrons and ions must be considered including parameters such as the geometry of the energy deposition and momentum effects.

EXPERIMENTAL TECHNIQUES

As described above there are a number of methods for both generating and detecting thermal waves and this leads to a wide variety of possible experimental configurations. The experimental setup used for some of the images presented in this paper using electron beam excitation and piezoelectric detection is shown in Fig. 2. A scanning electron microscope was modified to allow blanking of the electron beam and the samples are mounted on top of a piezoelectric detector. The output of the

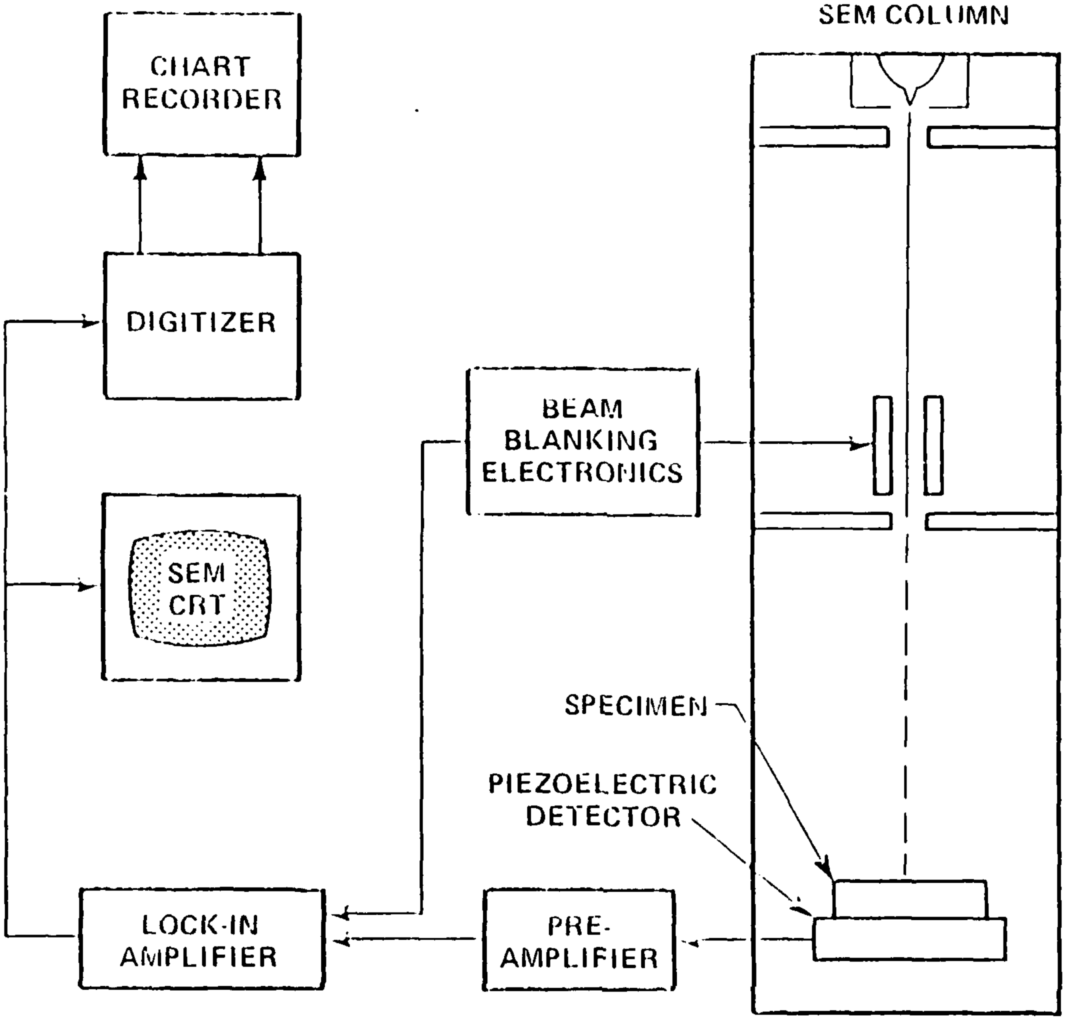

Fig. 2 Experimental Setup for Scanning Electron Acoustic Microscopy

detector is amplified and a lock-in amplifier is used to determine the amplitude and phase of the acoustic signal relative to the reference signal used to blank the electron beam. Either the amplitude or phase signal from the lock-in amplifier can be used in conjunction with the signal from the scan generators of the SEM to produce images on the SEM CRT. The experimental setups for other generation and detection schemes are in principal very similar. In each instance the heating beam is modulated and scanned across the sample surface. The amplitude and phase of the signal from the detector (e.g. position sensitive detector in optical beam deflection studies, laser interferometer, etc.) is then recorded as a function of position of the heating beam on the sample. A thermal wave image can then be constructed.

APPLICATIONS OF THERMAL WAVE IMAGING

Location of Cracks and Buried Defects

Many researchers have used thermal wave imaging to detect cracks in opaque materials (e.g. (5)), predominantly in experiments employing laser beam heating. Cracks and voids produce an abrupt change in the local thermal properties and are good candidates for investigation by thermal wave techniques. To illustrate the detection of a buried defect, Fig. 3 shows line scans of a buried double defect for a series of modulation frequencies using ion beam excitation and piezoelectric detec-

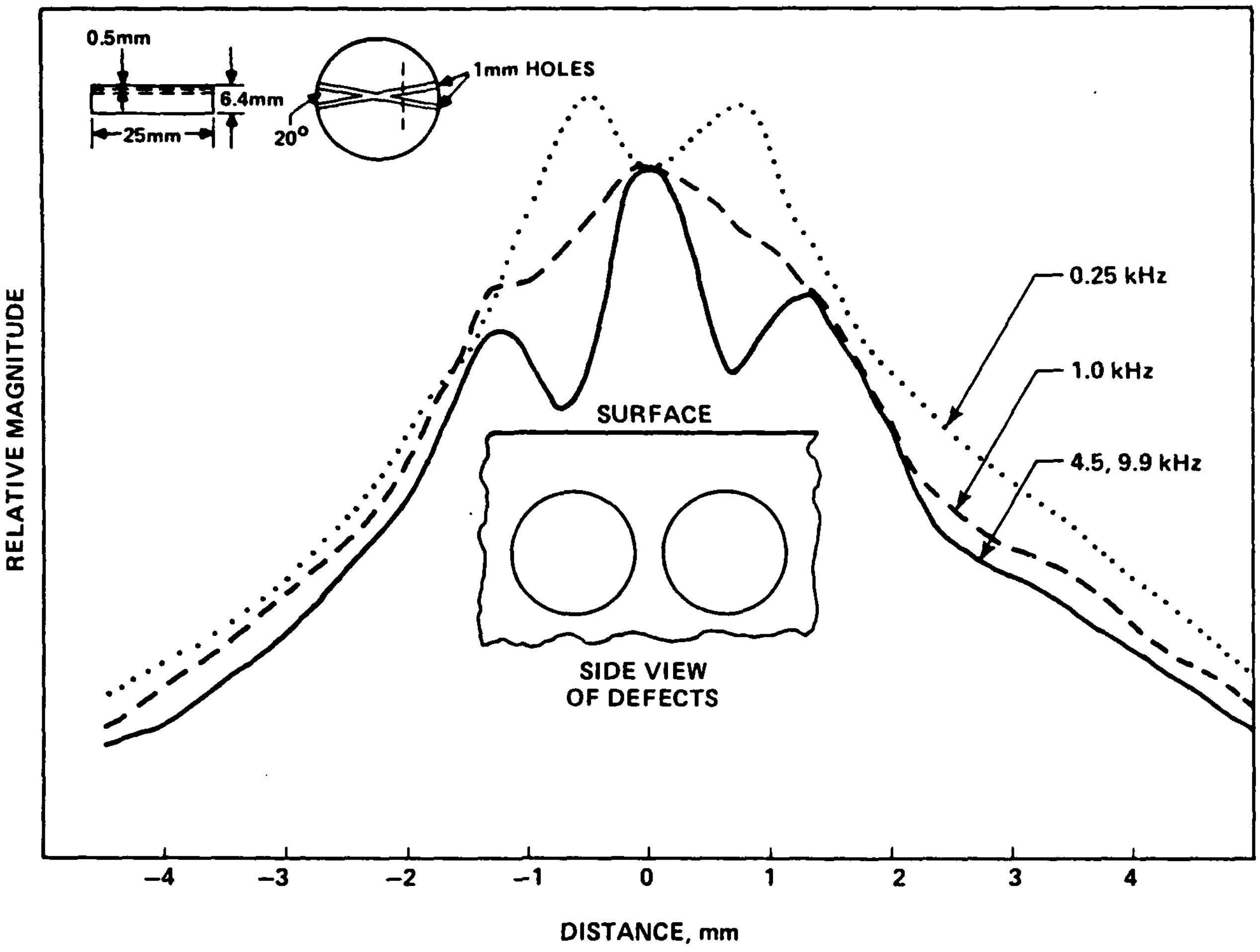

Fig. 3 Ion-Acoustic Scan of a Buried Double Defect

tion. An important feature of this result is that the defect is detected even at high modulation frequencies where the thermal diffusion length is much less than the depth of the defect. There is also a change in the signature of the signal when the thermal diffusion length becomes less than the defect depth. This suggests the presence of non-thermal contrast mechanisms for excitation with modulated particle beams such as ions and electrons.

Characterization of Grain Boundaries

Thermal wave imaging is proving to be a useful technique for the examination of microstructure. Details of grain size and martensitic structure are readily obtained without special surface preparation (e.g. (6)). Fig. 4 shows both secondary electron and thermal wave images of a polycrystalline sample of high purity aluminum produced with a scanning electron acoustic microscope as described above. While no grain structure is evident in the secondary electron image, contrast at grain boundaries and between grain interiors is clearly seen in the thermal wave image. In an attempt to better understand contrast mechanisms at grain boundaries another sample of high purity aluminum was polished and etched to produce a narrow channel (about 1.5 microns wide) along the grain boundary. This allowed the precise location of the boundary to be determined in the secondary electron image (see Fig. 5). The magnitude and phase of the signal from piezoelectric detector were then superimposed on the secondary electron image for 3 positions along the boundary. The variation in the signal for different locations along the boundary suggests variation in the

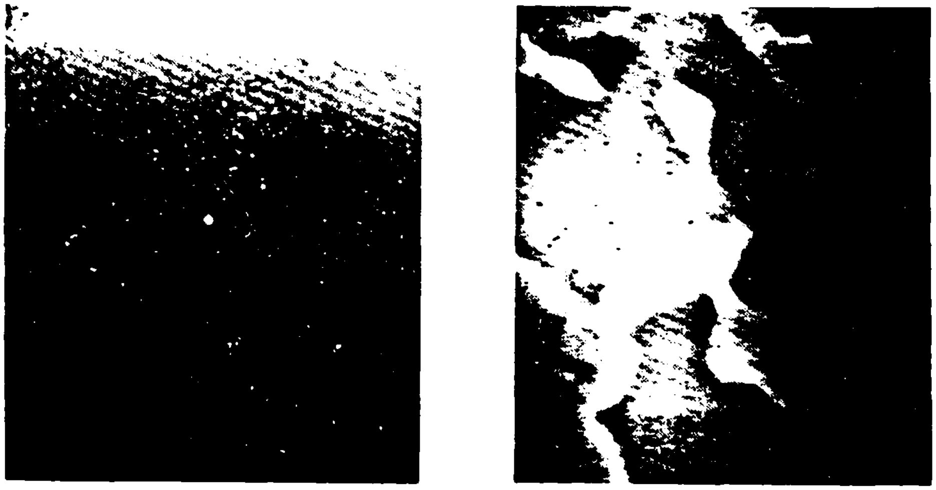

SECONDARY ELECTRON IMAGE **ACOUSTIC MAGNITUDE IMAGE**

Fig. 4 Secondary Electron and Electron-Acoustic Images of High Purity Polycrystalline Aluminum. (14.3 kHz, 20 keV).

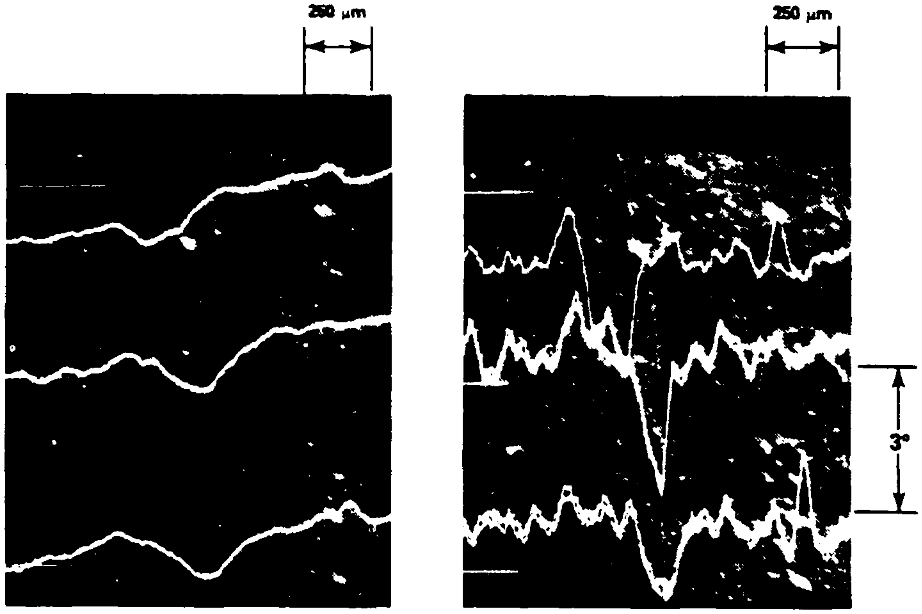

MAGNITUDE **PHASE**

Fig. 5 Secondary Electron Image of Aluminum Grain Boundary with Acoustic Magnitude and Phase Line Scans Superimposed. (43.0 kHz, 20 keV)

boundary thermal properties, perhaps indicating changes in impurity or vacancy concentrations. Examination of the grain boundary as a function of modulation frequency revealed that the apparent width of a grain boundary in a SEAM image is directly proportional to the thermal diffusion length.

Inspection of Integrated Circuits

Thermal wave imaging has been used to detect defects such as delaminations and subsurface cracks in semiconductor devices[7]. High resolution images of integrated circuits can be achieved using SEAM. In fact the resolution is much greater than the thermal diffusion length, suggesting the presence of more than a simple thermal contrast mechanism. Examples are shown in Fig. 6 where both secondary electron and thermal wave images are presented for two different primary beam energies. The effect of change in specimen-beam interaction volume is clearly seen in the secondary electron images where the low energy beam does not reveal any structure beneath a surface layer of carbon while the higher energy beam detects the subsurface structure easily. A companion dependence of the thermal wave image on primary beam energy is observed. At 5 keV the thermal wave image closely resembles the secondary electron image. At 30 keV, however, a subsurface structure is clearly revealed which is only faintly evident in the secondary electron image at 30 keV.

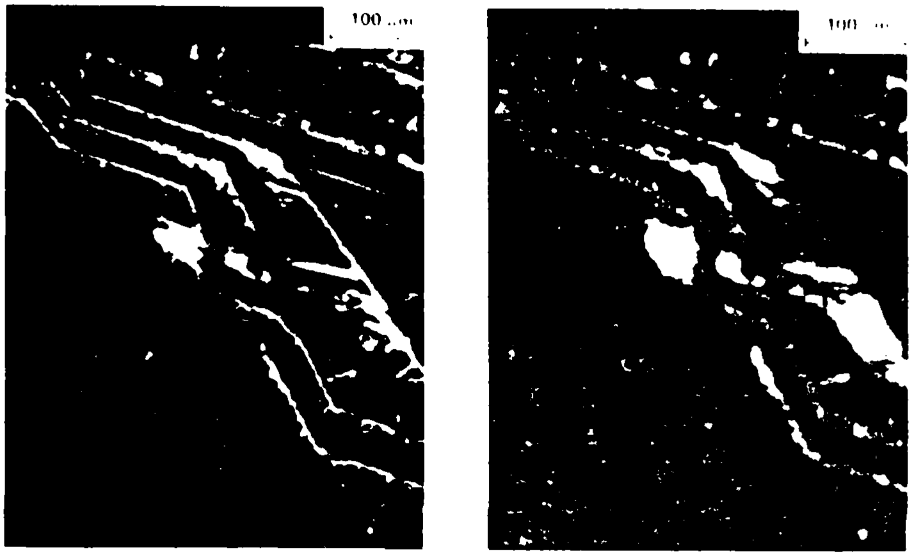

5 keV, S.E.   5 keV, ϕ, 480 kHz

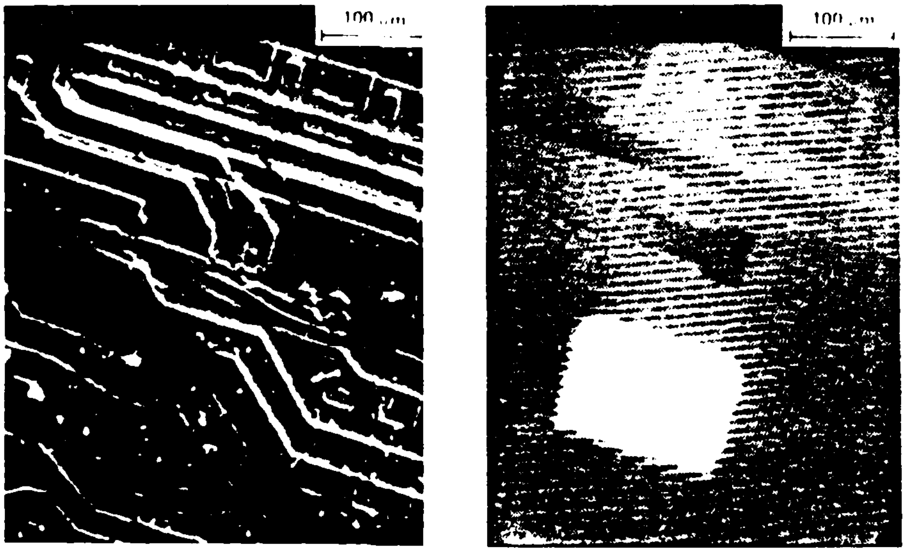

30 keV, S.E.   30 keV, ϕ, 480 kHz

Fig. 6. Secondary Electron and Electron Acoustic Images of Integrated Circuit at Primary Beam Energies of 5 keV and 30 keV.

Preliminary work suggests that thermal wave imaging will prove to be a useful technique for the nondestructive evaluation of composite materials. Failure processes such as fiber fracture, fiber-matrix debonding and matrix crazing are all candidates for examination. Figure 7 shows a thermal wave scan of a fiberglass epoxy composite material produced by laser excitation and detection by optical beam deflection with the probe laser in the reflective orientation. The presence of individual fibers and their orientations are clearly defined, leading to the possibility of monitoring damage to these fibers.

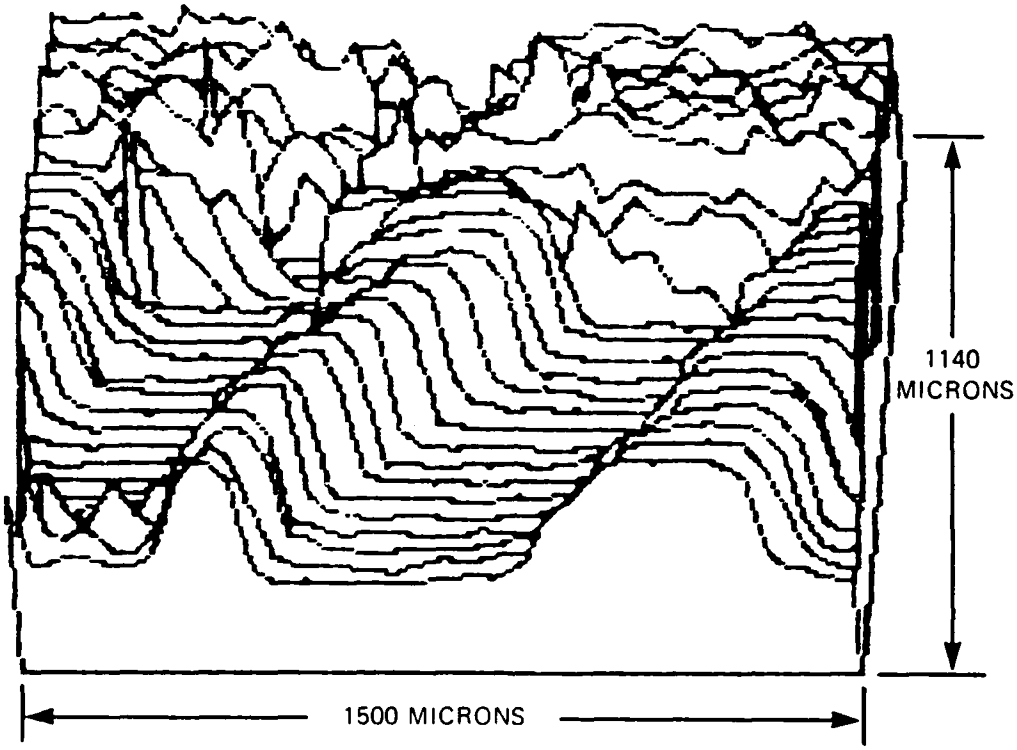

Fig. 7 Photothermal Scan of Fiberglass-Epoxy Composite Using Reflective Optical Beam Deflection.

SUMMARY

Thermal wave imaging is an emerging tool for nondestructive evaluation which has possible applications to many materials systems. Local variations in thermal properties due to a wide range of structures such as cracks, defects, delaminations, microstructure, dopant concentrations, etc. can be accurately mapped. The large number of excitation and detection techniques which are available allow implementation of thermal wave imaging in a wide variety of physical situations, including those requiring noncontact inspection. There are still questions, however, as to the precise physical nature of some of the contrast mechanisms involved, particularly for detection of elastic waves and excitation with particle beams. Also, nonlinear thermal and thermoelastic specimen responses have been observed suggesting a whole new collection of possible contrast mechanisms in thermal wave imaging.

*This work was supported by the U. S. Army Research Office and the U. S. Naval Sea Systems Command under Contract No. N00024-85-C-5301.

REFERENCES

1. D. Fournier & A. C. Boccara, "The Mirage Effect in Photothermal Imaging," Scanned Image Microscopy, ed. E. A. Ash, Academic Press, London, 1980, pp. 347-351.
2. J. C. Murphy & L. C. Aamodt, "Optically Detected Photothermal Imaging," Appl. Phys. Lett. 38, No. 4 (1981), p. 196.
3. P.-E. Nordal & S. O. Kanstad, "Photothermal Radiometry for Spatial Mapping of Spectral and Material Properties," Scanned Image Microscopy, ed. E. A. Ash, Academic Press, London, 1980, pp. 331-339.
4. A. Rosencwaig & G. Busse, "High Resolution Photoacoustic Thermal Wave Microscopy," Appl. Phys. Lett. 36, No. 9 (1980), p. 725.
5. K. R. Grice, L. J. Inglehart, L. D. Favro, P. K. Kuo & R. L. Thomas, "Thermal-wave Imaging of Closed Cracks in Opaque Solids," J. Appl. Phys. 54, No. 11 (1983), p. 6245.
6. L. J. Balk, D. G. Davies & N. Kultscher, "The Dependence of Scanning Electron Acoustic Microscopy (SEAM) Imaging on Chopping and Detection Frequency for Metal Samples," Phys. Stat. Sol. (a) 82 (1984), p. 23.
7. A. Rosencwaig, "Thermal-wave Imaging," Science 218 (1982), p. 223.

APPENDIX

PHOTOTHERMAL IMAGING OF DEFECTS IN METALS AND CERAMICS

4. F. G. Satkiewicz, J. C. Murphy, L. C. Aamodt, and J. W. Maclachlan, "Ion-acoustic Imaging of Subsurface Flaws in Aluminum," 4th International Topical Meeting on Photoacoustic, Thermal, and Related Sciences, Ville d'Esterel, Quebec, Aug. 4-8, 1985.

Ion-Acoustic Imaging of Subsurface Flaws in Aluminum*

F. G. Satkiewicz, J. C. Murphy, and L. C. Aamodt
Applied Physics Laboratory
The Johns Hopkins University
Johns Hopkins Road
Laurel, MD 20707 U.S.A.

By now a number of derivative imaging techniques broadly related to the photoacoustic process have been described. These techniques commonly use a localized excitation source which is scanned over the specimen surface and a detection process which measures some thermal, elastic or electronic property of the specimen which has been modulated by the excitation. Examples include Optical Beam deflection imaging[1,2], Scanned Photoacoustic imaging[3], and a variety of scanned laser and electron beam acoustic imaging techniques[4,5,6] which use attached piezoelectric transducers to monitor stress generated within the specimen. No effort has been made to make this a complete summary of available generation or detection methods.

Modulated beams of Ar ions are used to excite the specimen. The elastic response of the specimen is detected using an attached PZT transducer in a manner similar to that initially developed for electron-acoustic imaging in the SEM. In the present case a SIMS (Secondary Ion Mass Spectrometry) instrument was modified for ion-acoustic imaging studies. In keeping with the generally accepted theory of sputtering[7] which is based on momentum transfer from ions to solid, it was expected that the specimen elastic response would include a strong momentum component. This signal generation process has not been identified in prior imaging studies using laser or electron sources. Moreover, it was expected that the results would be related to work involving laser ultrasound generation[8] involving sample ablation.

Figure 1 shows line scans of PZT voltage as the ion beam is scanned over the sample surface. The specimen, an aluminum disc 1.4 cm in diameter and 3 mm thick containing a 1 mm slant hole, is shown schematically in the figure. The slant hole permits the hole signature to be studied for various depths below the surface. Other specimen geometries varying specimen diameter, thickness and hole depth, diameter and length have also been used. The main features of the result reported here are found also in all other specimens studied. In Figure 3 the modulation frequency for the ion beam is 4.2 kHz. There is a broad envelope response on which is superimposed a response characteristic of the defect location. Measurements on specimens of similar geometry with no subsurface hole show a virtually identical envelope response.

The main features of the defect signature in Figure 1 are the large increase in signal above the shallow defect, the change in signal profile for deeper defects and the decrease in overall defect signal magnitude with increasing frequency. Other features to be discussed later include broadening of the defect profile with depth and the dependence of the profile on the diameter of the buried hole. Studies of profile shape as a function of defect depth and modulation frequency indicate that the thermal diffusion length constitutes the criterion for the change in profile from shallow to deep defect type. Figure 2 displays profiles at the trace 2 position of Figure 1 for several modulation frequencies and indicates the reciprocity of depth and modulation frequency. The increased signal observed when d < delta is ascribed to inhibited thermal flow above the defect and a resulting increase in thermoelastic signal generation. The invariance of the signal profiles for d > delta indicates that a non-thermal contrast mechanism also is present. To our knowledge similar effects are not seen in laser or electron imaging. Resolution measurements on two subsurface channels meeting at a shallow angle have also been made. These experiments give results consistent with the single hole profiles and including the existence of two signal regimes. Issues related to the ultimate of ion imaging will be discussed.

Measurements of the PZT signal dependence on beam current and voltage have been made seeking to elucidate the signal generation mechanisms and the image contrast mechanisms. Figures 3, 4 show the dependence on beam parameters. The linear response with beam current at constant voltage is consistent with either a thermoelastic or momentum transfer mechanism for signal generation. However, the linear dependence on beam voltage appears to be inconsistent with a momentum transfer process, a result somewhat unexpected in light of general sputtering theory for ion-solid interactions. This issue is being actively pursued both experimentally and theoretically.

In summary, low resolution ion-acoustic images of buried defects in aluminum have been observed. Expected thermal interactions with the defect have been seen and provide image contrast. In addition defect imaging by non-thermal interactions has also been seen at depths more than ten times the thermal diffusion length. The generation and contrast processes operative in ion-acoustic imaging will be discussed with special emphasis on the relative importance of momentum exchange and thermoelastic processes.

[*] Work supported in part by U. S. Naval Sea Systems Command contract No. N00024-85-C-5301.

1. D. Fournier and A. C. Boccara in "Scanned Image Microscopy," E. A. Ash ed. (1980).
2. J. C. Murphy and L. C. Aamodt, Appl. Phys. Lett. 38, 196 (1981).
3. Y. L. Wong, R. L. Thomas, G. F. Hawkins, Appl. Phys. Lett. 32, 538 (1978).
4. G. Busse, A. Rosencwaig, Appl. Phys. Lett. 36, 815 (1980).
5. G. S. Cargill, Physics Today, October 1981.
6. A. Rosencwaig, Science, 223 (1982).
7. P. Sigmund in "Sputtering by Particle Bombardment I," R. Behrisch, ed. (1981), Springer.
8. R. J. Dewhurst, D. A. Hutchins, S. B. Palmer, C. B. Scruby, J. Appl. Phys. 53, 4064 (1982).

APPENDIX

PHOTOTHERMAL IMAGING OF DEFECTS IN METALS AND CERAMICS

5. F. G. Satkiewicz, J. C. Murphy, L. C. Aamodt, and J. W. Maclachlan, "Ion-Acoustic Imaging of Subsurface Flaws in Aluminum," Williamsburg, VA, June 23-28, 1985, Review of Progress in Quantitative NDE, Plenum Press, 1986.

ION-ACOUSTIC IMAGING OF SURFACE FLAWS IN ALUMINUM*

FRANK G. SATKIEWICZ, JOHN C. MURPHY, LEONARD C. AAMODT,
AND JANE W. MACLACHLAN
Applied Physics Laboratory, The Johns Hopkins University
and The center for Non-Destructive Evaluation, The Johns
Hopkins University

Abstract

Modulated beams of Ar ions have been used as sources for thermoelastic imaging studies of aluminum. The ion-specimen interaction process is discussed in the context of elastic wave generation and in light of the theory of sputtering. Imaging of buried subsurface features is demonstrated with detection of very deep flaws observed. Thermal and elastic contrast mechanisms are demonstrated. The implication of these findings for Scanning Electron Acoustic Microscopy (SEAM) is disucssed.

INTRODUCTION

Imaging methods based on specimen excitation by scanned laser and electron beams are now well established as nondestructive methods of characterizing materials properties and locating surface and near subsurface flaws in solids. Several classes of methods have been identified each distinguished by the method of generation or the means of detection. Examples include Optical Beam Deflection (OBD) imaging[1,2] Scanned Photo-accoustic imaging[3] and a variety of scanned laser and electron beam acoustic imaging techniques[4,5,6] which use attached piezoelectric transducers to monitor stress generated within the specimen. Because many of these methods monitor changes in specimen temperature or a parameter related to specimen temperature, these imaging methods have been broadly termed thermal wave imaging (TWI). Nonthermal image contrast mechanisms may exist in cases where specific beam-specimen interactions are present. The term TWI is therefore a convenient but inaccurate way of categorizing scanned image methods using modulated beams.

In this paper we describe the use of modulated ion beams[7] as excitation sources for TWI. Indeed one of the effects of ion beam-specimen interaction is local generation of heat much in the manner of laser or electron beams. The images observed in this regime with ion excitation are similar to those obtained with either electron or laser sources. These studies of ion beam images using thermoelastic (TE) detection with a PZT transducer have shown that the observed image contrast has distinct thermal and elastic components. These results have been confirmed using laser and electron beam sources. This resolves a controversy which had existed over the question of the origin of contrast in SEAM imaging.

Ion beams offer the prospect of nonthermal contrast processes related to beam-specimen interactions specific to individual ion sources. In this work we investigate the possible contribution of one such mechanism, particle momentum transfer, from heavy rare gas ion beams at energies in the 1 to 10 kV range. Note that reactive particle beams (e.g. O_2^-) can also be used. In such cases non-thermal image contrast characteristic of the reaction of the ions and local constituents of the specimen may be observed. As a third example for light ion beams such as H^+, the capture cross section as a function of incident energy has a large peak at a specific depth (the range). This feature, which does not exist for heavier ions, opens the prospect of depth profiling.

ION-ACOUSTIC IMAGING OF SURFACE FLAWS IN ALUMINUM

BACKGROUND

Figure 1 illustrates the wide variety of excitation and detection techniques applicable to TWI. The details of the images produced depend on the distinct group of physical parameters exploited by each detection technique, from purely thermal parameters in optical beam deflection measurements or IR radiometric measurements to a combination of thermal, thermoelastic and elastic parameters with optical interferometric or piezoelectric detection. Similarly, differences in thermal wave images might be expected for different excitation sources based on specific beam-specimen interactions. We compare use of ions, electrons and photons later in this paper.

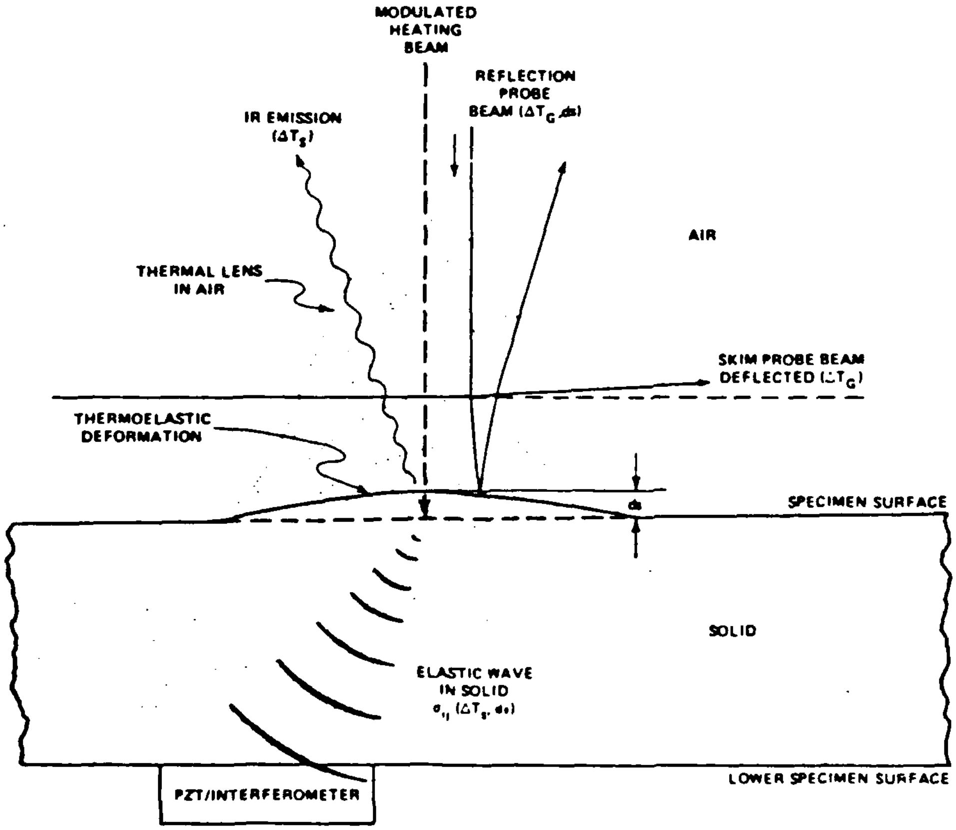

FIGURE 1 Summary of thermal wave imaging detection methods.

Figure 2 depicts the experimental configuration used for ion imaging. The primary beam optics of a Secondary Ion Mass Spectrometer (SIMS) was modified to allow blanking of the primary beam using electrostatic deflection plates. The sample was mounted on a piezoelectric detector and the magnitude and phase of the detector voltage were measured with the lockin amplifier or a spectrum analyzer. In the present configuration line scans are generated by moving the sample in front of the ion beam. The net specimen current was measured simultaneously and used as a monitor of the beam energy deposited in the specimen at fixed primary beam voltage. In these experiments the primary beam voltage ranged from 1 to 10 kV, the beam currents from 0.3 to 14 uA and the modulation frequencies from 15 Hz to 20 kHz. The ion beam diameter was about 300 μm.

Companion electron-acoustic images (SEAM) were made for some of the specimens used for ion imaging using an ETEC Auto-

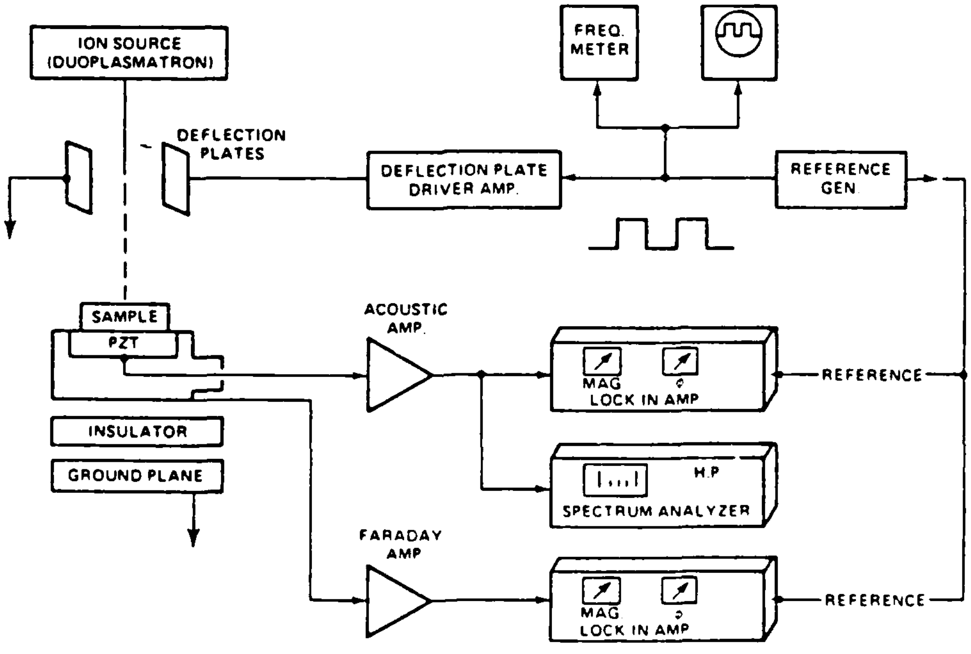

FIGURE 2 Schematic diagram of imaging system.

scan scanning electron microscope which had been modified to allow beam blanking. Laser acoustic and optical beam deflection images were also made of these same specimens using an argon laser as the excitation source. Here beam modulation was accomplished using an acousto-optic modulator. All specimens used for comparative studies of different excitation beams used the same mounting of specimen and acoustic detector with no breakage of the specimen-detector bond. The beam diameters for the electron and laser experiments were about 0.1 μm and 5 μm respectively.

ION-ACOUSTIC GENERATION PROCESSES

The acoustic signal generated in a solid by a modulated beam of Ar^+ ions depends in general on the specific energy and momentum of each ion, on the ion flux and on the composition of the solid. In this paper the samples were an aluminum alloy, probably in the 2024 series. Specimen specific changes in acoustic signal generation have been observed for a number of other elemental samples but will not be discussed here.

Figure 3 shows the dependence of the magnitude of the acoustic signal on specimen current for fixed primary beam voltage at a modulation frequency of 2 kHz. The dependence is approximately linear with a mean slope of 0.96. Measurements taken at other frequencies in the range 15 Hz to 20 kHz also show the same mean -- linear dependence on beam current.

Figure 4 shows the corresponding dependence on primary beam voltage for constant beam current. In this case the observed slopes fall in a range around 0.85 as shown in the figure. Measurements at other frequencies yield slopes also clustered in the range around 0.85. The origin of this nonlinear dependence of acoustic signal on the primary beam voltage has not been fully established. Complex ion-specimen

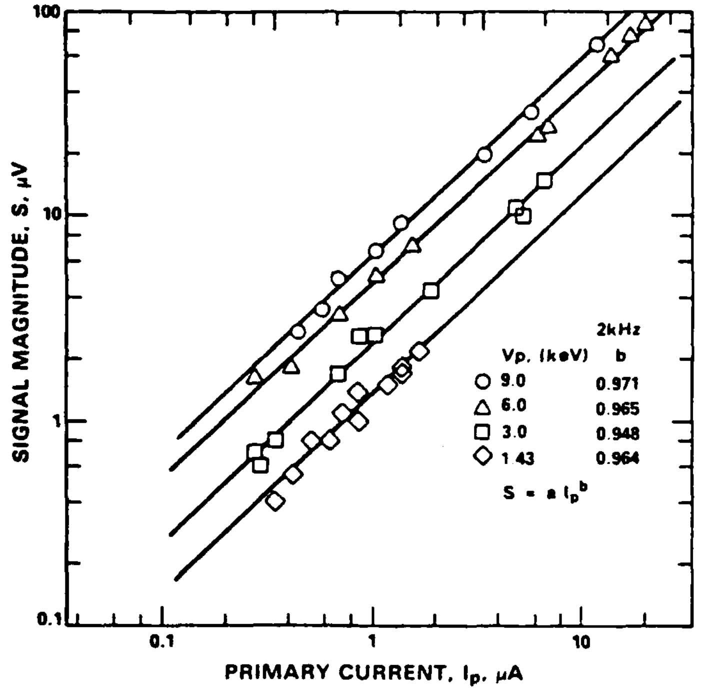

FIGURE 3 Signal magnitude dependence on primary beam current at various primary voltages: 2 kHz; Ar^+ on Aℓ.

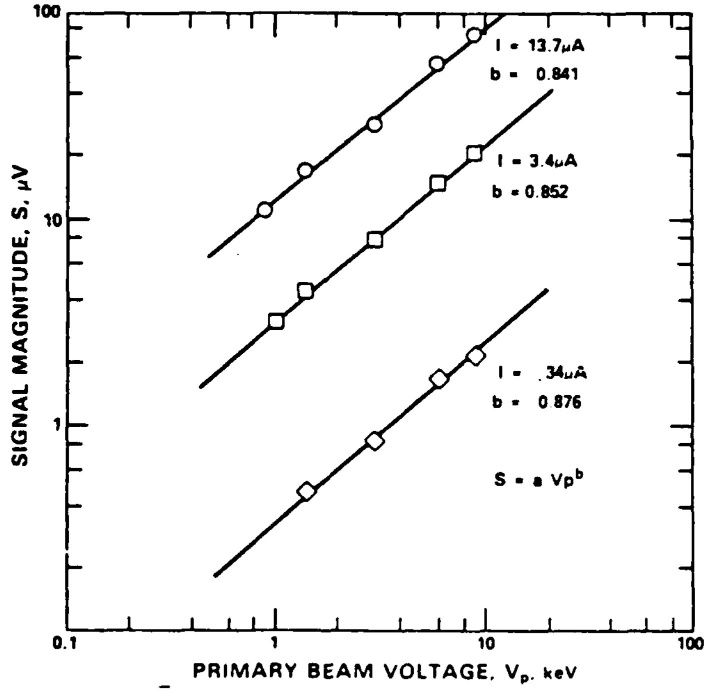

FIGURE 4 Signal magnitude dependence on primary beam voltage at various primary currents: 2 kHz; Ar^+ on Aℓ.

interactions and sputtering processes are known to occur under our experimental conditions however. The data does suggest that a nonthermal mechanism contributes to the acoustic signal generation process. If the observations are viewed from an energy perspective, they suggest a weakly non-linear dependence on the specific energy of each incident ion with the non-linearity decreasing with increasing ion energy. While this suggestion is possible, it seems unlikely since most processes become increasingly non-linear as the level of excitation increases. An alternative explanation recognizes that the Ar ions possess momentum as well as energy ($P_{ar}/P_e \sim 4x10^4$ for beams of equal energy where P_{ar} is the momentum of an argon ion and P_e the momentum of an electron.) If acoustic generation via momentum transfer coexists with thermoelastic acoustic generation, then the slope of the dependence of acoustic signal on primary beam voltage should be less than 1 as observed. In the limiting case where only momentum transfer is present, the slope should be 0.5.

The data shows that the thermoelastic mechanism is the major source of signal (i.e., the slopes are closer to 1.0 than to 0.5). This result is confirmed by imaging studies described in the next section. It is however inconsistent with the generally accepted theories of sputtering[8] where momentum transfer is approximately an order of magnitude more efficient than local thermal heating in producing sputtering. Further work is in progress in an effort to elucidate these dependences.

IMAGING USING ION BEAMS

These studies were conducted using aluminum disk samples 1.4 cm in diameter and 3 mm thick containing 1 mm holes drilled subsurface at various depths and locations. Figure 5 shows the sample/detector mount used in this work. The sample is mounted

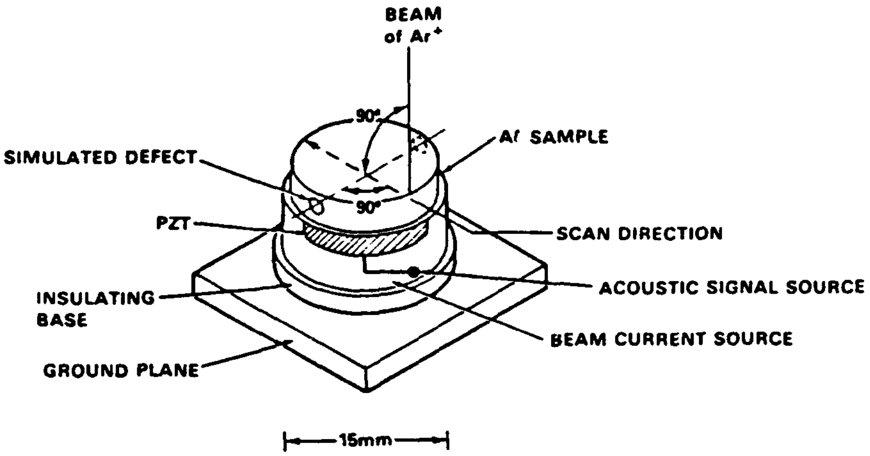

FIGURE 5 Schematic of sample and detection assembly showing simulated defect and method for simultaneous measurement of beam current.

on a PZT detector with provision for measurement of specimen current.

Figure 6 shows a series of line scans taken at varied frequencies on a specimen with two intersecting 1 mm holes buried at a depth D = 0.5 mm below the surface. Cross sectional views of the sample are shown in the inset to the figure. At low frequencies, where the ratio $\delta/D > 1$ with δ the one dimensional thermal diffusion length, the acoustic signal increases above each hole. When $\delta/D < 1$, the signal decreases above each hole. The contribution of each hole is resolved in the figure despite that for 15 Hz $\delta = 1.45$ mm approximately equal to the lateral spacing of the buried holes. This reflects the fact that the resolution is determined by the ion beam diameter not δ in this case.

Figure 7 is a set of scans taken at fixed modulation frequency on a slant hole specimen with a 1 mm hole drilled at an angle to the specimen surface. At fixed modulation frequency the epicentral depth of the hole below the beam may be varied by changing the location of the scan. When the depth D is small, the signal increases above the hole. For larger D a

ION-ACOUSTIC IMAGING OF SURFACE FLAWS IN ALUMINUM

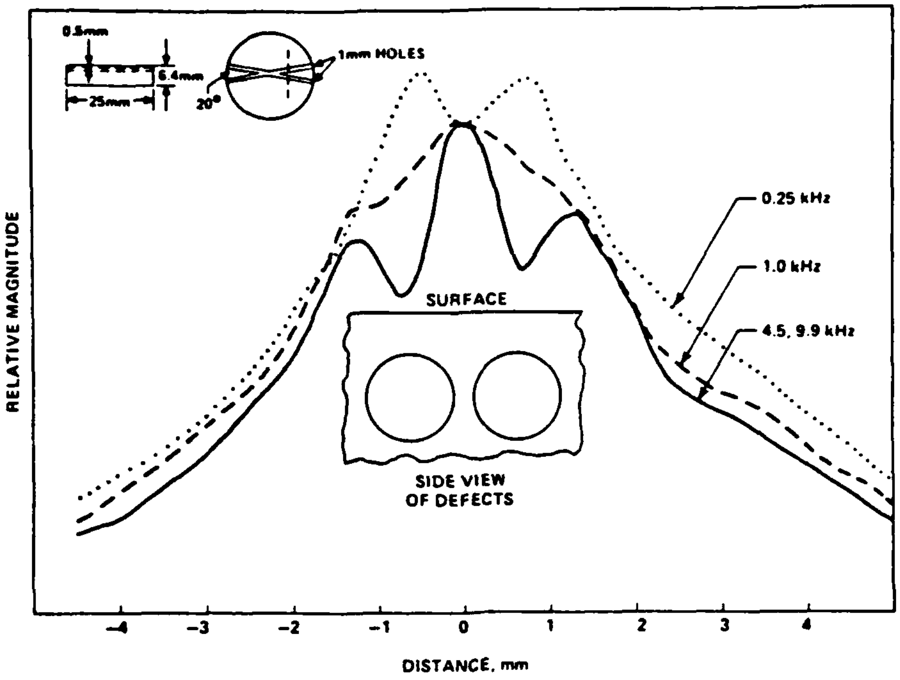

FIGURE 6 Acoustic signals observed for specimen with two intersecting 1 mm holes at D = 0.5 mm depth. At low frequency ($D/\delta < 1$) the signal increases above the hole. At high frequency ($D/\delta > 1$) the signal decreases.

signal decrease above the hole center is seen. Alternatively, the modulation frequency may be varied at fixed scan position. Figure 8 shows the variation with frequency observed for the slant hole specimen for the D = 0.30 mm scan of Figure 7. Comparison of the line scans in Figs. 7, 8 shows an approximate $\omega^{-0.5}$ dependence for the transition between the two signal regimes. This result is consistent with diffusive thermal wave interaction with the buried hole in the $\delta/D > 1$ regime on the scale of the thermal diffusion length $\delta = [2\alpha/\omega]^{1/2}$ where α is the thermal diffusivity and ω the angular frequency. Conversely, the regime $\delta/D < 1$ cannot involve a direct contribution of thermal wave-defect interaction to the contrast process.

FG SATKIEWICZ, JC MURPHY, LC AAMODT, JW MACHLACHLAN

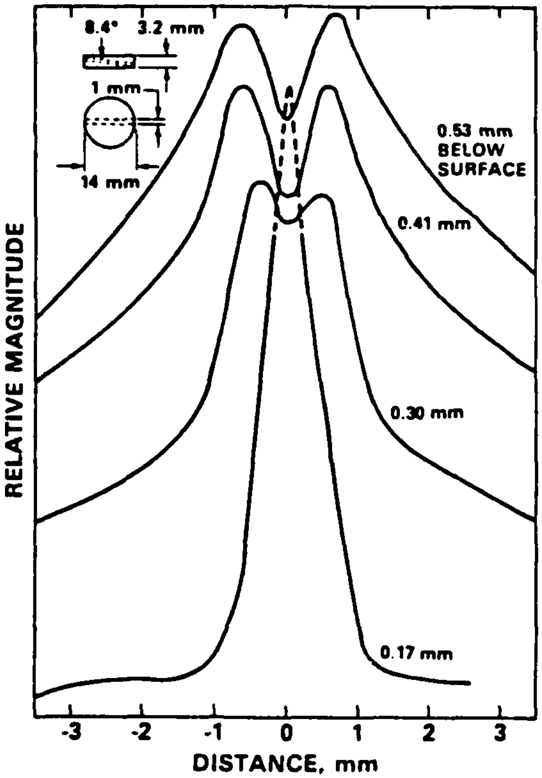

4.1 kHz; 6 keV Ar$^+$ ON Al

FIGURE 7 Slant hole specimen scans showing profiles at constant f and varying depth. Note that the spatial response of the detector has not been removed.

Figure 9 shows an SEAM image and SEAM and laser acoustic line scans of the same slant hole specimen taken at 78 kHz. The higher modulation frequency and the beam steering electronics built into the SEAM permit high quality images to be obtained readily. Both the image and the line scans show two contrast regions. Note that the hole is close to the sample surface near the top of the figure and farther from it near the bottom. In the image and in the line scans the hole is still visible for $D/\delta > 22$. This clearly shows that the contrast cannot be thermal. Some of the substructure seen in both laser and electron line scans is due to surface damage by the ion

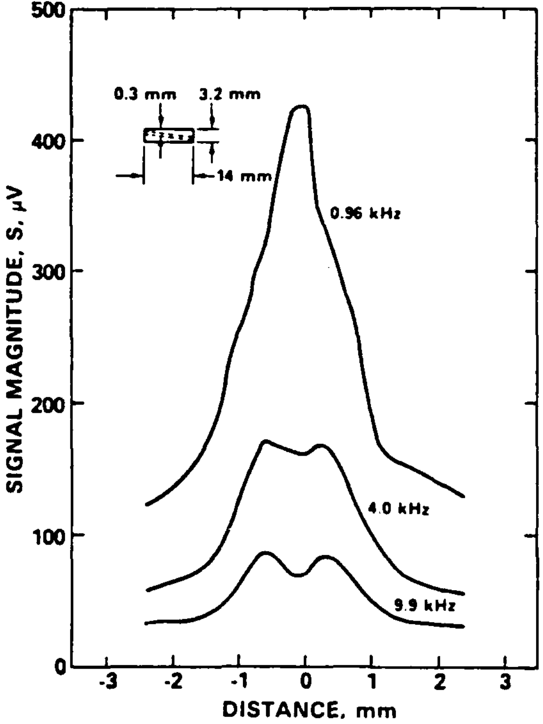

FIGURE 8 Slant hole specimen image obtained using SEAM and laser excitation. In SEAM image with the thermal region is visable at top corresponding to line scan. "Elastic" region appears in image also with corresponding line scan data. Flaw depth increases toward bottom of image.

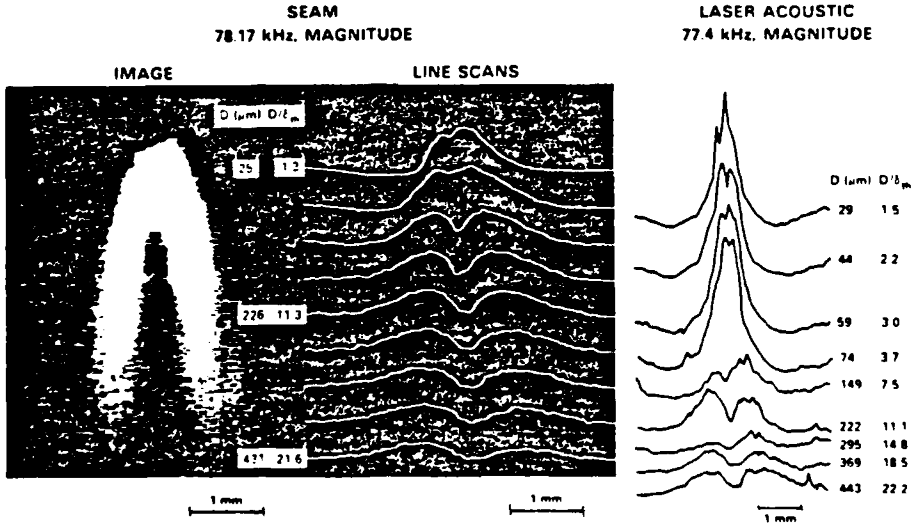

FIGURE 9 Buried slant hole in Al.

beam. In the nonthermal regime, the laser and electron line scan profiles closely resemble those obtained using the ions. In addition the image shows a relatively small angular spread of the signal with depth. This small spread applies equally to the overall defect signal and the dip over the hole center within the limits set by the experiment. Thermal stress generated near surface by the modulated beams coupled elastically to the defect is suggested to be the origin of the contrast in this regime. This finding has direct impact on SEAM imaging. SEAM images of specimen microstructure must consider both direct thermal and elastic contrast processes.

In order to further examine the issue of thermal contrast, comparative laser acoustic and OBD experiments were performed. Figure 10 compares the thermal regime in the laser acoustic scans with OBD scans. The laser acoustic scans show the hole at roughly twice the depth as do the OBD scans. This result is consistent with OBD detection being a surface temperature measurement requiring two way thermal transport to sense a buried defect. Laser acoustic detection requires only one way thermal transport coupled with acoustic generation near the defect to sense the defect's presence. While not shown in Figure 9, the laser acoustic scans show the elastic contrast regime at greater depths.

CONCLUSIONS

This work introduces the use of ion beams as sources for "thermal wave" imaging. The range of beam-specimen interactions available using ions makes them potentially significant for many analytical applications. In this work we show that some evidence for non-thermal interaction mechanisms exist even for the case of rare gas ions where no surface reaction is expected. Momentum transfer is considered as a possible non-

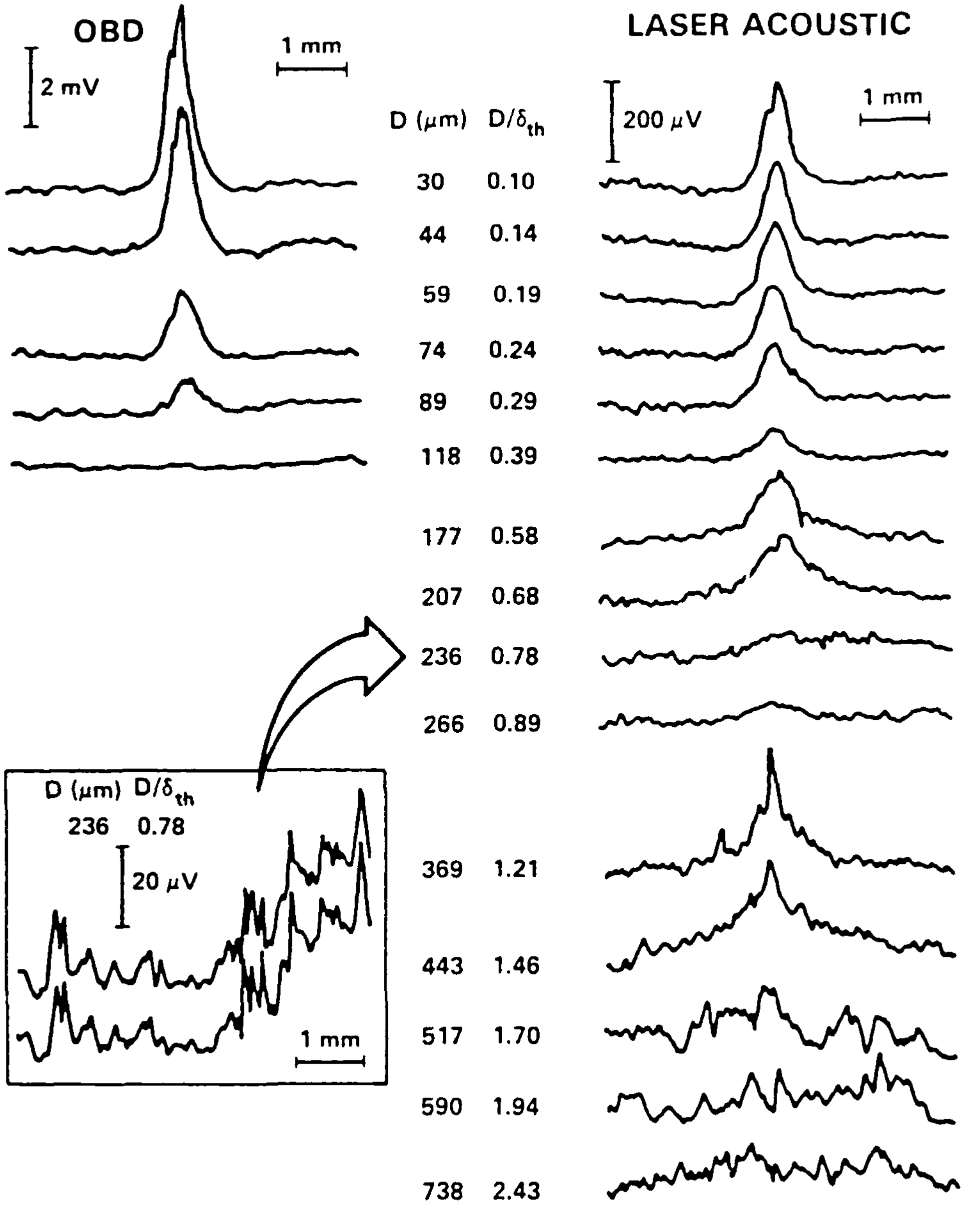

FIGURE 10 Buried slant hole in Al, 330 Hz, magnitude.

thermal source. It is noted that momentum transfer generation should be a source of elastic waves since momentum transfer plays the dominant role in sputtering using rare gas ions in this energy range. However, the momentum contribution to elastic wave generation inferred from these ion acoustic experiments seems far too small to be consistent with the theory of sputtering.

Ion beams have also been used to image buried subsurface defects in aluminum. Two mechanisms are identified which contribute to the contrast observed. One of these is shown to have a thermal origin, the other to have an elastic origin. Both contrast mechanisms exist in SEAM and laser acoustic imaging as well. These results demonstrate that the microstructural contrast observed in SEAM cannot have a purely thermal origin. It is now clear that both thermal and elastic contrast can exist and must be considered.

REFERENCES

* Work supported in part by U.S. Army Research Office and U.S. Naval Sea Systems Command under contract No. N00024-85-C-5301.

1. D. Fournier and A. C. Boccara in Scanned Image Microscopy, E. A. Ash ed. (1980).
2. J. C. Murphy and L. C. Aamodt, Appl. Phys. Lett. 38, 196 (1981).
3. Y. L. Wong, R. L. Thomas, G. F. Hawkins, Appl. Phys. Lett. 32, 538 (1978).
4. G. Busse, A. Rosencwaig, Appl. Phys. Lett. 36, 815 (1980).
5. G. S. Cargill, Physics Today, October 1981.
6. A. Rosencwaig, Science, 223, (1982).
7. J. C. Murphy, F. G. Satkiewicz, and L. C. Aamodt, Bull. Am. Phys. Soc. 30, 474 (1985).
8. P. Sigmund in Sputtering by Particle Bombardment I, R. Behrisch, ed. (1981), Springer.

AD-A175 487 PHOTOTHERMAL IMAGING OF DEFECTS IN METALS AND CERAMICS 2/3
(U) JOHNS HOPKINS UNIV LAUREL MD APPLIED PHYSICS LAB
J C MURPHY ET AL OCT 86 JHU/APL/RC-TPS-012
UNCLASSIFIED ARO-210661 11-MS N00024-85-C-5301 F/G 11/6 NL

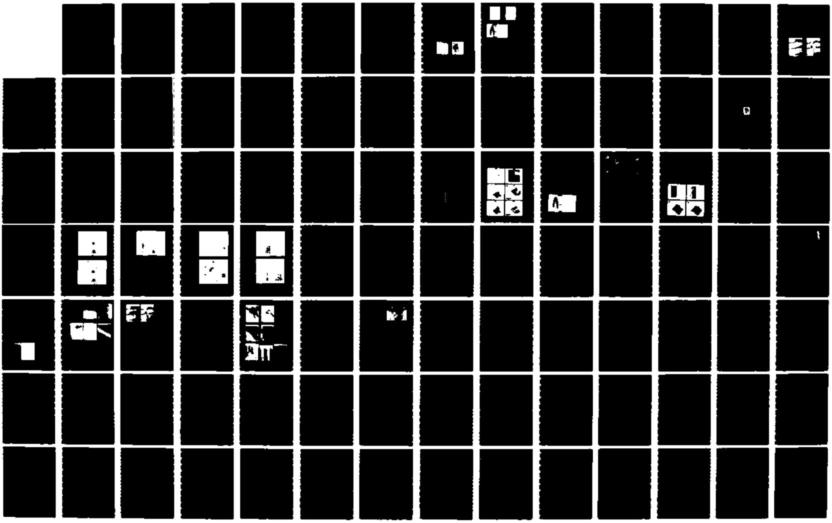

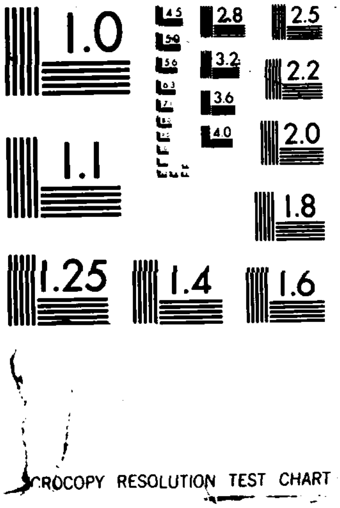
1.0
4.5
5.0
5.6
2.8
2.5
3.2
2.2
3.6
4.0
2.0
1.1
1.8
1.25
1.4
1.6
CROCOPY RESOLUTION TEST CHART

APPENDIX

PHOTOTHERMAL IMAGING OF DEFECTS IN METALS AND CERAMICS

6. J. C. Murphy, J. W. Maclachlan, R. B. Givens, F. G. Satkiewicz, and L. C. Aamodt, "The Generation of Ultrasound by Laser, Electron and Ion Probes and Its Application to the Characterization of Materials," Ultrasonics International '85 -- Conference Proceedings, London: Butterworth Scientific, 1985.

THE GENERATION OF ULTRASOUND BY LASER, ELECTRON AND ION PROBES AND ITS APPLICATION TO THE CHARACTERIZATION OF MATERIALS

J.C. Murphy, J.W. Maclachlan, R.B. Givens, F.G. Satkiewicz, and L. C. Aamodt

Applied Physics Laboratory, The Johns Hopkins University, Laurel, MD, U.S.A.

Illumination of a specimen by temporally or positionally modulated laser and particle beams is known to induce a number of specimen responses including generation of elastic waves. In this paper we consider elastic wave generation by laser, electron, and argon ion beams. These waves are used to image the surface and near subsurface features of several classes of material. Thermal and elastic wave contrast mechanisms are shown to contribute to the image formation process.

INTRODUCTION

Imaging methods based on specimen excitation by scanned laser[1,2,3,4] and electron[5,6,7] beams are by now well established as nondestructive methods of characterizing materials properties and locating surface and near subsurface flaws in opaque solids. Several classes of methods have been identified each distinguished by the method of detection or the means of generation. Because many of these classes involve local heating of the specimen at some stage in the image formation process, these methods have become broadly (and loosely) titled thermal wave imaging. In this paper we discuss imaging methods based on generation of elastic waves and the related contrast mechanisms and beam-specimen interactions. It should be noted that there is an important related body of work under the heading of laser generated ultrasound[8,9] wherein the time and spatial response characteristics of ultrasound generated by short pulse lasers is investigated. This is distinguished from the work described here where only cw excitation is used.

BACKGROUND

Figure 1 depicts some of the detection methods used for thermal wave imaging. The modulated laser or particle beam illuminates a specimen and induces a time-dependent change in the near surface temperature. Local thermoelastic distortion of the surface occurs as well as generation of propagating elastic waves in the specimen. These waves may be detected by a transducer attached to one of the sample surfaces or by optical interferometric techniques. The characteristics of the waves depend on boundary conditions present at the specimen surface.[10] Thermal diffusion in the specimen and in the medium above the specimen also occurs and leads to time dependent temperature fields. These fields influence the elastic wave generation process in the specimen and also lead to the formation of a thermal lens above the specimen as shown in the figure. A thermal imaging method termed optical beam deflection (OBD) imaging exploits the properties of this lens.[3,4] Finally, time dependent, enhanced IR radiation from the heated sample also occurs and may be used for imaging.[11] In this paper we shall emphasize images obtained using the attached transducer method but shall include a comparison with the OBD method to illustrate the significant differences in the image formation process which exist for the two methods.

Thermoelastic (TE) generation of elastic waves in an isotropic solid is determined by two coupled sets of equations together with appropriate boundary conditions.

$$\nabla^2 u - \frac{1}{v_\ell^2}\frac{\partial^2 u}{\partial t^2} = \frac{3K\beta}{3K+4\mu}\nabla T \tag{1}$$

$$\nabla^2 T - \frac{1}{\alpha}\frac{\partial T}{\partial t} = -H(t) \tag{2}$$

where u is the particle displacement, T the temperature v_ℓ the longitudinal sound velocity, α the thermal diffusivity, K the bulk modulus, μ the shear modulus and β the thermal expansion coefficient.

The term on the right hand side of Equation 1 can ordinarily be neglected with the result that these equations may be treated by first solving the uncoupled thermal diffusion equation (Eq. 1) and then using the temperature field so determined as the source of elastic waves in the medium (Eq. 2). Both thermal and elastic boundary conditions must be applied at the illuminated surface of the sample. The specimen dimensions are assumed to be large. Note that, for OBD and IR imaging, changes in the surface temperature, $T_s(x,y)$ of one of the faces of the specimen constitute the basis of the thermal images. Changes in $T_s(x,y)$ caused by subsurface features require these features to be within approximately one thermal diffusion length of the surface. Conversely for transducer detection the temperature field, $T(x,y,z)$ inside the sample generates elastic waves via Eq. 2. Changes in $T(x,y,z)$ near the subsurface feature can contribute to the elastic wave amplitude and phase with the result that features deeper than two thermal diffusion lengths can be detected. This increased sampling depth for thermal interaction with subsurface thermal features of the sample will be illustrated later.

Non-thermoelastic wave generation mechanisms including wave generation by momentum transfer may exist for excitation with particle beams such as electrons or ions. Ion beams should exhibit larger momentum contribtions than electron beams since for Ar^+ the momentum ratio $P_{Ar+}/P_e = 270$. Momentum transfer from ion-beam-specimen interaction has been identified as the primary mechanism of sputtering.[12] The relative importance of momentum and thermal contributions to sputtering might then be assessed by measurement of the relative contribution of momentum and thermoelastic processes to elastic wave amplitude as a function of beam and specific ion energies. The thermal contribution should increase linearly with energy while the momentum contribution *should increase as the square* root of the energy. As discussed later in the experimental section, only a linear dependence is observed contrary to the sputtering theory expectations.

EXPERIMENTAL

Comparative SEM and SEAM images and data are presented in Fig. 2 for polycrystalline aluminum and reveal contrast at the grain boundaries and sometimes within grains. Similar images have been obtained for frequencies between 5 kHz and 1 MHz. Images of this type have also been presented in prior SEAM studies (cf reference 7). However, there has been some controversy regarding the origin of the contrast observed for microstructural features in the specimens. In particular, the relative importance of thermal, thermoelastic and elastic contrast mechanisms appears to remain an open question. In this work we examine several of these contrast mechanisms experimentally and show that both thermal and elastic contrast mechanisms contribute to he images obtained. The relative importance of each mechanism may depend on the depth of the feature below the surface as well as on other material parameters. Note, however, that some of the contrast in these images is due to visual processing of image data by a human observer (Craik-O'Brien effect[13]). Hence, reliable image data requires complementary use of numerical or line scan presentation of the data.

In order to focus initially on the contrast observed at the grain boundaries, experiments were conducted on bicrystals of pure aluminum grown with vertical grain boundaries in the Materials Science Department at Johns Hopkins University. Figure 3 shows an SEM image of a section of one of these bicrystals on which is superposed several SEAM line scans. The specimen was polished and then slightly etched to show the location of the grain boundary in the SEM image. The positions of the line scans relative to the image are indicated by the markers. The width of the boundary seen by SEAM varies with modulation frequency as $\omega^{-0.5}$ but in general is greater than the visual boundary. In addition the SEAM boundary signal varies exponentially with distance from the visual boundary with argument proportional to the thermal diffusion length in aluminum. Both observations are consistent with a thermal diffusion contrast model.

Comparative SEM/SEAM studies have been made on a fabricated sample of aluminum in which a 1 mm diameter hole has been drilled at an approximate angle of 8 degrees relative to the specimen surface. The primary objective for use of the fabricated specimens is to elucidate the contrast mechanisms responsible for the microstructural information present in thermal acoustic images. As discussed later, this sample also was used for ion-acoustic imaging studies and for laser optical beam deflection imaging in order to further investigate image contrast and acoustic generation mechanisms.

Figures 4a, b show the SEAM image and spatially coordinated SEAM line scans. Hole depth increases linearly toward the bottom of the image. Two image regions are seen. In Region I, at shallow depths ($D < 2.5\ \delta_{th}$), the acoustic signal increases above the hole and decreases with hole depth, D at a rate determined by the modulation frequency. In addition the boundary between Regions I and II also shifts to shallower depths with increasing frequency. These findings suggest that in Region I the modulated temperature field in the specimen interacts with the hole. Image Region II exists when the hole depth is substantially greater than a thermal diffusion length. Experimental data has been obtained to $D/\delta_{th} > 25$. In this region the signal decreases above the hole while symmetrical regions around the hole center show a signal increase. This pattern is relatively frequency independent over a range 100 Hz < f < 500 kHz. The width of the interaction region increases with depth. This feature suggests that the electron beam generates a conical radiation pattern in the specimen with an angular width of approximately 50 degrees. The image contrast observed for this region cannot be thermal. Instead, contrast caused by elastic wave interaction with the hole is assumed, with the resolution determined by the angular spread in the radiation pattern rather than by the acoustic wavelength. The waves are assumed to be thermally generated. Note that the dominance of thermal contrast near the surface does not imply elastic contrast is absent.

Figure 4c illustrates a parallel laser acoustic measurement at the same frequency and with the same sample-bond-transducer configuration used in Fig. 4a, b. Comparison of these figures demonstrates the close agreement with the SEAM data. This shows that in these experiments the image contrast mechanisms are not dependent on the specific excitation source and supports the notion that temperature is the primary mechanism for elastic wave generation.

A comparison of OBD and laser acoustic line scans were made on the same slant hole sample under identical conditions. The results appear in Figure 5 for the signal magnitudes. This data indicates that the volume sensed thermally by the acoustic method is at least twice as deep as that probed by the OBD method. This result might be anticipated by recalling that the temperature field may be modified locally near a defect (the laser acoustic case) without causing a perceptible local change in the surface temperature (the OBD case). Note that the laser acoustic data shown in Figure 5 was not corrected for spatial changes in detector responsivity.

Image scans on this slant hole specimen were also obtained using a modulated beam of Ar^+ ions as the excitation source. Figure 6 shows a portion of these results. Again, two image contrast regions are observed. Data taken at varying depths and constant frequency as well as varying frequencies and constant depth show that the boundary between the two regions varies as $\omega^{-.5}$. This result is consistent with both a thermal diffusion controlled contrast mechanism in Region I and an elastic contrast mechanism in Region II.

To further examine the ion-acoustic generation mechanisms and image contrast mechanisms involving ion-beam-solid interactions, we measured the elastic wave amplitude as a function of incident ion beam energy. Both energy and momentum in the beam increase at a linear rate. Figure 6 shows the variation of the acoustic signal as a function of beam voltage at constant beam current. In this case energy increased linearly but momentum increases as $E^{1/2}$. The figure suggests that momentum transfer is not a primary source of the acoustic signal at the sensitivity of these experiments.

SUMMARY AND CONCLUSIONS

Laser, electron and ion beams show some similar features when used as sound generation sources for imaging applications. Thermal contrast mechanisms are seen in the near surface region defined by the thermal diffusion length. However, this normalized depth is at least a factor of two larger than that observed in front surface temperature thermal imaging methods such as OBD. In addition elastic wave contrast processes are seen. These waves are thermoelastically generated but their interaction with the subsurface region is non-thermal. The radiation pattern produced by the modulated beams is relatively confined and observation of buried features at depths very large compared with a thermal diffusion length is possible. These results confirm the speculation that image contrast in SEAM and related techniques involve both thermal and elastic contrast processes. Nonetheless, the thermal contrast processes are important. SEAM grain boundary contrast in aluminum bicrystals has a boundary width determined by the thermal diffusion length for modulation frequencies up to 500 kHz. Finally, ion-acoustic imaging has been applied to studying the mechanisms of elastic wave generation including momentum transfer. No momentum contribution was identified in experiments with Ar^+ ions to this time. The result was unexpected in light of the role momentum transfer plays in the theory of sputtering of heavy rare gas ions. This issue and the relationship of sputtering processes and acoustic imaging are under study at this time.

REFERENCES

1. L.D. Favro, P.K. Kuo, J.J. Pouch, and R.L. Thomas, "Photoacoustic Microscopy of an Integrated Circuit," Appl. Phys. Lett. 36(12), 953-954 (1980).
2. G. Busse and A. Ograbeck, "Optoacoustic Images," J. Appl. Phys. 51(7), 3576-3578 (1980).
3. D. Fournier and A.C. Boccara, "The Mirage Effect in Photothermal Imaging," Scanned Image Microscopy, ed. E.A. Ash, Academic Press, London, 347-351 (1980).
4. J.C. Murphy and L.C. Aamodt, "Reflective Photothermal Imaging," Journal de Physique C6, 10, 44, Oct. 1983.
5. C.S. Cargill, III, "Electron-Acoustic Microscopy," Scanned Image Microscopy, ed. E.A. Ash, Academic Press, London, 319-330 (1980).
6. A. Rosencwaig, "Depth Profiling of Integrated Circuits with Thermal Wave Electron Microscopy," Elec. Lett. 16, 928-930 (1980).
7. L.J. Balk, D.G. Davies, and N. Kultscher, "The Dependence of Scanning Electron Acoustic Microscopy (SEAM) Imaging on Chopping and Detection Frequency for Metal Samples," Phys. Stat. Sol. (a) 82, 23-33 (1984).
8. R.J. Dewhurst, D.A. Hutchins, S.B. Palmer, and C.B. Scruby, "Quantitative Measurements of Laser Generated Acoustic Waveforms," J. Appl. Phys. 53(6), 4064-4071 (1982).
9. C.K. Jen, P. Cielo, F. Nadeau, J. Bussiere, G. W. Farnell, "Laser Generation of Annular Converging Surface WAves," IEEE 1984 Ultrasonics Symposium, 660-665.
10. R.J. von Gutfeld and R.L. Melcher, "20 MHz Acoustic Waves from Pulsed Thermoelastic Expansions of Constrained Surfaces," Appl. Phys. Lett. 20(6), 257-259 (1977).
11. P.-E. Nordal and S.O. Kanstad, "Photothermal Radiometry for Spatial Mapping of Spectral and Material Properties," Scanned Image Microscopy, ed. E.A. Ash, Academic Press, London, 331-339 (1980).
12. P. Sigmund, "Sputtering by Ion Bombardment: Theoretical Concepts" in Topics in Applied Physics, Vol. 47, p. 9, ed. R. Behrisch, Springer Verlag (1981).

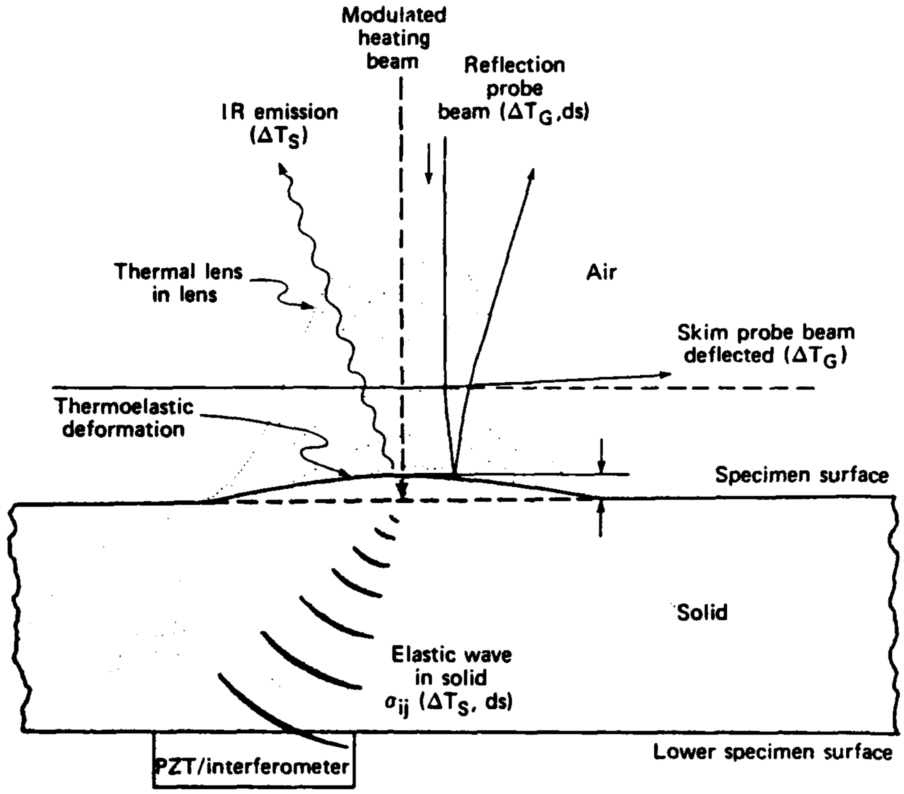

Fig. 1 **Detection methods used for thermal wave imaging.**

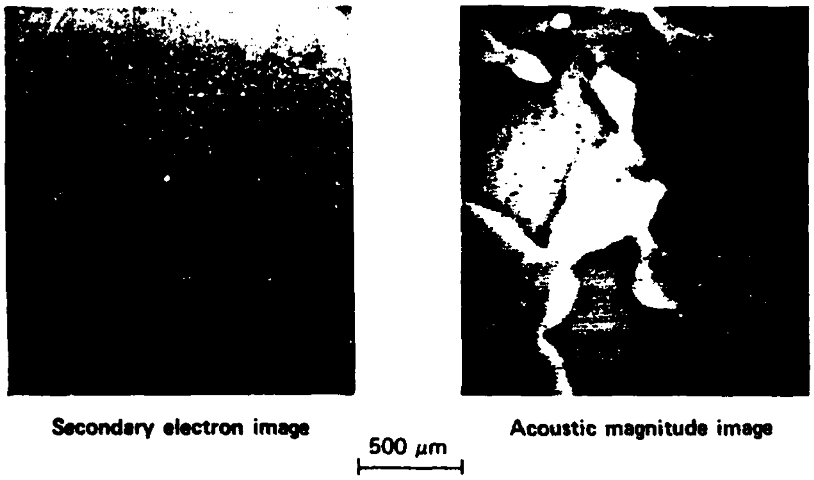
Secondary electron image

Acoustic magnitude image

Fig. 2 **SEM and SEAM images of polycrystalline aluminum at 14.287 kHz.**

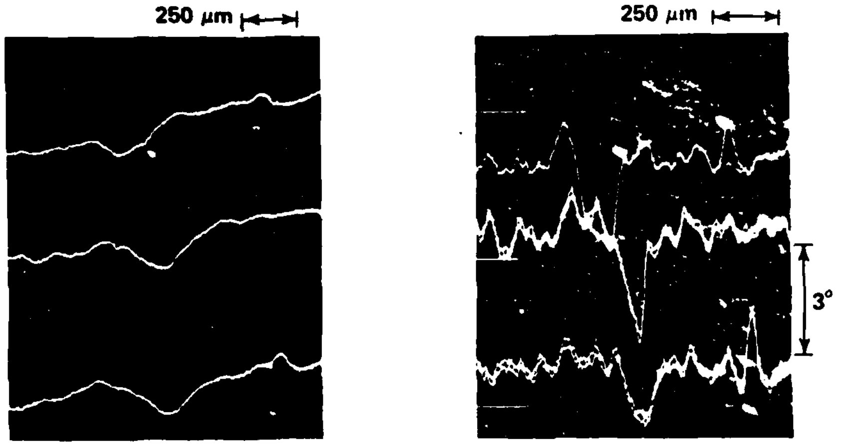

Magnitude Phase

Fig. 3 SEAM magnitude and phase line scans at 43.0 kHz superimposed on SEM image for grain boundary in high purity aluminum.

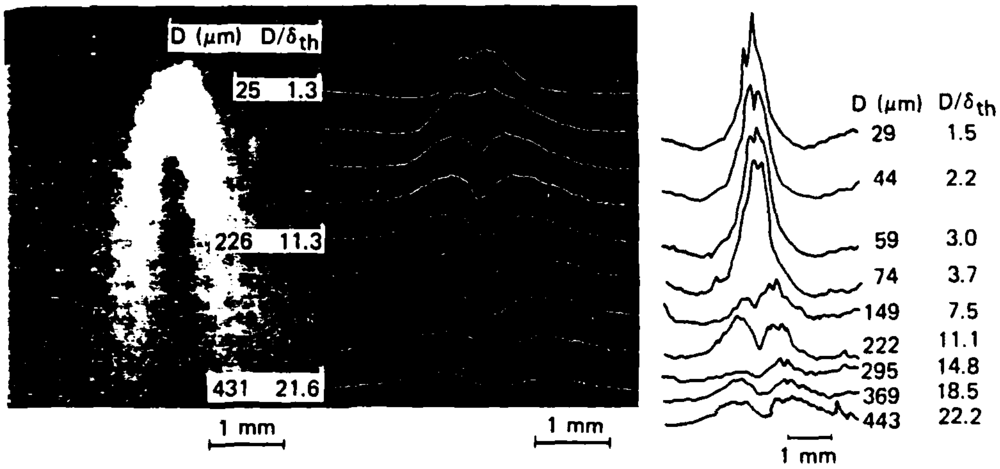

(a) Image (b) Line scans (c) Laser acoustic

Fig. 4 Buried slant hole in aluminum. (a) SEAM magnitude image, 78.17 kHz; (b) SEAM magnitude line scans, 78.17 kHz; (c) laser acoustic magnitude line scans, 77.4 kHz.

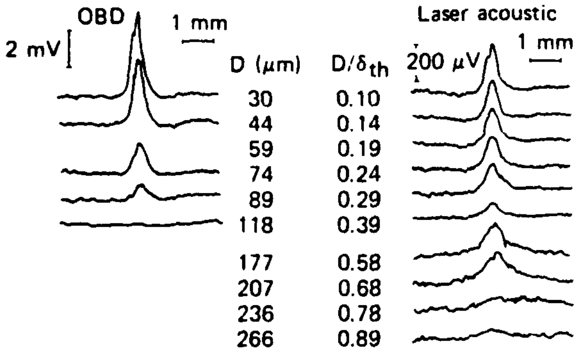

Fig. 5 Comparison of OBD and laser acoustic line scans of buried slant hole in Al, 330 Hz.

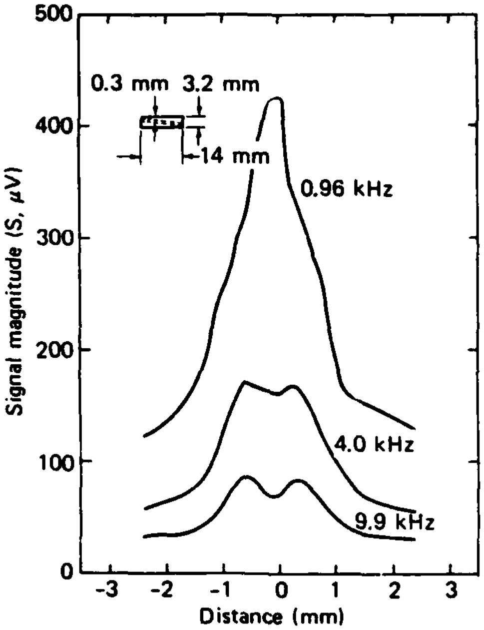

Fig. 6 Ion acoustic line scans of buried slant hole in Al at same position for three frequencies (0.96 kHz, 4.0 kHz, 9.9 kHz).

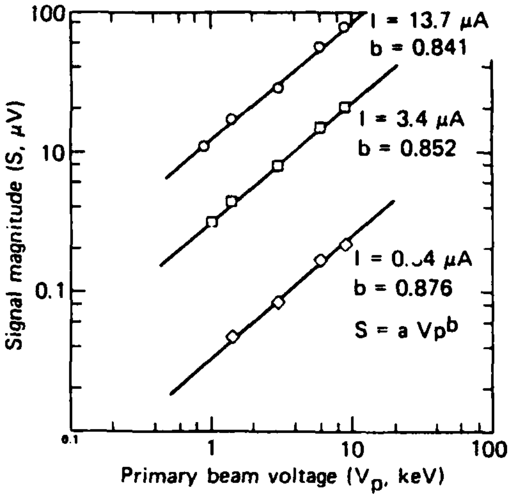

Fig. 7 Dependence of ion acoustic signal on primary beam voltage at three primary beam currents.

APPENDIX

PHOTOTHERMAL IMAGING OF DEFECTS IN METALS AND CERAMICS

7. J. W. Maclachlan, R. B. Givens, J. C. Murphy, and L. C. Aamodt, "Contrast Mechanisms in Scanning Electron Acoustic Imaging of Grain Boundaries," 4th International Topical Meeting on Photoacoustic, Thermal, and Related Sciences, Ville d'Esterel, Quebec, Aug. 4-8, 1985.

Contrast Mechanisms in Scanning Electron Acoustic Imaging of Grain Boundaries*

J. W. Maclachlan
Dept. of Materials Science & Engineering
The Johns Hopkins University
Baltimore, MD 21218

R. B. Givens, J. C. Murphy, and L. C. Aamodt
Applied Physics Laboratory
The Johns Hopkins University
Laurel, MD 20707

Scanning Electron Acoustic Microscopy (SEAM) produces dramatic images of the microstructure of metals and other materials which are not readily obtained by other means. Although the origins of the contrast in these images has been widely discussed, the contrast mechanisms are not yet fully understood[1,2,3]. Since there are a number of possible contributions to contrast (local variations in electron-specimen interaction, thermal properties, thermoelastic generation and elastic wave propagation), the relative importance of different contrast mechanisms must be determined if SEAM is to become a quantitative tool for the investigation of microstructure. The present work examines contrast at grain boundaries in high purity aluminum using both SEAM images and individual line scans of the magnitude and phase signals across the boundary. The line scans allow the functional dependence of the signal magnitude and phase to be measured in the grain boundary region. This functional dependence is examined for a series of frequencies and for different positions along the grain boundary.

An ETEC Autoscan scanning electron microscope was modified to allow blanking of the electron beam over a frequency range of 1 kHz to 500 kHz. The sample was mounted on a localized piezoelectric detector (NBS Conical Transducer) and the output of the detector was amplified and sent to a lock-in amplifier for analysis of the magnitude and phase components of the signal. The magnitude and phase signals were then used to construct either full screen images with the acoustic signal modulating the z-axis of the CRT or individual line scans showing magnitude or phase as a function of position. The primary electron energy was 20 keV and the beam current was 1×10^{-7} A for all of the measurements reported here. The samples used were high purity aluminum bicrystals which had been grown by a solidification and seeding technique[4]. The samples were mechanically polished and then chemically etched, producing a 1.5 micron wide channel along the length of the grain boundary. This channel allowed the position of the boundary to be precisely located in the secondary electron image.

The grain boundary was easily detected in the SEAM images. Fig. 1 shows a secondary electron image of the grain boundary with magnitude and phase line scans at three indicated positions along the boundary for a modulation frequency of 24.4 kHz. This measurement was repeated at a series of frequencies and summaries of the magnitude and phase line scans for the central position in Fig. 1 are shown in Figs. 2 (a) and (b). To investigate the frequency dependence of the apparent width of the boundary, the half width, half maximum of the phase signal was measured to the right and to the left of the grain boundary. These results are plotted in Fig. 3 as a function of $\omega^{-1/2}$ along with the thermal diffusion length in aluminum.

It is apparent from Fig. 1 that the contrast observed due to the grain structure of the aluminum arises from the presence of the grain boundary itself and that no real contrast is detected between the interiors of the two grains. Contrast between grain interiors, in addition to contrast at the boundary, has been observed in large grained pure aluminum samples prepared by a strain-anneal recrystallization technique. The origins of the grain interior contrast are currently under investigation. The data in Fig. 3 suggest a strong thermal component to the contrast since the half width, half maximum of the phase signal across the boundary shows a $\omega^{-1/2}$ dependence, particularly for the right hand side of the boundary (the erratic results for the left hand side of the boundary will be discussed below). Since the thermal conductivity and thermal expansion coefficient are isotropic in a cubic material such as aluminum, the contrast cannot arise simply from the misorientation of the lattice across the grain boundary. The contrast observed suggests the presence of a thermal boundary, possibly due to preferential segregation of impurity elements and oxides at the grain boundary or due to the dislocation structure of the boundary.

The magnitude and phase signal profiles vary with position along the grain boundary. This may well be due to variations in the actual structure or impurity concentration along the grain boundary. The presence of an additional defect to the left of the grain boundary is suggested by the data of Fig. 1. In the top trace, the phase line scan shows a broad minimum whose right corner corresponds exactly to the position of the grain boundary. Further evidence of additional structure to the left of the boundary is found in the variation of the frequency dependence of the HWHM of the phase line scan on the left and right sides of the boundary (see Fig. 3). The left side of the boundary does not exhibit the same $\omega^{-1/2}$ dependence found on the right side of the grain boundary.

As described above, there appears to be a strong thermal contribution to the contrast observed at grain boundaries in aluminum. In order to investigate the effect of the anisotropy in elastic moduli expected across the boundary, preliminary "pitch-catch" experiments have been performed with the electron beam on the same side and on the opposite side of the grain boundary from the localized detector. While the presence of elastic contrast mechanisms is not yet confirmed, there is a strong acoustic contribution to contrast due to the acoustic resonances excited in the sample[5]. These resonant modes are a function of the specimen geometry and do not give information on spatial variation in the elastic properties of the samples. The acoustic contribution to contrast must be noted, however, since it can lead to dramatic contrast reversals across acoustic nodal lines in the sample.

The presence of a thermal contribution to contrast at grain boundaries in aluminum has been demonstrated. Since the thermal properties are isotropic in aluminum and since there is considerable variation in the signal profile at different locations along the boundary, it is believed that the thermal wave images are sensitive to grain boundary related phenomena such as the presence of dislocations, impurity atoms and vacancies. While an acoustic contribution to contrast is readily apparent, the importance of elastic contrast mechanisms has yet to be established.

* Supported in part by U.S. Naval Sea Systems Command under Contract No. N00024-85-C-5301.

1. D. G. Davies, "Scanning Electron Acoustic Microscopy," Scanning Electron Microscopy III, 1163-1176 (1983).
2. L. J. Balk, D. G. Davies and N. Kultscher, "The Dependence of Scanning Electron Acoustic Microscopy (SEAM) Imaging on Chopping and Detection Frequency for Metal Samples," Phys. Stat. Sol. (a) 82, 23-33 (1984).
3. G. A. D. Briggs, "Scanning Electron Acoustic Microscopy and Scanning Acoustic Microscopy III, 1041-1052 (1984).
4. R. B. Pond, private communication.
5. G. S. Cargill, "Electron-Acoustic Microscopy," in Scanned Image Microscopy, ed. E. A. Ash, Academic Press, London, 319-330 (1980).

ELECTRON-ACOUSTIC LINE SCANS OF GRAIN BOUNDARY
IN HIGH PURITY ALUMINUM
24.1 kHz

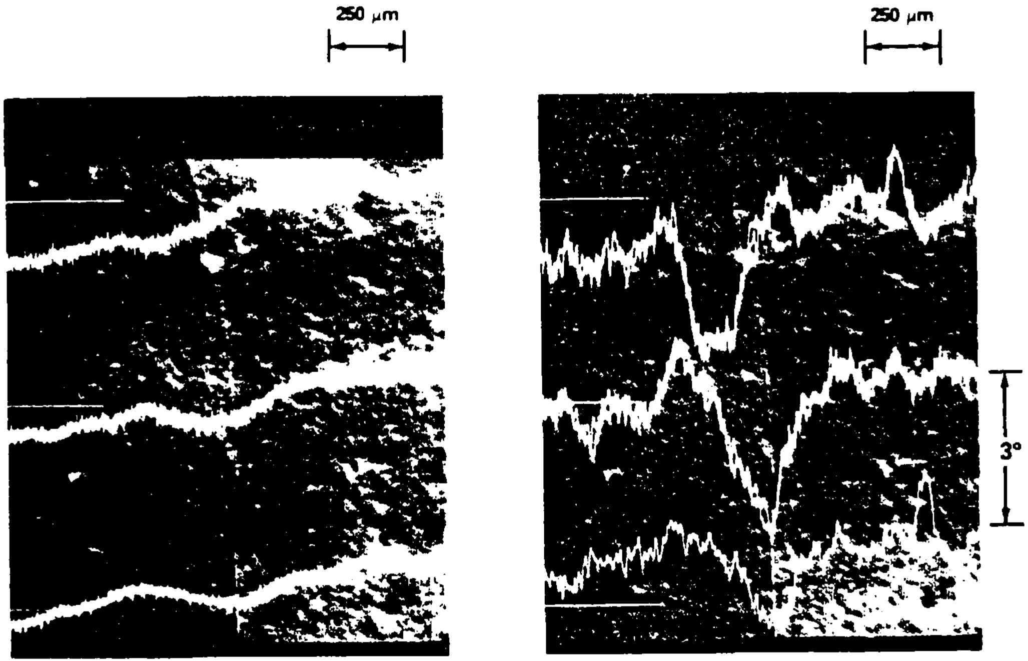

MAGNITUDE PHASE

Figure 1

APPENDIX

PHOTOTHERMAL IMAGING OF DEFECTS IN METALS AND CERAMICS

8. Grover C. Wetsel, Jr, "Photothermal Generation of Thermoelastic Waves in a Composite Media", IEEE Transactions on Ultrasonics, Ferroelectrics, and Frequency Control, Vol. 33, No. 5, pp. 450-461, 1986.

450 IEEE TRANSACTIONS ON ULTRASONICS, FERROELECTRICS, AND FREQUENCY CONTROL, VOL. UFFC-33, NO. 5, SEPTEMBER 1986

Photothermal Generation of Thermoelastic Waves in Composite Media

GROVER C. WETSEL, Jr.

Abstract—**The essential physics of photothermal generation of thermoelastic waves is reviewed, principally with the use of one-dimensional models of composite media. The emphasis is placed on understanding the effects of material and dynamical parameters on the thermoelastic generation process. Thermoelastic coupling, the propagating mode, and the nonpropagating mode are described. Theoretical temperature and elastic displacement distributions in composite structures are presented. Variations of ultrasonic amplitude and intensity with structure dimensions, optical attenuation, frequency, and material parameters are discussed and compared with reported experimental data. Bulk heating models, surface heating models, thermoelastic-backing models, and idealized-backing models are compared. It is shown that the material-parameter group most important in photothermal elastic-wave generation is $\alpha(D)^{1/2}$, where α is effectively a thermal-expansion coefficient, and D is the thermal diffusivity. Transitions from linear to nonlinear photothermal thermoelastic effects are described.**

I. Introduction

THE ABSORPTION of light in condensed matter produces heat via nonradiative transitions. Because of thermoelastic coupling elastic disturbances are also produced. When the light source (usually a laser) is pulsed or harmonically modulated, nonpropagating thermal waves and propagating elastic waves are generated. Photothermal generation of thermoelastic waves (PGTEW) in condensed matter has become an important research subject with applications in materials characterization, imaging, and processing [1]-[7].

The usual configuration of PGTEW experiments is such that one can expect the excitation of longitudinal bulk, transverse bulk, and surface elastic waves as well as thermal waves. Modeling of these effects in three dimensions is a formidable problem, even for an infinite medium. Since in practice the generated waves carry information characteristic of adjacent media as well as the generating medium, three-dimensional modeling of composite media becomes even more untractable. Fortunately, the essential features of the generation process—the effects of material and dynamic parameters—can be understood using one-dimensional models.

In this paper the essential physics of photothermal generation of thermoelastic waves is discussed, principally with the use of one-dimensional models of composite media. The emphasis is placed on understanding the effects of material and dynamic parameters on the thermoelastic generation process. A historical review that highlights theoretical models incorporating these features is presented. *No attempt to include a comprehensive review of approximate models or models appropriate to specialized experimental configurations is made.* Predictions of theoretical models are compared with experimental results.

The first theoretical treatment of thermoelastic wave generation with a clear relation to PGTEW interests was given by White [8]. White's one-dimensional model consists of an infinitesimal surface heat source, a semi-infinite thermoelastic sample, and an idealized-backing medium. The backing medium has no thermoelastic material properties and hence no thermal nor elastic disturbance is excited in it. Solutions to the thermal-diffusion and elastic-wave equations were obtained in the time domain for a rectangular heating pulse and in the frequency domain for a harmonic heating source. The temperature and elastic displacement in the sample were determined subject to the thermal boundary condition that no heat is conducted into the backing, and for two cases of the elastic boundary condition at the heated surface: 1) stress-free surface and 2) clamped (perfectly rigid) surface. Gournay [9] treated the problem of bulk optical absorption in a semi-infinite liquid sample. Temporal solutions to the thermoelastic equations corresponding to a rectangular (laser) heating pulse were obtained for stress-free and clamped elastic boundary conditions with no heat transferred into the backing medium. The first theoretical treatment of photothermal elastic wave generation to take into account the effects of all the material parameters of backing, light-absorbing medium, and sample appeared in a series of papers by Wetsel [10]-[14]. One-dimensional models of both surface and bulk heating of multimaterial structures were considered in both the frequency and time domains. Calculations of temperature and elastic-displacement distributions were made for several material combinations of interest and a range of dynamical parameters. These results revealed that for efficient elastic wave generation the important material-parameter group for each medium is $\alpha(D)^{1/2}$, where α is effectively a thermal-expansion coefficient and D is the thermal diffusivity. A three-dimensional theory of the elastic waves generated by a point

---

Manuscript received February 28, 1986; revised March 27, 1986. This work was supported in part by the U.S. Army Research Office, Durham, NC, and the U.S. Naval Sea Systems Command under contract N00024-85-C-5301

The author is with The John Hopkins University, Applied Physics Laboratory Laurel, MD 20707, USA.

IEEE Log Number 8609257.

heat source in an elastic half-space has been given by Rose [15]. Partition of energy among longitudinal bulk, transverse bulk, and surface waves was discussed. Detailed results were presented for wavefront expansions, the elastic displacement on the surface and along the symmetry axis, the directivity pattern, and the epicentral displacement of a plate. McDonald [16] has recently determined the time variations of the surface displacement produced by a Gaussian laser pulse in an extension of Rose's model. The elastic displacement within and near the source region and on a time scale comparable to that of the laser pulse was computed.

II. THEORY

A. *The Thermal-Diffusion and Elastic-Wave Equations*

Generation of thermal and elastic waves due to the conversion of light into heat is described by the coupled thermal-diffusion and elastic-wave equations. For condensed matter, the thermal-diffusion equation may be written in the form [17]

$$\sum_{i,j} \kappa_{ij} \frac{\partial^2 T}{\partial x_i \partial x_j} - \rho C_v \frac{\partial T}{\partial t} + H = T \sum_{i,j} \lambda_{ij} \frac{\partial u_{ij}}{\partial t} \tag{1}$$

where T is the temperature, H is the heat-source density, κ_{ij} is the (ij)-th component of the thermal-conductivity tensor, C_v is the specific heat at constant volume, and λ_{ij} is the (ij)-th component of the temperature-stress tensor. The quantity u_{ij} is the (ij)-th component of the elastic-strain tensor

$$u_{ij} = \frac{1}{2}\left[\frac{\partial u_i}{\partial x_j} + \frac{\partial u_j}{\partial x_i}\right] \tag{2}$$

where u_i is the ith component of the elastic-displacement vector. The (ij)-th component of the elastic-stress tensor is given by

$$\sigma_{ij} = \sum_{k,l} c_{ijkl} u_{kl} - \lambda_{ij}(T - T_e) \tag{3}$$

where c_{ijkl} is the $(ijkl)$-th component of the elastic-stiffness tensor and T_e is the equilibrium temperature. The temperature-stress tensor may be written in terms of the thermal-expansion coefficients α_{kl}:

$$\lambda_{ij} = \sum_{k,l} c_{ijkl} \alpha_{kl} \tag{4}$$

where $\alpha_{kl} = (\partial u_{kl}/\partial T)_\sigma$. The elastic-wave equation [17]

$$\rho \frac{\partial^2 u_i}{\partial t^2} = \sum_j \frac{\partial \sigma_{ij}}{\partial x_j} \tag{5}$$

where ρ is the density, may be written with the above relations in the form

$$\rho \frac{\partial^2 u_i}{\partial t^2} = \sum_{j,k,l} c_{ijkl} \frac{\partial u_{kl}}{\partial x_j} - \sum_j \lambda_{ij} \frac{\partial T}{\partial x_j}. \tag{6}$$

It can be seen by examination of (1) and (6) that heat H produces a temperature variation and hence an elastic disturbance by means of the terms connecting T and u_i.

For an isotropic solid, the thermal-diffusion and elastic-wave equations can be written, respectively, as [17]

$$\kappa \nabla^2 T - \rho C_v \frac{\partial T}{\partial t} + H = T\beta_t B \nabla \cdot \frac{\partial \boldsymbol{u}}{\partial t} \tag{7}$$

$$\rho \frac{\partial^2 \boldsymbol{u}}{\partial t^2} = \mu' \nabla^2 \boldsymbol{u} + (\lambda' + \mu') \nabla(\nabla \cdot \boldsymbol{u}) - \beta_t B \nabla T \tag{8}$$

where β_t is the volume thermal-expansion coefficient, λ' and μ' are the Lamé constants, and B is the bulk modulus, $B = (\lambda' + 2\mu'/3)$.

It is useful for purposes of illustrating a common approximation and estimating the magnitude of the PGTEW effect to consider (8) with the inertial term, $\rho(\partial^2 \boldsymbol{u}/\partial t^2)$, neglected. This is called the quasistatic [18] or long-wavelength approximation. If, in addition, only longitudinal disturbances are considered, $\nabla \times \boldsymbol{u} = 0$, the strain is $S = \nabla \cdot \boldsymbol{u}$ in this case, and (8) can be put in the form

$$\nabla[(\lambda' + 2\mu')(\nabla \cdot \boldsymbol{u}) - \beta_t B T] \cong 0 \tag{9}$$

from which it follows that

$$S \cong \frac{\beta_t B(T - T_e)}{(\lambda' + 2\mu')}. \tag{10}$$

Now, the right-hand side of (7) can usually be neglected as will be shown below. If, in addition, the thermal conduction term of (7) is neglected, then (7) becomes

$$T - T_e \cong \frac{1}{\rho C_v} \int H dt = \frac{(1 - R)E}{\rho C_v A d} \tag{11}$$

where E is the energy of the (slowly varying) incident light pulse, A is the cross-sectional area of the illuminated region of the sample, d is the depth of illumination, and R is the optical reflectance of the sample surface. If it is assumed that the depth of illumination is one optical-absorption length $d = \beta^{-1}$, where β is the optical absorption coefficient, then the sample temperature rise is given by

$$T - T_e \cong \frac{(1 - R)\beta E}{\rho C_v A} \tag{12}$$

and the sample strain is given by

$$S \cong \frac{(1 - R)\beta_t B \beta E}{\rho C_v (\lambda' + 2\mu')A}. \tag{13}$$

Consider as an example aluminum at an optical wavelength of 340 nm. The material parameters are [19] $\rho = 2.7 \times 10^3$ kg/m^3, $C_v = 907$ J/(kg − K), $\beta_t = 6.93 \times 10^{-5}$ K^{-1}, $\mu' = 2.5 \times 10^{10}$ N/m^2, $\lambda' = 6.1 \times 10^{10}$ N/m^2, $B = 7.77 \times 10^{10}$ N/m^2, $R = 0.923$, and $\beta = 3.7 \times 10^7$ m^{-1}. For $E = 1.0$ J/m^2, (12) and (13) give, respectively, $T - T_e \cong 1.16$ K, $S \cong 5.65 \times 10^{-5}$.

B. *Thermoelastic Coupling*

Consider now the one-dimensional thermoelastic problem [17], [20] for which the total temperature field is $T(x, t) + T_e$, $\boldsymbol{u} = \hat{i}u(x, t)$, and $H = 0$, where $\hat{i}$ is the unit vector giving the direction of the x-axis. (The heat is brought into the problem as a boundary condition.) The thermal-diffusion and elastic-wave equations then become, respectively

$$\kappa \frac{\partial^2 T}{\partial x^2} - \rho C_v \frac{\partial T}{\partial t} = T_e \lambda \frac{\partial^2 u}{\partial t \partial x} \tag{14}$$

$$\rho \frac{\partial^2 u}{\partial t^2} = c \frac{\partial^2 u}{\partial x^2} - \lambda \frac{\partial T}{\partial x} \tag{15}$$

where all nonessential subscripts have been omitted, $\lambda = \beta_t B$, and the total temperature has been replaced by T_e on the right-hand side of (14) in order to linearize the differential equations (small-signal approximation). Assume that all dynamical quantities vary harmonically with time so that

$$T(x, t) = T(x)\, e^{j\omega t} \tag{16}$$

$$u(x, t) = u(x)\, e^{j\omega t}. \tag{17}$$

Then, substitution of (16) and (17) into (14) and (15) yields two coupled ordinary differential equations:

$$\frac{d^2 T}{dx^2} - \mu^2 T = g \frac{du}{dx} \tag{18}$$

$$\frac{d^2 u}{dx^2} + k^2 u = a \frac{dT}{dx} \tag{19}$$

where $\mu^2 \equiv (j\omega\rho C_v/\kappa)$, $g \equiv (j\omega\lambda T_e/\kappa)$, $k^2 \equiv (\omega^2 \rho/c)$, and $a \equiv (\lambda/c)$. For an infinite medium, assume that the solutions to (18) and (19) are of the form:

$$T(x) = T_0 e^{-j\gamma x} \tag{20}$$

$$u(x) = u_0 e^{-j\gamma x} \tag{21}$$

where γ is to be determined. Substitution of (20) and (21) into (18) and (19) yields two linear, homogeneous, algebraic equations for the determination of the complex amplitudes T_0 and u_0:

$$(\gamma^2 + \mu^2) T_0 - jg\gamma u_0 = 0 \tag{22}$$

$$-ja\gamma T_0 + (\gamma^2 - k^2) u_0 = 0. \tag{23}$$

For a nontrivial solution, the determinant of the coefficients of T_0 and u_0 must vanish; the resulting secular equation is quadratic in γ^2 and has two roots for the eigenvalues:

$$\gamma_\pm^2 = \frac{\mu^2}{2}(1 + \delta - b) \cdot \left[-1 \pm \sqrt{1 + \frac{4b}{(1 + \delta - b)^2}} \right] \tag{24}$$

where

$$b \equiv \frac{k^2}{\mu^2} = \frac{-j\omega\kappa}{c C_v} \tag{25}$$

$$\delta \equiv \frac{ag}{\mu^2} = \frac{\lambda^2 T_e}{\rho c C_v}. \tag{26}$$

The temperature and elastic fields for an infinite medium are thus given by

$$T(x) = T_0^+ e^{-j\gamma_+ x} + T_0^- e^{-j\gamma_- x} \tag{27}$$

$$u(x) = u_0^+ e^{-j\gamma_+ x} + u_0^- e^{-j\gamma_- x}. \tag{28}$$

The ratios of eigenvectors, u_0^-/T_0^- and T_0^+/u_0^+, are obtained by substituting γ_- and γ_+, respectively, into either (22) or (23):

$$u_0^- = \frac{ja\gamma_- T_0^-}{\gamma_-^2 - k^2} \tag{29}$$

$$T_0^+ = \frac{(\gamma_+^2 - k^2) u_0^+}{ja\gamma_+}. \tag{30}$$

Absolute values of T_0^- and u_0^+ are determined by the boundary conditions.

For purposes of illustration, consider now the following model: a semi-infinite medium with a stress-free boundary and a surface heat source at $x = 0$. The stress $\sigma = c(\partial u/\partial x) - \lambda T$, at $x = 0$, is given by

$$\sigma_0 = -jc(\gamma_+ u_0^+ + \gamma_- u_0^-) - \lambda(T_0^+ + T_0^-). \tag{31}$$

Using (29) and (30), (31) becomes

$$\sigma_0 = -\frac{jck^2 u_0^+}{\gamma_+} + \frac{ack^2 T_0^-}{\gamma_-^2 - k^2}. \tag{32}$$

If the stress is zero at $x = 0$, $\sigma_0 = 0$, and (32) yields

$$u_0^+ = \frac{-ja\gamma_+ T_0^-}{\gamma_-^2 - k^2}. \tag{33}$$

The heat flux $\Phi = -\kappa(\partial T/\partial x)$, at $x = 0$, is given by

$$\Phi_0 = j\kappa(\gamma_+ T_0^+ + \gamma_- T_0^-) \tag{34}$$

which using (30) becomes

$$\Phi_0 = \kappa \left[j\gamma_- T_0^- + \frac{(\gamma_+^2 - k^2) u_0^+}{a} \right]. \tag{35}$$

If $\Phi_0 = h$ at $x = 0$, where h is the surface heat source density (in watts per square meter), then use of (33) and (35) gives

$$T_0^- = \frac{-j(\gamma_-^2 - k^2) h}{F} \tag{36}$$

where

$$F \equiv \kappa[\gamma_-^2(\gamma_-^2 - k^2) - \gamma_+(\gamma_+^2 - k^2)]. \tag{37}$$

It then follows from (29), (30), and (33) that

$$u_0^+ = \frac{-a\gamma_+ h}{F} \tag{38}$$

$$T_0^+ = \frac{j(\gamma_+^2 - k^2) h}{F} \tag{39}$$

$$u_0^- = \frac{a\gamma_- h}{F}. \tag{40}$$

TABLE I

THERMOELASTIC COUPLING PARAMETERS FOR SELECTED MATERIALS[1]

Material	ρ (kg/m^3)	c (N/M^2)	C_v (J/kg-K)	λ (N/m^2-K)	κ (W/m-K)	δ	$\|b\|$
Air	1.195	1.43×10^5	1006	4.83×10^2	2.58×10^{-2}	0.404	0.113
Water	998.2	2.2×10^9	4182	4.55×10^5	6.04×10^{-1}	6.61×10^{-3}	4.12×10^{-5}
Fused Quartz	2.2×10^3	7.85×10^{10}	686	4.54×10^4	1.44	5.1×10^{-6}	1.68×10^{-5}
Sapphire	3.99×10^3	5.02×10^{11}	773	3.29×10^6	25.1	2.1×10^{-3}	4.06×10^{-5}
Silicon	2.32×10^3	1.66×10^{11}	704	7.63×10^5	148	6.3×10^{-4}	7.97×10^{-4}
Aluminum	2.7×10^3	1.11×10^{11}	907	5.38×10^6	237	3.2×10^{-2}	1.48×10^{-3}
Copper	8.93×10^3	2.23×10^{11}	420	8.02×10^6	398	2.31×10^{-2}	2.67×10^{-3}

[1] Material parameters were obtained from the handbook literature [19]. The values of δ were calculated for $T_r = 300°$ K and the values of $|b|$ were calculated for $f = 1000$ MHz.

For condensed matter, $\delta << 1$, as shown for several materials of interest in Table I. Furthermore, even for microwave frequencies, $b << 1$ for condensed matter. In view of these inequalities, the first-order approximations for the eigenvalues are

$$\gamma_+ \cong k, \; \gamma_- \cong -j\mu, \tag{41}$$

$$\mu = (1 + j)\left[\frac{\omega\rho C_v}{2\kappa}\right]^{1/2}. \tag{42}$$

Correspondingly, the approximate expressions for the temperature and elastic fields are

$$T(x) \cong \frac{h}{\kappa\mu}\left[(b - \delta)b\, e^{-jkx} + e^{-\mu x}\right] \tag{43}$$

$$u(x) \cong \frac{\lambda h}{c\kappa\mu^2}\left[\frac{jke^{-jkx}}{\mu} - e^{-\mu x}\right]. \tag{44}$$

The eigenvalue γ_+ corresponds to a propagating mode; the eigenvalue γ_- corresponds to a nonpropagating mode. The propagating mode is a traveling wave without attenuation in the first-order approximation. The nonpropagating mode decreases to e^{-1} of its value at $x = 0$ in one thermal diffusion-length, $D = [2\kappa/(\omega\rho C_v)]^{1/2}$, in the first-order approximation. Both propagating and nonpropagating modes have temperature and displacement fields associated with them. The first term of (43) and the first term of (44) represent the propagating mode. The second term of (43) and the second term of (44) represent the nonpropagating mode. Since the first term of (43) is small compared to the second term, $T(x, t)$ is dominated by the second term and is usually referred to as a "thermal wave." For values of x greater than a few thermal-diffusion lengths $u(x, t)$ is dominated by the first term of (44), which corresponds to a traveling wave. Since the γ_- term dominates $T(x, t)$ and the γ_+ term dominates γ_+ term dominates $u(x, t)$, the γ_- mode is often called the *thermal mode* and the γ_+ mode is often called the *acoustic mode*. It is worth noting that the second-order approximation of γ_+ contributes a term to $-j\gamma_+ x$ of the form, $-[\omega^2\kappa/(\rho v^3 C_v)]x$, where $v = \sqrt{c/\rho}$ is the phase velocity of the elastic wave; this amounts to an attenuation of the elastic traveling wave due to thermal conduction. The first term of (43) is the result of elastic energy converted into heat due to the attenuation of the elastic wave.

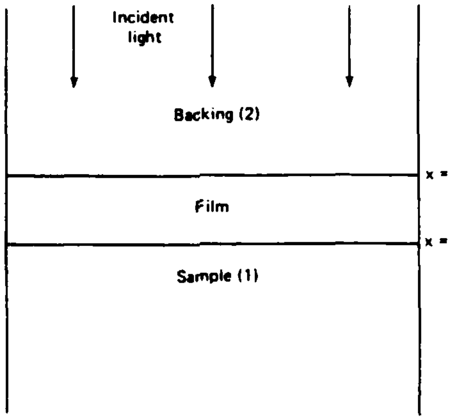

Fig. 1. One-dimensional model of transparent backing ($x < 0$), light-absorbing film ($0 \leq x \leq d$), and transparent sample ($x > d$) for frequency-domain calculations.

C. *One-Dimensional Composite-Media Model in Frequency Domain*

A one-dimensional model consisting of a transparent backing ($x < 0$), a light-absorbing film ($0 < x < d$), and a transparent sample ($x > d$) is illustrated in Fig. 1. As has been shown above, the right-hand side of (1) can be neglected to a good order of approximation. Thus the approximate thermal-diffusion equation

$$\kappa \frac{\partial^2 T}{\partial x^2} - \rho C_v \frac{\partial T}{\partial t} = -H \tag{45}$$

is first solved for all three regions. For sample and backing, $H = 0$, and for the absorbing film [21], [22]

$$H = \frac{\beta}{2} e^{-\beta x}(1 - R)\, I_0(t) \tag{46}$$

where β is the optical attenuation of the film and $I_0(t)$ is the incident intensity of the light (at $x = 0$). The incident light is imagined to be uniformly distributed over the plane $x = 0$. Continuity of temperature and heat flux at the boundaries are used to determine $T(x, t)$, $-\infty < x < \infty$. Then the elastic-wave equation

$$\rho \frac{\partial^2 u}{\partial t^2} = c \frac{\partial^2 u}{\partial x^2} + R_l \frac{\partial^3 u}{\partial x^2 \partial t} - \lambda \frac{\partial T}{\partial x} \tag{47}$$

is solved for all three regions using the solutions of (45) for T. A phenomenological loss term with loss factor R_l

has been included in (47) so that elastic-wave attenuation can be taken into account. Continuity of elastic displacement and stress at the boundaries are used to determine $u(x, t)$, $-\infty < x < \infty$.

Suppose that the incident light intensity is harmonically modulated with frequency $\omega/2\pi$ so that $I_0(t) = I_0 e^{j\omega t}$. Then solutions to (45) that take into account the finite nature of T at $x = \pm\infty$ and the standing-wave nature of T for $0 < x < d$ are for backing, film, and sample, respectively

$$T_2(x) = T_e + B_2 e^{\mu_2 x}, \qquad x < 0 \tag{48}$$

$$T(x) = T_e + B_+ e^{\mu x} + B_- e^{-\mu x} - \frac{b_0 e^{-\beta x}}{(\beta^2 - \mu^2)}, \qquad 0 < x < d \tag{49}$$

$$T_1(x) = T_e + B_1 e^{-\mu_1 x}, \qquad x > d \tag{50}$$

where

$$b_0 \equiv \frac{\beta(1 - R)I_0}{2\kappa} \tag{51}$$

and the thermal propagation factors (μ) are of the form given in (42) with material parameters appropriate to the medium. The boundary conditions $T_2(0) = T(0)$, $T(d) = T_1(d)$, $\kappa_2(\partial T_2/\partial x)_0 = \kappa(\partial T/\partial x)_0$, and $\kappa(\partial T/\partial x)_d = \kappa_1(\partial T_1/\partial x)_d$ give four algebraic equations:

$$B_+ + B_- - B_2 = \frac{b_0}{\beta^2 - \mu^2} \tag{52}$$

$$e^{\mu d} B_+ + e^{-\mu d} B_- - e^{-\mu_1 d} B_1 = \frac{b_0 e^{-\beta d}}{\beta^2 - \mu^2} \tag{53}$$

$$-\kappa\mu B_+ + \kappa\mu B_- + \kappa_2 \mu_2 B_2 = \frac{\kappa\beta b_0}{\beta^2 - \mu^2} \tag{54}$$

$$-\kappa\mu e^{\mu d} B_+ + \kappa\mu e^{-\mu d} B_- - \kappa_1 \mu_1 e^{-\mu_1 d} B_1 = \frac{\kappa\beta b_0 e^{-\beta d}}{\beta^2 - \mu^2}. \tag{55}$$

Equations (52)–(55) can be solved numerically for B_+, B_1, and B_2, the values of which are then substituted into (48)–(50) to calculate $T(x)$, $-\infty < x < \infty$.

The corresponding solutions to (47) for backing, film, and sample are, respectively

$$u_2(x) = A_2 e^{\gamma_2 x} + \frac{\lambda_2 \mu_2 B_2 e^{\mu_2 x}}{c_2'(\mu_2^2 - \gamma_2^2)}, \qquad x < 0 \tag{56}$$

$$\begin{aligned} u(x) = A_+ e^{\gamma x} + A_- e^{-\gamma x} &+ \frac{\lambda\mu}{c'(\mu^2 - \gamma^2)} \cdot [B_+ e^{\mu x} - B_- e^{-\mu x}] \\ &+ \frac{\lambda\beta b_0 e^{-\beta x}}{c'(\beta^2 - \gamma^2)(\beta^2 - \mu^2)} \\ &0 \le x \le d \end{aligned} \tag{57}$$

$$u_1(x) = A_1 e^{-\gamma_1 x} - \frac{\lambda_1 \mu_1 B_1 e^{-\mu_1 x}}{c_1'(\mu_1^2 - \gamma_1^2)}, \qquad x > d \tag{58}$$

where the elastic-wave propagation factors are of the form $\gamma = [\omega^2 R_l/(2C_v) + j(\omega/v)]$, the phase velocities are of the form $v = (c/\rho)^{1/2}$, and the effective elastic constants are of the form $c' = c + j\omega R_l$. The boundary conditions $u_2(0) = u(0)$, $u(d) = u_1(d)$, $\sigma_2(0) = \sigma(0)$, and $\sigma(d) = \sigma_1(d)$ give four algebraic equations:

$$\begin{aligned} &A_+ + A_- - A_2 \\ &\quad = -\frac{\lambda\beta b_0}{c'(\beta^2 - \gamma^2)(\beta^2 - \mu^2)} - \frac{\lambda\mu(B_+ - B_-)}{c'(\mu^2 - \gamma^2)} \\ &\qquad + \frac{\lambda_2 \mu_2 B_2}{c_2'(\mu_2^2 - \gamma_2^2)} \end{aligned} \tag{59}$$

$$\begin{aligned} &e^{\gamma d} A_+ + e^{-\gamma d} A_- - e^{-\gamma_1 d} A_1 \\ &\quad = -\frac{\lambda\beta b_0 e^{-\beta d}}{c'(\beta^2 - \gamma^2)(\beta^2 - \mu^2)} - \frac{\lambda_1 \mu_1 B_1 e^{-\mu_1 d}}{c_1'(\mu_1^2 - \gamma_1^2)} \\ &\qquad - \frac{\lambda\mu}{c'(\mu^2 - \gamma^2)} [e^{\mu d} B_+ - e^{-\mu d} B_-] \end{aligned} \tag{60}$$

$$\begin{aligned} &c'\gamma A_+ - c'\gamma A_- - c'\gamma_2 A_2 \\ &\quad = \frac{\lambda\gamma^2 b_0}{(\beta^2 - \mu^2)(\beta^2 - \gamma^2)} - \frac{\lambda\gamma^2(B_+ + B_-)}{(\mu^2 - \gamma^2)} \\ &\qquad + \frac{\lambda_2 \gamma_2^2 B_2}{(\mu_2^2 - \gamma_2^2)} \end{aligned} \tag{61}$$

$$\begin{aligned} &c'\gamma e^{\gamma d} A_+ - c'\gamma e^{-\gamma d} A_- + c_1' \gamma_1 e^{-\gamma_1 d} A_1 \\ &\quad = \frac{\lambda\gamma^2 b_0 e^{-\beta d}}{(\beta^2 - \mu^2)(\beta^2 - \gamma^2)} + \frac{\lambda_1 \gamma_1^2 B_1 e^{-\mu_1 d}}{(\mu_1^2 - \gamma_1^2)} \\ &\qquad - \frac{\lambda\gamma^2}{(\mu^2 - \gamma^2)} [B_+ e^{\mu d} + B_- e^{-\mu d}]. \end{aligned} \tag{62}$$

Equations (59)–(62) can be solved numerically for A_+, A_-, A_1, and A_2, the values of which are then substituted into (56)–(58) to calculate $u(x)$, $-\infty < x < \infty$.

D. One-Dimensional Composite-Media Model in Time Domain

Consider now the one-dimensional model illustrated in Fig. 2, which consists of a transparent backing ($x < 0$) and a sample with bulk absorption ($x > 0$). Suppose that the incident light pulse has a sine-squared shape with width τ

$$I_0(t) = \begin{cases} \sin^2(\pi t/\tau), & 0 \le t \le \tau \\ 0, & t > \tau,\ t < 0 \end{cases} \tag{63}$$

which is a good approximation to the shape of common laser pulses. The method of Laplace transforms can be used to obtain solutions to (45) and (47), which become, respectively

$$\frac{d^2\bar{T}}{dx^2} - \mu^2\bar{T} = -b_0 e^{-\beta x}\bar{I} \tag{64}$$

$$\frac{d^2\bar{U}}{dx^2} - k^2\bar{U} = \frac{\lambda}{c}\frac{d\bar{T}}{dx} \tag{65}$$

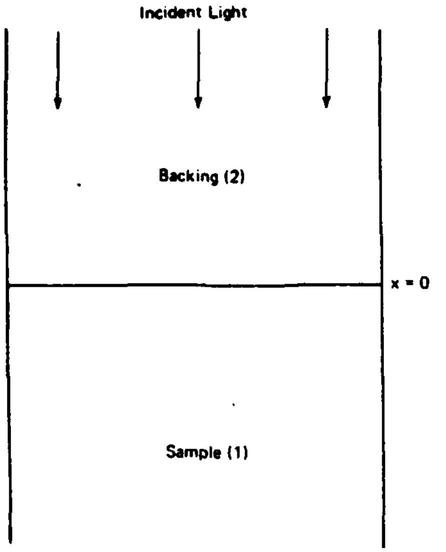

Fig. 2. One-dimensional model of transparent backing ($x < 0$) and light-absorbing sample ($x > 0$) for time-domain calculations.

where losses in the elastic-wave equation have been neglected. $\bar{T}(x, s)$ and $\bar{U}(x, s)$ are the Laplace transforms of $T(x, t)$ and $u(x, t)$, respectively; $k^2 = (\rho s^2/c)$; $\mu^2 = (\rho C_v s/\kappa)$; and $\bar{I}(s)$ is the Laplace transform of (63)

$$\bar{I}(s) = \frac{2\pi^3\tau(1 - e^{-\tau s})}{\tau s[(\tau s)^2 + 4\pi^2]}. \tag{66}$$

The solution to (64) with $\bar{I} = 0$ for the backing is of the form

$$\bar{T}_2(x, s) = B_2 e^{\mu_2 x}, \qquad x < 0. \tag{67}$$

The solution to (64) for the sample is of the form

$$\bar{T}_1(x, s) = B_1 e^{-\mu_1 x} - \frac{b_0 \bar{I}(s) e^{-\beta x}}{(\beta^2 - \gamma_1^2)}. \tag{68}$$

The solutions to (65) for the backing and sample are, respectively, of the forms

$$\bar{U}_2(x, s) = A_2 e^{k_2 x} + \frac{\lambda_2 \mu_2 B_2 e^{\mu_2 x}}{c_2(\mu_2^2 - k_2^2)} \tag{69}$$

$$\bar{U}_1(x, s) = A_1 e^{-k_1 x} + \frac{\lambda_1 \mu_1 B_1 e^{-\mu_1 x}}{c_1(\mu_1^2 - k_1^2)} + \frac{\lambda_1 \beta b_0 \bar{I}(s) e^{-\beta x}}{c_1(\beta^2 - \mu_1^2)(\beta^2 - k_1^2)}. \tag{70}$$

The quantities B_1, B_2, A_1, and A_2 are evaluated using continuity of temperature and heat flux at $x = 0$, and continuity of particle velocity, $\partial u/\partial t$, and stress at $x = 0$. The inverse Laplace transforms can be computed numerically to give $T(x, t)$ and $u(x, t)$, $0 < t < \infty$, $-\infty < x < \infty$.

III. RESULTS

A. Temperature and Elastic-Displacement Distributions for Composite-Media Model in the Frequency Domain

The temperature distribution was calculated for several material combinations chosen principally because they had been used in reported experiments. Results are shown in Fig. 3 for the case: backing = sapphire, film = molybdenum, sample = fused quartz; results are shown in Fig. 4 for the case: backing = air, film = molybdenum, and sample-fused quartz. In both cases the film thickness was taken to be 0.2 μm, the modulation frequency to be 20 MHz, and $(1 - R)I_0 = 1.0$ W/m². The material parameters were taken from the literature [19]. The optical attenuation β used in these calculations is characteristic of molybdenum at a wavelength of 580 nm; it corresponds to an optical absorption length β^{-1} of 15.4 nm. Since the thermal-diffusion length in molybdenum at 20 MHz is 920 nm, the film is optically thick and thermally thin in these cases. The temperature distributions for the two sets of material combinations are similar.

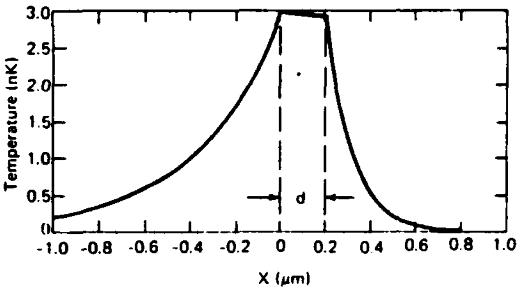

Fig. 3. Temperature vs. x for backing = sapphire, film = molybdenum, sample = fused quartz, $d = 0.2$ μm, $\beta = 6.51 \times 10^7$ m^{-1}, $f = 20$ MHz, and $(1 - R)I_0 = 1.0$ W/m².

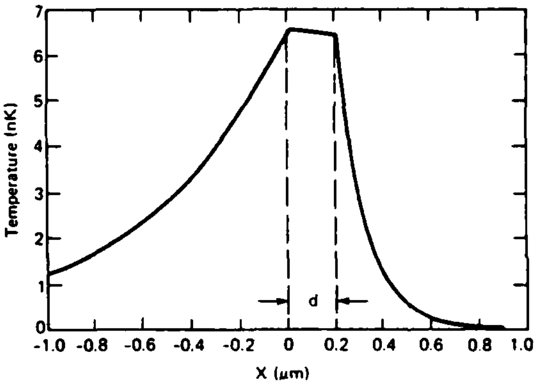

Fig. 4. Temperature vs. x for backing = air, film = molybdenum, sample = fused quartz, $d = 0.2$ μm, $\beta = 6.51 \times 10^7$ m^{-1}, $f = 20$ MHz, and $(1 - R)I_0 = 1.0$ W/m².

The elastic-displacement distributions calculated for the cases corresponding to the temperature distributions of Figs. 3 and 4 are shown in Figs. 5 and 6, respectively. By comparing Figs. 5 and 6, one can see that there is a substantial difference in $u(x)$ for the two cases, both in the shapes of the curves and in the magnitudes of the displacement in the quartz sample. It is interesting to note that an air backing—even though it has a large acoustic impedance mismatch to molybdenum—has a nonnegligible effect on the ultrasonic-wave generation in the film and sample. This calculation indicates that treating air as presenting a stress-free boundary with no heat conduction may be a poor approximation in photothermal generation of elastic waves at an air–solid interface. As will be shown

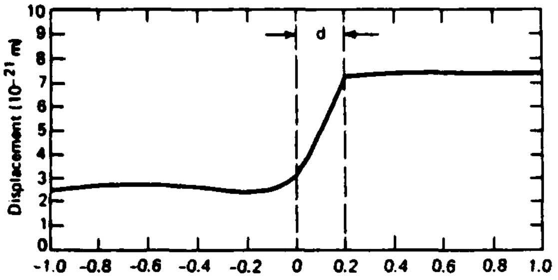

Fig. 5. Elastic displacement vs. x for backing = sapphire, film = molybdenum, sample = fused quartz, $d = 0.2$ μm, $\beta = 6.51 \times 10^{7}$ m^{-1}, $f = 20$ MHz, and $(1 - R)I_0 = 1.0$ W/m^2.

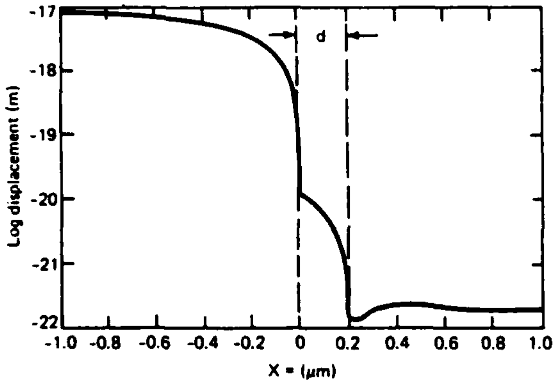

Fig. 6. Elastic displacement vs. x for backing = air, film = molybdenum, sample = fused quartz, $d = 0.2$ μm, $\beta = 6.51 \times 10^{-7}$ m^{-1}, $f = 20$ MHz, and $(1 - R)I_0 = 1.0$ W/m^2.

below, this is because of the high thermal-expansion coefficient of air.

B. Effects of Dynamic and Material Parameters on Photothermal Generation of Elastic Waves in the Frequency Domain

The variations of A_1, the amplitude of the traveling elastic wave in the sample, with optical attenuation β and film thickness d, both show saturation [11]. The amplitude of the photothermally generated elastic wave increases with increasing β for a given value of d until all the light is absorbed in the film. This is essentially accomplished when $\beta \cong (5/d)$, i.e., when the film thickness is equal to about five optical-absorption lengths. Similarly, A_1 increases with increasing d for fixed β until all the light is absorbed in the film. If the thermal-diffusion length D of the film is large compared to its thickness (the film is thermally thin), then the thermal properties of the sample are of essential importance in determining T and u. For an optically thick ($d >> \beta^{-1}$) and thermally-thin ($d << D$) film, the source of heat can be assumed to be at the surface of the sample, and the material properties of the film can be neglected.

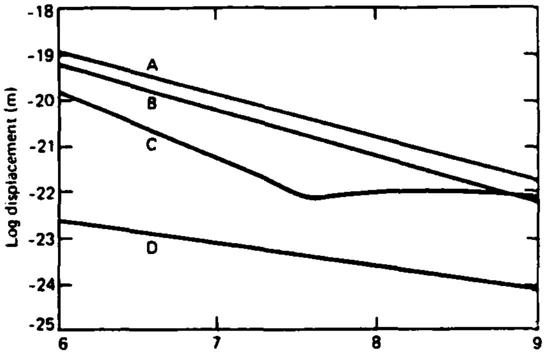

Fig. 7. Amplitude of elastic wave in sample vs. frequency for h or $(1 - R)I_0$ equal to 1.0 W/m^2. (a) Sapphire-molybdenum-quartz, $\beta = 6.51 \times 10^{7}$ m^{-1}, $d = 0.2$ μm. (b) Quartz with surface heat source and ideal-clamp backing. (c) Air-molybdenum-quartz, $\beta = 6.51 \times 10^{7}$m^{-1} $d = 0.2$ μm. (d) Quartz with surface heat source and ideal stress-free backing.

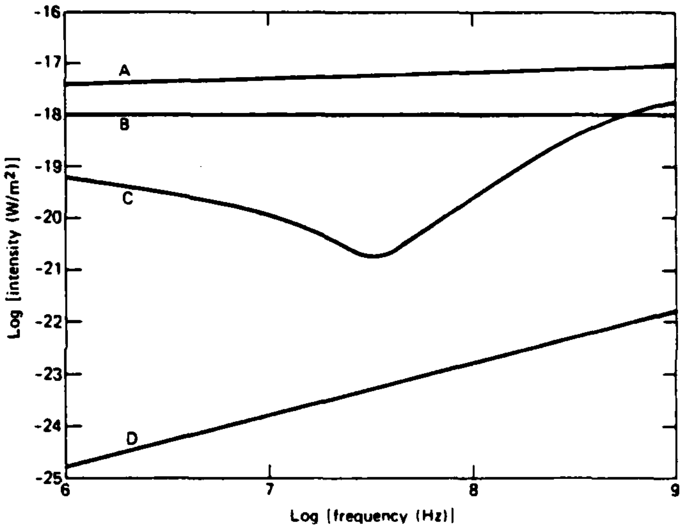

Fig. 8. Intensity of elastic wave in sample vs. frequency for h or $(1 - R)I_0$ equal to 1.0 W/m^2. (a) Sapphire-molybdenum-quartz, $\beta = 6.51 \times 10^{7}$ m^{-1}, $d = 0.2$ μm. (b) Quartz with surface heat source and ideal-clamp backing. (c) Air-molybdenum-quartz, $\beta = 6.51 \times 10^{7}$ m^{-1}, $d = 0.2$ μm. (d) Quartz with surface heat source and ideal stress-free backing.

The variations with frequency of the amplitude and intensity of the elastic wave in the sample are of particular interest. The time-averaged intensity for harmonic elastic waves in the sample is given by $I_1 = -\frac{1}{2}\,\mathrm{re}(-\sigma_1 \dot{u}_1^*)$, where $\dot{u}_1^*$ is the complex conjugate of $\partial u_1/\partial t$, the particle velocity and σ_1 is the stress. The functional variations of A_1 and I_1 with frequency depend on the material parameters of the composite structure and thus cannot be expressed in simple analytical terms except in special cases (see below). For sapphire-molybdenum-quartz and air-molybdenum-quartz, A_1 is shown as a function of frequency in Fig. 7, curves (A) and (C), respectively. The intensity I_1 is shown as a function of frequency for sapphire-molybdenum-quartz and air-molybdenum-quartz in Fig. 8, curves (A) and (C), respectively. The sapphire backing gives a significantly greater efficiency of photothermal elastic-wave generation than the air backing and gives a different frequency dependence. Since $T_1 \propto I_0$, then $u_1 \propto I_0$ and $I_1 \propto I_0^2$ for all linear thermoelastic cases.

The various effects on the amplitude and intensity of photothermally generated elastic waves due to the mate-

TABLE II

THEORETICAL VALUES OF SURFACE TEMPERATURE AND AMPLITUDE AND INTENSITY OF ELASTIC WAVES[1]

Backing (2)	Sample (1)	A_2 (m)	A_1 (m)	I_2 (W/m^2)	I_1 (W/m^2)	T_s (K)
Sapphire	Fused Quartz	3.41×10^{-21}	1.15×10^{-20}	4.11×10^{-18}	1.38×10^{-17}	8.68×10^{-9}
Air	Sapphire	1.42×10^{-17}	1.53×10^{-22}	6.56×10^{-16}	8.25×10^{-21}	1.01×10^{-8}
Air	Fused Quartz	8.43×10^{-17}	2.39×10^{-21}	2.32×10^{-14}	5.91×10^{-19}	6.03×10^{-8}
Air	Molybdenum	6.62×10^{-18}	3.41×10^{-22}	1.43×10^{-16}	6.28×10^{-20}	4.72×10^{-9}
Sapphire	Molybdenum	1.39×10^{-20}	9.24×10^{-21}	6.83×10^{-17}	4.61×10^{-17}	3.22×10^{-9}
Air	Silicon	8.05×10^{-18}	3.97×10^{-22}	2.11×10^{-16}	2.45×10^{-20}	5.74×10^{-9}
Air	Aluminum	5.47×10^{-18}	3.07×10^{-21}	9.74×10^{-17}	1.27×10^{-18}	3.79×10^{-9}

[1] In backing and sample for several material combinations using surface-heat-source model: $h = 1.0$ W/m^2, $f = 20$ MHz.

TABLE III

THEORETICAL VALUES OF SURFACE TEMPERATURE AND AMPLITUDE AND INTENSITY OF ELASTIC WAVE[1]

Model	Backing	Film	Sample	T_s (K)	A_1 (m)	I_1 (W/m^2)
B	Sapphire	200 nm Mo	Fused Quartz	5.19×10^{-9}	7.27×10^{-21}	5.49×10^{-18}
B	Air	200 nm Mo	Sapphire	5.07×10^{-9}	6.64×10^{-23}	1.56×10^{-21}
S	Sapphire	—	Fused Quartz	8.68×10^{-9}	1.15×10^{-20}	1.38×10^{-17}
S	Ideal Clamp	—	Fused Quartz	6.05×10^{-8}	3.05×10^{-21}	9.65×10^{-19}
S	Ideal Stress-Free	—	Sapphire	1.01×10^{-8}	4.82×10^{-23}	8.20×10^{-22}

[1] In sample for several structures: $f = 20$ MHz, B = bulk optical absorption in film, $\beta = 6.5 \times 10^7$ m^{-1}, $(1 - R) I_0 = 1.0$ W/m^2, S = surface heat source, $h = 1.0$ W/m^2.

rial parameters of the composite structure can best be understood using an analytical rather than a numerical solution. This can be accomplished using an extension of White's [8], surface-heat-source model to include the effects of the thermoelastic parameters of the backing material [10], [12]. This model consists of semi-infinite backing ($x < 0$), an infinitesimal harmonic heat source with density $he^{j\omega t}$ ($x = 0$), and semi-infinite sample ($x > 0$). This model is, of course, the limiting case of the model of Fig. 1 as $d \rightarrow 0$ and all the light is absorbed at the surface (see above). For the surface-source model, (45) with $H = 0$ is first solved for backing ($x < 0$) and sample ($x > 0$). The heat source is introduced via the boundary condition at $x = 0$

$$-\kappa_1 \frac{\partial T_1}{\partial x} + \kappa_2 \frac{\partial T_2}{\partial x} = h. \tag{71}$$

The constants in the temperature solutions for the two media are determined by (71) and continuity of temperature at $x = 0$. Then, the solutions of (47) for backing and sample are obtained as above for the finite film. The surface temperature at $x = 0$ is given by

$$T_s = \frac{(1 - j)h}{\sqrt{2\omega}(\kappa_1 a_1 + \kappa_2 a_2)} \tag{72}$$

where $a \equiv (\rho C_v/\kappa)^{1/2}$. The amplitude of the traveling elastic wave in the sample is given by [10]

$$A_1 = \frac{h}{(1 + r)(\kappa_1\mu_1 + \kappa_2\mu_2)} \cdot \left[\frac{\lambda_1\gamma_1(r + \mu_1/\gamma_1)}{c_1'(\mu_1^2 - \gamma_1^2)} + \frac{\lambda_2\gamma_2(\mu_2/\gamma_2 - 1)}{c_2'(\mu_2^2 - \gamma_2^2)}\right] \tag{73}$$

where $r \equiv [c_1'\gamma_1/(c_2'\gamma_2)]$ is the ratio of the characteristic acoustic impedance in the sample to that of the backing. The amplitude of the traveling elastic wave in the backing is given by

$$A_2 = \frac{h}{(1 + r)(\kappa_1\mu_1 + \kappa_2\mu_2)} \cdot \left[\frac{r\lambda_1(\gamma_1 - \mu_1)}{c_2'(\mu_2^2 - \gamma_2^2)} - \frac{\lambda_2(\gamma_2 + r\mu_2)}{c_2'(\mu_2^2 - \gamma_2^2)}\right]. \tag{74}$$

If $\mu_1^2 >> \gamma_1^2$, $\mu_2^2 >> \gamma_2^2$, and the attenuation of elastic waves is neglected:

$$A_1 \cong \frac{(1 - j)h}{(1 + r)\sqrt{2\omega}(\kappa_1 a_1 + \kappa_2 a_2)} \cdot \left\{\frac{r\lambda_1}{c_1 v_1 a_1^2} + \frac{(1 - j)}{\sqrt{2\omega}}\left[\frac{\lambda_1}{a_1 c_1} + \frac{\lambda_2}{a_2 c_2}\right]\right\} \tag{75}$$

$$A_2 \cong \frac{-(1 - j)h}{(1 + r)\sqrt{2\omega}(\kappa_1 a_1 + \kappa_2 a_2)} \cdot \left\{\frac{\lambda_2}{c_2 v_2 a_2^2} + \frac{(1 - j)r}{\sqrt{2\omega}}\left[\frac{\lambda_1}{a_1 c_1} + \frac{\lambda_2}{a_2 c_2}\right]\right\} \tag{76}$$

where $r \equiv [\rho_1 v_1/(\rho_2 v_2)]$ and v_1 and v_2 are the phase velocities of elastic waves in sample and backing, respectively.

Calculations based on this surface-heat-source model are shown in Table II. The surface temperature T_s and the amplitude and intensity of the elastic waves in backing and sample are given for several material combinations. Comparison of calculations based on the bulk-absorption model, the surface-heat-source model, and White's idealized models is shown in Table III for cases of particular interest. The frequency dependences of A_1 and I_1 for White's models are shown in Figs. 7 and 8.

TABLE IV
THEORETICAL VALUES OF SURFACE TEMPERATURE AND AMPLITUDE OF ELASTIC WAVE[1]

Model	Backing	Sample	T_s (K)	A_1 (m)
S	Air	Fused Quartz	6.03×10^{-8}	2.39×10^{-21}
ISF	—	Fused Quartz	6.05×10^{-8}	4.67×10^{-24}
S	Air	Sapphire	1.01×10^{-8}	1.53×10^{-22}
ISF	—	Sapphire	1.01×10^{-8}	4.82×10^{-23}
S	Air	Aluminum	3.79×10^{-9}	3.07×10^{-21}
ISF	—	Aluminum	3.79×10^{-9}	2.99×10^{-21}
S	Air	Silicon	5.74×10^{-9}	3.97×10^{-22}
ISF	—	Silicon	5.74×10^{-9}	2.83×10^{-22}

[1] In sample for $h = 1.0$ W/m^2, $f = 20$ MHz; comparison of surface heat source model (S) and idealized stress-free model (ISF).

It can be seen by inspection of Table III that the values of A_1 for the sapphire-molybdenum and sapphire-quartz surface-source models are 2 and 4 dB, respectively, greater than that for the sapphire-molybdenum-quartz bulk-absorption model. This increase in A_1 is due to the production of the same amount of heat, 1.0 W/m^2 in an infinitesimal as opposed to a 200-nm thick film. The difference in A_1 between the two surface cases is due to the differences in the pertinent material-parameter groups. It should also be noticed in Table III that A_1 for sapphire-quartz is 11.5 dB greater than quartz backed by an ideal clamp.

A particularly interesting result of these calculations concerns the effects of an air backing. Because of its low characteristic acoustic impedance (ρv) compared to that of condensed matter, air can in many elastic boundary-value problems be treated as presenting a stress-free surface. However, because of the thermal properties of air, White's idealized stress-free model may be inappropriate, as shown in Table IV. The value of A_1 for air-quartz is 54 dB greater than that given by quartz with an ideal stress-free backing for the case shown. The disparity between the surface-source model and the idealized stress-free model is not always so great; for air-silicon, A_1 is only 2.9 dB greater than that given by silicon with an ideal stress-free backing.

The essential physics of photothermal generation of harmonic elastic waves is contained in (75). The most efficient elastic-wave generation occurs when either backing or sample (or both) has a large value of $\lambda/(ac)$ and there is not a large acoustic-impedance mismatch (r not large). Since the thermal diffusivity is $D = \kappa/(\rho C_v)$, $a = D^{-1/2}$; furthermore, λ/c is effectively a thermal-expansion coefficient α. Thus a material with a large value of $\alpha(D)^{1/2}$—on either side of the heated interface—will produce efficient thermoelastic wave generation. If the backing is air, then $r >> 1$, the first term in brackets of (75) dominates at frequencies of interest here, and (75) gives results very similar to the results given by White's idealized stress-free backing. However, if it should happen that the sample has a relatively low value of $\lambda/(ac)$—as is the case for fused quartz—then the thermal properties of air cannot be neglected, and the remaining terms in the curly brackets of (75) are significant.

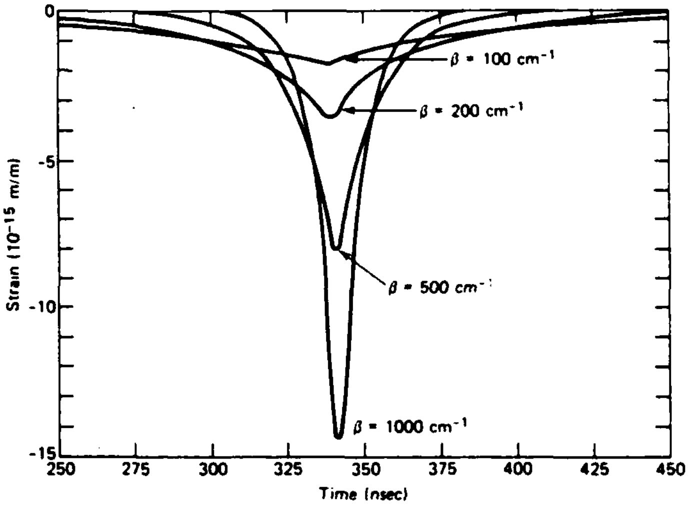

Fig. 9. Strain in sample vs. time for sample = water, backing = fused quartz, sine-squared laser pulse with $(1 - R)I_0 = 1.0$ W/m^2, $\tau = 10$ ns, $x = 0.5$ mm, and several values of β in cm^{-1}.

C. Pulse Shapes in Time Domain

Calculations based on the model of Section II-D show that the temperature pulse characteristically rises rapidly following the heating pulse and decays relatively slowly. As for the case of harmonic heating, the peak temperature increases with increasing β until saturation occurs. The calculated strain in the sample (water doped with a suitable dye to make it optically absorbing) with a fused-quartz backing is shown in Fig. 9 as a function of time for several values of β. The shape of the strain pulse changes as it propagates, attaining its eventual shape when $x \sim 5\beta^{-1}$, that is, about five absorption lengths [14]. The pulses shown in Fig. 9 have attained their eventual shapes reasonably well. It should be noticed that the peak strain increases with increasing β over this range of β. Furthermore, the pulse width decreases as β increases. For the pulses shown, the full-width-half-maximum strain is of the order of $(\beta v)^{-1}$, where v is the elastic-wave velocity of the sample.

The effect of a substantially different backing material on the strain pulse is shown in Fig. 10, where strain is shown as a function of time for several values of β. In this case, the sample is again water, but the backing is air, which has a large acoustic-impedance mismatch to

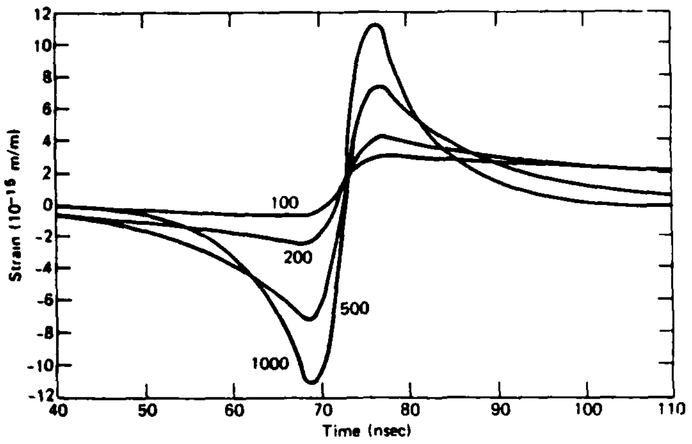

Fig. 10. Strain in sample vs. time for sample = water, backing = air, sinc-squared laser pulse with $(1 - R)I_0 = 1.0$ W/m^2, $\tau = 10$ ns, $x = 0.1$ mm, and several values of β in cm^{-1}.

water. The pulse shapes are markedly different from those shown for quartz–water in Fig. 9. These effects are, of course, just the time-domain manifestations of the frequency dependences discussed in Section III-B. Gournay [9] calculated pulse shapes similar to those in Fig. 9 for an idealized clamped boundary condition at $x = 0$ and similar to those shown in Fig. 10 for an idealized stress-free boundary condition at $x = 0$.

IV. COMPARISON WITH EXPERIMENT

Although a complete experimental evaluation of the preceding theoretical ideas on photothermal thermoelastic wave generation is not yet available, the published evidence in a variety of experiments is consistent with the general features of the models.

Linear thermoelastic theory predicts that the elastic-wave amplitude is a linear function of heating intensity and hence that the ultrasonic intensity is a quadratic function of heating intensity. The amplitude of the piezoelectrically detected elastic wave produced by a pulsed electron beam was measured as a function of peak electron-beam power for Cu and Mo samples by White [23]. The results showed that the elastic-wave amplitude was a linear function of electron-beam power. Cachier [24] obtained "rough" experimental verification of the predicted quadratic dependence of ultrasonic power on excitation power using Q-switched laser pulses absorbed by several solids. Kohanzadeh *et al.* [25] measured the amplitude of the acoustic signal as a function of excitation power for several liquids using a chopped Ar$^+$ laser beam; they found good agreement with the above predictions. Aindow *et al.* [26] used attached longitudinal and transverse wave transducers to detect laser generated pulses at free metal surfaces; they obtained a linear dependence of ultrasonic amplitude on laser intensity up to a point, but carried the experiments beyond the thermoelastic regime. Scruby *et al.* [27] also verified the predicted dependence of A_1 on I_0 using unfocused laser pulses incident on metals and detection with a capacitance transducer. It appears that the intensity dependence of photothermal thermoelastic wave generation is well understood provided that the heating intensity is not sufficiently high to produce some nonlinear effect such as variation of material parameters with temperature or strain, melting, ablation, or plasma formation [26]–[31].

Some aspects of the effects of material parameters on photothermal elastic wave generation can be quantitatively evaluated using the experimental results reported by von Gutfeld and Melcher [32], who used 5-ns laser pulses to generate ultrasonic waves in two devices that correspond to the models of Section II: a) backing = sapphire, film = Mo, sample = fused quartz and b) backing = air, film = Mo, sample = sapphire. A band of the excited Fourier spectrum was detected by a 20-MHz resonant transducer attached to the sample. Theoretical calculations of these cases are shown in the first two rows of Table III, where it can be seen that the amplitude of the elastic wave in the sample for case a) is 40.8 dB greater than for case b). Von Gutfeld and Melcher reported that the detected ultrasonic amplitude in the sample for case a) was about 40 dB greater than for case b). However, since the elastic wave in case b) of their experimental configuration traveled through a sapphire–quartz interface to the transducer thereby suffering a 1.5 dB reflection loss, the theoretical value, 40.8 + 1.5 = 42.3 dB, should be compared with their experimental value of 40 dB. Agreement of theory and their experiment is quite good, particularly so in view of the fact that a relatively broadband spectrum centered at 20 MHz was used in the actual experiment.

An important result of the theory of Section II is that efficient photothermal elastic wave generation will occur if the value of $\alpha(D)^{1/2}$ for the material on either side of the heated interface is large. For example, if a liquid such as acetone, which has a large thermal expansion coefficient, is used as a backing to fused quartz, the calculated increase in A_1 is about 21 dB over that for sapphire–quartz. Evidence for the validity of this guideline is provided by the data and analysis of von Gutfeld and Budd [33], who measured laser-generated ultrasonic waves for several liquid samples.

Another good test of the models is the frequency dependence, which is different for different material combinations as illustrated in Figs. 7 and 8. Measurement of the amplitude of the generated elastic wave as a function of frequency over a broad range is a formidable experimental problem, particularly in the more interesting high-radio to microwave frequency range. However, excitation of temporally narrow pulses is straightforward using lasers and fast-risetime detection in the time domain is feasible, though exacting, particularly for very narrow pulses. Of course, the same information is contained in time-domain and frequency-domain measurements, in principle. Only a few experimental efforts to evaluate theoretical pulse shapes have been published, as discussed below.

Using 20–60 ns laser pulses absorbed in dye solutions and piezoelectric detection, Gournay [9] compared de-

TABLE V
THEORETICAL VALUES OF SURFACE TEMPERATURE AND AMPLITUDE AND STRAIN OF ELASTIC WAVE[1]

Backing	Sample	T_s (K)	A_1 (m)	S_1 (m/m)
Air	Aluminum	97.8	8.31×10^{-11}	2.48×10^{-7}
Air	Silicon	148	1.67×10^{-11}	3.72×10^{-8}

[1] In sample for several material combinations using surface-heat-source model: $h = 10^{10}$ W/m^2, $f = 3$ MHz.

tected stress-pulse shapes for two cases: a) backing = air, sample = liquid ("unconstrained" surface) and b) backing-glass plate, sample = liquid ("constrained" surface). Although no quantitative comparison was shown, approximate agreement of detected pulse shapes with an idealized-free-surface model for case a) and an idealized-clamp model for case b) was reported.

Wetsel *et al.* [14] used a photoelastically deflected probing laser beam to detect elastic waves excited in a highly absorbing water solution backed by a quartz cuvette wall. The exciting laser pulse had a FWHM of 8 ns; the detected strain pulse has a FWHM of 80 ns. Although accurate quantitative comparison was hampered by uncertainty in the value of β, the observed broad strain pulse is consistent with the result of Section III-C that the eventual FWHM of the strain pulse is of the order of $(\beta v)^{-1}$.

Quantitative measurements of laser-generated elastic waveforms using a capacitance transducer were reported by Dewhurst *et al.* [29]. A three-dimensional point-source model [15] has shown some success in accounting for such measured features as pulse shapes and radiation directivity patterns.

V. DISCUSSION

Generation of thermal and elastic waves by optical absorption occurs because of heat transferred to the sample and thermal expansion. Coupling of the temperature and elastic fields is described by the thermal-diffusion and elastic-wave equations. Simultaneous solution of the two equations results in a propagating mode and a nonpropagating mode. Both propagating and nonpropagating modes have temperature and displacement fields associated with them. The propagating mode is a traveling wave without attenuation in the first-order approximation and is usually referred to as the "acoustic" mode. The nonpropagating mode decreases to e^{-1} of its initial value in one thermal-diffusion length in the first-order approximation and is usually referred to as the "thermal" mode.

One-dimensional composite-media models reveal that the thermal and elastic material parameters of the optically-absorbing region and regions adjacent to it are important in determining quantitative features of the generated waves. The most effective elastic-wave generation occurs when materials in or adjacent to the heated region have large values of $\alpha(D)^{1/2}$. This means that it is usually true that a condensed-matter backing produces a much larger amplitude of the elastic wave in the sample than a gas backing. Since the thermal and elastic waves carry information about the generation and adjacent regions, condensed-matter backings may be undesirable in imaging applications where only sample features are of interest.

The characteristics of photothermal generation of thermal and elastic waves discussed in this paper so far are valid in the linear thermoelastic regime. However, it is quite easy to observe nonlinear behavior in PGTEW experiments [26]-[31]. For example, a 1.0 W Ar$^+$ laser beam focused with a microscope-object lens to a 5-μm beam waist produces a laser intensity of 10^{11} W/m^2; even unfocused pulsed lasers such as Nd:YAG can easily produce such an intensity, or greater. In Table V, the surface-temperature rise, amplitude of elastic displacement, and strain in the sample are shown for a heating intensity of 10^{10} W/m^2 and a frequency of 3 MHz. In the case of aluminum, even the temperature rise of nearly 100 K is insufficient to cause a substantial nonlinearity in the thermal conductivity, because the thermal conductivity of aluminum is a weak function of temperature near 300 K. On the other hand, the nearly 150-K surface temperature rise for silicon represents a very substantial nonlinearity in thermal conductivity since κ for silicon is a strong function of temperature near 300 K. The strain levels in both cases are well below the value that would be expected to result in an elastic nonlinearity. Since the ratio of the principal third-order elastic constant to the second-order elastic constant is typically of the order of 0.1, a ten-percent nonlinearity in elasticity would occur for a strain amplitude of about unity. Thus it is expected that typical samples are driven thermally nonlinear well before they are driven elastically nonlinear by photothermal conversion. The data of Scruby *et al.* [27] on aluminum at 3 MHz is consistent with this analysis. The open-circuit voltage for typical resonant transducers used to detect the strain levels of Table V is of the order of hundreds of millivolts. One should therefore be careful in any PGTEW experiment to determine whether observed signals are in the thermoelastic regime.

REFERENCES

[1] A. Rosencwaig, *Photoacoustics and Photoacoustic Spectroscopy*. New York: John Wiley, 1981. (See also C. K. N. Patel and A. C. Tam, "Pulsed optoacoustic spectroscopy of condensed matter," *Rev. Mod. Phys.*, vol. 53, pp. 517-550, 1981.)

[2] W. B. Jackson *et al.*, "Photothermal deflection spectroscopy and detection," *Appl. Opt.*, vol. 20, pp. 1333-1334, 1981. (See also G. C. Wetsel Jr., and S. A. Stotts, "Absolute measurement of optical attenuation," *Appl. Phys. Lett.*, vol. 42, pp. 931-933, 1983.)

[3] H. K. Wickramasinghe et al., "Photoacoustics on a microscopic

scale," *Appl. Phys. Lett.*, vol. 33, pp. 923-925, 1978. (See also R. L. Thomas *et al.*, "Subsurface flaw detection in metals by photoacoustic microscopy," *J. Appl. Phys.*, vol. 51, 1152-1156, 1980.)

[4] L. C. Aamodt and J. C. Murphy, "Thermal effects in photothermal spectroscopy and photothermal imaging," *J. Appl. Phys.*, vol. 54, pp. 581-591, 1983. (See also F. A. McDonald and G. C. Wetsel, Jr., "Resolution and definition in thermal imaging," in *Proc. 1984 Ultrasonics Symp.*, 1984, pp. 622-628.)

[5] D. O. Thompson and D. E. Chimenti, Eds., *Review of Progress in Quantitative Nondestructive Evaluation* (vol. 4). New York: Plenum, 1986.

[6] J. F. Gibbons *et al.*, Eds., *Laser and Electron-Beam Solid Interactions and Material Processing*. Amsterdam: North-Holland, 1981.

[7] C. E. Yeack, *et al.*, "Transient photoacoustic monitoring of pulsed laser drilling," *Appl. Phys. Lett.*, vol. 41, pp. 1043-1044, 1982.

[8] R. M. White, "Generation of elastic waves by transient surface heating," *J. Appl. Phys.*, vol. 34, pp. 3559-3567, 1963.

[9] L. S. Gournay, "Conversion of electromagnetic to acoustic energy by surface heating," *J. Acoust. Soc. Amer.*, vol. 40, pp. 1322-1330, 1966.

[10] G. C. Wetsel, Jr., "Thermoelastic wave generation by the heated interface between two media," in *Proc. 1980 Ultrason. Symp.*, 1980, pp. 645-648.

[11] ——, "Ultrasonic-wave generation by photoacoustic absorption in a thin film between two media," in *Proc. 1981 Ultrason. Symp.*, 1981, pp. 810-814.

[12] ——, "Ultrasonic-wave generation by harmonic heating in composite structures," *Appl. Phys. Lett.*, vol. 41, pp. 511-513, 1982.

[13] ——, "Ultrasonic-wave generation by surface and bulk heating in multimaterial structures," in *Acoutical Imaging* (vol. 12), E. A. Ash and C. R. Hill, Eds. New York: Plenum, 1982, pp. 137-145.

[14] G. C. Wetsel, Jr., *et al.*, "Photothermal excitation of elastic waves by 10 ns laser pulses and detection by photoelastic laser-beam deflection," *J. de Physique Coll.*, vol. 44, no. C6, pp. 67-71, 1983.

[15] L. R. F. Rose, "Point-source representation for laser-generated ultrasound," *J. Acoust. Soc. Amer.*, vol. 75, pp. 723-732, 1984.

[16] G. C. Wetsel, Jr., *et al.*, "Optical generation and detection of temporally-narrow wave pulses," in *Proc. Ultrason. Int.* Surrey, UK: Butterworth, 1985.

[17] R. N. Thurston, "Wave propagation in fluids and normal solids," in *Physical Acoustics* (vol. I), Part A, W. P. Mason, Ed. New York: Academic, 1964, pp. 1-110.

[18] C. B. Scruby *et al.*, "Quantitative studies of thermally generated elastic waves in laser-irradiated metals," *J. Appl. Phys.*, vol. 51, pp. 6210-6216, 1980. (See also W. Jackson and N. M. Amer, "Piezoelectric photoacoustic detection: Theory and experiment," *J. Appl. Phys.*, vol. 51, pp. 3343-3353, 1980.)

[19] *Amer. Inst. of Phys. Handbook*, 3rd ed., D. E. Gray, Ed. New York: McGraw-Hill, 1972. (See also *Thermophysical Properties of Matter* (vols. 1, 2, 4, 5, 12, and 13) Y. S. Touloukian, Ed. New York: Plenum, 1970.)

[20] P. M. Morse and K. U. Ingard, *Theoretical Acoustics*. New York: McGraw-Hill, 1968.

[21] A. Rosencwaig and A. Gersho, "Theory of the photoacoustic effect with solids," *J. Appl. Phys.*, vol. 47, pp. 64-69, 1976.

[22] F. A. McDonald and G. C. Wetsel, Jr., "Generalized theory of the photoacoustic effect," *J. Appl. Phys.*, vol. 49, pp. 2313-2322, 1978.

[23] R. M. White, "Elastic wave generation by electron bombardment or electromagnetic wave absorption," *J. Appl. Phys.*, vol. 34, pp. 2123-2124, 1963.

[24] G. Cachier, "Laser excitation of microwave sound in solids," *J. Acoust.*, vol. 49, pp. 974-978, 1971.

[25] Y. Kohanzadhe *et al.*, "Thermoelastic waves generated by laser beams of low power," *J. Acoust. Soc. Amer.*, vol. 57, pp. 67-71, 1975.

[26] A. M. Aindow *et al.*, "Laser-generated ultrasonic pulses at free metal surfaces," *J. Acoust. Soc. Amer.*, vol. 69, pp. 449-455, 1981.

[27] C. B. Scruby *et al.*, "Quantitative studies of thermally generated elastic waves in laser-irradiated metals," *J. Appl. Phys.*, vol. 51, pp. 6210-6216, 1980.

[28] D. A. Hutchins *et al.*, "Laser-generated ultrasound at modified metal surfaces," *Ultrason.*, vol. 19, pp. 103-108, 1981.

[29] R. J. Dewhurst *et al.*, "Quantitative measurement of laser-generated acoustic waveforms," *J. Appl. Phys.*, vol. 53, pp. 4064-4071, 1982.

[30] G. E. Jamieson and G. C. Wetsel, Jr., "Optical-beam-deflection probing of blast waves near solid surfaces," in *Proc. 1985 Ultrason. Symp.*, 1985, pp. 451-456.

[31] G. C. Wetsel, Jr., and J. B. Spicer, "Nonlinear effects in photothermal-optical-beam-deflection imaging," *Canadian J. Phys.*, June 1986.

[32] R. J. von Gutfeld and R. L. Melcher, "20-MHz acoustic waves from pulsed thermoelastic expansions of constrained surfaces," *Appl. Phys. Lett.*, vol. 30, pp. 257-259, 1977.

[33] R. J. von Gutfeld and H. F. Budd, "Laser-generated MHz elastic waves from metallic-liquid interfaces," *Appl. Phys. Lett.*, vol. 34, pp. 617-619, 1979.

Grover C. Wetsel, Jr. (S'56-M'64) was born in Dallas, TX, on August 7, 1935. He received the B.S. degree in electrical engineering from Southern Methodist University in 1958, and the M.A. and Ph.D. degrees in physics from Rice University in 1961 and 1964, respectively.

In 1963-1964, he was Research Engineer and Assistant Professor of Electrical Engineering, The University of Texas, Austin, TX. Since 1964, Dr. Wetsel has been with the Department of Physics at Southern Methodist University, where he is presently Professor of Physics and Chairman of the Department. In 1979-1980, he was on leave in industry working on ultrasonic modulators for ink-jet printers. In 1984-1986, he was on research leave from SMU as Visiting Scientist at the Applied Physics Laboratory and Adjunct Professor in the Department of Materials Science and Engineering, The Johns Hopkins University. His research interests have involved ultrasonic paramagnetic resonance, attenuation and nonlinear effects in microwave ultrasonics, ultrasonic properties of nematic liquid crystals, capillary-wave propagation on liquid jets, and ultrasonic transducer design. Recently, his research has been in photoacoustics, photothermal-optical-beam-deflection imaging, and laser generation of thermal and elastic waves.

Dr. Wetsel is a member of the American Physical Society, the American Association of Physics Teachers, Sigma Xi, and Eta Kappa Nu. He served on the Local Committee and the Technical Program Committee for the 1984 Ultrasonics Symposium.

APPENDIX

PHOTOTHERMAL IMAGING OF DEFECTS IN METALS AND CERAMICS

9. G. C. Wetsel, J. B. Spicer, J. W. Maclachlan, and J. C. Murphy, "Comparison of Photoacoustic and Photothermal Optical Beam Deflection Imaging of Subsurface Structure in Solids," 1985 IEEE Ultrasonics Symposium Proceedings, San Francisco, October 1985.

III, 1.2

COMPARISON OF PHOTOACOUSTIC AND PHOTOTHERMAL-OPTICAL-BEAM-DEFLECTION IMAGING OF SUBSURFACE STRUCTURE IN SOLIDS+

G. C. Wetsel, Jr.*, J. B. Spicer**, J. W. Maclachlan**, and J. C. Murphy

Applied Physics Laboratory
The Johns Hopkins University
Laurel, MD 20707

Abstract

Solid samples with subsurface structure, principally vertical cracks, have been studied using both photoacoustic and photothermal-optical-beam-deflection imaging. Quantitative comparison of images is presented. It was found that the transverse, peaked-on-normal, optical-beam-deflection image most readily sensed microscopic cracks.

I. Introduction

Focused laser beams can be used to locally heat a metallic sample via photothermal conversion. With the use of short-focal-length lenses such as microscope objectives, the heating (pump) laser beam waist can be as small as a few micrometers. Scanning of the pump beam relative to the sample surface makes possible the investigation of the thermoelastic properties of microstructure near the heated surface. Detection of local variations in thermoelastic properties can be accomplished by measuring temperature variations using photothermal optical-beam deflection (PTOBD), e.g., or by measuring variations in the generation of elastic disturbances using a piezoelectric transducer attached to the sample, e.g. Since the limiting factor in definition/resolution is not the thermal diffusion length [1-3], features of the order of the pump beam or smaller in size can be investigated, even at relatively-low pump-laser-beam modulation frequencies.

Important applications of the PTOBD and photoacoustic (PA) techniques include sensing and characterization of metallic interfaces. For example, the spatial extent of the variation of physical parameters in the neighborhood of the grain boundary in high-purity, carefully prepared bicrystals is sufficiently small to require high-definition imaging instrumentation and to severely test the ultimate definition capabilities of PTOBD and PA imaging [4,5]. In order to better understand such interfaces, a sample with a prepared interface has been fabricated for use in comparison of PTOBD and PA images. We report the results of investigations of that sample and another, a compact-tensile sample with a closed crack.

II. Experiment

The PTOBD images are obtained by measuring the deflection of a focused He-Ne probe laser beam using a position sensor. Both normal and transverse components of the deflection are measured. The PA images are obtained by measuring the signal from a piezoelectric transducer attached to the sample. In both cases heating is produced by a modulated, focused, Ar^+ laser beam. Two-spatial-dimensional images are formed by scanning the sample under HP 9836CS computer control [6]. Both in-phase and phase-quadrature signals are simultaneously measured using an EG&G Princeton Applied Research 5301 dual-channel lock-in amplifier. Amplitude and phase images are then constructed using the computer.

The sample (WJ2) with the prepared interface was fabricated from two aluminum alloy plates, each 6.35 mm × 11.4 mm × 25.4 mm. The two plates were lapped and polished on the mating surfaces and then fastened together with screws. The top surface of the assembly was then lapped and polished to a mirror finish. The resulting interface is optically invisible over most of the sample.

The second sample is an aluminum-magnesium alloy compact-tensile specimen with a crack that varies from open to closed. The scans were taken across the closed portion of the crack.

III. Results and Discussion

The amplitude and phase of the transverse PTOBD signal are shown in line scans across the interface of sample WJ2 in Fig. 1. In this case, the transverse signal is "peaked on normal," that is, the probe beam is located at the position for maximal normal-deflection signal and minimal transverse-deflection signal when the pump beam is positioned well away from the interface [7]. With this configuration, the transverse signal will be zero when the scan is over homogeneous material, that is, the homogeneous background signal is zero. In practice, the lock-in amplifier is measuring noise in this configuration, until the scan approaches the interface. The rapid and wide variation in the phase when the scan position is away from the interface is a result of the noise. Near the interface, its resistance to heat transfer across it causes a temperature variation that is wetsel

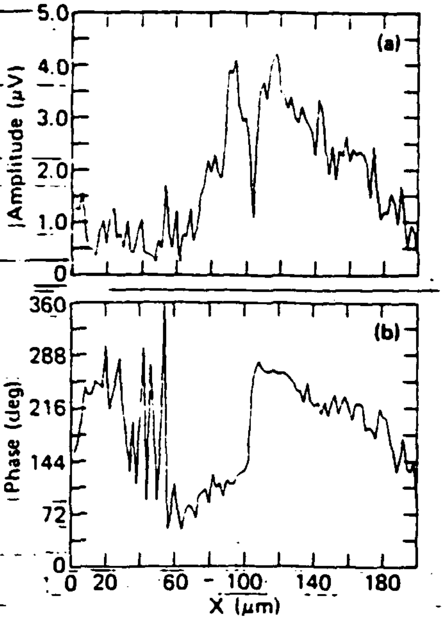

Fig. 1 Transverse, peaked-on-normal PTOBD line scan across sample WJ2 interface, f = 1.04 kHz. (a) Amplitude, (b) phase.

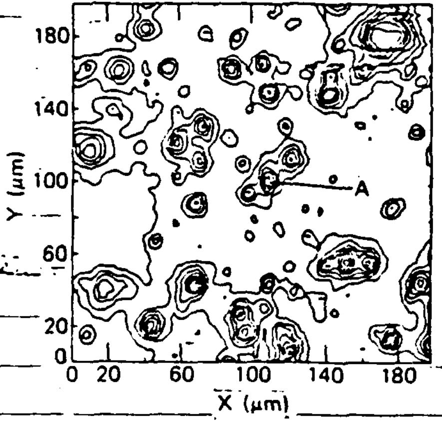

Fig. 2 Normal PTOBD amplitude contour map for sample WJ2 interface, f = 1.04 kHz.

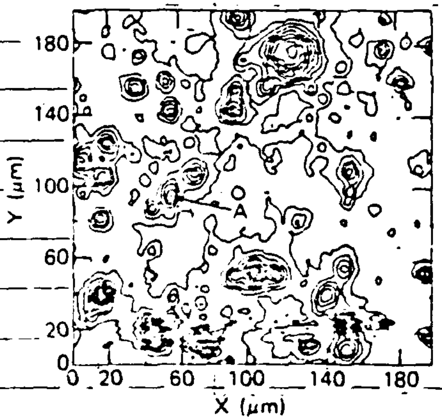

Fig. 3 Transverse PTOBD amplitude contour map for sample WJ2 interface, f = 1.04 kHz.

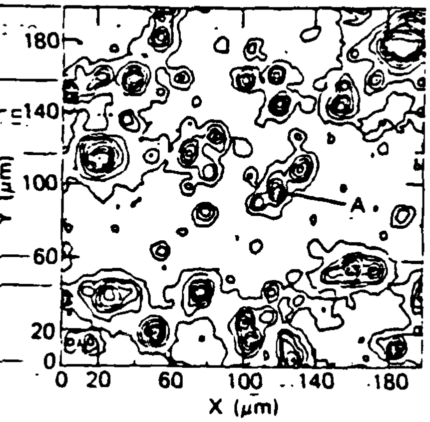

Fig. 4 Attached transducer amplitude contour map for sample WJ2 interface, f = 1.04 kHz.

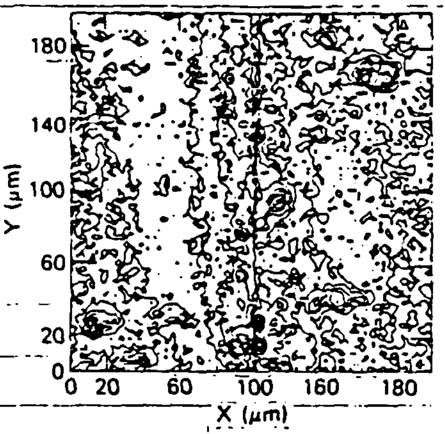

Fig. 5 Transverse, peaked-on-normal PTOBD amplitude contour map for sample WJ2 interface, f = 1.04 kHz.

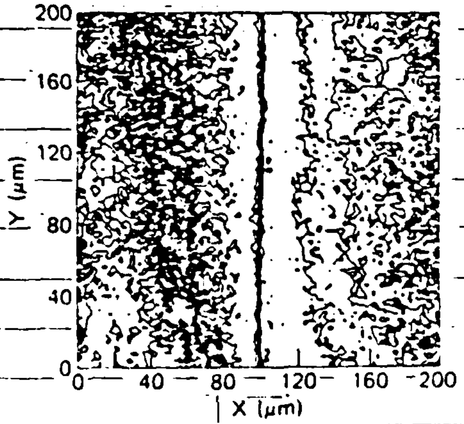

Fig. 6 Transverse, peaked-on-normal PTOBD phase contour map for sample WJ2 interface, f = 1.04 kHz.

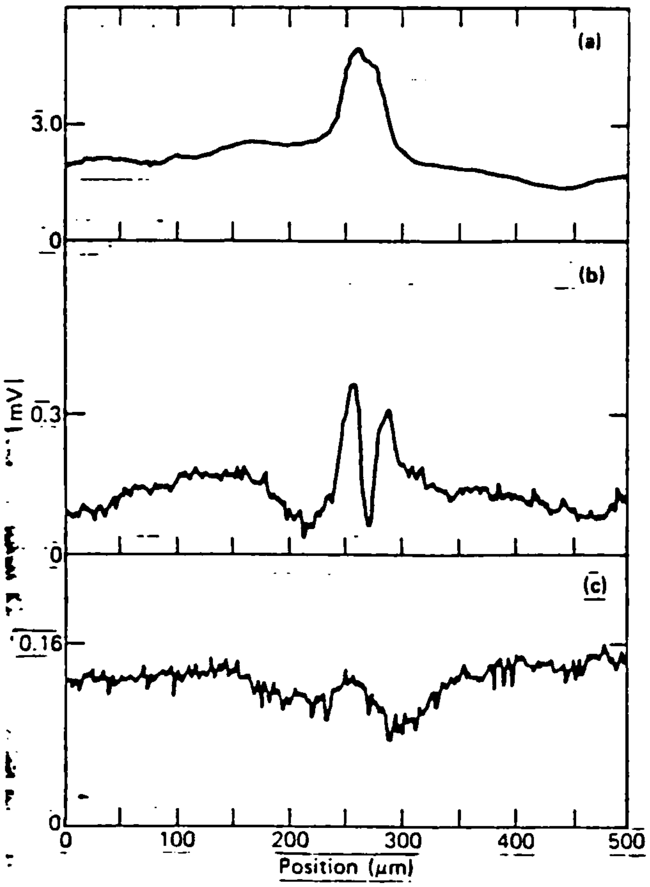

Fig. 7 Amplitude line scans across closed crack in compact-tension sample, f = 750 Hz. (a) Normal PTOBD, (b) transverse, peaked-on-normal PTOBD, (c) attached-transducer.

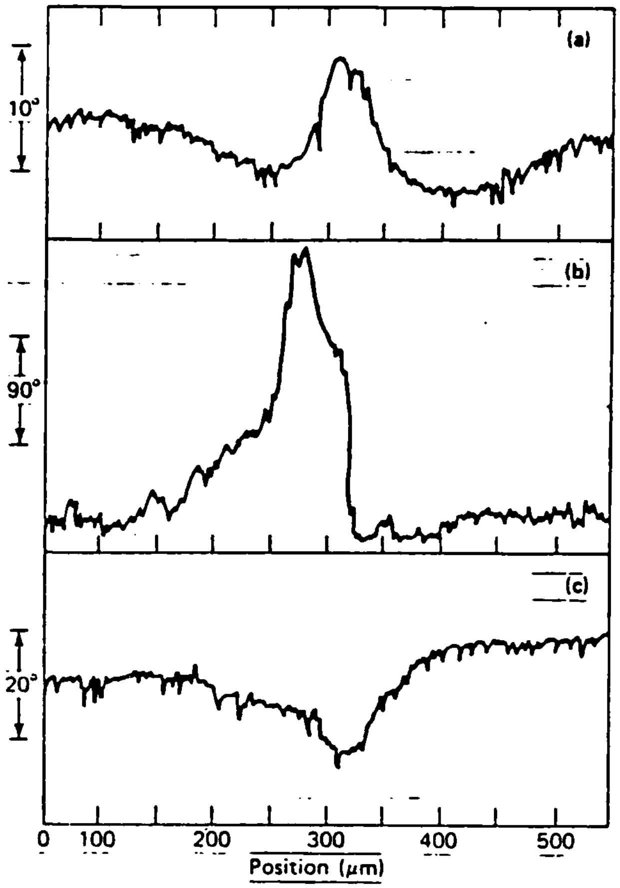

Fig. 8 Phase line scans across closed crack in compact-tension sample, f = 750 Hz. (a) Normal PTOBD, (b) transverse, peaked-on-normal PTOBD, (c) attached-transducer.

characteristic of the interface when the interface is deeper than a thermal-diffusion length, which is the case here. Thus, the characteristic signal of such an interface is illustrated by the double-peak in the amplitude and the 180° phase shift as the scan crosses the interface. This characteristic signal is theoretically understood [5].

Images in the form of a contour map for 200 μm × 200 μm areas of sample WJ2 near the interface are shown in Figs. 2-6 at a frequency of 1.04 kHz. Because the relative positions of probe and pump beam are slightly different in each case, the areas are slightly displaced. However, one can readily identify common features in the images; point A in Figs. 2-4, for example, is the same point on the sample. The features in Figs. 2-4 are most probably due to inclusions in the aluminum alloy [4]. The size and frequency of occurrence of the features correspond to the typical values for the alloy. These inclusions may either be on the surface or subsurface.

It is important to notice that whereas the inclusion signals are apparent in the normal PTOBD, transverse PTOBD, and PA amplitude images of Figs. 2-4, no indication of the interface is observed even though it is located near x=100 μm. However, the interface is observed in the transverse, peaked-on-normal PTOBD amplitude image of Fig. 5. Furthermore, it is spectacularly revealed -- because of the 180° phase shift -- in the transverse, peaked-on-normal PTOBD phase image of Fig. 6. It is particularly important to notice that the interface is revealed in the transverse, peaked-on-normal PTOBD signals even in the presence of strong inclusion signals.

Amplitude and phase line scans across the closed crack of the aluminum-magnesium alloy compact-tensile sample are shown in Figs. 7 and 8 for a frequency of 750 Hz. Some indication of the existence of the crack is observed in both amplitude and phase of the normal PTOBD, transverse (peaked-on-normal) PTOBD, and PA signals. However, again it is the transverse, peaked-on-normal PTOBD signal that gives the clearest indication of the presence of the crack.

In conclusion, vertical interfaces in metals have been studied using PTOBD and PA imaging techniques. It has been found that even microscopic interfaces can be detected and that the transverse, peaked-on-normal PTOBD configuration is particularly useful for this purpose.

We gratefully acknowledge the design and fabrication skills of Mr. Wayne Johnston.

+ This work has been supported in part by the U. S. Army Research Office, Durham, NC.

* Permanent address: Dept. of Physics, Southern Methodist University, Dallas, TX 75275

** Permanent address: Dept. of Materials Science and Engineering, The Johns Hopkins University, Baltimore, MD 21218

1. G. C. Wetsel, Jr. and F. A. McDonald, J. Appl. Phys. 56, 3031 (1984).
2. F. A. McDonald and G. C. Wetsel, Jr., 1984 IEEE Ultrasonics Symposium Proceedings, pp. 622-628, IEEE, New York (1984).
3. F. A. McDonald, G. C. Wetsel, Jr., and G. E. Jamieson, "Spatial Resolution of Subsurface Structure in Photothermal Imaging," to be published in Acoustical Imaging, Vol. 14 (1985).
4. G. C. Wetsel, Jr., J. W. Maclachlan, J. B. Spicer, and J. C. Murphy, "Nondestructive Evaluation and Materials Characterization Using Photothermal-Optical-Beam-Deflection Imaging," to be published in the proceedings of Review of Progress in Quantitative NDE, Williamsburg, VA (1985).
5. F. A. McDonald, G. C. Wetsel, Jr., and G. E. Jamieson, "Photothermal Beam Deflection Imaging of Vertical Interfaces in Solids," submitted for publication in the Canadian Journal of Physics.
6. F. A. McDonald, G. C. Wetsel, Jr., and S. A. Stotts," Scanned Photothermal Imaging of Subsurface Structure," Acoustical Imaging, Vol. 12, pp. 147-155, E. A. Ash and C. A. Hill, Ed., Plenum, London (1982).
7. L. C. Aamodt and J. C. Murphy, J. Appl. Phys. 52, 4903 (1981).

APPENDIX

PHOTOTHERMAL IMAGING OF DEFECTS IN METALS AND CERAMICS

10. J. W. Maclachlan and J. C. Murphy, "Thermal Wave Imaging for Materials Characterizations," Proceedings of 2nd International Symposium on the Non-Destructive Characterization of Materials, Montreal, July 1986, Plenum Press, 1986.

THERMAL WAVE IMAGING FOR MATERIALS CHARACTERIZATION

J. W. Maclachlan and J. C. Murphy

Center for Nondestructive Evaluation &
Applied Physics Laboratory
The Johns Hopkins University
Laurel, MD 20707

INTRODUCTION

Novel techniques for materials characterization and nondestructive evaluation are being continually developed to meet the requirements of examining an ever-increasing range of new materials. A wide range of physical properties and processes are exploited in the current measurement technologies and it is often necessary to match the characterization technique to the materials problem at hand. A very recent addition to the repertoire of materials characterization techniques is thermal wave imaging. This field encompasses a wide range of techniques for exciting and detecting periodic temperature fields or "thermal waves" in solids. The physical probe for this materials characterization technique is heat and thermal wave imaging thus provides information about local variations in sample thermal properties such as the thermal conductivity and the heat capacity. Thermal wave imaging is a developing technique and although the contrast mechanisms can be identified in simple situations, understanding the contrast in thermal wave images for complicated sample geometries and detection schemes is very involved (1). It is readily apparent that many topics of interest in materials science lend themselves well to characterization on the basis of variations in the sample's thermal properties. The examples considered in this paper consider interfaces and show that the measurement of variations in the interruption of heat flow across these interfaces provides an effective means for characterizing the structure of the interface.

BACKGROUND

The basic principles of thermal wave imaging are illustrated in Fig. 1. A heating beam which is modulated in time strikes the sample causing a periodic temperature field to be set up in the solid. The details of this temperature field will depend on the local thermal properties of the sample as well as on the specifics of the interaction of the heating beam with the surface. For example, electrons have a range of 1-10 μm in metals for energies in the range of 5 to 30 keV, while the absorption length for photons is of the order of nanometers. The depth of penetration of the heating source relative to the depth of the thermal structures of interest can be important in determining whether these structures are detected. This has been demonstrated for thermal wave imaging of a semiconductor device using electron beam heating where increasing the interaction depth of the electrons allowed improved detection of subsurface structures (2).

Theoretical modelling of the temperature distribution in the solid involves solution of the thermal diffusion equation subject to the appropriate boundary conditions. In a simple one-dimensional model of a semi-infinite solid with surface heating the solution is of the form:

$$T(x,t) = T_s \exp(-\frac{x}{\delta}) \exp[i(\omega t - \frac{x}{\delta})] \tag{1}$$

where T_s is the surface temperature, x is the distance into the solid and δ is a parameter known as the thermal diffusion length which is given by the expression:

$$\delta = [\frac{2\kappa}{\omega\rho C_v}]^{1/2} \tag{2}$$

where κ is the thermal conductivity, π is the density and C_v is the specific heat capacity. Although Eq. 1 resembles the solution to a wave equation with losses (thus giving rise to the term "thermal wave"), this expression for the temeprature field arises from the solution of a diffusion equation with a periodic source term. The thermal diffusion length, δ, is related to both the "thermal wavelength" and the rate of decay of the thermal waves and is thus a useful unit of measure for discussion of thermal wave measurements.

A number of direct and indirect methods are available for probing the temperature field in the solid and these techniques enable changes in the temperature field to be monitored as the heating beam is scanned over different regions of the sample. Method 1 indicated in the figure is the optical beam deflection or "mirage" technique (3,4). This measurement is based on the development of a "thermal lens" in the air layer just above the sample due to conduction of heat from the sample surface to the gas. The source of this thermal lens is the temperature-dependence of the index of refraction of air. A probe laser beam is then sent through this lens and very small variations in the amount of deflection of the beam are measured by a position sensitive detector. The deflection is given by:

$$\vec{\phi} = \int_p \frac{1}{n} \frac{dn}{dT_g} \nabla T_g \times d\vec{\ell} \tag{3}$$

where n is the gas index of refraction, T_g is the gas temperature, p is the probe beam path over the sample. Two orthogonal probe beam deflections exist, one in the plane defined by the probe ray direction and normal to the specimen surface (normal component) and the second, orthogonal to this plane (transverse component). For all relative positions of the excitation and probe beams, the normal deflection component monitors changes in spcimen temperature while the transverse deflection component monitors the specimen temperature gradient in the direction orthogonal to the probe ray.

The probe beam can also be oriented in a vertical configuraton as indicated by Method 2 in the figure (5-7). The deflection signal now has two components: deflection due to passage through the thermal lens and deflection due to local variation in the sample surface topography due to thermal expansion effects. Thermoreflectance or the thermal modulation of specimen reflectivity may also be a factor in these measurements (8). Photothermal radiometry (Method 3) is another "thermal" method for detection and is based on the enhanced IR emission of a heated object (9,10). The fourth detection method illustrated in Fig. 1 is based on the detection of the displacement generated by the periodic thermal expansion of the sample. This displacement can be monitored using a number of techniques including an attached transducer (11,12) or optical interferometry (13).

The experiments reported here incorporate combined thermal and thermoelastic detection using a system where both optical beam deflection and piezoelectric detection methods are employed. The sample mounted on a piezoelectric transducer (NBS conical transducer) is scanned beneath an argon ion laser pump beam and a helium-neon laser probe beam under computer control and line scans or images can be generated. Both the magnitude and the phase of the normal or transverse component of the optical beam deflection signal or of the piezoelectric signal can be used for imaging. A similar procedure is used for creating thermal wave images using an electron beam for heating. A scanning electron microscope has been modified to allow blanking of the electron beam over the range 0.1 to 500 kHz. The sample is mounted on a piezoelectric transducer and the magnitude or phase of the piezoelectric signal is used in conjunction with the imaging electronics in the SEM to generate both line scans and images.

SUBSURFACE HORIZONTAL BOUNDARIES

The first materials characterization problem to be presented here is the detection of subsurface horizontal boundaries. Two sample geometries

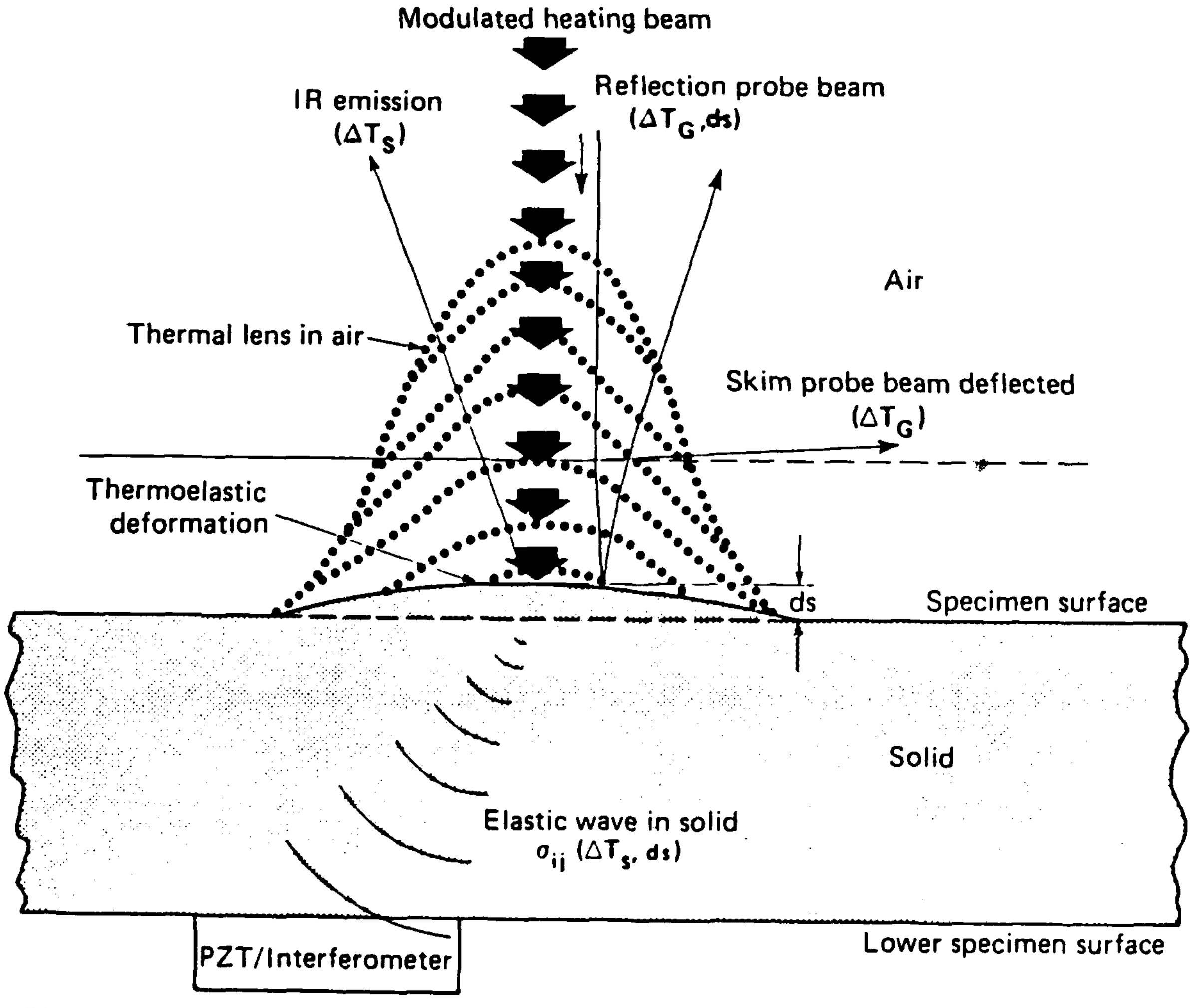

Fig. 1 Schematic representation of the physical processes involved in thermal wave imaging with 4 different detection schemes.

are considered. The buried slant slot sample is a disk of 2024 aluminum, 1 cm in diameter and 3 mm thick containing a slot halfway through the diameter of the sample at an angle of about 17° to the top surface. The buried slant hole sample is a similar disk but with a hole of diameter 1 mm drilled through the disk, also at an angle of about 17° to the top surface. Scans over the tops of these samples allow the examination of defects of ever-increasing depth in the same sample.

Figure 2(a)-(f) show both the magnitude and phase of the normal component of the optical beam deflection signal (NOBD) for the buried slant slot sample. The data is presented in image form in (a) and (b) and in a perspective plot representation in (c) and (d) to better show the func-

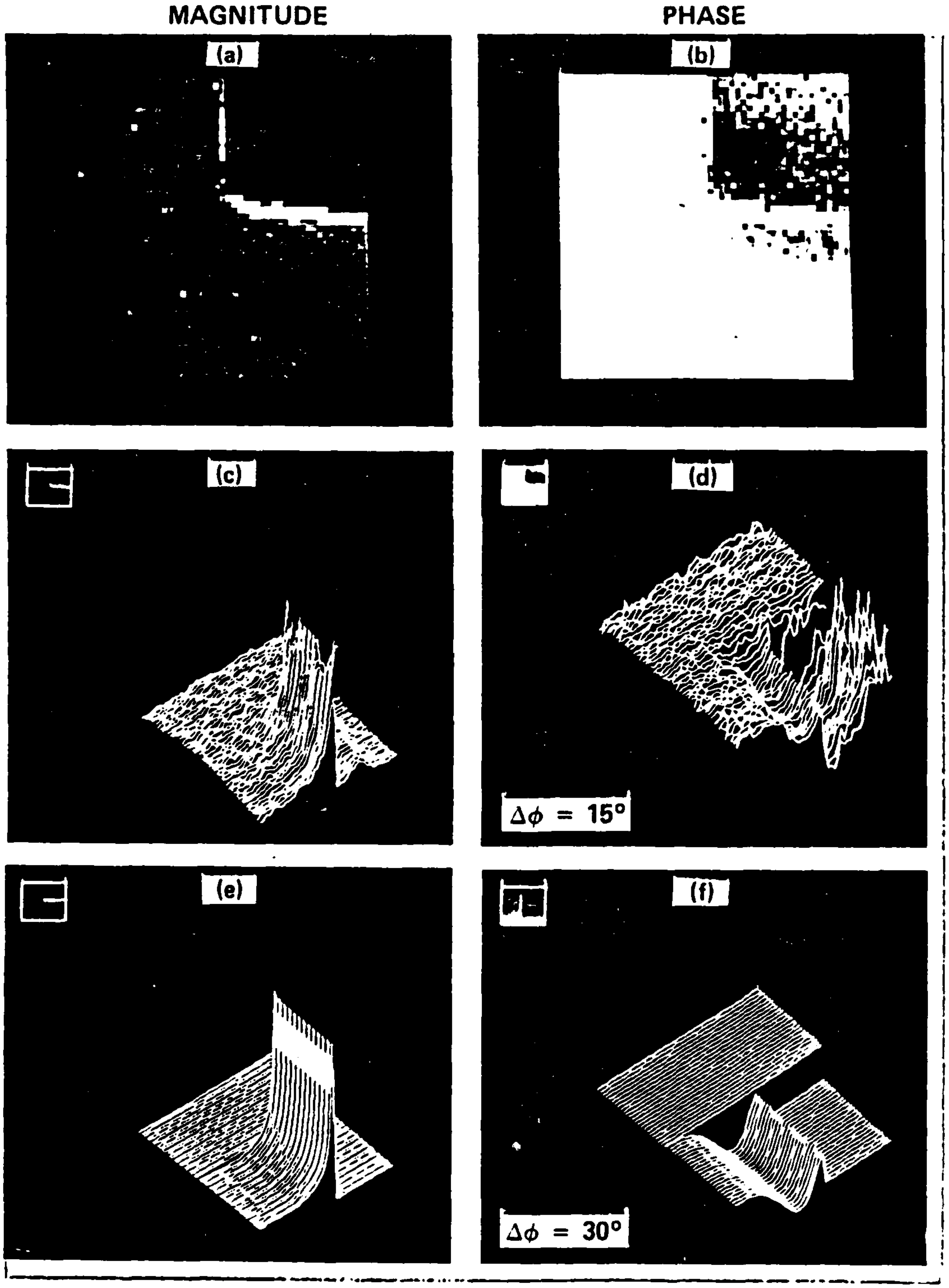

Fig. 2 Experimental (a-d) and theoretical (e-f) magnitude and phase images of buried slant slot using detection by NOBD.

tional dependence of the signal over the slot. The slot is breaking through the surface near the middle of the right hand side of the image and by the bottom of the image the slot has a depth of about 300 µm or about 1.8 thermal diffusion lengths at the modulation frequency of 500 Hz used in this experiment. The results of a one-dimensional calculation of the magnitude and phase of the surface temperature over the buried slant slot are given in (e) and (f) and show a favorable comparison with the experimental data. Although the phase gives indication of the defect to deeper depths than the magnitude, there is very little indication of the presence of the defect when it is greater than 1 to 2 thermal diffusion lengths in depth for detection by a thermal method such as optical beam deflection.

Detection of buried defects using piezoelectric detection is illustrated in Fig. 3. In this experiment the buried slant hole sample has been scanned using both electron beam (Fig. 3(a) and (b)) and laser beam (Fig. 3(c)) excitation at a modulation frequency of about 78 kHz. The results are similar for both excitation methods. The ratio of the defect depth, D to the thermal diffusion length, δ is indicated for each of the line scans in the figure and it is clear that not only does piezoelectric detection allow defects of depth up to 20 thermal diffusion lengths to be detected, but the functional dependence of the piezoelectric signal also changes as a function of depth. The source of this signal shape is under investigation but it is clearly not a scattering of the ultrasonic wave from the hole since the wavelength in aluminum at this frequency is about 70 times the diameter of the hole.

VERTICAL CRACKS

Comparison of three different detection methods, piezoelectric detection and the normal and transverse components of the optical beam deflection are shown in Fig. 4 for a 200 µm by 20 µm scan over a vertical closed crack in an aluminum alloy compact tensile specimen with all measurements made at a laser beam modulation frequency of 750 Hz. Such vertical interfaces can be very difficult to detect with conventional nondestructive testing techniques. Although the crack can be detected in both the magnitude and phase scans for piezoelectric and NOBD detection, the most telling

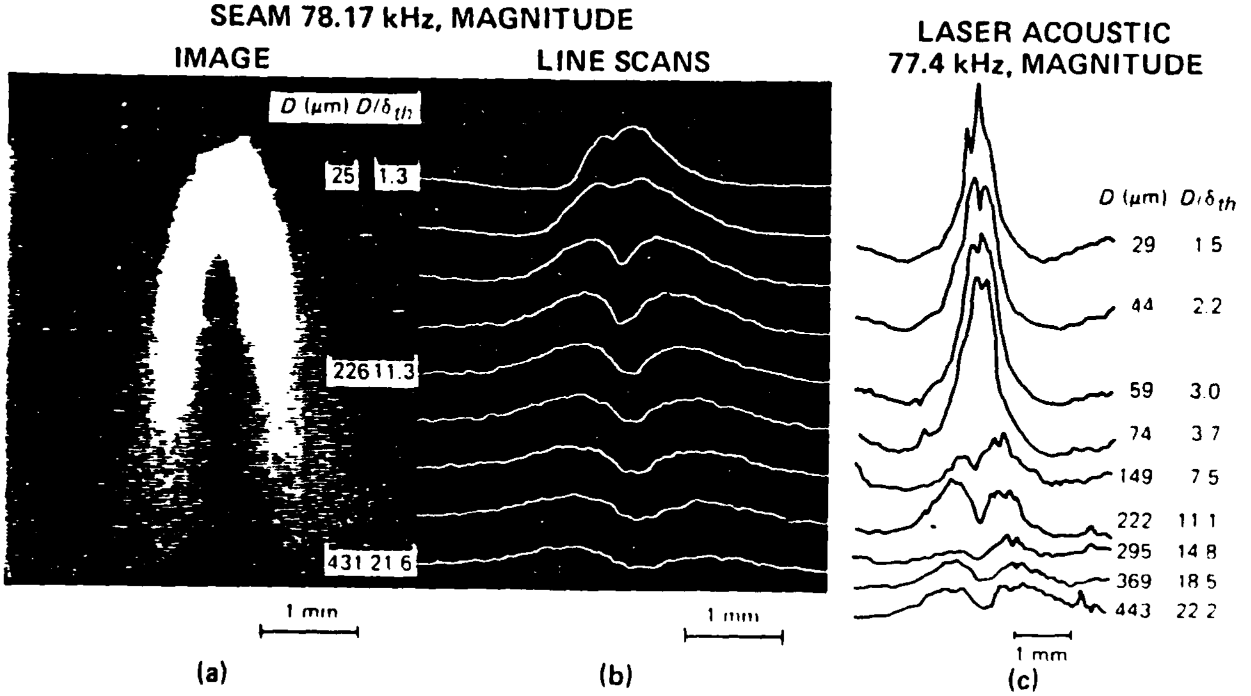

Fig. 3 Thermal wave images of buried slant hole using piezoelectric detection and excitation by (a), (b) electron beam and (c) laser beam.

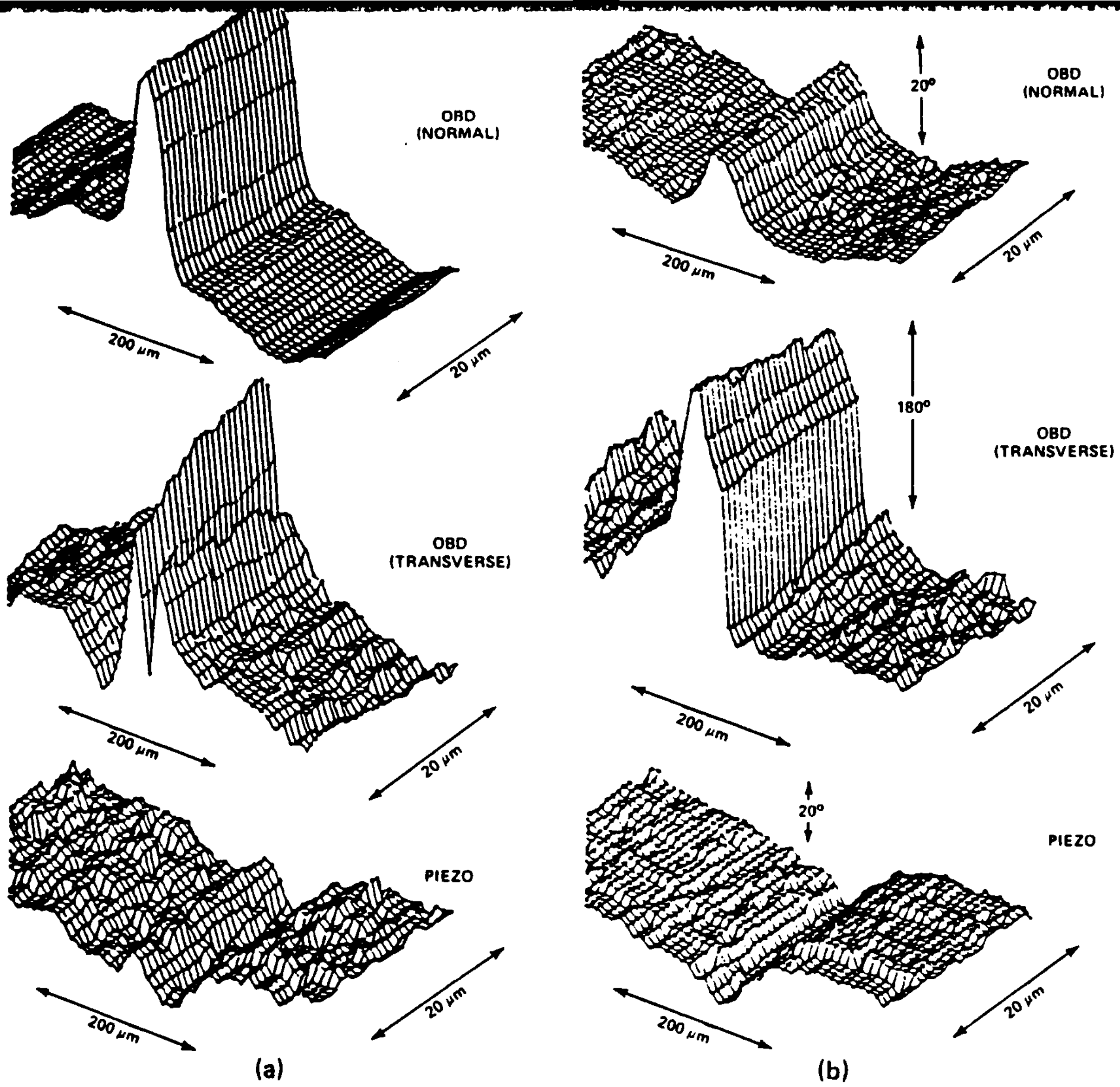

Fig. 4 A comparison of three different detection methods -- NOBD, TOBD and piezoelectric -- for thermal wave imaging of a vertical crack (a) magnitude, (b) phase.

indication of the crack presence is obtained from the double peak in the magnitude and the 180° shift in the phase of the transverse OBD signal. This is expected since the transverse signal monitors the gradient in the temperature distribution in the direction orthogonal to the probe beam direction. A vertical crack effectively interrupts this temperature gradient. The piezoelectric and NOBD signal are more dependent on the actual sample temperature and a crack in a vertical orientation does not have as large an effect on the surface temperature.

CORROSIVE ATTACK OF INCONEL 600

The final sample to be examined here is a specimen of Inconel Alloy 600 with a grain size ranging from 40 to 80 µm which has been subjected to a corrosive environment to produce intergranular attack. Such an attack results in fine cracks along grain boundaries which would be expected to strongly affect heat flow in the sample. Intact grain boundaries have been imaged using thermal wave imaging (14), but the problem in this sample is more similar to the imaging of vertical cracks as described above. Fig. 5

shows both image and perspective plot data for the magnitude and phase of the normal OBD signal at 500 Hz ($\delta \approx 50$ μm) for a scan which covers attacked material on the left and good material on the right. There is a marked difference in signal level between the good and the attacked material for both the magnitude and phase. Also, greater structure is evident in the attacked region, perhaps indicating groups of grains which are separated from other groups of grains. Other scans at higher magnification measuring the transverse OBD component revealed regions in the attacked material with 180° phase excursions, thus indicating the presence of vertical cracks.

CONCLUSIONS

We have presented examples which demonstrate that thermal wave imaging is a viable technique for materials characterization, particularly for the study of interfaces such as horizontal boundaries and vertical cracks. Just as it is often important in other materials characterization techniques to select the appropriate measurement technique for the particular materials problem, it is necessary in a thermal wave measurement to employ methods for excitation and detection of the thermal waves which best suit the material properties and sample geometry of the problem at hand. It has been shown that subsurface defects can be easily detected by optical beam deflection provided they are at a depth of a thermal diffusion length or less. For deeper defects, piezoelectric detection is required.

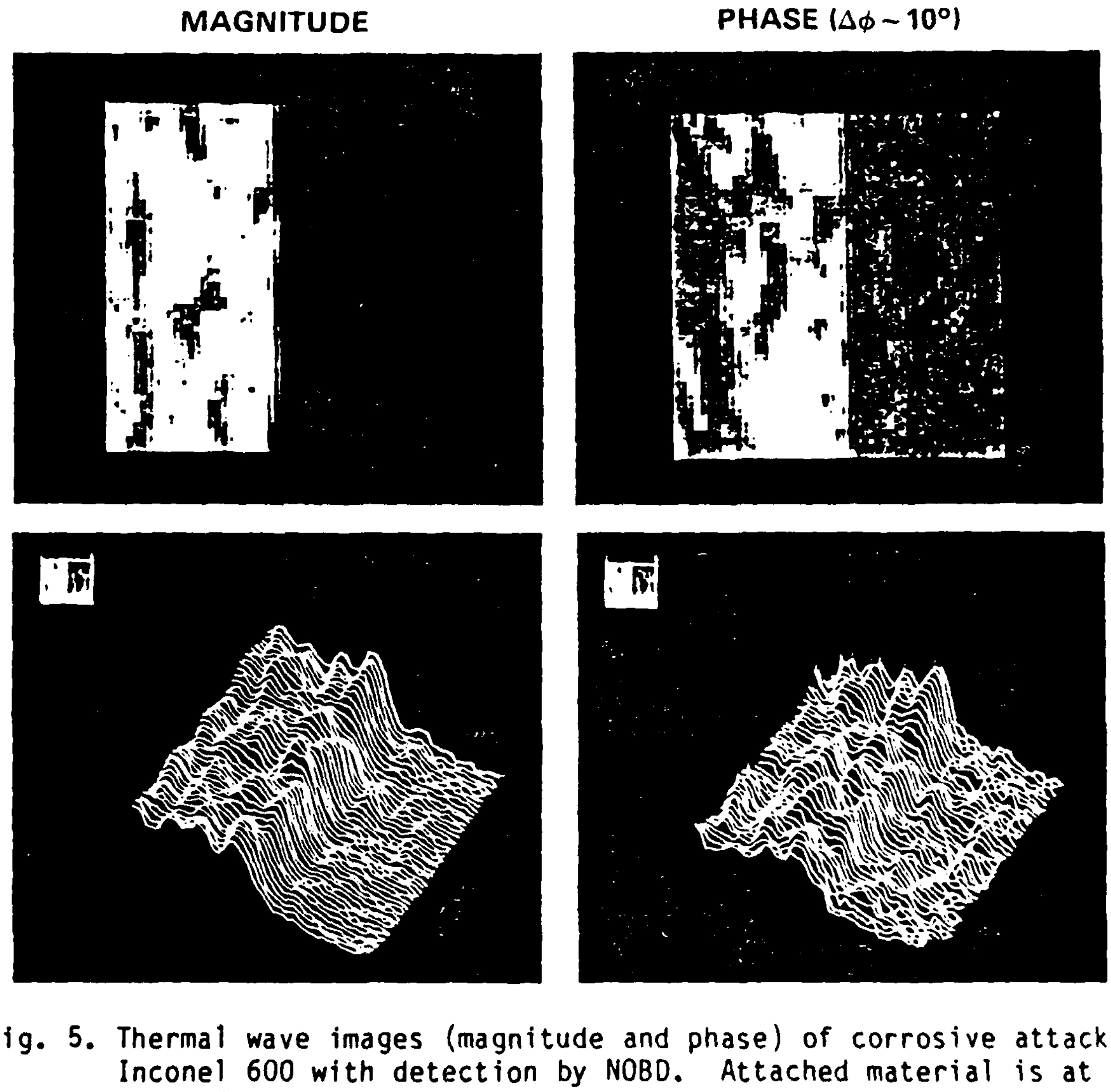

MAGNITUDE

PHASE ($\Delta\phi \sim 10°$)

Fig. 5. Thermal wave images (magnitude and phase) of corrosive attack in Inconel 600 with detection by NOBD. Attached material is at the left of the image and good material is at the right.

ACKNOWLEDGEMENTS

We thank Ed Hackett of NSRDC, Annapolis, MD who provided us with the compact tension specimen and Jack Lareau of Combustion Engineering, Inc., Windsor, CN who prepared the Inconel 600 sample with corrosive attack. The assistance of Maureen Madey with many of the experimental measurements is also gratefully acknowledged. Funding sources for this work included The Johns Hopkins University Center for Nondestructive Evaluation and the U. S. Army Research Office and U. S. Naval Sea Systems Command under Contract No. N00024-85-C-5301. In addition, one of the authors (JWM) was supported by an AAUW International Fellowship.

REFERENCES

1. J. C. Murphy, J. W. Maclachlan, and L. C. Aamodt, Image contrast processes in thermal and thermoacoustic imaging, to appear in IEEE Trans. on Ultrasonics, Ferroelectrics and Frequency Control (1986).
2. J. W. Maclachlan, J. C. Murphy, R. B. Givens, and F. G. Satkiewicz, Linear thermal wave imaging, in: "Proceedings of 11th World Conference on Nondestructive Testing, November 1985, Las Vegas, Nevada, Volume 1," Taylor Publishing Company, Dallas (1985).
3. A. C. Boccara, D. Fournier, and J. Badoz, Thermo-optical spectroscopy: Detection by the mirage effect, Appl. Phys. Lett. 36:136 (1980).
4. J. C. Murphy and L. C. Aamodt, Optically detected photothermal imaging, Appl. Phys. Lett. 38:196 (1981).
5. M. A. Olmstead, N. M. Amer, S. Kohn, D. Fournier, and A. C. Boccara, Photothermal displacement spectroscopy: A new optical probe for solids and surfaces, Appl. Phys. A 32:141 (1983).
6. A. Rosencwaig, J. Opsal, and D. L. Willenborg, Thin film thickness measurements with thermal waves, Appl. Phys. Lett. 43:166 (1983).
7. J. C. Murphy and L. C. Aamodt, Reflective photothermal imaging, J. Physique C6-513 (1983).
8. A. Rosencwaig, J. Opsal, W. L. Smith, and D. L. Willenborg, Detection of thermal waves through optical reflectacne, Appl. Phys. Lett. 46:1013 (1985).
9. P. E. Nordal and S. O. Kanstad, Photothermal radiometry, Physica Scripta 20:659 (1979).
10. G. Busse, Photothermal transmission probing of a metal, Infrared Phys. 20:419 (1980).
11. G. Busse and A. Rosencwaig, Subsurface imaging with photoacoustics, Appl. Phys. Lett. 36:815 (1980).
12. G. S. Cargill, Electron-acoustic microscopy, in: "Scanned Image Micrososcopy" E. A. Ash, ed., Academic Press, London (1980).
13. S. Ameri, E. A. Ash, V. Neuman and C. R. Petts, Photo-displacement imaging, Elec. Lett. 17:337 (1981).
14. J. W. Maclachlan, R. B. Givens, J. C. Murphy, and L. C. Aamodt, Contrast Mechanisms in Scanning Electron Acoustic Imaging of Grain Boundaries, 4th International Topical Meeting on Photoacoustic, Thermal and Related Sciences, Ville d'Esterel, Quebec, Aug. 4-8, 1985.

APPENDIX

PHOTOTHERMAL IMAGING OF DEFECTS IN METALS AND CERAMICS

11. G. C. Wetsel, Jr., J. W. Maclachlan, J. B. Spicer, and J. C. Murphy, "NonDestructive Evaluation and Materials Characterization Using Photothermal-Optical-Beam-Deflection Imaging," Review of Progress in Qunatitative NonDestructive Evaluation, Edited by D. O. Thompson and D.E Chimenti (Plenum Pub. Co), Vol. 5A, p. 713 (1986).

From: REVIEW OF PROGRESS IN QUANTITATIVE NONDESTRUCTIVE
EVALUATION, Vol. 5A
Edited by Donald O. Thompson and Dale E. Chimenti
(Plenum Publishing Corporation, 1986)

NONDESTRUCTIVE EVALUATION AND MATERIALS CHARACTERIZATION USING PHOTOTHERMAL-OPTICAL-BEAM-DEFLECTION IMAGING

G. C. Wetsel, Jr.*, J. W. Maclachlan**, J. B. Spicer**, and
J. C. Murphy

The Johns Hopkins University, Applied Physics Laboratory
Johns Hopkins Road, Laurel, MD 20707

INTRODUCTION

Photothermal-optical-beam-deflection (PTOBD) imaging involves use of a focused, modulated laser beam to locally heat a sample and a second laser beam to probe the resulting changes in sample temperature. For opaque samples, the photothermal heating occurs essentially at the surface and temperature changes in the bulk occur via thermal diffusion to a depth below the surface of the order of a thermal-diffusion length, $\delta = (2\kappa/\rho C\omega)^{1/2}$, where κ is the thermal conductivity, ρ is the density, C is the specific heat, and ω is the modulation frequency. Since the limiting factor in definition/resolution is not the thermal diffusion length [1,2], features of the order of the heating-laser-beam diameter or smaller can be investigated, even at relatively low modulation frequencies. Lateral spatial resolution for subsurface features much closer to the surface than a diffusion length is independent of the diffusion length and is determined principally by the diameter of the heating beam, although the diameter of the probe beam can affect the resolution [1-4]. Generally, the limiting factors on spatial resolution in PTOBD imaging are the heating-beam diameter, the shape and depth of the subsurface feature being imaged, and the modulation frequency (to a lesser extent) [2,4]. This paper presents images of a number of important classes of materials with resolution less than 10 µm. Some contrast issues and underlying materials issues are discussed qualitatively.

The PTOBD images are formed by measuring the deflection of a He-Ne probe-laser beam caused by an Ar^+-laser heating beam scanning the sample [5]. The diameter of the heating beam is estimated to be about 5 µm. The probe beam was unfocused in these experiments and had a diameter of approximately 0.8 mm. Both the amplitude and phase of the normal and transverse deflection signals were measured using an EGG Princeton Applied Research 5301 dual channel lockin amplifier. In this paper these images are presented using a 16 level gray scale. Control of the experiment was provided by a HP 9836C computer [6].

DISCUSSION

PTOBD images of a polished specimen of 2024 aluminum are shown in Figures 1-3. Image detail of a few microns is clearly resolved. This scale is commensurate with the 1 µm step size of the translators moving the

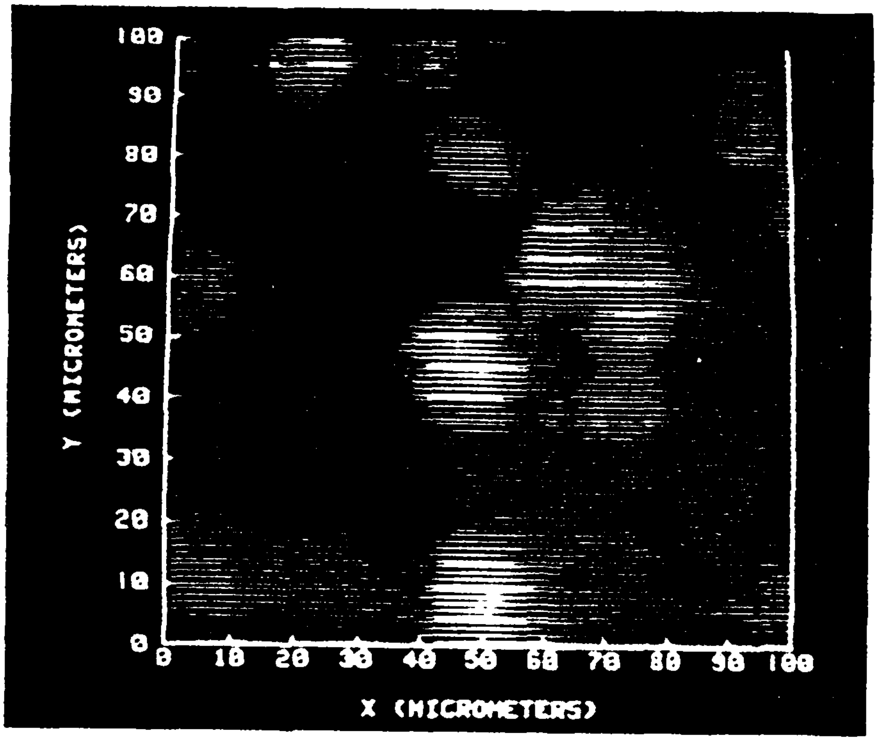

Fig. 1. Normal PTOBD amplitude image of sample of 2024 aluminum, f = 2 kHz.

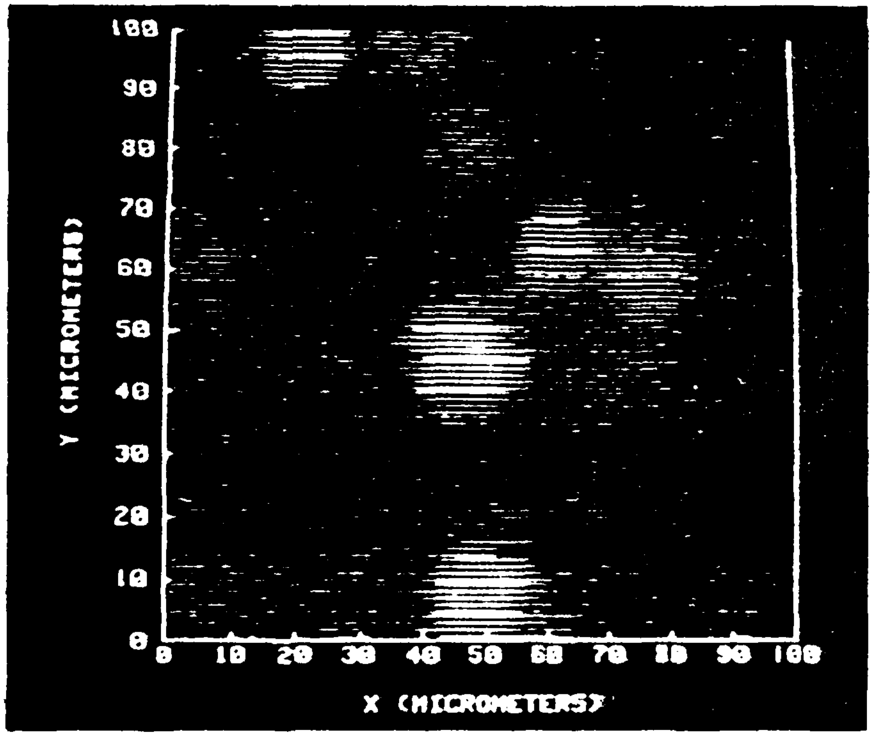

Fig. 2. Normal PTOBD phase image of sample of 2024 aluminum, f = 2 kHz.

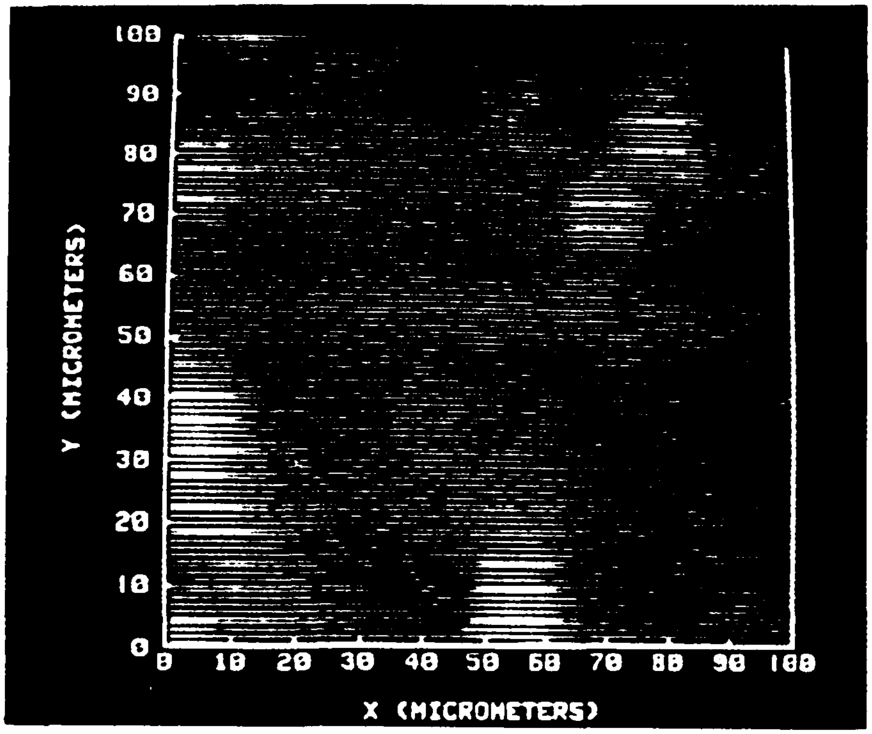

Fig. 3. Transverse PTOBD amplitude image of sample of 2024 aluminum, f = 2 kHz.

specimen and with the estimated diameter of the Ar$^+$ pump beam. Note that since the amplitude image (Fig. 1) and the phase image (Fig. 2) show similar structure, thermal contrast, not optical contrast, is the basis of the images observed. Notice also that the transverse PTOBD image (Fig. 3) is strikingly different from the normal image. Optical and SEM micrographs and SEM/EDAX (energy dispersive X-ray analysis) images have also been made for this sample. They reveal the presence of inclusions associated with iron and manganese impurities within the aluminum matrix. The geometric scale of these inclusions is approximately 10 μm in linear aspect consistent with the PTOBD feature sizes. We tentatively associate inclusions with the PTOBD contrast observed in Figs. 1-3. The issue of how coherent these inclusions are with the matrix has not yet been resolved. This question and the associated question of the relationship of coherency and thermal boundary impedance are important issues for future study. They may be connected with the differences observed between normal and transverse iamges.

Figures 4 and 5 show normal OBD images of a refractory Ni-based alloy covered with a diffusion-bonded aluminum coating. Again, the images show micrometer-scale thermal features as well as features which, while of the same geometric size, are clearly of optical origin. The microstructural basis of the PTOBD image features has not been unambiguously determined at this time. However, SEM micrographs of the interface of other samples in this series indicate that the coating penetrates the substrate with long "fingers" whose cross-section approximates 10 μm. The size of these features of the interface corresponds to the image features observed and suggests that the thermal features in the PTOBD image are representations of the subsurface fingers.

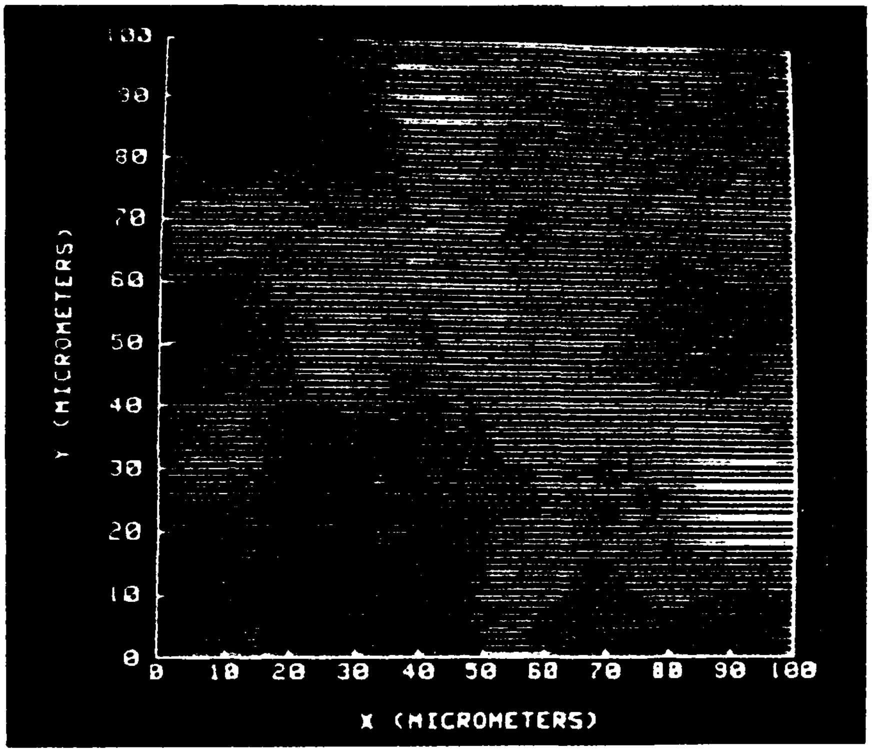

Fig. 4. Normal PTOBD amplitude image of sample with diffusion-bonded coating, f = 500 Hz.

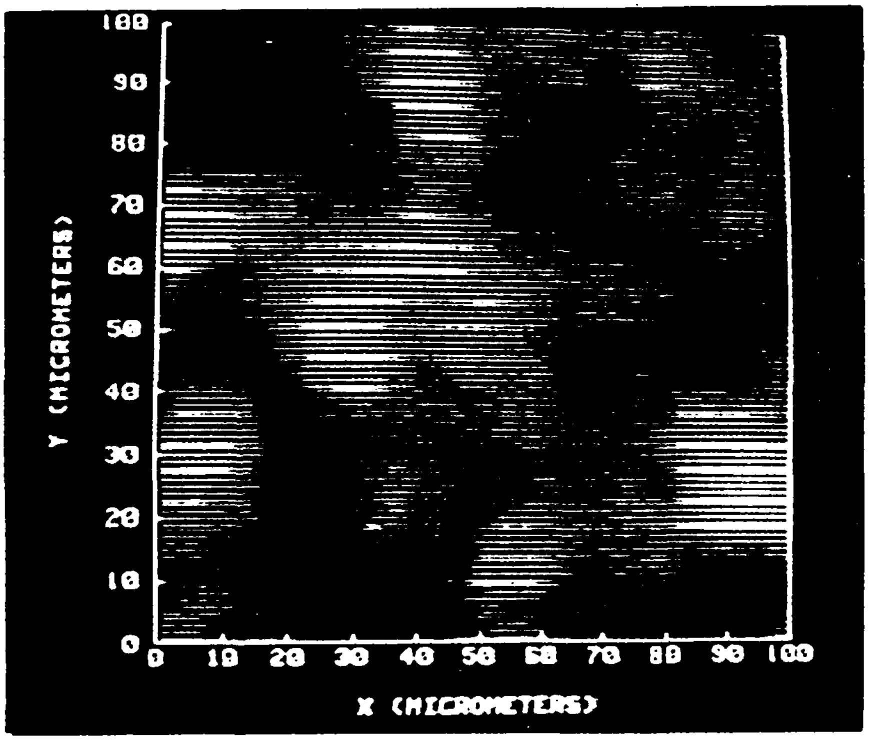

Fig. 5. Normal PTOBD phase image of sample with diffusion-bonded coating, f = 500 Hz.

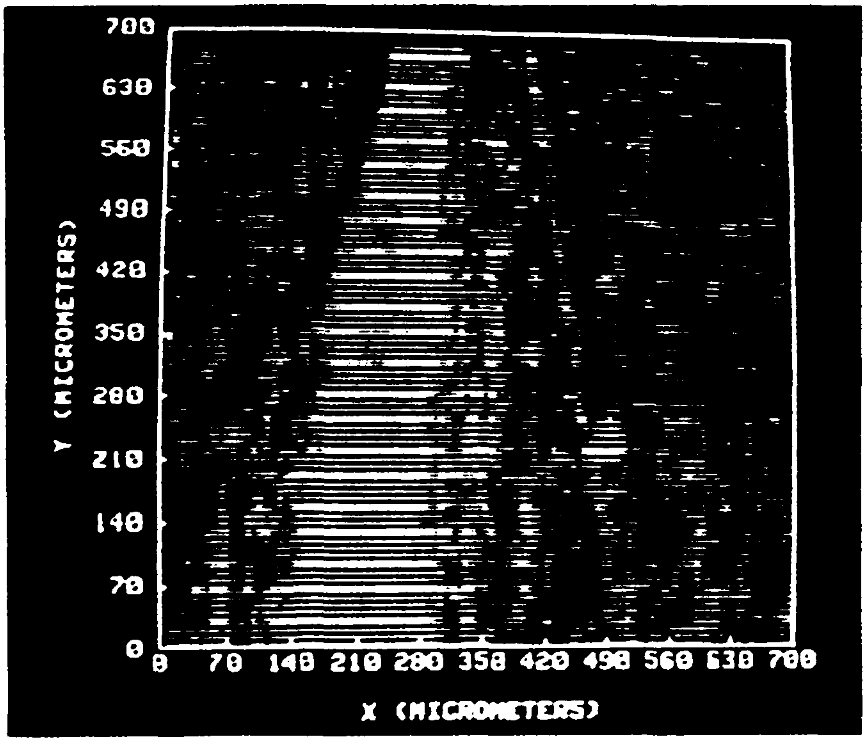

Fig. 6. Normal PTOBD amplitude image of sample of graphite-aluminum composite material, f = 200 Hz.

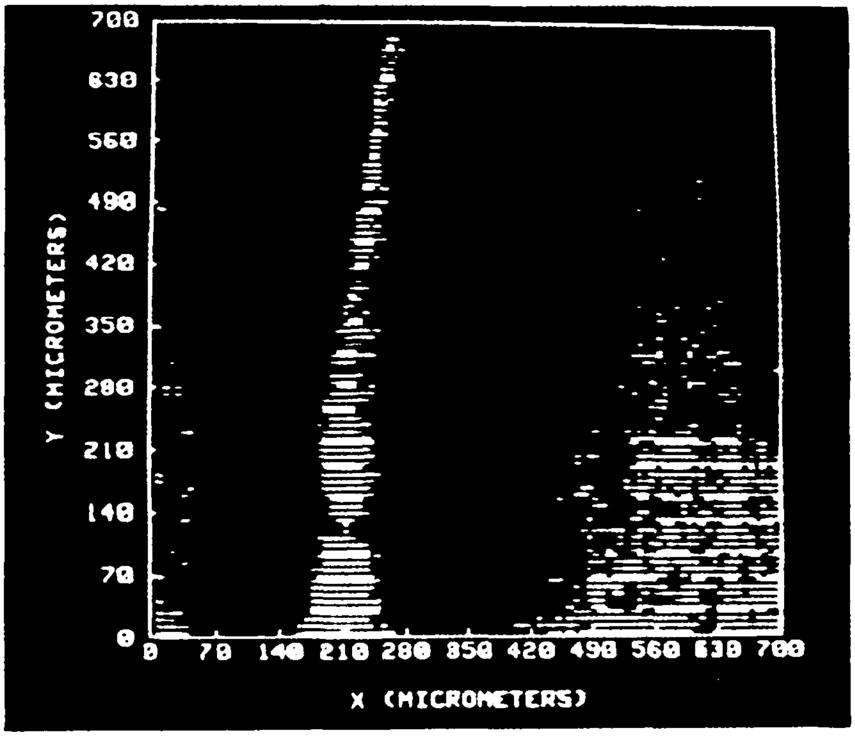

Fig. 7. Normal PTOBD phase iamge of sample of graphite-aluminum composite material, f = 200 Hz.

Normal-deflection PTOBD amplitude and phase images of a unidirectional graphite aluminum composite are shown in Figures 6 and 7. This specimen had breaks in the aluminum coatings parallel to the fiber direction which presumably occurred through differential contraction during fabrication. In the PTOBD images contrast is seen at the break and in regions on either side of the visual break. The extension of the PTOBD contrast beyond the visual region may be related to changes in the fiber-aluminum bond caused by stress. In other studies on this material using scanning electron acoustic techniques (SEAM), periodic "puckers" were observed on a line orthogonal to the break direction. These also suggested local regions of directed internal stress. In the SEAM experiments the largest break opening was coincident with the location of the "puckers".

As a final example of PTOBD applications, Figure 8 is a transverse deflection scan of a grain boundary in a high-purity aluminum bicrystal. The sample was grown from the melt using two separated seeds. The resulting crystals were allowed to have a common interface in the melt at a point above the seeds. X-ray topographic analysis has shown that each region is single crystalline with some substantial lattice distortion occurring at points parallel to the grain boundary. For the PTOBD studies, the specimen was first mechanically polished and subsequently chemically polished. The sample was intentionally somewhat overetched to make the boundary visible for image registration purposes. The scan shown in Figure 8 represents 200, 1.6 micron steps. For this case a focused probe beam was used with estimated diameter of 0.07 μm.

Figure 8 shows an amplitude minimum at the grain boundary. On either side of the boundary there are relative maxima whose amplitudes depend weakly on frequency in the range 250-4000 Hz. Similar results were obtained for the normal PTOBD scans. This signal variation is characteristic of the temperature dependence predicted for a thermally insulating plane

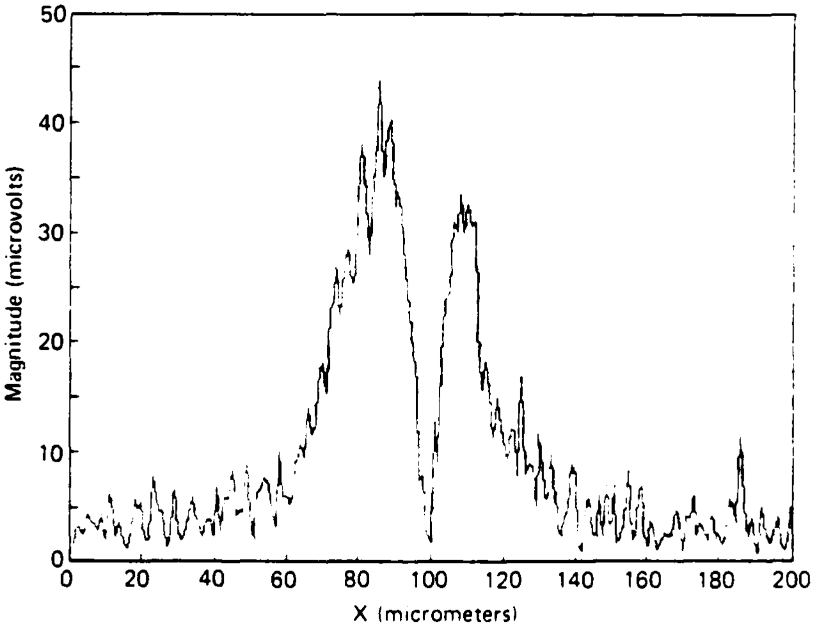

Fig. 8. Transverse PTOBD amplitude vs. X for aluminum bicrystal in neighborhood of grain boundary, f = 2 kHz

perpendicular to the sample surface that inhibits heat flow parallel to the surface of the sample. For a scanned point excitation source, a temperature increase on either side of the insulating boundary occurs [2] as the source approaches the boundary. Both normal and transverse scans also show evidence of subsurface structure. Similar evidence of near boundary structure has been developed in SEAM imaging of the same specimen. Significantly, the PTOBD signal varies in amplitude along the interface. On occasion the boundary is not observed. This is in contrast to the SEAM scans where the boundary is always seen, although with varying spatial signature. This suggests that the observed PTOBD signal is associated with spatial variations in the thermal impedance of the grain boundary, possibly related to the presence of lattice deformation or to impurities at the interface. It then appears that a modification of the temperature distribution by thermal properties associated with the interface between two crystals has been observed. However, the contrast between the PTOBD and acoustic detection imaging methods leaves questions of the nature of the mechanisms yet unresolved.

In summary, PTOBD methods are sensitive, relatively high resolution probes of specimen microstructure which are applicable to a wide range of specimens.

REFERENCES

* Permanent address: Department of Physics, Southern Methodist University, Dallas, TX 75275
** Permanent address: Department of Materials Science and Engineering, The Johns Hopkins University, Baltimore, MD 21218

1. G. C. Wetsel, Jr. and F. A. McDonald, J. Appl. Phys. 56, 3081 (1984).
2. F. A. McDonald and G. C. Wetsel, Jr., "Resolution and Definition in Thermal Imaging," 1984 IEEE Ultrasonics Symposium Proceedings, pp. 622-628, IEEE, New York (1984).
3. L. C. Aamodt and J. C. Murphy, J. Appl. Phys. 52, 4903 (1981).
4. F. A. McDonald, G. C. Wetsel, Jr., and G. E. Jamieson, "Spatial Resolution of Subsurface Structure in Photothermal Imaging," in Acoustical Imaging, Vol. 14, Plenum, London (1985).
5. L. C. Aamodt and J. C. Murphy, Appl. Opt. 21, 111 (1982).
6. F. A. McDonald, G. C. Wetsel, Jr., and S. A. Stotts, "Scanned Photothermal Imaging of Subsurface Structure," Acoustical Imaging, Vol. 12, pp. 147-155, E. A. Ash and C. R. Hill, Ed., Plenum, London (1982).

APPENDIX

PHOTOTHERMAL IMAGING OF DEFECTS IN METALS AND CERAMICS

12. John C. Murphy, Leonard C. Aamodt, Frank G. Satkiewicz, R.Ben Givens, and P. Ronald Zarriello, "Materials and Microstructure," Johns Hopkins APL Technical Digest, Vol. 7, pp. 187-199 (1986).

JOHN C. MURPHY, LEONARD C. AAMODT, FRANK G. SATKIEWICZ,
R. BEN GIVENS, and P. RONALD ZARRIELLO

MATERIALS AND MICROSTRUCTURE

A knowledge of the microstructure of electronic materials and devices as well as structural materials is a key factor in understanding their properties. Thermal wave imaging is a relatively new technique that provides images that display microstructural features; it also allows local material properties to be measured. The technique has been used to locate localized defects (such as subsurface cracks and voids) in metals and ceramics and to study grain structure in metals. Contrast mechanisms in imaging are discussed, and various thermal wave techniques are described and compared.

INTRODUCTION

New materials with special properties have played a prominent role in the history of human civilization. Epochs entitled the Stone, Iron, and Steel Ages (and perhaps now the Silicon Age) give a sense of the impact these developments have had on human affairs. What is sometimes overlooked is that the elemental composition of these materials defines their properties only to a limited extent. Cast iron and steel, for example, can have the same elemental composition yet have significantly different properties because of the special grain structure present in steel that arises from the processes of heat treatment and metalworking used in its formation. Microstructure can determine macroscopic properties.

Fiber-matrix composites and crystalline ceramics provide another example. Here two or more distinct materials are brought together in a controlled structure to produce a final product with properties measurably different from those of either of the starting constituents. Again, microstructure determines macroscopic properties at the price of complex spatial variations in sample properties across the specimen. Conversely, microstructural failure of the fiber-matrix bond in the composite or microcracking in the ceramic implies failure of the larger structure.

Semiconductors provide a final example. Here, device performance is jointly determined by specimen properties; intentional structure is provided by circuit architecture, and unintentional structure is represented by processing defects, dislocations, grain boundaries, and other flaws in the base material. As the scale of electronics continues to shrink, the role of microstructure will continue to grow. For some structured materials now under development, ordering occurs at the atomic or molecular level, and the question of microstructural control becomes more important.

THERMAL WAVE IMAGING

Our everyday experience with the diffusive nature of heat suggests that temperature is an unlikely tool for studying microstructure; nevertheless, temperature patterns produced by modulated heating provide an excellent way to study the local properties of many solids and to study specimen microstructure as well.

Thermal wave imaging refers to a family of methods that uses time-varying changes in sample temperature to study the local properties of solids.[1-3] The modulated sample temperature is produced by a modulated excitation source that is scanned over the specimen surface. An image, obtained by monitoring some temperature-dependent property during the scan, provides information about the optical, electronic, structural, and thermal properties of the specimen. In addition, when particle beams such as electron and ion beams are used for excitation, the image contains information about the nature of the beam-specimen interaction, including possible nonthermal interactions.

Figure 1 illustrates some basic features of thermal wave imaging. A time-varying energy beam incident on the sample is fractionally absorbed and converted to heat with a consequent rise in specimen temperature. The modulated temperature changes a number of specimen properties, and several of these can be used to determine both the volume and surface temperature. Members of the family of thermal wave imaging methods are classified by the physical property used for detection and by the source used for excitation. Several detection methods are schematically represented in Fig. 1; their characteristics are summarized in Table 1. Specific features of the methods illustrated will be discussed later. For now, note that the images obtained on a given sample using different detection methods can differ radically even though they are initiated by the same temperature change. The reason lies in the role of the thermal parameter being detected and its effect on image contrast. The issue of image contrast is basic to the use of thermal wave imaging methods as quantitative tools for materials characterization and nondestructive evaluation of materials. The quantitative interpretation of image data is currently one of the important research topics in the field.

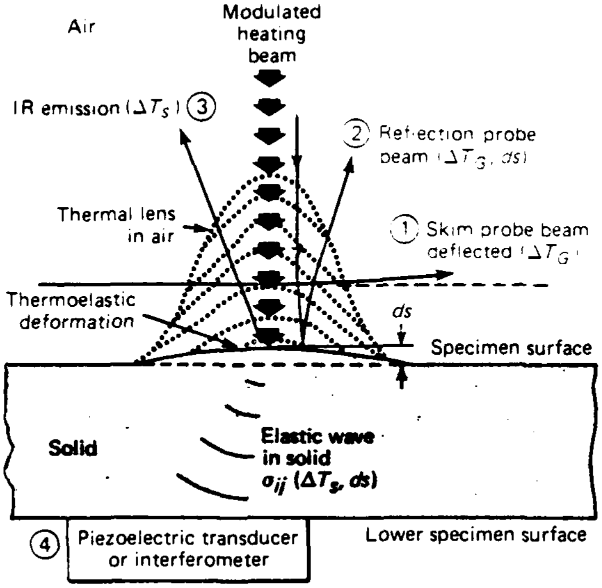

Figure 1—Composite sketch summarizing several thermal wave imaging methods: (1) optical beam deflection, (2) reflective optical beam deflection, (3) infrared radiometric, (4) thermoelastic (transducer or interferometric). (T_G is the gas temperature.)

THEORETICAL BACKGROUND

For an elastic solid illuminated by a modulated excitation source, the temperature and elastic displacement are determined by the two coupled thermoelastic equations,[4]

$$\nabla^2 T - \alpha^{-1}\, \partial T/\partial t = -H/\kappa + (T\,\beta_t B/\kappa)\, \nabla \cdot \partial \mathbf{u}/\partial t \tag{1}$$

$$\nabla^2 \mathbf{u} + (1 + \lambda/\mu)\, \nabla\, (\nabla \cdot \mathbf{u}) - (\rho/\mu)\, \partial^2 \mathbf{u}/\partial t^2 = (\beta_t B/\mu)\, \nabla T\,, \tag{2}$$

where T is the temperature, $\mathbf{u}$ is the elastic displacement vector, κ is the thermal conductivity, α is the thermal diffusivity, β_t is the volume thermal-expansion coefficient, λ and μ are the Lamé constants, ρ is the density, and B is the bulk modulus. H is the thermal source term, which in general varies throughout the volume of the specimen. The specific form that H assumes depends on the source and the nature of the beam-specimen interaction. (No mechanical source term is assumed.)

Equation 1 is the heat equation that governs heat flow within the sample. The final term on the right-hand side of the equation represents the heat produced by elastic motion of the specimen; in many cases, it can be neglected. With that term omitted, the equations are partly decoupled, and the specimen temperature can be found by solving Eq. 1 alone without knowledge of the elastic displacement field. Equation 2, on the other hand, is the thermoelastic equation; therefore, the thermal expansion term on the right-hand side is the only source term present and cannot be omitted. Based on this analysis, the dynamic thermal imaging methods represented in Fig. 1 can be divided into (a) purely thermal imaging methods based exclusively on the solution to Eq. 1 and (b) thermoelastic methods using attached transducer detection or interferometric detection based on Eq. 2. Solution of Eq. 2 assumes that solutions of Eq. 1 are known.

"THERMAL" THERMAL IMAGING

A complete analysis of imaging using focused laser or particle beams requires the solution of Eqs. 1 and 2. For purely thermal imaging, however, the basic physical principles underlying the relationship between modulated temperature, heat flow, and materials properties can be visualized using a one-dimensional model. In one dimension, Eq. 1 becomes

Table 1—Characteristics of thermal wave imaging detection methods.

		Mechanism		*Detection*		
Method	*Temperature monitored*	*Major mechanism*	*Diffusion dependent*	*Type of localization*	*Scalar or vector*	*Effect measured*
Photoacoustic	Surface	Thermal	Yes	Nonlocalized	Scalar	Gas pressure
Optical beam deflection	Surface	Thermal	Yes	Line	Vector	Refractive index
Reflective optical beam deflection	Surface	Thermal and mechanical	Yes	Point	Vector	Local surface distortion
Piezoelectric transducer	Bulk	Thermo-elastic	No	Point	Scalar	Stress waves
Infrared radiation	Surface	Thermal	Yes	Point	Scalar	Optical emission
Interferometric	Bulk	Thermo-elastic	No	Point	Scalar	Surface motion

$$\partial^2 T/\partial z^2 - \alpha^{-1}\partial T/\partial t = -H(z,t)/\kappa\ , \qquad (3)$$

where $H(z,t) = H_0 \exp(-\beta z) \exp(j\omega t)$. This choice of H applies to the specific case of optical or laser illumination and for specimens with optical absorption followed by a rapid conversion to heat. Other forms of H are appropriate for ion or electron beams and for samples such as semiconductors with long carrier lifetimes. When energy storage and migration occur outside the thermal system, the analysis must also be modified to include these effects.[5,6]

Figure 2 shows a sample specimen mounted on a transparent substrate, with its top face in contact with air. In each region, α is constant. Under these conditions, the surface temperature is

$$T(z{=}0) = T_s = \frac{\delta(\beta\delta)}{\kappa}$$

$$\times \left[\frac{1}{1+\beta\delta} + \frac{2\Gamma \exp(-2d/\delta)}{1+\Gamma\exp(-2d/\delta)}\ \frac{\beta\delta}{1-\beta^2\delta^2}\right], \quad (4)$$

where $\delta = \sqrt{\alpha/j\omega}$ is the complex thermal diffusion length and

$$\Gamma = \left(\frac{\delta}{\kappa} - \frac{\delta_s}{\kappa_s}\right) \Big/ \left(\frac{\delta}{\kappa} + \frac{\delta_s}{\kappa_s}\right)$$

describes the thermal mismatch with the substrate at the interface (s indicates substrate). Note that the relative optical absorption spectra, $\beta(\bar{\lambda})$, can be found by measuring T_s when $d/\delta > 1$ and $\beta\delta \ll 1$. In this case,

$$T_s = (\delta^2/\kappa)\ \beta(\bar{\lambda})\ . \qquad (5)$$

By sweeping through a range of excitation beam wavelengths, $\bar{\lambda}$, an optical spectrum can be obtained. Since Eq. 5 is valid even for a sample with no light transmission, the optical spectra of opaque materials can be obtained as well as the spectra of other materials such as gels, pastes, and highly scattering materials that cannot be studied using conventional optical techniques. This is the basis of photoacoustic spectroscopy.

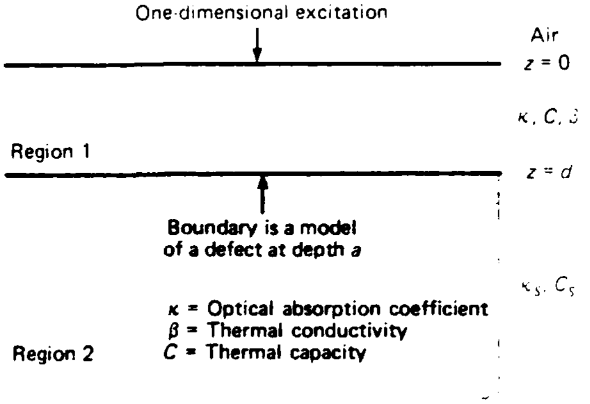

Figure 2—Cross-sectional view of layered sample.

When $\beta\delta > 1$ and $d/\delta > 1$, $T_s = \delta/\kappa$, and it is independent of β. In this "photoacoustic saturation" regime, T_s depends principally on the thermal properties of the sample, C and κ. It also depends on microstructural features such as cracks, voids, and grain boundaries, which inhibit heat flow. To illustrate this, assume that a void exists at $z = d$. For a void, $\kappa_s C_s \approx 0$ and $\Gamma = -1$. If the sample is also opaque, ($\beta d \gg 1$) and

$$T(z{=}0) = T_s = \frac{\delta}{\kappa}\left[1 + \frac{2\exp(-2d/\delta)}{1-\exp(-2d/\delta)}\right]. \qquad (6)$$

As is apparent in Eq. 6, the presence of the void at $z = d$ affects ($T(z{=}0)$) only when $d/\delta < 1$. As δ changes with the modulation frequency, ω, it is possible to vary δ/d above and below 1 and hence to change T_s based on the location of the lower boundary layer. This is an example of the depth profiling ability of thermal wave imaging. Experimental examples of depth sensing are presented later. Note that lateral thermal boundaries associated with surface breaking cracks and grain boundaries can show effects similar to those discussed here for depth profiling when a focused exciting beam is used.[7] This will be illustrated later for grain boundary contrast. Also, under the same conditions,

$$T(z) = \frac{\delta}{\kappa}(\beta\delta)\left\{\frac{e^{-z/\delta}}{1+(\beta\delta)^2} + \frac{e^{-\beta z} - e^{-z/\delta}}{1-(\beta\delta)^2}\right.$$

$$\left. + \frac{\Gamma e^{-2d/\delta}}{1+\Gamma e^{-2d/\delta}}\left[\frac{2\beta\delta\ e^{-z/\delta}}{1-(\beta\delta)^2} + \frac{e^{z/\delta} - e^{-z/\delta}}{1-\beta\delta}\right]\right\} \quad (7)$$

if $\beta d \gg 1$. This result applies to thermoelastic imaging experiments where bulk temperature is important.

THERMOELASTIC IMAGING FUNDAMENTALS

Two thermal wave imaging methods designated in Fig. 1 use piezoelectric transducers or optical interferometers to detect specimen strain produced by modulated thermal expansion. This process is described in principle by the solution of Eq. 2 for the displacement $\mathbf{u}(\underline{r},t)$, assuming that T is known from Eq. 1 and that appropriate elastic boundary conditions are also known. This problem has not been solved for the general case of continuous wave excitation. However, some analysis is available in special cases.

Certain features of the problem are immediately evident. First, the elastic displacement, $\mathbf{u}(\underline{r},t)$, depends on the elastic properties and structure of the specimen as well as on thermal properties. The relative importance of thermal and elastic contrast mechanisms in the image formation process is an important current topic for study. Second, elastic waves are generated throughout the sample wherever temperature gradients exist. These waves propagate to the surface with little differential phase delay, since the wavelength of sound waves is longer than the sample size for the modulation frequencies used for thermal wave imaging. Hence, the source of the elastic effects measured by the piezoelectric transducer or interferometric detector is that portion of the sample volume where the modulated temperature is large.

Thermoelastic imaging can also detect a buried layer in an opaque specimen. Both $T(z)$ and $T(z=0)$ depend on the layer depth, d, in Fig. 2 by means of Eqs. 4 and 7. The bulk temperature is more sensitive to the presence of the buried subsurface layer than the more distant surface temperature, T_s; hence we should expect thermoelastic imaging to show greater sensitivity to subsurface objects then purely thermal imaging. This expectation has been confirmed.

After generation, the acoustic wave propagates through the sample and is reflected by elastic boundaries and interfaces. This elastic microstructure contributes to the image contrast in addition to the thermal microstructure. In fact, thermoelastic imaging has been compared in some of its features to high-frequency (> 400 kilohertz) acoustic microscopy where only elastic contrast is present.[8] The detail revealed in the images makes this a potentially powerful method if a detailed analysis can be developed to obtain quantitative data about specimen properties.

OVERVIEW OF IMAGING METHODS

Table 1 summarizes some of the detection methods used for thermal wave imaging. The three major thermal methods—photoacoustic, optical beam deflection, and infrared imaging—measure different specimen parameters but ultimately monitor T_s, the specimen surface temperature. The types of localization possible with the three methods differ. The photoacoustic technique measures the temperature integrated over the entire specimen surface, with localization being entirely dependent on the use of a localized excitation source such as a focused laser or particle beam. The optical beam deflection technique measures components of the temperature field along the path of the probe rays, a process discussed in more detail in the following section. The infrared technique is in principle a point technique, while in practice it measures infrared emission over a small region of the sample. All three have approximately equal sensitivity in that they can detect modulated temperature changes of 10^{-3}°C or less.

Figure 3 shows the optical beam deflection process in greater detail and the temperature pattern produced in the gas layer in thermal contact with the specimen. The probe laser beam passes through the temperature region somewhat off the center of the exciting beam and is deflected by the time-modulated thermal lens produced by the thermally induced index of refraction gradient in the air above the sample surface. The beam deflection can be decomposed into components normal or transverse to the sample surface. The normal component is maximum when the probe and exciting beams intersect and has been shown to be proportional to the sample surface temperature.[9] The transverse component, on the other hand, is null when the probe and excitation beams intersect, reversing sign at that point. This component has been shown to be proportional to the specimen temperature gradient perpendicular to the probe ray in the plane of the sample. The transverse optical beam deflection signal is particularly useful in studying sample heterogeneity. For a radially symmetric source and a homogeneous sample, the surface temperature is symmetric, and the transverse signal is null when the probe and excitation beams intersect. However, a thermal boundary in the plane of the specimen breaks the thermal symmetry and causes the transverse deflection near the boundary to appear as a signal against a null background.

The variant of the optical beam deflection process labeled 2 in Fig. 1 (the reflective optical beam deflection)

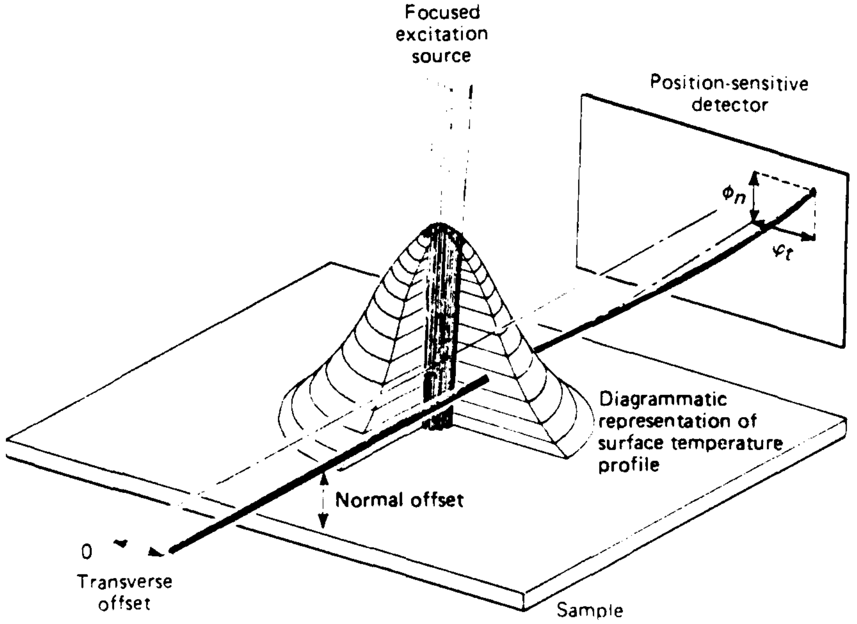

Figure 3—Schematic of the optical beam deflection imaging method showing the two deflection components mentioned in the text.

has elements of both thermal and thermoelastic imaging. In this method, the probe beam strikes the sample and is reflected. The ray path of the reflected ray is deviated by the thermal lens as in optical beam deflection imaging and also by the thermoelastically induced curvature of the surface.

The thermoelastic imaging methods measure specimen elastic response at points away from the point where heating occurs. The delay time for elastic wave propagation from source to detector is much faster than thermal diffusion times. Hence, the range of modulation frequencies that can be used in thermoelastic experiments ($20 < f < 10^6$ hertz) is much greater than in optical beam deflection and other thermal imaging ($20 < f < 10^4$ hertz). The image formation time for thermoelastic imaging is shorter than purely thermal imaging; in addition, some improvement in resolution is possible because of the smaller values of δ and the resultant reduced lateral thermal spreading.

EXPERIMENTAL THERMAL IMAGING

Figure 4 shows a system used to obtain simultaneous optical beam deflection and piezoelectric transducer images. The acousto-optic modulator allows amplitude and position modulation of the beam from the argon laser. For the ordinary case of harmonic modulation, the magnitude and phase of both detected signals are available from the lock-in amplifier for imaging. When thermal effects are important, the phase signal offers the advantage that incidental changes in specimen reflectivity do not contribute to the measured signal and that phase delays associated with thermal diffusion can be measured directly. Sample motion using a computer-controlled *x-y* stage allows scanning of the exciting beam relative to the sample. The probe beam retains a fixed position relative to the exciting beam in this configuration. The experiment was designed to explore differences in image contrast between the two methods. Since optical beam deflection detection is thermal while piezoelectric transducer detection is thermoelastic, the images should show characteristic differences if elastic contrast effects are important.

Figure 5 shows optical beam deflection and piezoelectric transducer magnitude images of a sample of the aluminum alloy 2024-T.[10] The specimen was fabricated to study the effect of lateral thermal impedance on image contrast. Two aluminum sections were cut, lapped, polished, and then joined along their polished faces by clamping. The top and bottom faces that contained the line of joining were also polished so that (except at the specimen edges) the joint was not seen in a standard normal incidence image taken with a scanning electron microscope. The width of the joined region estimated from scanning electron microscope images at the sample edges was approximately 2 micrometers.

Most features seen in the normal optical beam deflection image (Fig. 5c) and the piezoelectric transducer image (Fig. 5d) are metallic inclusions formed of elements present in the alloy. The close similarity of the two images suggests that elastic contrast is unimportant for this experimental condition. The inclusions are less evident in the transverse amplitude image (Fig. 5a) and absent in the transverse phase image (Fig. 5b). The images suggest that the inclusions are thermally coupled to the matrix, since little phase delay occurs. Other aluminum alloy specimens, especially those where fatigue processes have occurred, show large phase contrast at inclusions, presumably because of inclusion-matrix disbonding and poor thermal contact. A second conclusion is that the interface is made visible in the transverse deflection images because it inhibits thermal flow and influences the component of the temperature gradient perpendicular to the boundary. The scalar temperature images show no evidence of a boundary.

In a related experiment, cracks produced in notched tensile specimens of a naval aluminum alloy by tensile loading were studied. In regions where incomplete closure of the crack occurred, both normal and transverse components were seen; but where closure occurred, only the transverse component showed the presence of the

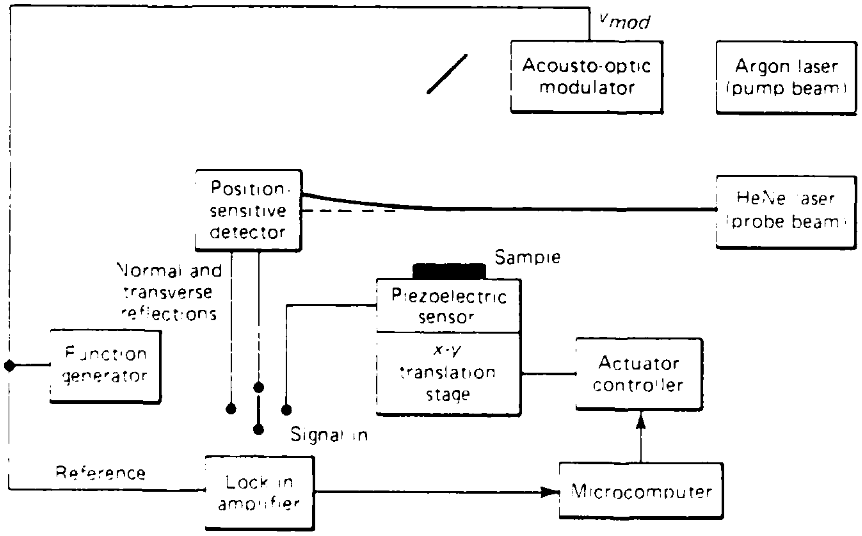

Figure 4—Block diagram of laser source optical beam deflection and acoustic imaging system.

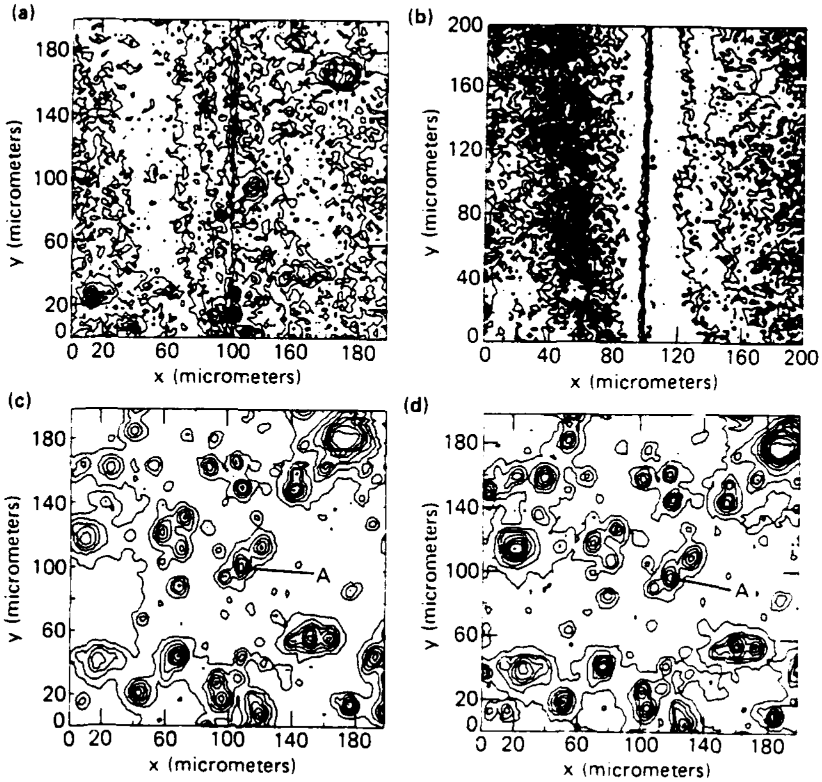

Figure 5—Contour images of a fabricated crack sample: (a) transverse magnitude, (b) transverse phase, (c) normal magnitude, and (d) piezoelectric transducer magnitude. Inclusions are seen in (a), (c), and (d) and the crack only in (a) and (b), as discussed in the text.

thermal boundary. This is consistent with the results obtained on the fabricated sample. In addition, some evidence of a plastic zone ahead of the crack tip was seen. This region is predicted by the theory of fracture mechanics; it is important for studies of the mechanisms of crack advance and, hence, failure of materials.

Another example, which compares piezoelectric transducer and optical beam deflection imaging and shows some of the depth-sensing abilities of these methods, appears in Fig. 6. The sample was an aluminum cylinder containing a 1-millimeter hole drilled subsurface at an angle of 15 degrees to the surface so that the depth of the hole varied with location on the sample. No evidence of the hole was present on the illuminated sample surface. Each line scan crossed the centerline of the buried hole at a different depth. The signal decreased approximately exponentially with hole depth for both optical beam deflection and piezoelectric transducer imaging. However, the exponential constant was approximately one thermal diffusion length for optical beam deflection imaging and two thermal diffusion lengths for piezoelectric transducer detection. These results are consistent with the analysis, which showed that optical beam deflection images are proportional to T_s, while piezoelectric transducer images sense a portion of the volume temperature field. The sample will be discussed again later in connection with electron beam and ion excitation.

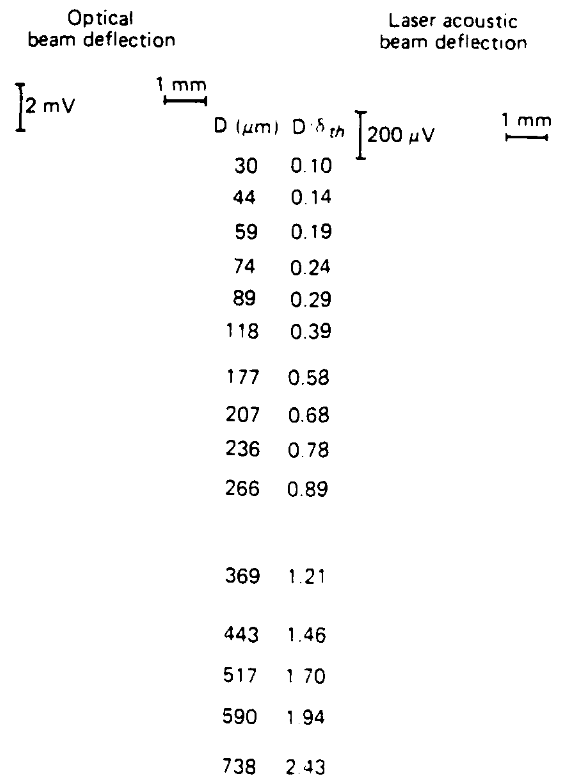

Figure 6—Laser acoustic and laser optical beam deflection line scans of the slant hole sample.

ELECTRON AND ION EXCITATION

Electron and ion beams can be used as thermal imaging sources. Figure 7 is a block diagram of the instrumentation used for these studies. The electron source is a modified ETEC scanning electron microscope, where beam blanking plates have been installed in the electron column to modulate the beam current. With this modification and a piezoelectric transducer detector attached to the specimen, it becomes a scanning electron acoustic microscope. The ion imager is a modified scanning ion mass spectrometer that also uses electrostatic beam blanking plates for modulation. In both cases, a piezoelectric transducer is used for detection.

Depth Profiling/Contrast Mechanisms in Aluminum

Figure 8 is a scanning electron acoustic microscope image of the slant hole sample described in the previous section obtained at ≈70 kilohertz.[11] For reference, line [illegible] obtained using a laser source at the same modulation frequency are also shown. Because the modulation frequency is much higher than in the prior data, the thermal diffusion length is proportionately smaller.

In the electron image, D represents the depth of the hole. Two regions are seen. Near the top of the image, $D < \delta$, and thermal contrast dominates the image, which shows the interaction of the modulated temperature with the hole. However, at the bottom of the figure, where $D >> \delta$, contrast due to the hole is still seen. The contrast cannot be thermal. Instead, it is likely that this region demonstrates the role of elastic contrast in image formation. Both ion and electron sources give virtually the same results. The similarity of the electron and laser scans suggests that for metals such as aluminum, thermoelastic signal generation processes dominate and other nonthermal beam-specimen interactions are relatively unimportant.

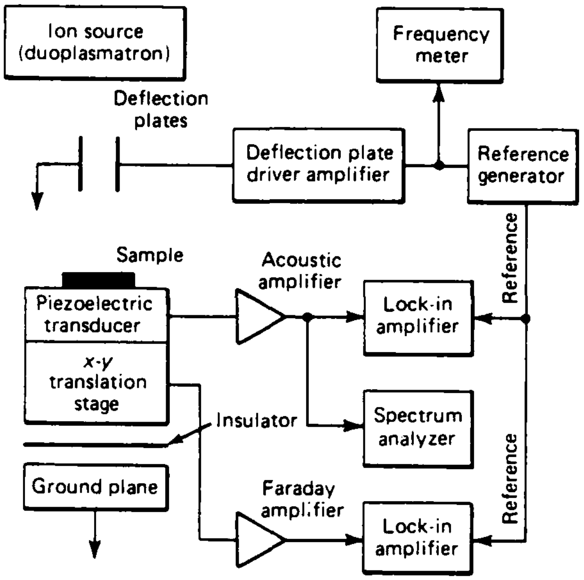

Figure 7—Block diagram of electron or ion acoustic detection system showing simultaneous detection of specimen current.

Grain Structure

Comparative scanning electron microscopy and scanning electron acoustic microscope experiments show that grain boundary structure can be observed in metals. Figure 9 shows a polycrystalline aluminum sample. The scanning electron microscope image is on the left, and the scanning electron acoustic microscope image is on the right. The contrast mechanisms are clearly differ-

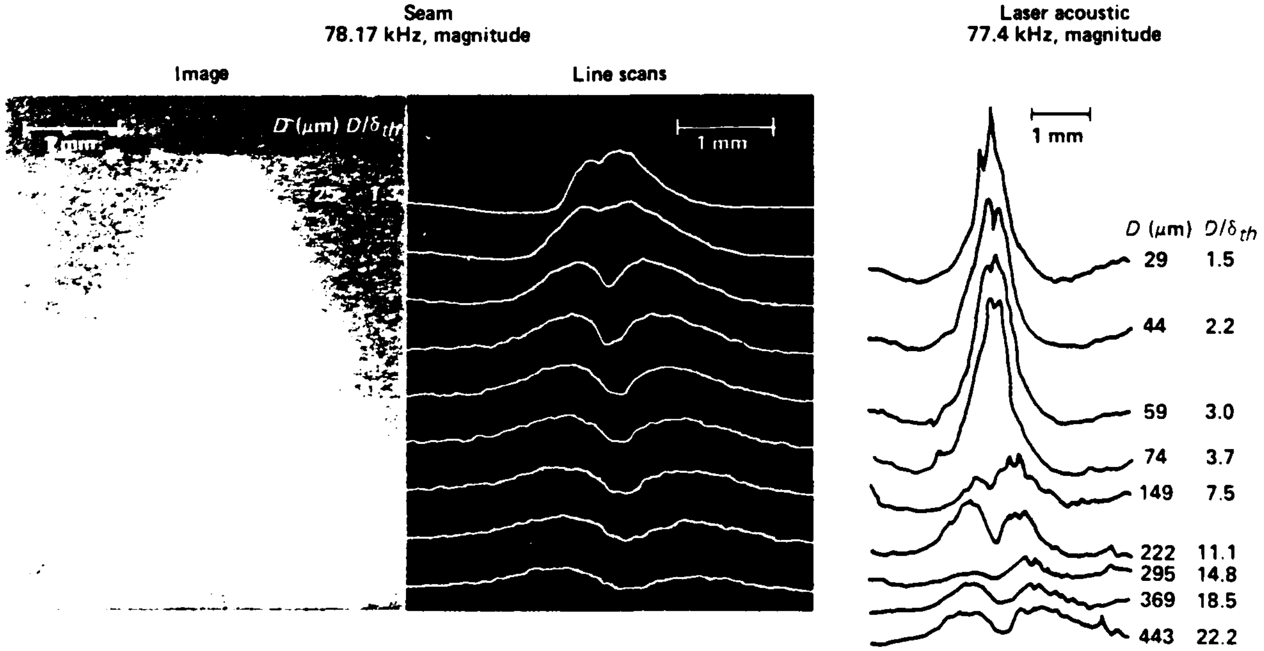

Figure 8—Electron acoustic image and line scans of slant hole sample. Laser acoustic line scans are also seen. Particle and laser excitation yields similar specimen response.

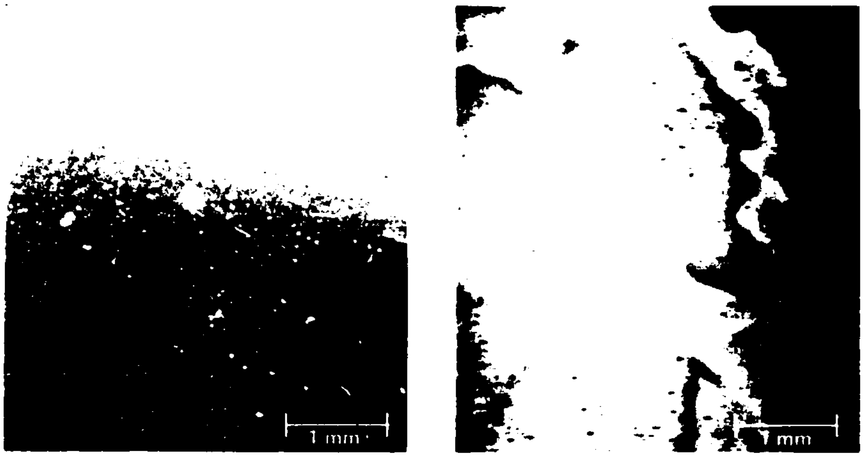

Scanning electron image **Acoustic magnitude image**

Figure 9—Electron acoustic image of grains in high-purity aluminum. Note the presence of contrast at the grain boundaries and between the interiors of grains.

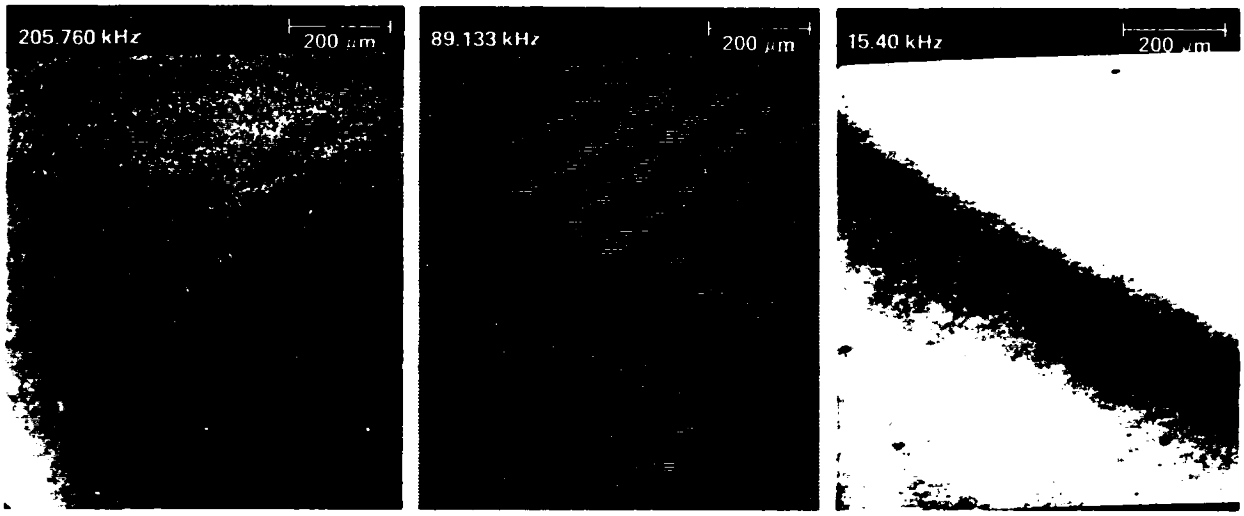

Figure 10—Grain boundary images of aluminum grains as a function of modulation frequency. The width varies as $1/\sqrt{\omega}$.

ent. Even within the scanning electron acoustic microscope image, it is possible to distinguish between contrast that occurs at the grain boundary and contrast that occurs between grains. Considering only contrast at grain boundaries, Fig. 10 shows scanning electron acoustic microscope images at various modulation frequencies, and Fig. 11 shows the dependence of the apparent boundary width on modulation frequency. This width varies as $1/\sqrt{\omega}$, a result consistent with the dependence expected for thermal contrast mechanisms where the thermal diffusion length $|\delta| = \sqrt{2\alpha/\omega}$. Figure 12 is an overlay of scanning electron acoustic microscope line scans on a scanning electron microscope image taken at fixed modulation frequency. On the right-hand side of the boundary, the amplitude of the scanning electron acoustic microscope signal varies exponentially with distance at a rate consistent with the modulation frequency. The picture relates features of the line scans of the scanning electron acoustic microscope with the grain boundary shown by the scanning electron microscope.

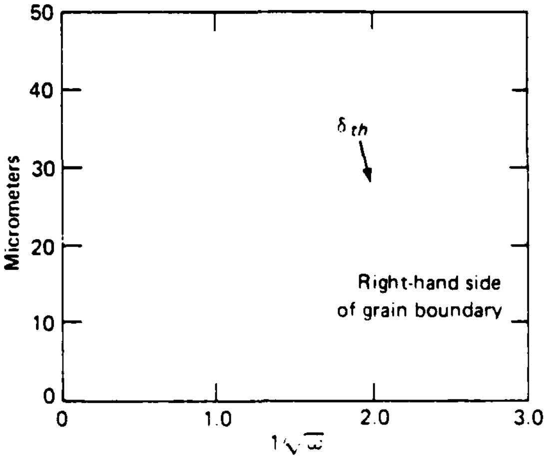

Figure 11—Plot of grain boundary width versus $1/\sqrt{\omega}$. The solid line is the thermal diffusion length of aluminum calculated using a diffusivity, α, of 1 square centimeter per second.

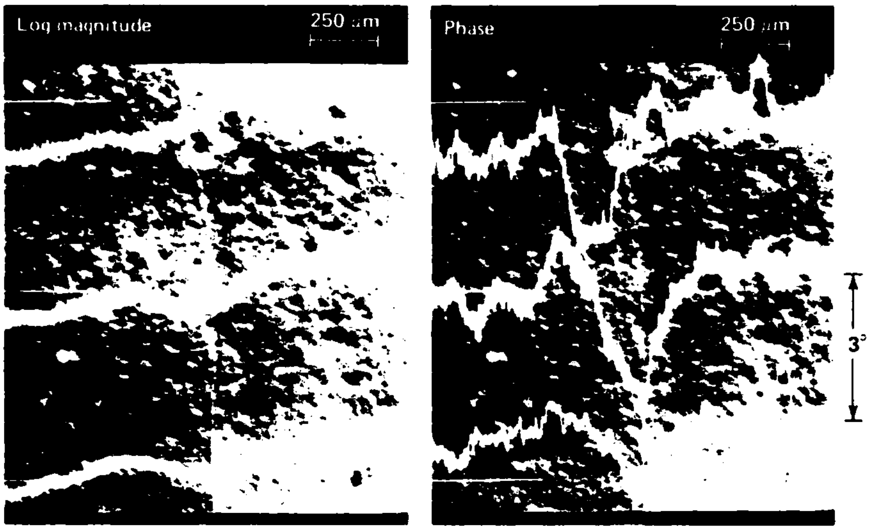

Figure 12—Scanning electron image with an overlay of electron acoustic line scans taken on a large bicrystal of aluminum. The crystal was over-etched to show the boundary. The position of the scans is indicated by the horizontal lines in the figure. Data for Fig. 12 used the response on the right-hand side of the boundary because of the interfering subsurface structure seen on the left-hand side.

The origin of the interior contrast within the grain is still an open question. In this specimen of pure aluminum, impurity segregation at the boundary and within grains should be absent. (This was confirmed with electron-induced energy-dispersive X-ray analysis of this sample. X-ray topographic studies of microstructure near the boundary were made using the Brookhaven synchrotron.) Possible sources of contrast include anisotropic elastic effects and symmetry-lowering internal stresses within grains in combination with thermally generated acoustic waves.

Particle Beam Contrast

Figures 13 and 14 suggest that the thermoelastic signal generation process is important for particle beam acoustic generation using argon ions. Figure 13 shows line scans taken using beams of argon ions at a fixed modulation frequency and various hole depths using the sample of Figs. 7 and 8. Line scans made using all three sources (ion, electron, and laser) closely resemble one another when account is taken of the different frequencies used. Figure 14 shows similar data obtained for ions at a fixed hole depth and several frequencies. Again the profiles show an approximate $1/\sqrt{\omega}$ dependence, indicating that thermal diffusion effects dominate the contrast. These experiments suggest that thermoelastic processes control acoustic signal generation for low ion beam voltages and low modulation frequencies.

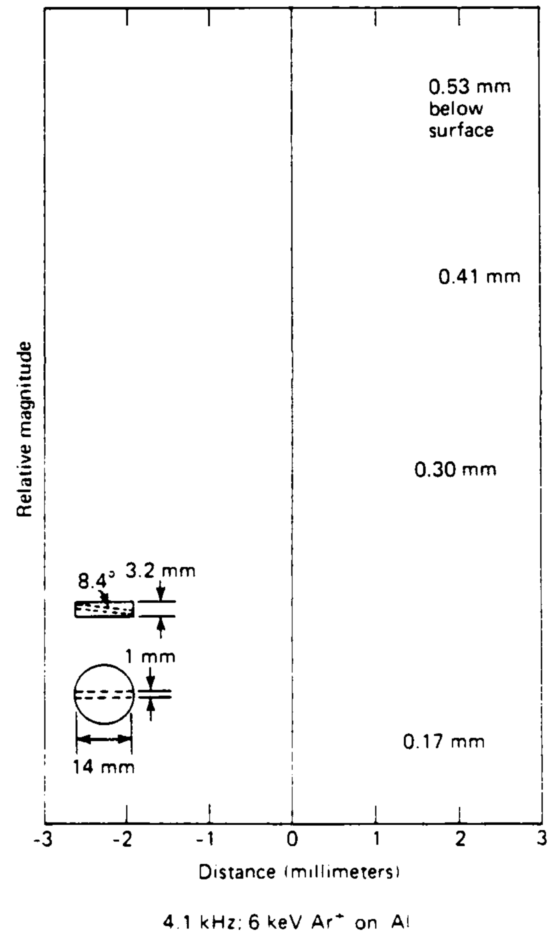

Figure 13—Ion acoustic profiles for a slant hole sample at various depths and at 4.1 kilohertz.

BEAM-SPECIMEN CONTRAST

Interaction between the exciting beam and the specimen can give rise to image contrast and depth profiling. Figure 15 shows scanning electron microscope and scanning electron acoustic microscope images of an area of an integrated circuit at two values of primary beam voltage, V_B. For $V_B = 5$ kilovolts, the scanning electron microscope and scanning electron acoustic microscope images are essentially the same and show the surface features of the device, including areas of metallization. Minor differences are related to electron penetration of an ink layer covering a portion of the chip. On the other hand, the 30-kilovolt scanning electron microscope and scanning electron acoustic

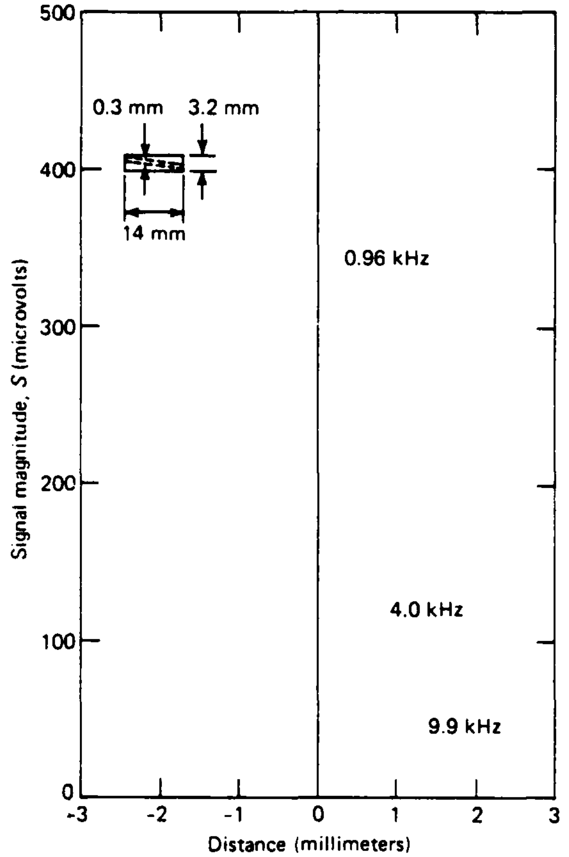

Figure 14—Ion acoustic profiles for a sample containing a subsurface slant hole. At low frequencies, thermal interaction with the hole causes a signal increase. At high frequencies, the signal generation process is still thermal, but the contrast interaction is nonthermal.

microscope images are entirely different. The scanning electron acoustic microscope image shows little surface structure but strong contrast associated with a buried subsurface structure.

A second related example is shown in Fig. 16, where a scanning electron microscope image and scanning electron acoustic microscope magnitude and phase images of another integrated circuit are shown. The images presented are of the same section of the integrated circuits. Again, the scanning electron acoustic microscope images show subsurface features not visible in the scanning electron microscope image. These are thought to be related to the range of electron penetration into the sample, followed by selective interaction with different dopant regions present. Studies of the dependence of the scanning electron acoustic microscope images on V_B and ω show that at low primary voltages ($V_B \leq 5$ kilovolts) the scanning electron microscope and scanning electron acoustic microscope images are equivalent. As V_B increases, the images begin to differ, and a sequence of scanning electron acoustic microscope images becomes visible as the primary voltage is increased. These may correspond to successive layers within the chip. Some lateral resolution in the images is lost by thermal spreading. Comparison of images at 10 kilohertz with images at 400 kilohertz shows less image definition at the lower frequency. The result is consistent with an increased thermal diffusion length at the lower frequency. However, the image features remain the same, indicating that the depth profiling is not the thermal diffusion length profiling discussed previously; instead, it depends on the depth in the sample where energy is deposited. This presents a number of unresolved questions for the present understanding of the origin of the very strong contrast in Fig. 16. The role of carrier diffusion effects on the image must be clarified as well as the presence of a direct electron-lattice mechanism for stress generation. Also, the energy loss with depth in semiconductors must be re-evaluated.

Ion acoustic imaging is another area where nonthermal signal generation and image contrast processes may exist.[11] Some evidence was presented showing that the thermoelastic process is important at low frequencies. However, ion interactions with solids are known to cause a wide variety of nonthermal effects, including both sputtering and ion implantation in semiconductors and metals.[12,13] These processes are important for materials processing and for analysis. Studies of ion acoustic imaging have been conducted in order to help understand these processes better.

Sputtering is a complex process in which bombardment of a solid with energetic ions causes erosion of the surface of the solid and substantial surface and subsurface damage to the remaining material. Several mechanisms for sputtering have been suggested, including momentum transfer and thermal evaporation from regions having very high excess temperatures generated by ion-solid interactions. Most current thought favors the momentum process.

We have investigated this issue using ion acoustic imaging with the energetic rare gas ions (neon, argon, and xenon) of known primary energy to induce sputtering in several metals and nonmetals. Two types of studies were conducted. For each ion type, measurements were made of the acoustic signal as a function of primary beam voltage. Since the ratio of beam momentum to beam energy varies with voltage, the ratio of the thermoelastic signal (which is energy related) to a possible momentum transfer signal (which depends on momentum) should also vary with beam voltage.

Figure 17 shows some of the results of this study. At fixed beam voltage and variable beam current, the acoustic signal has a linear dependence on beam energy. However, at fixed current and variable voltage, the dependence deviates from linearity in the direction predicted by a momentum contribution to the acoustic signal. This result is called into question, however, by results obtained using different ions with different masses. For the same beam energy, a marked difference should exist in the acoustic signal generated by ions of different masses if the momentum transfer is an important generation process. No such difference was found, and the puzzle is still being studied.

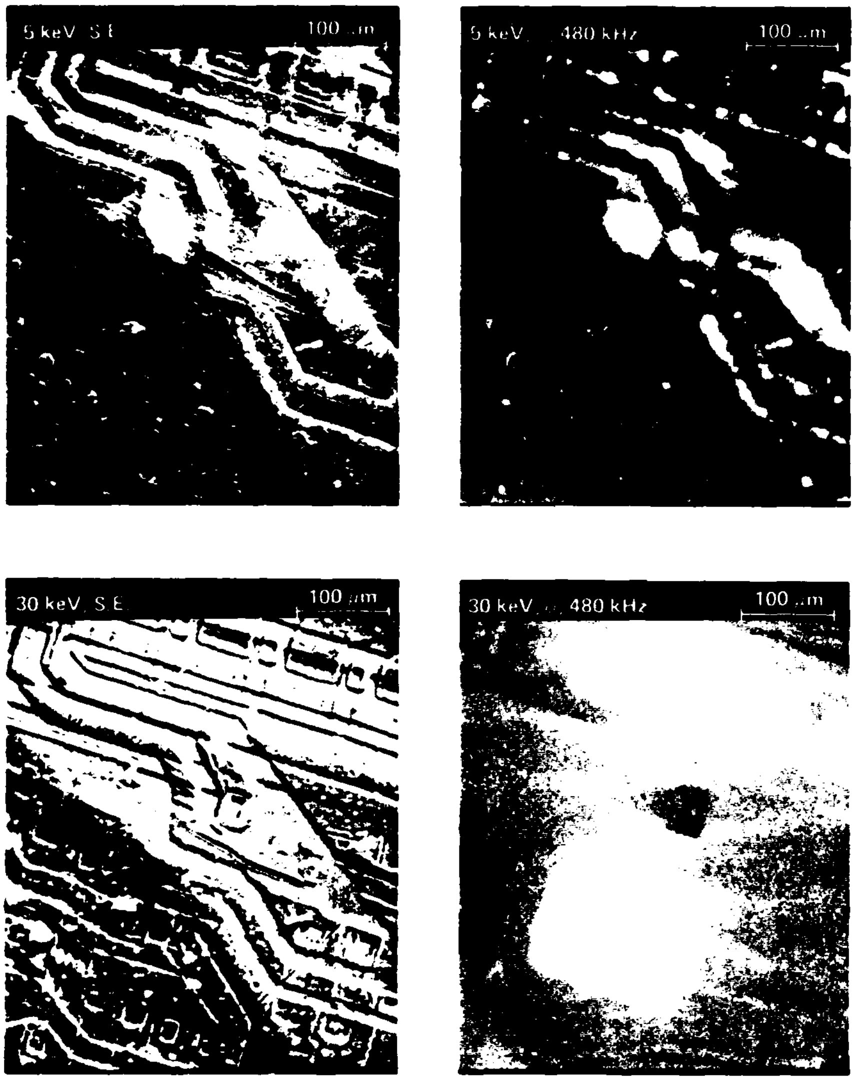

Figure 15—Scanning electron and electron acoustic images at two primary beam voltages showing beam specimen contrast.

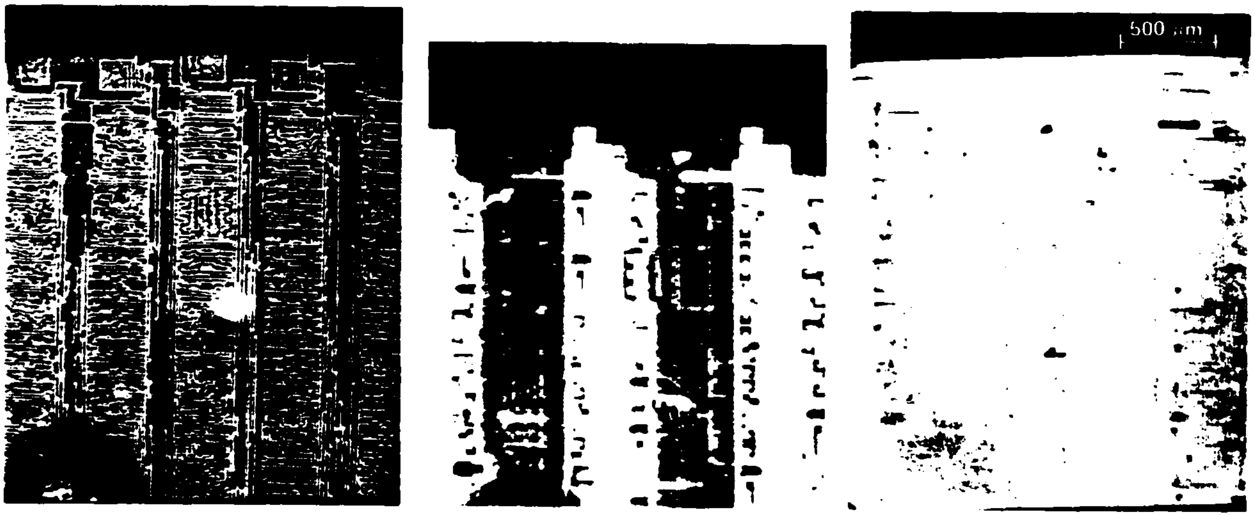

30 kV, 42X

19 kV, 42X, 209.03 kHz, magnitude

19kV, 42X, 209.03 kHz, phase

Figure 16—Scanning electron microscope and scanning electron acoustic microscope magnitude and phase images of a complementary metal oxide semiconductor chip. Subsurface structure is apparent.

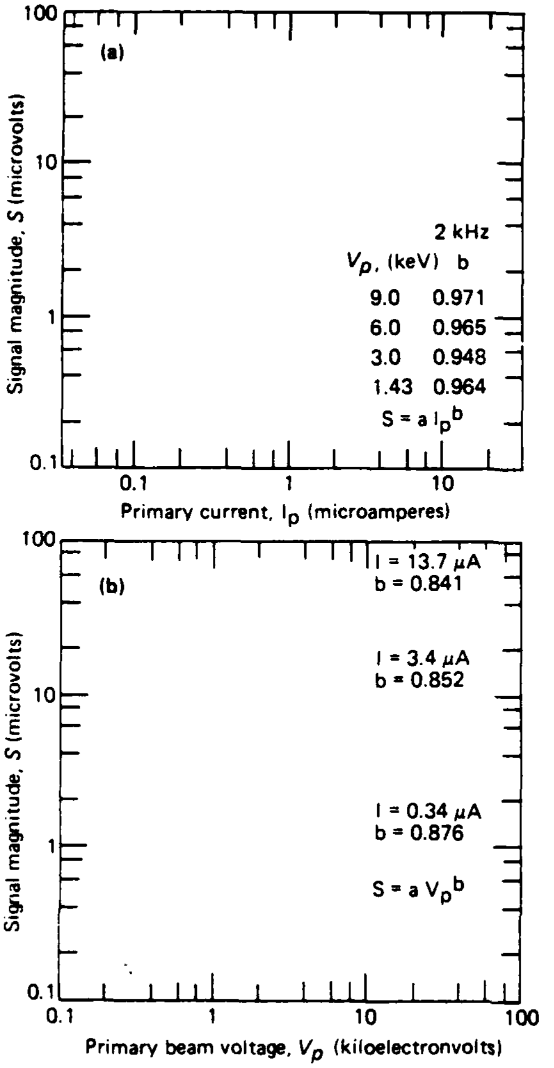

Figure 17—Dependence of ion acoustic signal on beam current (a) and on beam voltage (b).

CONCLUSION

The limited scope of this article does not reveal the broad range of physical problems that have been studied using photothermal techniques. Photothermal techniques can often be used in situ, allowing application to biological systems and other physical systems that must be measured in process. A brief list of recent work includes topics such as the curing of epoxy, properties of photosynthetic pigments, oxygen evolution in leaves and dynamics of the photosynthetic process, phase transitions, thickness of sprayed coatings, hydration of human stratum corneium (a component of skin), malarial parasites, metastable electron states of dye molecules, densification of ceramics, and fiber-matrix bonding in composites. The ability to image while making quantitative measurements of materials properties will be a significant factor in further developments in the field. However, for thermal wave imaging to become a basic and routine tool for materials analysis and processing, it is necessary to understand the basic processes involved. This begins with an understanding of beam-specimen interactions and continues through an understanding of the process of thermalization and detection.

Substantial progress has been made in this direction, but more is required to meet the minimum needs of the applications that are possible. At the present time, the imaging process and the underlying contrast mechanisms of optical beam deflection and infrared imaging methods are best understood. Some progress has been made in understanding various aspects of thermoelastic imaging using a laser source, but substantial uncertainty exists regarding the role of elastic contrast in overall image contrast. To make thermal wave imaging a quantitative tool for analyzing materials, it is necessary to resolve these issues.

REFERENCES

[1] Y. H. Wong, R. L. Thomas, and G. F. Hawkins, "Surface and Subsurface Structure of Solids by Laser Photoacoustic Spectroscopy," *Appl. Phys. Lett.* **32**, 538 (1978).

[2] W. B. Jackson, N. Amer, A. C. Boccara, and D. Fournier, "Photothermal Deflection Spectroscopy and Detection," *Appl. Opt.* **20**, 1333 (1981).

[3] J. C. Murphy and L. C. Aamodt, "Optically Detected Photothermal Imaging," *Appl. Phys. Lett.* **38**, 196 (1981).

[4] W. Nowacki, *Thermoelasticity*, Addison-Wesley, London (1962).

[5] J. C. Murphy and L. C. Aamodt, "Photoacoustic Spectroscopy of Luminescent Solids: Ruby," *J. Appl. Phys.* **49**, *3502-3509* (1977).

[6] V. A. Sablikov and V. B. Sandomirskii, "Photoacoustic Effect in Semi-Conductors," *Phys. Stat. Sol.* (*B*) **120**, 471-480 (1983).

[7] L. C. Aamodt and J. C. Murphy, "Effect of 3-D Heat Flow near Edges in Photothermal Measurements," *Appl. Opt.* **21**, 111 (1982).

[8] G. A. D. Briggs, "Scanning Electron Acoustic Microscopy and Scanning Acoustic Microscopy: A Favorable Comparison," *Scan. Elec. Microsc.* **III**, 1041 (1984).

[9] L. C. Aamodt and J. C. Murphy, "Photothermal Measurements Using a Localized Excitation Source," *J. Appl. Phys.* **52**, 4903 (1981).

[10] G. C. Wetsel, J. B. Spicer, J. W. Maclachlan, and J. C. Murphy, "Comparison of Photoacoustic and Photothermal Optical Beam Deflection Imaging of Subsurface Structure in Solids," in *1985 IEEE Ultrasonics Symposium Proc.*, San Francisco (Oct 1985).

[11] J. C. Murphy, J. W. Maclachlan, R. B. Givens, F. G. Satkiewicz, and L. C. Aamodt, "The Generation of Ultrasound by Laser, Electron and Ion Probes and Its Application to the Characterization of Materials," in *Proc. of Ultrasonics International 1985*, Butterworths Scientific, London (1985).

[12] O. Auciello and R. Kelly, eds., *Ion Bombardment Modification of Surfaces*, Elsevier Science Publishers, Amsterdam (1984).

[13] P. Sigmund, "Sputtering by Ion Bombardment: Theoretical Concepts," in *Topics in Applied Physics* **47**, *Sputtering by Particle Bombardment I*, R. Behrisch, ed., Springer-Verlag, Berlin (1981).

ACKNOWLEDGMENTS—The authors wish to recognize the contributions of Grover C. Wetsel (Southern Methodist University) who is on sabbatical at the Applied Physics Laboratory and Jane W. Maclachlan, a doctoral candidate in the Materials Science Department at The Johns Hopkins University.

THE AUTHORS

JOHN C. MURPHY (right) is a physicist in the Materials Science Group in the Milton S. Eisenhower Research Center. Born in Wilmington, Del., he obtained a B.A. degree from The Catholic University of America in 1957, an M.S. from Notre Dame University in 1959, and a Ph.D. from The Catholic University in 1970. His work at APL has included experimental studies of excitation transfer in luminescent systems using optical and microwave spectroscopy, measurement of nonradiative relaxation processes using photoacoustic spectroscopy, and, more recently, remote sensing of corrosion using AC magnetometry. He is currently a member of the Executive Committee of the Johns Hopkins Center for Nondestructive Evaluation, a corporately funded interdisciplinary center involving participation of the Homewood and Medical School faculties and APL's Research Center.

LEONARD C. AAMODT (seated) is a physicist in the Materials Science Group in APL's Milton S. Eisenhower Research Center. He was born in Salt Lake City and earned a B.S. degree in electrical engineering from the University of Utah in 1943 and a Ph.D. degree from Columbia University in 1955. During World War II, he worked at the Westinghouse Research Division and on the Manhattan District Project in Brooklyn, in Oak Ridge, and at Columbia University. Prior to coming to APL, he was an assistant professor in the Departments of Mathematics, Physics, and Electrical Engineering at Brigham Young University in Provo, Utah. His research interests at APL have been in the general areas of photothermal processes and thermal wave imaging.

FRANK G. SATKIEWICZ's biography and photograph can be found on p. 180.

R. BEN GIVENS (center, standing) was born in Huntington, W. Va. He graduated from the Army Electronics School in 1955 and the Capital Radio Engineering Institute in 1957. He worked as a quality control specialist for Litton Industries prior to joining APL in 1965 and is presently an engineering staff associate in the Materials Science Group of the Milton S. Eisenhower Research Center.

P. RONALD ZARRIELLO (left) was born in Baltimore in 1933. In 1952, he joined Bendix Radio Corp., where he worked to develop the VHF electronic subsystems for jet aircraft. In 1954, he joined the JHU Radiation Laboratory in Baltimore where he worked in Dr. Jan Minkowski's group on the four-level MASER. In 1956, he joined the Los Alamos Scientific Laboratory, where he was involved in thermal shock wave testing. While working at Los Alamos, he attended the University of California and the University of New Mexico. In 1958, Mr. Zarriello returned to the JHU Radiation Laboratory and was involved in the fabrication of the first ruby laser used in experiments at Hopkins. In 1968, he joined APL's Milton S. Eisenhower Research Center, where he is now an associate engineer working in the Materials Characterization and Evaluation Group.

APPENDIX

PHOTOTHERMAL IMAGING OF DEFECTS IN METALS AND CERAMICS

13. L. C. Aamodt and J. C. Murphy, "Thermal Effects in Materials with Continuously Varying Optical and Thermal Properties in One Dimension," Can. J. Phys. to be published.

THERMAL EFFECTS IN MATERIALS WITH CONTINUOUSLY VARYING OPTICAL AND THERMAL PROPERTIES IN ONE-DIMENSION.

L. C. Aamodt and J. C. Murphy

Johns Hopkins University Applied Physics Laboratory
Johns Hopkins Road, Laurel, Maryland, USA 20707
301-953-5000

Index classification: 4430,4490,7820,7850,8630S

ABSTRACT

The complex heat flow pattern in a heterogeneous sample makes the thermal analysis of these materials difficult. In this paper, we consider heterogeneous materials with continuously varying parameters in one dimension. While this analysis is directed toward photothermal applications, specifically toward photothermal applications using broad beam illumination, it has many features in common with general harmonic heat flow.

The analysis shows that harmonic heat flow is interrupted by spatial variations in the sample's thermal and optical properties via two different types of heat barriers, one depending exclusively on thermal properties (thermal barriers) and the other depending upon both optical and thermal properties (opto/thermal barriers). Thermal barriers are created by spatial variations in thermal effusivity while the opto/thermal barriers are created by spatial variations in the ratio of the thermal diffusion length to the optical absorption length. The character of the opto/thermal barriers is affected by optical saturation in the sample.

The temperature distribution in a heterogeneous sample is interpreted in terms of thermal waves providing an intuitive guide for analyzing heat flow in heterogeneous materials.

The surface temperature is also obtained in a general form suitable for both heterogeneous and homogeneous calculations.

INTRODUCTION

The rapid growth of photothermal and photoacoustic spectroscopy and imaging has created an interest in periodic heat flow in materials. In photothermal applications, where a sample is periodically heated by light (or some other energy source such as an electron beam), a periodic heat flow pattern is established which depends upon the sample's optical, thermal, and geometric properties, and is distorted by the presence of defects and flaws. Consequently a knowledge of the temperature distribution provides information about each of these factors.

A variety of techniques can be used to study this temperature pattern including detection of pressure variations produced thermally in a gas cell(1,2), detection of infrared radiation(3,4), detection of thermally induced surface displacement(5), detection of thermally generated elastic waves(6), and detection of a thermally generated index of refraction gradient in a sample or in a fluid in thermal contact with the sample(7-9).

While each of these methods utilizes a different thermally-dependent phenomena, all of them depend upon the modulated temperature pattern produced within or on the surface of the sample. To relate this data to sample properties, two steps are required. First, the experimental signal (pressure, displacement, deflection, etc.) must be related to the sample temperature, and then the observed temperature pattern must be related to the thermal, optical, and geometric properties of the material. In this paper we consider only the second step, the dependence of the harmonic temperature on the thermal and optical properties of the sample.

In general, heterogeneous materials have received little theoretical attention in photothermal applications because of their complicated heat flow patterns. In this paper we consider heterogeneous materials whose thermal and optical properties vary spatially in one dimension. These materials are of interest both scientifically and technologically. Materials in this category include thin films on planar surfaces, layered samples, materials fabricated by deposition, and samples with impurities that vary predominantly with depth in the sample. We consider planar samples with no discrete flaws or discontinuities and assume that the excitation beam and cross sectional area of the sample (perpendicular to the heterogeneous dimension) are large enough so that heat flow is essentially one dimensional. Although this solution is for a special geometric case, it contains many features of general harmonic heat flow.

HETEROGENEITY IN PHOTOTHERMAL MEASUREMENTS

In photoacoustic and photothermal spectroscopic studies, the sample is assumed to be thermally homogeneous so that changes in the photothermal signal are attributable to changes in the optical absorption constant. Thermal properties merely provide the "thermal environment" in which these changes are manifest, and thus only parametrically affect the result.

In spectroscopic measurements, the presence of *thermal* heterogeneity usually degrades the quality of the experimental result. For small heterogeneities, an uncertainty is introduced in the value of the thermal parameters, and for more significant heterogeneities, the temperature pattern may be altered so as to make the application of simple theory questionable. On the other hand, spatial *optical* heterogeneity is of interest, and in some spectroscopic studies, such as those involving depth probing, it may be central to the study.

By contrast, the object of photothermal imaging is to locate thermal heterogeneities within and on the surface of the sample and interprete their significance. This includes the study of homogeneous media with localized defects where the sample and defect can be viewed as a single entity, and the defect considered to be a special type of heterogeneity characterized by a spatially abrupt change in thermal and/or optical properties.

Different demands can be placed on photothermal imaging. A detailed knowledge of the relationship between the photothermal signal and sample properties is not needed if a sample is merely compared with a reference sample and accepted or rejected depending upon the absence or presence of significant differences. On the other hand, if a particular thermo/optical property is being studied, it is essential that the relationship between the photothermal signal and thermo/optical properties of the sample be known. Such studies might involve monitoring changes in a parameter associated with the aging of a sample or investigating changes that might indicate incipient flaw formation, etc.

APPROACH

The complexity of heterogeneous heat flow necessitates a consideration of special cases. In reference 10, heterogeneous materials having local homogeneity were considered, where thermal and optical properties varied slowly compared with a thermal diffusion length. In this approximation, a three-dimensional calculation was possible, but abrupt spatial changes in sample properties could not be studied.

In this paper we consider samples with planer surfaces and one-dimensional heterogeneities. The simple form of the temperature distribution and boundary conditions in one-dimension make it possible to obtain an exact solution with minimal limitations.

As in reference 10, the main intent of this paper is not to compute temperature patterns but rather to provide a guide for intuitive thinking about heat flow in heterogeneous materials. Nevertheless, the expressions obtained in this paper can be used to model the temperature pattern for an assumed distribution of sample properties. Specifically we investigate what combinations of thermal and optical parameters can be interpreted as thermal and opto/thermal barriers in the sample and determine how these barriers contribute to the sample temperature pattern. (Opto/thermal barriers are described in section D.) A simple thermal wave interpretation of our results also provides a means for visualizing the details of complicated heat flow in heterogeneous materials.

THEORY

If thermal properties of a sample vary in one dimension only, and if mechanical coupling is ignored, heat flow is determined by the equation,

$$[1] \qquad \partial/\partial z[\kappa(z)\ \partial T(t,z)/\partial z] = C(z)\ \partial T(t,z)/\partial t - H\ (t,z),$$

Where κ is the thermal conductivity, C is the thermal capacity per unit volume and H, is the heat input per unit volume. (Mechanical coupling in photothermal applications is discussed in reference 11.)

Solving eqn. 1 requires a knowledge of the spatial dependence of κ and C, and, if a solution is obtainable, it may have a different form for different spatial patterns. To avoid this difficulty, we consider a multilayered sample composed of n+1 homogeneous layers and let n approach infinity. This allows use of the simple homogeneous temperature distribution within each level. In this approach, a formal solution is obtained in integral form. The spatial distribution of κ and C can then be inserted to evaluate the integrals.

A. HOMOGENEOUS HEAT FLOW

We begin by expressing the temperature pattern in a homogeneous medium in a form that will be convenient for subsequent calculations. For homogeneous materials, κ is spatially uniform so eqn. 1 reduces to

$$\partial^2 T/\partial z^2 = (C/\kappa)\ \partial T/\partial t - H(t,z)/\kappa\ ,$$

and, if I is the intensity of an energy source that is exponentially absorbed in the sample, and β is the absorption constant, then $H = \beta I \exp(-\beta z)$, where positive z is measured downward from the upper surface. If we operate in the temporal Fourier transform domain and limit ourselves to the harmonic case [H , $T \sim \exp(j\omega t)$], then

$$\partial^2 T/\partial z^2 = T/\mu^2 - \beta I \exp(-\beta z)/\kappa \tag{2}$$

where $\mu = (\kappa/j\omega C)^{1/2}$ is the <u>complex</u> thermal diffusion length. Since μ^{-1} appears frequently in our calculations, we define $\gamma = 1/\mu$ to be the reciprocal <u>complex</u> thermal diffusion length.

The homogeneous and particular solutions of eqn. 2 are $T = \exp(\pm\gamma z)$ and $T = \Gamma I \exp(-\beta z)$, respectively, where $\Gamma = y\varepsilon/(\varepsilon^+\varepsilon^-)$, $y = \mu/\kappa$, $\varepsilon = \beta\mu$, and $\varepsilon^\pm = 1 \pm \varepsilon$. (In general, the notation $a^\pm$, will be used as an abbreviation for $1 \pm a$.) Each of these terms has physical significance. ε is the ratio of the thermal diffusion length μ, to the optical absorption length β^{-1}, and y is inversely proportional to the thermal effusivity (or thermal inertia) of the sample, $e = (\kappa C)^{1/2}$. y is both complex and frequency dependent. Since μ and y are independent variables, it is possible to use them as the fundamental thermal parameters instead of κ and C. In terms of these parameters, $\kappa = \mu/y$ and

$j\omega C = 1/(y\mu)$.

Using these solutions, the complex sample temperature can be written

$$[3] \qquad T(z) = T^1 \exp(\gamma z) + T^2 \exp(-\gamma z) + \Gamma\, I \exp(-\beta z),$$

where T^1 and T^2 are constants to be determined by boundary conditions. The corresponding flux in the z direction is

$$[4] \qquad F = -\kappa \partial T/\partial z = -\kappa\gamma[T^1 \exp(\mu z) - T^2 \exp(-\mu z)] + \kappa\beta\Gamma I \exp(-\beta z).$$

For ease in making calculations, we write T and F as components of the vector, $\vec{\tau} = \begin{vmatrix} T \\ F \end{vmatrix}$. Eqns. 3 and 4 can then be written in vector form as

$$[5] \qquad \vec{\tau}(z) = P[J\, E(z)\, \vec{T} + \vec{g}\, \Omega \exp(-\beta z)]$$

where $\Omega = \Gamma I$, $\qquad E(z) = \begin{vmatrix} \exp(\gamma z) & 0 \\ 0 & \exp(-\gamma z) \end{vmatrix}$,

$$\vec{T} = \begin{vmatrix} T^1 \\ T^2 \end{vmatrix}, \quad \vec{g} = \begin{vmatrix} 1 \\ \varepsilon \end{vmatrix}, \quad J = \begin{vmatrix} 1 & 1 \\ -1 & 1 \end{vmatrix}, \text{ and } \quad P = \begin{vmatrix} 1 & 0 \\ 0 & y^{-1} \end{vmatrix}.$$

Using a vector formulation has several advantages including the ease of matching boundary conditions. At each interface, continuity of $\vec{\tau}$ provides continuity of both temperature and thermal flux.

Using the abbreviations, $\vec{T'}(z) = E(z)\,\vec{T}$ and

$\Omega'(z) = \Omega \exp(-\beta z)$, eqn. 5 simplifies to

$$[6] \qquad \vec{\tau}(z) = P[J\ \vec{T}'(z) + \vec{g}\ \Omega'(z)].$$

We interprete the terms in eqn. 6 as traveling thermal waves (Figure 1). The components of $T'(z)$ are two damped waves, one traveling upward and the other traveling downward, with amplitude T at $z = 0$. $E(z)$ is a propagation matrix that describes the change in amplitude and phase of these waves as they travel through the sample and depends only on the thermal properties of the sample. Mathematically, these waves satisfy boundary conditions. Physically, they represent thermal waves reflected(12) by a thermal mismatch at sample interfaces.

We also view $\vec{g}\ \Omega'(z)$, which is the source term for the thermal system, as a thermal wave with a magnitude, Ω, at $z = 0$ and with a propagation factor, $\exp(-\beta z)$. This propagation factor is purely attenuating. It depends only on the sample's optical properties, and is real as long as the conversion of absorbed energy to heat is instantaneous. Since this wave is created by heat generated within the sample, it is present regardless of any thermal constraints existing at the sample surface. Accordingly, we call it the fundamental or heat-generated thermal wave.

The amplitude of the fundamental wave, Ω, is essentially a measure of how easily harmonic energy can produce a temperature in a particular thermal environment. Ω is frequency dependent and is a function of all three opto/thermal parameters, β, κ, and C.

$\Gamma = -y/\epsilon = -1/\kappa\beta$, in an optically saturated sample ($|\epsilon| >> 1$), while in an unsaturated sample ($|\epsilon| << 1$), $\Gamma = y\epsilon = \beta/j\omega C$.

B. LAYERED SAMPLES

Consider a sample of thickness, L, whose upper surface is in thermal contact with a fluid, G, (gas or liquid) and whose lower surface is in thermal contact with a backing material, B, (gas, liquid or solid). We assume that no heat is generated in either G or B, that both of these regions have spatially uniform thermal parameters, and that both regions are thermally thick (i.e are thermal half-spaces). We consider the sample to consist of n+1 homogeneous layers (Figure 2). The temperature pattern within each layer can then be described by eqns. 5 or 6, where z is measured downward from the upper surface of the layer.

1. The Effect of Surface Boundaries.

In order to separate surface effects from bulk effects, we temporarily ignore thermal and optical properties within the sample except for two small zones close to the sample surfaces (Figure 3).

Since G and B are homogeneous, their temperature and flux can be written,

$$\vec{\tau}_g = P_g \overrightarrow{J_-} T_g \exp(\gamma_g z) \quad \text{and} \quad \vec{\tau}_b = P_b \overrightarrow{J_+} T_b \exp[-\gamma_b(z-L)]$$

where T_g and T_b are constants determined by boundary conditions, y_g and y_b are the thermal admittances of regions G and B, respectively, and

$$\vec{J}_{\pm} = \begin{vmatrix} 1 \\ \pm 1 \end{vmatrix}, \qquad P_i = \begin{vmatrix} 1 & 0 \\ 0 & y_i^{-1} \end{vmatrix} \quad (i = b, g).$$

At $z = 0$ and $z = L$, $\vec{\tau}_0(0) = \vec{\tau}_g$ and $\vec{\tau}_n(\ell_n) = \vec{\tau}_b$, respectively. Thus,

$$[7] \qquad P_0[J\,\vec{T}_0 + \vec{g}_0\,\Omega_0] = P_g\,\vec{J}_-\,T_g$$

$$[8] \qquad P_n[J\,\vec{T}_L + \vec{g}_n\,\Omega_L] = P_b\,\vec{J}_+\,T_b$$

where $\vec{T}_L = \vec{T}'_n(\ell_n)$ and $\Omega_L = \Omega'_n(\ell_n)$.

The relationship between $\vec{T}_L$ and $\vec{T}_0$ depends upon the thermal and optical properties of the sample bulk. Initially, we leave these properties unspecified and write

$$[9] \qquad \vec{T}_L = \Phi\,\vec{T}_0 + \vec{\psi}/2$$

where the matrix, Φ, and the vector, $\vec{\psi}$, are to be determined later. Φ is the effective propagation factor for a thermal wave traveling through the sample, and $\vec{\psi}$ represents additional thermal waves created by thermal reflections within the sample. We call the pair $[\Phi, \vec{\psi}]$, the thermo-optical transmission of the sample. These two terms completely characterize the heterogeneity of the sample.

Subsequent calculations will be simplified if we separate Φ into a product of two terms, $\Phi = \phi\, E(0L)$, where

$$E(0L) = \begin{vmatrix} \exp(\gamma_{avg}L) & 0 \\ 0 & \exp(-\gamma_{avg}L) \end{vmatrix},$$

and $\gamma_{avg} = L^{-1} \int_0^L \gamma(z)\, dz$. $E(0L)$ is the propagation factor for a thermal wave moving from surface to surface in a homogeneous sample having a reciprocal diffusion length equal to the average reciprocal diffusion length of the heterogeneous sample.

Using eqn. 9, eqns. 7-8 can be reordered and expressed in the simplified form,

$$\vec{T}_0 + \vec{A} = \vec{B}\, T_g \qquad\qquad \vec{T}_0 + \vec{C} = \vec{D}\, T_b .$$

Solving for $\vec{T}_0$,

$$\vec{T}_0 = (\vec{D},\vec{B}) \begin{vmatrix} \det(\vec{A},\vec{B}) \\ \det(\vec{D},\vec{C}) \end{vmatrix} / \det(\vec{B},\vec{D})$$

where $(\vec{D},\vec{B})$ is the matrix $\begin{vmatrix} D_1 & B_1 \\ D_2 & B_2 \end{vmatrix}$. Evaluating determinents, and substituting $\vec{T}_0$ into eqn. 6, the surface temperature at $z = 0$ is found to be,

$$[10] \quad T_s = T(0) = [(1+\rho_g)/2] \frac{[\det(\vec{\sigma}_0, \tilde{\phi}\vec{\rho}_b) - \det(\vec{\sigma}_L, \vec{\rho}_b) - \det(\vec{\psi}\,, \vec{\rho}_b)]}{\det(\vec{\rho}_g, \tilde{\phi}\, \vec{\rho}_b)}$$

where

$$\tilde{\Phi} = \det(\Phi)\, \Phi^{-1}, \qquad \vec{\sigma}_i = \Omega_i \vec{\varepsilon}_i, \qquad \vec{\varepsilon}_i = \begin{vmatrix} \varepsilon_i^- \\ \varepsilon_i^+ \end{vmatrix} \qquad (i = 0,L),$$

$$\rho_i = \pi_i^-/\pi_i^+ \quad (i = g,b), \qquad \vec{\rho}_b = \begin{vmatrix} \rho_b \\ 1 \end{vmatrix}, \qquad \vec{\rho}_g = \begin{vmatrix} 1 \\ \rho_g \end{vmatrix}.$$

$$\pi_g = y_0/y_g = e_g/e_0, \qquad \text{and} \qquad \pi_b = y_L/y_b = e_b/e_L.$$

Eqn. 10 is a general expression, applicable to both homogeneous and heterogeneous samples. To complete the solution, Φ and $\vec{\psi}$ must be determined for the material being studied.

For homogeneous samples the term, $\det(\vec{\psi},\vec{\rho}_b)$, vanishes since there are no internal thermal reflections within the sample, and ϕ reduces to the unit diagonal matrix, $I = \begin{vmatrix} 1 & 0 \\ 0 & 1 \end{vmatrix}$. For homogeneous materials, eqn. 10 is more easily recognized when the determinants are expanded and the equation is reordered in the form

$$[11] \quad T_s = \Gamma \frac{(1-\varepsilon)(1+\pi_b)\ \Lambda - (1-\pi_b)(1+\varepsilon)\ \Lambda^{-1} - 2(\pi_b - \varepsilon)\ \exp(-\beta L)}{(1+\pi_b)(1+\pi_g)\ \Lambda - (1-\pi_b)(1-\pi_g)\ \Lambda^{-1}}$$

where $\Lambda = \exp(\gamma L)$. Except for slight differences in nomenclature, this equation is identical to the one commonly used in photothermal calculations when 3-dimensional effects need not be taken into account. (See reference 2. Our results and those of R & G can be correlated by letting $\pi_g \rightarrow g$, $\pi_b \rightarrow b$, $\varepsilon \rightarrow r$, $\gamma \rightarrow \sigma_s$, and $\Lambda \rightarrow \exp(\sigma_s L)$.)

Before determining Φ and $\vec{\psi}$ for a heterogeneous sample, we briefly discuss the physical significance of the terminology used in eqn. 10.

2. Terminology

The quantity, π, is the ratio of thermal effusivities at an interface. When the sample is thermally matched, $\pi = 1$, and $\rho = 0$. We designate ρ_i as the magnitude of the discrete thermal barrier at interface, i. Since π ranges from 0 to ∞, ρ ranges from 1 to -1. When $\rho = -1$ the medium interfacing with the sample has zero thermal effusivity; when $\rho = +1$ the medium interfacing with the sample has infinite thermal effusivity. When ρ is negative, the interfacing medium is usually a better heat conductor than the sample, while if ρ is positive, the medium is usually a better insulator, and if $\rho = 0$, there is a thermal match and heat flow is not disrupted.

In the absence of internal reflections, the matrix, Φ, is diagonal and the elements, Φ_{11} and Φ_{22}, are the propagation factors for an upward and downward traveling thermal wave, respectively, moving from surface to surface. When internal reflections are present, off-diagonal terms (Φ_{12}, Φ_{21}) are introduced.

Ω is a measure of the ability of the modulated heating source to produce an harmonic temperature in the sample. Roughly speaking, it can be said to describe the amount of harmonic temperature created per unit of harmonic heat input. For one-dimensional heat flow, the absolute magnitude of Γ is $|\Gamma| = \beta/(\kappa^2\beta^4 + \omega^2 C^2)^{1/2}$. When β is small, Γ is linear in β and inversely proportional to C. When $\beta > |1/\mu|$, $|\Gamma|$ monotonically decreases with β and κ, indicating that as absorption increases, energy absorbed at a depth below $z=|\mu|$ becomes increasingly ineffective in altering the surface temperature. In general, however, Ω is a function of all three opto/thermal variables since at any particular point in the sample the temperature is affected by the amount of heat created there (β), by how well heat is retained at, or introduced into, that point (κ), and by how much energy is needed to produce a temperature at that point in the absence of thermal conduction (C).

C. THERMAL WAVES IN A HETEROGENEOUS MEDIUM.

In a thermally thick homogeneous sample, where there is no thermal reflection at the bottom surface, the temperature pattern is a simple exponential. This pattern can be represented by a fundamental wave having a magnitude, Ω, at $z=0$. As the wave moves through the sample, it is attenuated by the propagation factor, $\exp(-\gamma z)$. Since Ω is spatially uniform, temperature is produced with the same effectiveness at all depths in the sample. In a heterogeneous sample, where β, κ, and C are functions of z, Ω varies with depth and consequently temperature is produced with varying effectiveness at different sample depths. The temperature pattern in a heterogeneous sample depends upon z through both Ω and through the propagation factor, $E(z)$.

To separate these effects, we call Ω the strength of the fundamental wave. In a homogeneous material, this strength is constant, while in a heterogeneous material, it varies with depth depending upon the spatial distribution of the opto/thermal parameters, $\beta(z)$, $\kappa(z)$, and $C(z)$.

As shown in the following section, any spatial change in the fundamental wave strength results in a reflected thermal wave in a manner similar to the production of reflected waves by thermal mismatches at sample surfaces.

D. THERMAL AND OPTO/THERMAL BARRIERS

To obtain Φ and $\vec{\Psi}$ for a heterogeneous sample, $\vec{\tau}$ must be matched at each of the interfaces in the n+1 level system. Details of this calculation are found in the appendix. Here we consider the effect of spatial variations in the opto/thermal parameters in a simpler, less precise, but more direct, manner.

In our layered sample, $\vec{T}$ and Ω are spatially uniform within each layer, but may vary from layer to layer. We identify the value of these quantities by a subscript indicating the layer number (e.g., $\vec{T}_i$). As $n \to \infty$, and as the layer thickness $\to 0$, $\vec{T}$ and Ω can be considered to be functions of z. In addition, if β, κ, and C are continuous and their spatial derivatives exist, the difference in sample properties in adjacent layers becomes infinitesimal. Under these conditions, we can write the difference between $\vec{\tau}$ on either side of an interface at an arbitrary depth, $z=\zeta$, as

$$\partial\vec{\tau}/\partial z\ (\zeta) = [\partial[P\overrightarrow{JT'}]/\partial z + \partial[P\vec{g}\Omega']/\partial z]_{z=\zeta}.$$

Solving for $\partial\vec{T}'/\partial z$ and noting that $\vec{\tau}$ is constant across the interface, and $\partial y/y\partial z = -\partial e/e\partial z$ (where e is the thermal effusivity), we obtain,

$$[12] \quad \partial\vec{T}'/\partial z\ (\zeta) = \left[-\begin{vmatrix} 1 & -1 \\ -1 & 1 \end{vmatrix}(\partial e/e\partial z)\,\vec{T}'/2 + (\varepsilon\Omega')(\partial e/e\partial z)\,\vec{J}_{-}/2 - \partial(\vec{\varepsilon}\ \Omega')/2\partial z\right]_{z=\zeta}$$

A more exact solution gives the same relationship. The first term in eqn. 12 represents the incremental change in the propagation factor created by spatial variations in the opto/thermal parameters. The remaining terms are reflected thermal waves produced by heat barriers located at $z=\zeta$.

The first of these reflected waves depends exclusively on thermal properties, specifically on the spatial logarithmic derivative of the thermal effusivity at $z=\zeta$. The second reflected wave depends upon both optical and thermal properties. These differing dependencies suggest the existence of two different types of heat barriers, one created by spatial variations in thermal properties alone, and the other created jointly by spatial variations in the optical and thermal properties. We call these heat barriers, thermal barriers and opto/thermal barriers, respectively. The structure of these barriers will be discussed in section F.

It is helpful to retain a distinction between these two types of heat barriers when examining heat flow in a heterogeneous sample. A change in thermal properties can produce both types of barriers, but it is apparent that even in a thermally homogeneous sample, spatial changes in the optical absorption coefficient produce thermal wave reflections that may be interpreted as opto/thermal heat barriers within the sample.

E. REFLECTED THERMAL WAVES

In our layered sample, each layer has a different value of Γ, resulting in n+1 different temperature distribution patterns, $\Omega_n = (\Gamma I)_n \exp(-\beta_n \zeta)$. As $\Delta z \to 0$, these temperature distribution patterns form a continuum, $\Omega(\zeta)$, where, $\Omega(\zeta)$ is the temperature pattern that would exist in a homogeneous sample having optical and thermal properties identical with those existing in a heterogeneous sample at the depth ζ. Rewriting eqn. A3 (in the appendix) in the form,

$$[13] \qquad \vec{\Psi} = \int_0^L E(\zeta L)\, \vec{S}(\zeta)\, \Omega(\zeta)\, d\zeta$$

where

$$[14] \qquad \vec{S} = 1/2 \left[e^{-1} (\partial e/\partial\zeta)\, \vec{J}_{+} - \varepsilon^{-1}(\partial\varepsilon/\partial\zeta) \begin{vmatrix} \overset{-}{\varepsilon} / \overset{+}{\varepsilon} \\ \varepsilon^{+} / \varepsilon^{-} \end{vmatrix} \right],$$

we see that the temperature pattern developed by thermal reflections in a heterogeneous sample can be expanded using $\Omega(\zeta)$ as basis functions. In this expansion $\vec{S}(\zeta)$ is a weighting factor indicating the contribution of the local ("homogeneous") temperature pattern, $\Omega(\zeta)$ to the total heterogeneous temperature pattern. This formulation also provides a convenient means for defining thermal and opto/thermal barrier densities.

F. BARRIER DENSITIES

In contrast with homogeneous samples, where thermal barriers exist only at sample surfaces, heterogeneous samples have a continuum of thermal and opto/thermal barriers (Figure 4). Internal reflections occur at each depth in the sample where the thermal effusivity, e, or the ratio of the thermal diffusion length and the optical absorption length, ε, are not spatially uniform. We define the density of thermal barrier at $z=\zeta$ to be $M_t(\zeta) = \partial e(\zeta)/2e(\zeta)\partial z$ and the density of the opto/thermal barriers to be $M_{o/t}(\zeta) = \partial\varepsilon(\zeta)/2\varepsilon(\zeta)\partial z$.

Since $\partial C/\partial\zeta$ and $\partial\kappa/\partial\zeta$, are finite in our development, abrupt changes (discontinuities) in the thermal effusivity at the sample surfaces (or at any other depth in the sample) do not appear in the $M_t(\zeta)$. These discontinuities are introduced through the ratios, π. If the thermal admittance at the surface were considered to be continuous in z, with a steep, but finite, slope, the surface thermal barriers could then be included in $M_t(\zeta)$, and the whole space, including the sample and regions G and B, could be considered to be one thermal body with spatially varying thermal properties.

G. DEPENDENCE ON β, κ, AND C

In our calculations, the parameters, κ, and C, appear only as a ratio, κ/C (in μ), or as a product, κC (in y and in e).

Also, except for its appearance in the propagation factor, $\exp(-\int\beta\, d\zeta)$, β appears only in the product, $\varepsilon = \beta\mu$. The concise form that photothermal equations take when ε, μ, and y (instead of κ, β, and C) are used as the optical and thermal parameters indicates the basic nature of these combinations. It also shows that thermal effusivity must be taken into account as well as the thermal diffusion length when analyzing heat flow. The fact that β almost always appears in the ratio $\mu/\beta^{-1} = \beta\mu = \varepsilon$ shows the close relationship between optical and thermal properties in producing harmonic heat flow and indicates that many photothermal features depend only on the ratio of these quantities and not on the value of either one individually. The fact that the modulation frequency appears only in combination with thermal capacity (as $j\omega C$) indicates that only those effects involving heat capacity are frequency dependent.

Replacing the parameters, ε, μ, with β, κ, and C, the barrier density, $M_t(\zeta)$, becomes $M_t(\zeta) = (2C)^{-1}\partial C/\partial\zeta + (2\kappa)^{-1}\partial\kappa/\partial\zeta$ indicating that logarithmic changes in κ and C are equally effective in creating thermal barriers, and that changes in κ and C produce changes of like sign in M. [This same dependence on κ and C is also evident in locally excited heterogeneous samples with local homogeneity. (Ref 10.)] Since the internal thermal barriers are not related to the generation of heat, they are independent of changes in the sample's optical absorption properties.

The effect of heterogeneity on the heat-generated temperature distribution, $\Omega(z)$, is more complicated. The weighting factor,

$\vec{S}$, (eqn. 14) has a simple dependence on effusivity, but its dependence on ε depends upon the degree of optical saturation. When the sample is unsaturated,

$$|\varepsilon| << 1, \text{ and } \begin{vmatrix} \varepsilon^{-}/\varepsilon^{+} \\ \varepsilon^{+}/\varepsilon^{-} \end{vmatrix} \rightarrow \begin{vmatrix} 1 \\ 1 \end{vmatrix} = \vec{J}_{+}$$

and,

$$\vec{S} = \tfrac{1}{2}[(\partial e/e\partial\zeta - \partial\varepsilon/\varepsilon\partial\zeta)\ \vec{J}_{+}] = \tfrac{1}{2}[(e\varepsilon)^{-1}\partial(e\varepsilon)/\partial\zeta\ \vec{J}_{+}]$$

$$= -\tfrac{1}{2}[(\partial\beta/\beta\partial\zeta - \partial C/C\partial\zeta)\ J_{+}].$$

But if the sample is saturated,

$$|\varepsilon| >> 1, \text{ and } \begin{vmatrix} \varepsilon^{-}/\varepsilon^{+} \\ \varepsilon^{+}/\varepsilon^{-} \end{vmatrix} \rightarrow -\vec{J}_{+},$$

and,

$$\vec{S} = \tfrac{1}{2}[(\partial e/e\partial\zeta + \partial\varepsilon/\varepsilon\partial\zeta)\ \vec{J}_{+}] = \tfrac{1}{2}[(e/\varepsilon)\ (\partial(e/\varepsilon)/\partial\zeta)\ \vec{J}_{+}]$$
$$= \tfrac{1}{2}[\partial\beta/\beta\partial\zeta + \partial\kappa/\kappa\partial\zeta]\ \vec{J}_{+}.$$

Thus at the depths where the sample is optically unsaturated, the simple homogeneous temperature pattern is distorted by spatial variations in optical absorption and thermal capacity only. And, at depths where the sample is optically saturated, it is distorted by spatial variations in optical absorption and thermal conduction only (Figure 5). (See ref. 10 for similar relationships in heterogeneous sample with local homogeneity).

In general, then, in a heterogeneous sample the simple homogeneous temperature pattern is distorted by spatial changes in β, at all depths where the fundamental wave is significant, but distortion produced by spatial changes in κ and C at a particular depth depends upon the degree of optical saturation at that depth.

H. DISCRETE OPTO/THERMAL BARRIERS

The temperature at the upper surface of a sample depends upon the collective magnitudes and phases of all of the thermal waves evaluated at the upper sample surface. This can be seen most easily in homogeneous samples, where, if the determinants in eqn. 10 are expanded, we obtain

$$[15] \quad T_s=[(1+\rho_g)/2][\varepsilon^-(\Omega_0-\Omega_L\Lambda^{-1})-\rho_b\varepsilon^+(\Omega_0\Lambda^{-2}-\Omega_L\Lambda^{-1})]/(1-\rho_b\rho_g\Lambda^{-2})$$

where $\Lambda^{-1}=\exp(-\gamma L)$.

Each term in eqn. 15 is associated with a particular discontinuity in y or Γ (i.e., with a particular thermal wave), and each discontinuity (thermal wave) is represented by a term in eqn 15.

If we consider the sample plus regions G and B to comprise a single physical continuum with varying optical and thermal properties, two fundamental discontinuities always exist at the sample surfaces regardless of whether there is a thermal mismatch at these surfaces or not since, moving in the z-direction, the spatial rate at which heat is generated changes abruptly as we enter and leave the sample. To see the effect of these surface opto/thermal barriers, we temporarily assume that there are no thermal barriers at the sample surfaces (i.e., ρ_b, $\rho_g = 0$). The temperature at the upper surface then reduces to

$$[16] \qquad T_s = \varepsilon^-(\Omega_0 - \Omega_L \Lambda^{-1})/2 = \varepsilon^- \Gamma I(1-\Lambda^{-1}\exp(-\beta L))/2$$

The first term in the bracket results from a heat-source, or fundamental, discontinuity at the upper surface with propagation factor, 1 (since it originates at this surface). The second term comes from the heat source, or fundamental, discontinuity at the lower surface (with propagation factors, exp(-βL) and Λ^{-1}.

The factor 1/2 in eqn. 16 arises from the absence of a thermal barrier at the upper sample surface. Consequently, heat flows into region G equally as well as into the sample. If the thermal wave is totally reflected at the upper surface), (i.e. $\rho_g = 1$) then $(1+\rho_g)/2 = 1$ (instead of 1/2), and all heat generated near the upper surface of the sample remains within the sample.

If we now insert a thermal barrier ($\rho_b \neq 0$) at z = L, thermal waves are reflected at this surface, and two additional terms appear,

$$[17] \qquad \rho_b[-\varepsilon^+\Omega \, \Lambda^{-2} + \varepsilon^+\Omega \, \Lambda^{-1}\exp(-\beta L)]$$

The first term originates at the thermal mismatch at z=0 and has a "reflective" propagation factor, Λ^{-2}, indicating two passages through the sample (i.e., reflection from the lower surface) while the second term, created by a thermal mismatch at $z = L$, has a propagation factor, Λ^{-1}, indicating a single passage through the sample.

Multiple reflections occur when ρ_b and ρ_g are both non-zero and are introduced, mathematically, by the term, $\rho_g \rho_b \Lambda^{-2}$. in the denominator of eqn. 15.

Eqn. 16 can be put in another form which parallels the formulation for heterogeneous materials. At the upper surface $\varepsilon^{-}\Omega_0 = \Delta(\varepsilon^{-}\Omega)_0$ is the incremental change in $\varepsilon^{-}\Omega(z)$ as we move through this interface in the positive z direction, while $-\varepsilon^{-}\Omega_L = \Delta(\varepsilon^{-}\Omega)_L$, is the incremental change in $\varepsilon^{-}\Omega(z)$ at $z = L$ as we move through this interface also in the positive direction.

Using this notation, eqn. 16 becomes

$$[18] \qquad T_s = 1/2\ [\Delta(\varepsilon^{-}\Omega)_0 + \Delta(\varepsilon^{-}\Omega)_L \Lambda^{-1}].$$

To summarize -- each term in the sample surface temperature is associated with a particular thermal wave which is generated at some thermal or optical discontinuity in the sample, and each discontinuity in the sample contributes a term in T_s. An opto/thermal discontinuity always exist at the two sample surfaces if heat is generated only within the sample. In heterogeneous samples, the discrete surface thermal barriers are augmented by a continuum of thermal and opto/thermal barriers within the sample bulk.

SUMMARY AND CONCLUSIONS

In photothermal applications using broad beam illumination, heat flow in samples whose thermal and optical parameters vary in one dimension only may be interpreted in terms of a continuum of opto/thermal and thermal barriers. At each depth in the sample (including the sample surfaces) wherever the ratio of the thermal diffusion length to the optical absorption length varies, an opto-/thermal barrier is created. Similarly, wherever the thermal effusivity varies with depth, a thermal barrier is created. In heterogeneous samples, a continuum of such barriers exist, resulting in a continuum of reflected thermal waves.

The source term in the temperature distribution can also be considered to be a thermal wave. The strength of this (fundamental) wave describes how effectively a harmonic heat source produces a harmonic temperature in a particulatr thermal environment. In homogeneous samples, this strength is spatially uniform. In a heterogeneous sample, it varies with depth. Thermal barriers can also be interpreted in terms of spatial changes in the strength of the fundamental wave.

The effect of an opto/thermal barrier at a particular depth depends upon the degree of optical saturation at that depth. At all depths where the fundamental wave is significant, spatial changes in β are important. At optically saturated depths, it also depends upon spatial changes in κ, while at depths that are unsaturated, it depends on spatial changes in C.

Although the complexity of heterogeneous heat flow will always make its analysis difficult in photothermal applications, viewing this flow pattern in terms of heat barriers provides a useful, intuitive, guide for working with these problems.

ACKNOWLEDGEMENT: This work has been jointly supported by the U.S. Naval Sea Systems Command and the U.S. Army Research Office under contract No. N00024-85-C-5301.

APPENDIX

We consider a sample whose optical and thermal properties are spatially uniform in the transverse (x,y) plane, but vary with depth. We further assume that β, κ, and C are continuous functions of z, that their derivatives, $\partial C/\partial z$, $\partial\kappa/\partial z$, and $\partial\beta/\partial z$, exist and are piecewise continuous, and that broad beam excitation is used so that heat flow is one-dimensional.

We initially divide the sample into n+1 zones, each of width Δz, and assume that the thermal and optical parameters are spatially uniform within each zone, but, in general, differ from zone to zone. Since each zone is homogeneous, its temperature and flux is given by eqn. 2 as long as z is measured downward from the upper surface of the zone.

Energy absorption in preceding zones must be taken into account. If I_0 is the beam intensity at z = 0, then,

$$I_n = I_0 \exp(-\sum_{k=0}^{n-1} \beta_k \Delta z),$$

[A1] $$\Omega_n(0) = \Gamma_n I_0 \exp(-\sum_{k=0}^{n-1} \beta_k \Delta z),$$

and $$\Omega_n(\zeta) = \Omega_n(0) \exp(- \beta_n \zeta).$$

The arbitrary constants, $\vec{T} = \begin{vmatrix} T^1 \\ T^2 \end{vmatrix}$, in each zone can be determined by satisfying boundary conditions at the zone's upper and lower surfaces. In particular, at the interface of zones m and m+1, $\vec{\tau}_{m+1}(0) = \vec{\tau}_m(\Delta z)$ (Figure 6).

Solving for $\vec{T}_{m+1}$,

$$\vec{T}_{m+1}(0)=J^{-1}\begin{vmatrix} 1 & 0 \\ 0 & \pi_m \end{vmatrix} J\, \vec{T}'_m(\Delta z)+J^{-1}[\begin{vmatrix} 1 & 0 \\ 0 & \pi_m \end{vmatrix} \vec{g}_m \Omega'_m(\Delta z) - \vec{g}_{m+1}\Omega_{m+1}(0)]$$

where $\pi_m = y_{m+1}/y_m$.

If the thermal and optical properties of these zones differ only incrementally ($y_{m+1} = y_m + \Delta y_m$), and

[A2] $$\vec{T}_{m+1}=[I+Q\Delta y_m/2y_m]\vec{T}'_m(\Delta z)-[\vec{\varepsilon}_{m+1}\Omega'_{m+1}-\vec{\varepsilon}_m\Omega_m(\Delta z)]/2 +\varepsilon_m \vec{J}_- \Delta y_m/2y_m\Omega_m$$

where I is the unit matrix and $Q= \begin{vmatrix} 1 & -1 \\ -1 & 1 \end{vmatrix}$.

Thus,

$$\Delta\vec{T}_m = Q\,\vec{T}_m\,(\Delta y/2y)_m - \Delta(\vec{\varepsilon}\,\Omega_m/2) - \varepsilon_m\,\vec{J}_-\,(\Delta y/2y)_m\,\Omega_m\,.$$

We find Φ and $\vec{\psi}$ by iterating eqn. A2, retaining terms to first order in Δz only, and letting $\Delta z \rightarrow 0$. Determining $\vec{T}_L$ in terms of $\vec{T}_0$, we find that

$$\Phi = E(0L)\,\phi \qquad \phi = I - \int_0^L \begin{vmatrix} 1 & \eta(\zeta) \\ \eta^{-1}(\zeta) & 1 \end{vmatrix} (\partial e/2e\partial\zeta)\;d\zeta$$

and

$$[A3]\quad \vec{\Psi} = \int_0^L E(\zeta L)[\varepsilon(\zeta)\Gamma(\zeta)\,(\partial e/2e\partial\zeta)\,\vec{J}_- - \partial(\vec{\varepsilon}\Gamma)/\partial\zeta]\,I_0 \exp(-\beta(\zeta)\zeta)d\zeta.$$

Here $E(ab) = \begin{vmatrix} \Lambda(ab) & 0 \\ 0 & \Lambda^{-1}(ab) \end{vmatrix}$, $\Lambda(ab) = \exp(\int_a^b \gamma(\zeta)\,d\zeta)$,

and $\eta = -\exp(-2\int_0^\zeta \gamma(z)\,dz)$.

In the limit, eqn. A1 becomes

$$\Omega(z) = \Gamma(z)\,I_0 \exp(-\int_0^z \beta\,d\zeta) \quad \text{and} \quad \Omega(L) = \Gamma(L)\,I_0 \exp(-\beta_{avg}L).$$

The many similar features of heterogeneous and homogeneous temperature patterns makes it possible to separate the surface temperature of a heterogeneous sample into two parts, $T_s = T_{hom} + T_{het}$, where T_{het} specifically describes heterogeneous effects, and T_{hom} is identical to the homogeneous solution for a sample whose reciprocal thermal diffusion length and optical absorption constant are equal to the corresponding spatially averaged values of these quantities in the heterogeneous sample. T_{het} will not be given here because of its complexity, but it can be obtained by a straight forward, but algebraically complicated, reordering of the terms in eqn. 10.

Figure Captions

1. A symbolic representation of the reflected and fundamental (or heat-generated) thermal waves, indicating terminology and wave characteristics.
2. The n+1-level structure used as a starting point in the analysis of a heterogeneous sample with properties varying with depth only. Each level is assumed to be internally homogeneous with similar temperature patterns, but different parameters. The temperature and thermal flux is given for a typical, i th level.
3. Surface bulk effects can be separated by matching temperature and thermal flux at sample surfaces while leaving bulk properties in terms of a generalized propagation factor, Φ, and internally generated reflected waves, $\vec{\psi}$.
4. A diagramatic comparison of thermal wave propagation in heterogeneous and homogeneous samples.
5. A comparison of thermal and opto/thermal barriers. Opto/thermal barriers are characterized by a change (or fluctuation) in the effectiveness of a harmonic heat source in producing a harmonic temperature, and thus these barriers can also be called Heat Source Fluctuation Barriers.
6. Matching temperature and thermal flux at an arbitrary depth, ζ, relates the undetermined constants in adjacent levels. By iteration, $\vec{T}_L$ can be expressed in terms of $\vec{T}_0$, giving Φ and $\vec{\psi}$.

References

1. L. C. Aamodt, J. C. Murphy, and J. G. Parker. J. Appl. Phys. 48. 927(1977).
2. A. Rosencwaig and A. Gersho. J. Appl. Phys. 47. 64(1976).
3. W. P. Leung and A. C. Tam. Optics Letters. 9. 93(1984).
4. P. E. Nordal and S. O. Kanstad. Appl. Phys. Lett. 38. 486(1981).
5. N. M. Amer and M. A. Olmstead. Surf Sci. 132. 168(1983).
6. R. L. Thomas, L. D. Favro, K. R. Grice, L. J. Inglehart, P. K Kuo, and L. Lhota. Proceedings of the 1982 Ultrasonic Symposium edited by B. R. McAvoy, NY, 1982, page 586.
7. J. C. Murphy and L. C. Aamodt. J. Appl. Phys. 51. 4580(1980); 52. 4903(1981)
8. A. C. Boccara, D. Fournier, and J. Badoz. Appl. Phys. Lett. 36. 130(1980).
9. W. B. Jackson, N. M. Amer, A. C. Boccara, and D. Fournier. Appl. Opt. 20. 1333(1981).
10. L. C. Aamodt and J. C. Murphy. J. Appl. Phys. 54. 581(1983).
11. F.A. McDonald and G. C. Wetzel, Jr. J. Appl. Phys. 49. 2313(1978).
12. Rosencwaig, Allan. Ultrason. Symp. Proc. 1980, 2, 600-7

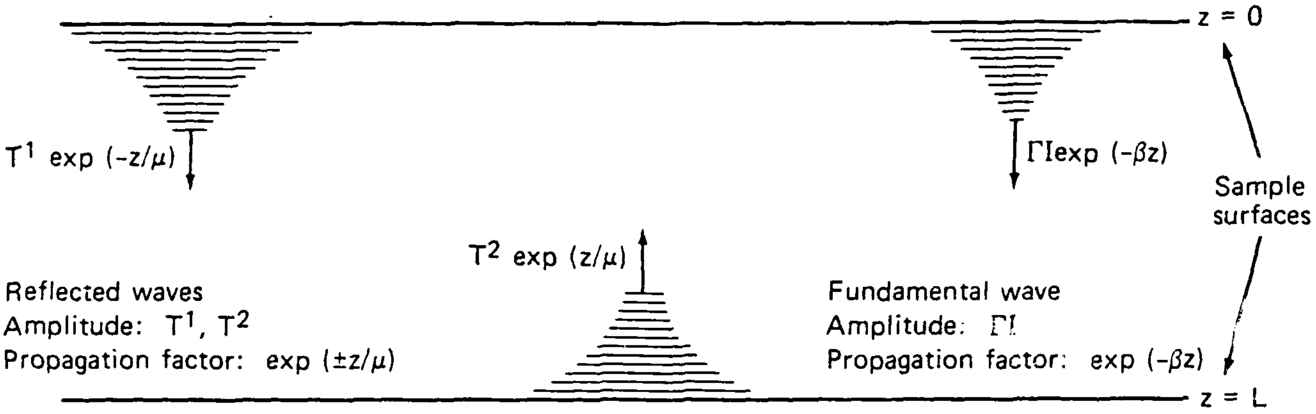

Propagation factor:
Reflected waves: complex, function of thermal properties only
Fundamental wave: real, function of optical properties only

Interpretation of homogeneous heat equation in terms of thermal waves

Figure 1

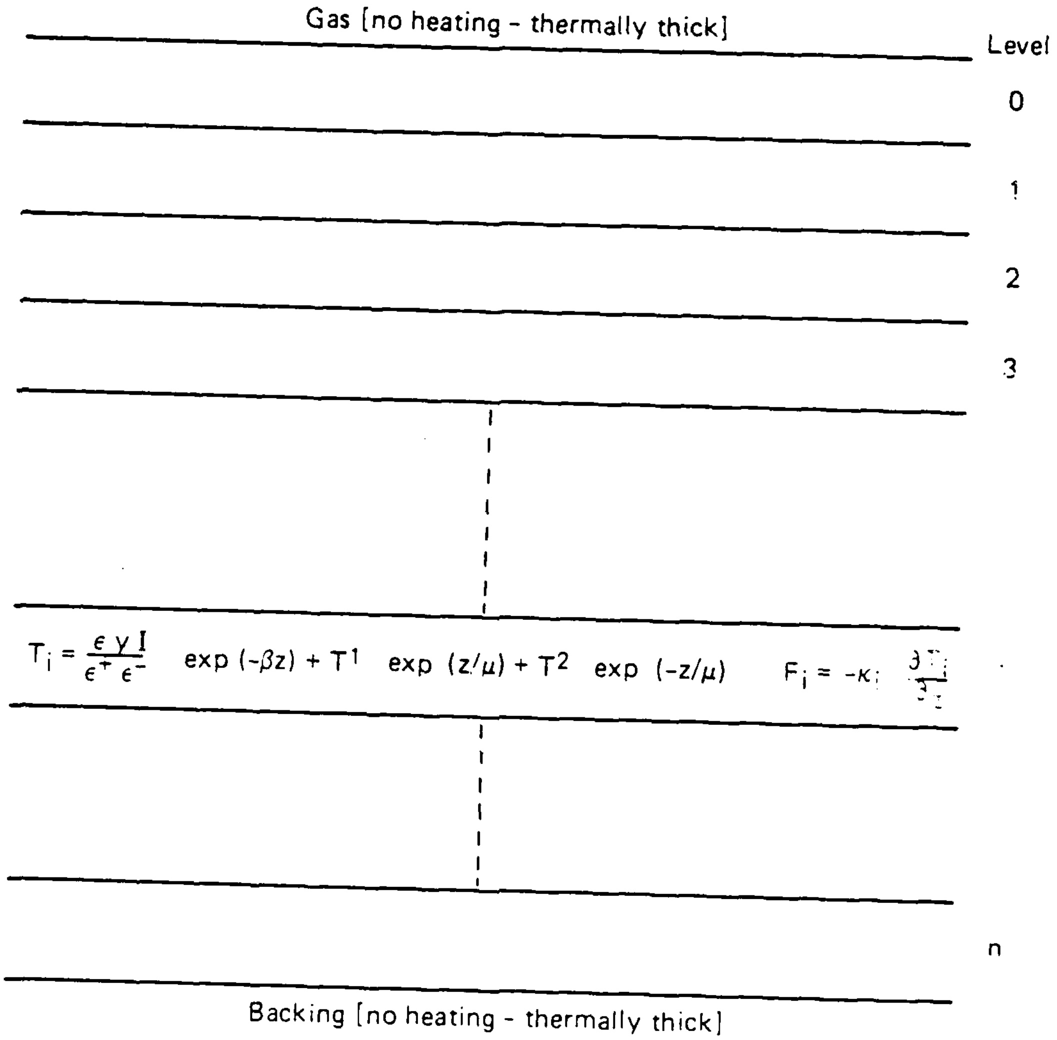
Gas [no heating - thermally thick]
Level
0
1
2
3
$T_i = \frac{\epsilon \gamma I}{\epsilon^+ \epsilon^-} \exp(-\beta z) + T^1 \exp(z/\mu) + T^2 \exp(-z/\mu)$
$F_i = -\kappa_i \frac{\partial T_i}{\partial z}$
n
Backing [no heating - thermally thick]

Figure 2

AD-A175 487 PHOTOTHERMAL IMAGING OF DEFECTS IN METALS AND CERAMICS 3/3
(U) JOHNS HOPKINS UNIV LAUREL MD APPLIED PHYSICS LAB
J C MURPHY ET AL OCT 86 JHU/APL/RC-TPS-012
UNCLASSIFIED ARO-21066I 11-MS N00024-85-C-5301 F/G 11/6 NL

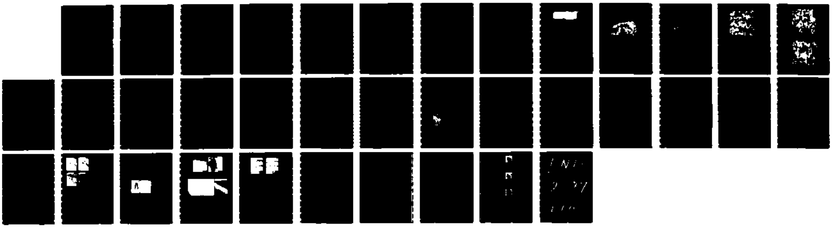

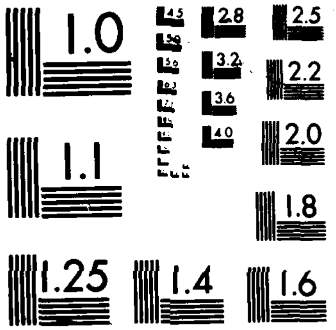

CROCOPY RESOLUTION TEST CHART

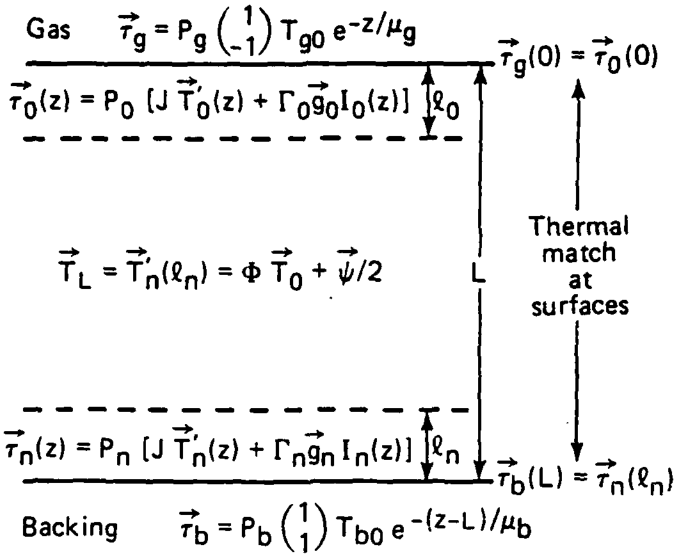
Gas
$\vec{\tau}_g = P_g \begin{pmatrix} 1 \\ -1 \end{pmatrix} T_{g0}\, e^{-z/\mu_g}$
$\vec{\tau}_g(0) = \vec{\tau}_0(0)$
$\vec{\tau}_0(z) = P_0\, [J\, \vec{T}'_0(z) + \Gamma_0 \vec{g}_0 I_0(z)]$
ℓ_0
$\vec{T}_L = \vec{T}'_n(\ell_n) = \Phi\, \vec{T}_0 + \vec{\psi}/2$
L
Thermal match at surfaces
$\vec{\tau}_n(z) = P_n\, [J\, \vec{T}'_n(z) + \Gamma_n \vec{g}_n\, I_n(z)]$
ℓ_n
$\vec{\tau}_b(L) = \vec{\tau}_n(\ell_n)$
Backing
$\vec{\tau}_b = P_b \begin{pmatrix} 1 \\ 1 \end{pmatrix} T_{b0}\, e^{-(z-L)/\mu_b}$

Figure 3

Comparison of Thermal Wave Propagation in Homogeneous and Heterogeneous Materials

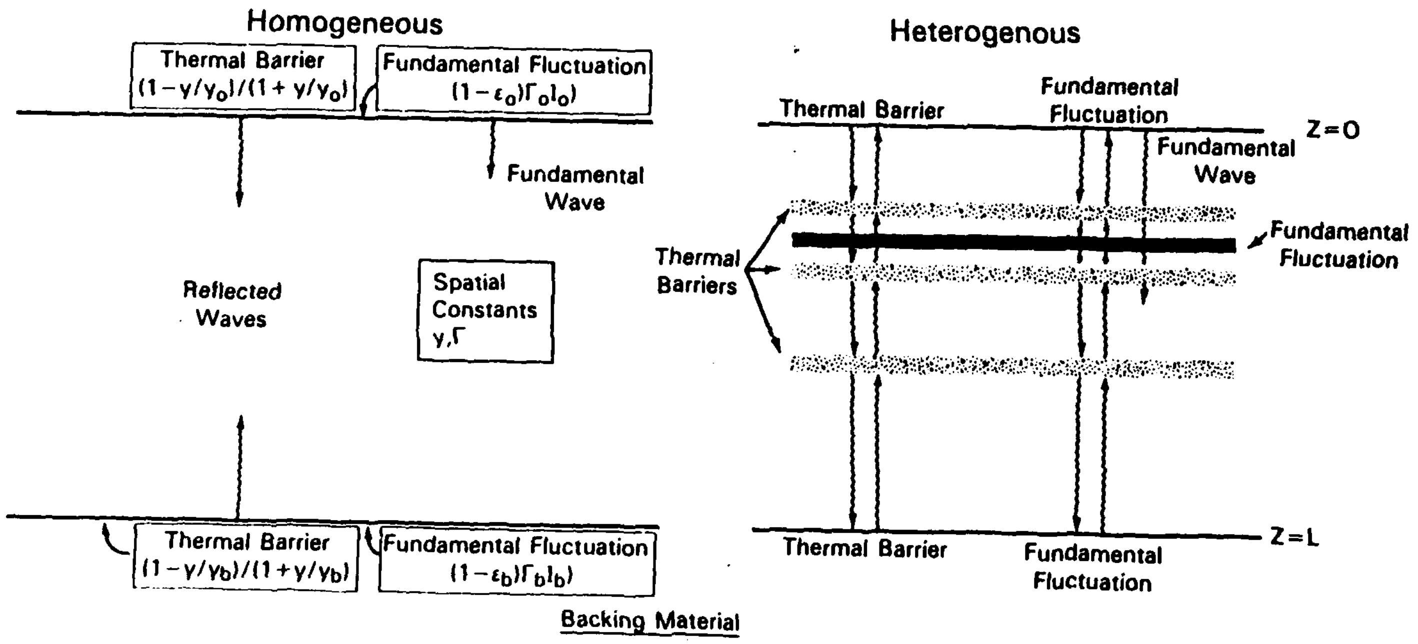

γ_b = Thermal admittance of backing
γ_o = Thermal admittance of media at upper surface

A fundamental fluctuation usually occurs at all thermal barriers but a heat source fluctuation can occur where there is no thermal barrier if β changes only.

Figure 4

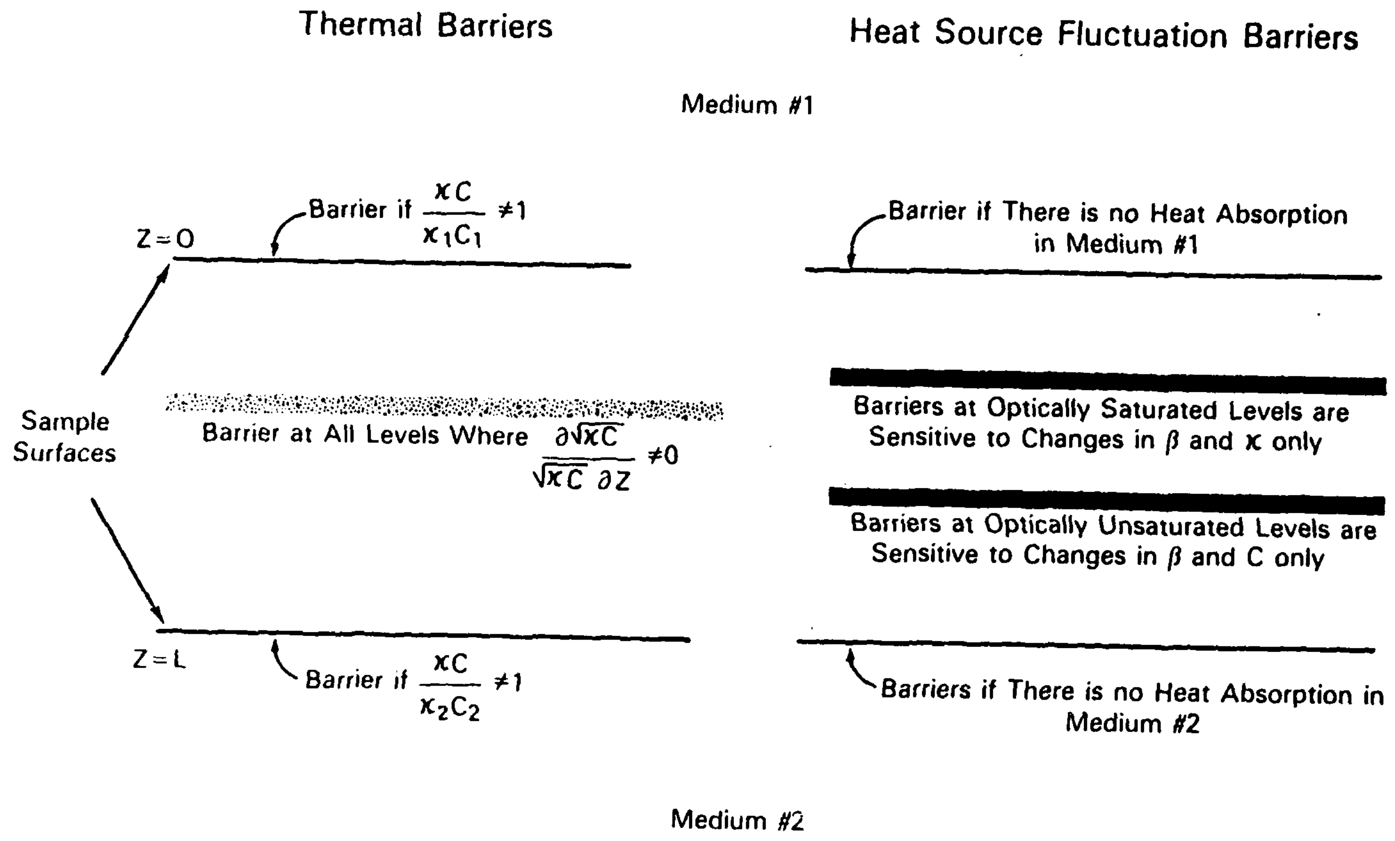
Thermal Barriers
Heat Source Fluctuation Barriers
Medium #1
Z=O
Barrier if $\frac{\kappa C}{\kappa_1 C_1} \neq 1$
Barrier if There is no Heat Absorption in Medium #1
Sample Surfaces
Barrier at All Levels Where $\frac{\partial \sqrt{\kappa C}}{\sqrt{\kappa C}\, \partial Z} \neq 0$
Barriers at Optically Saturated Levels are Sensitive to Changes in β and κ only
Barriers at Optically Unsaturated Levels are Sensitive to Changes in β and C only
Z=L
Barrier if $\frac{\kappa C}{\kappa_2 C_2} \neq 1$
Barriers if There is no Heat Absorption in Medium #2
Medium #2

Figure 5

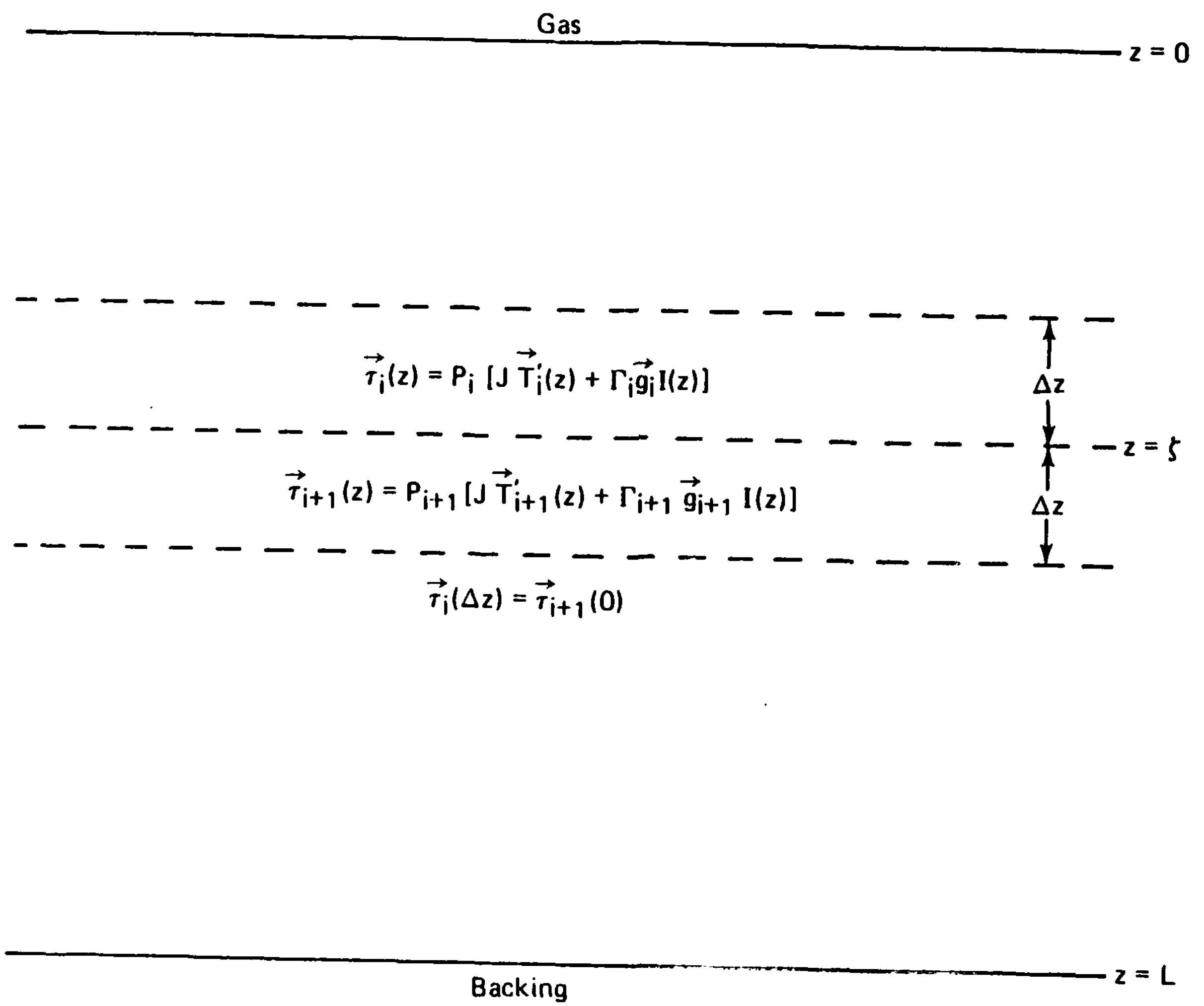
Gas
z = 0
$\vec{\tau}_i(z) = P_i\,[J\,\vec{T}_i'(z) + \Gamma_i \vec{g}_i I(z)]$
Δz
z = ζ
$\vec{\tau}_{i+1}(z) = P_{i+1}\,[J\,\vec{T}_{i+1}'(z) + \Gamma_{i+1}\,\vec{g}_{i+1}\,I(z)]$
Δz
$\vec{\tau}_i(\Delta z) = \vec{\tau}_{i+1}(0)$
z = L
Backing

Figure 6

APPENDIX

PHOTOTHERMAL IMAGING OF DEFECTS IN METALS AND CERAMICS

14. G. C. Wetsel, Jr., J. C. Murphy, and L. C. Aamodt, "Non-Destructive Characterization of Coatings on Metal Alloys", Review of Progress in Quantitative NDE, to be published.

QNDE 86

NONDESTRUCTIVE CHARACTERIZATION OF COATINGS ON METAL ALLOYS*

G. C. Wetsel, Jr.†, J. C. Murphy, and L. C. Aamodt
The Johns Hopkins University
Applied Physics Laboratory
Laurel, MD 20707

INTRODUCTION

There is a need to nondestructively evaluate coatings on metal alloys that must endure high-temperature or highly oxidizing environments, such as for aircraft turbine blades. Such coatings are opaque and of the order of 25 μm in thickness. Characteristics of interest include the uniformity and thickness of the coating, which must be sufficient to protect the substrate from oxidation at high temperatures.

In this paper we report the results of measurements on samples of IN 738 alloy substrates covered by AEP 32 coatings. The samples were in the forms of cylindrical reference standards and actual aircraft turbine blades. Characterization methods included photothermal-optical-beam-deflection (PTOBD) imaging [1], optical microscopy, and surface profilometry, with the principal method being the first.

RESULTS

A turbine blade is shown in Fig. 1. The coating has been abrasively removed to the right of the arrow exposing the substrate. Optical micrographs of 1.14 mm × 0.889 mm areas on each side of the boundary indicated by the arrow in Fig. 1 are shown in Fig. 2. The substrate, shown in Fig. 2a, exhibits inclusions typical of metal alloys and scratches (presumably put there by the abrasion process). The coating, shown in Fig. 2b, exhibits a porous, sponge-like appearance. Evidently, the coating is nonuniform.

A transverse PTOBD amplitude contour map of a 1 mm × 1 mm area near the boundary between coated substrate and exposed substrate indicated by the arrow in Fig. 1 is shown in Fig. 3. The boundary is clearly visible as a dark arc across the center of the figure. The exposed substrate is in the upper part of Fig. 3; the coated substrate is in the lower part of Fig. 3. This photothermal image indicates that the coated substrate has thermal inhomogeneities on a scale of 0.1 mm, whereas the exposed substrate is relatively homogeneous.

In Fig. 4, a profilometer scan across the boundary between the exposed substrate and the coated substrate is shown. The surface roughness of the coating can be seen to be greater than the surface roughness of the substrate.

Three standard samples of cylindrical shape were studied: (a) DC#12, 12.1 mm in diameter × 10.5 mm long, with a nominal coating thickness of 38-51 μm; (b) DC#13, 12.1 mm in diameter × 9.6 mm long, with a nominal coating thickness of 25-38 μm long; (c) DC#15, 12.1 mm diameter × 10.5 mm long with a nominal coating thickness of 56-64 μm. Optical micrographs of a 572 μm × 445 μm area of the coating surface are shown for each sample in Fig. 5.

Normal PTOBD amplitude contour maps of a 500 μm × 500 μm area of the coating on the three cylindrical samples are shown in Figs. 6, 8, and 9. In each case, the photothermal images indicate substantial thermal inhomogeneity. The transverse PTOBD amplitude contour map of Fig. 7 should be compared with Fig. 6. The area imaged in Fig. 7 is shifted along the x axis to the left of the imaged area of Fig. 6 by 150 μm. Generally, the thermal inhomogeneities that are so prominent in the normal component of beam deflection of Fig. 6 are not prominent in the transverse component of beam deflection of Fig. 7. The "hot spot" shown near the origin in Fig. 7 is an area not included in the area imaged in Fig. 6.

DISCUSSION

The results of the PTOBD imaging measurements clearly show that in each sample studied the AEP 32 coatings are substantially inhomogeneous. The lateral dimensions of the inhomogeneities may be several times as large as the nominal coating thickness. It is not known at this time if the observed inhomogeneities are due to variations in the coating composition, variations in the coating thickness, variations in heat transfer from coating to substrate (an indication of bonding variation), or all of the above. Surface profilometry reveals that surface topography variations can be of the order of 25% of the nominal coating thickness or greater. Optical micrographs reveal coating variations on a scale consistent with the other two methods of measurement. These coating variations, particularly the thickness variations, are serious potential failure hazards.

---

[*] Supported in part by the Air Force Program in Quantitative Nondestructive Evaluation.

[†] Permanent address: Department of Physics, Southern Methodist University, Dallas, Texas 75275

1. G. C. Wetsel, Jr., J. W. Maclachlan, J. B. Spicer, and J. C. Murphy, "Nondestructive Evaluation and Materials Characterization Using Photothermal-Optical-Beam-Deflection Imaging," Review of Progress in Quantitative Nondestructive Evaluation, Vol. 5A, Ed. by D. O. Thompson and D. E. Chimenti, pp. 713-719, Plenum, New York (1986).

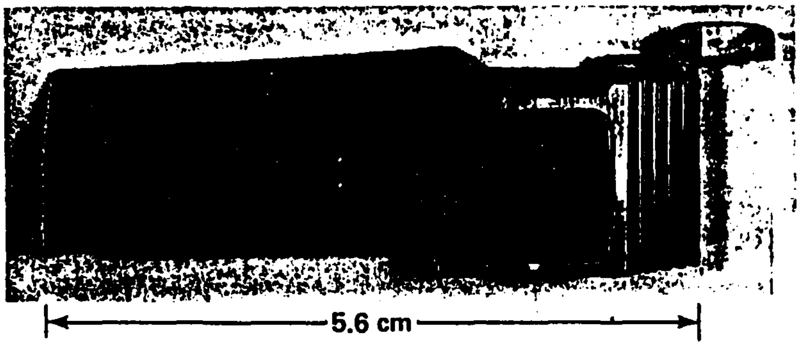

Fig. 1 Photograph of turbine blade: IN 738 alloy substrate, AEP 32 coating.

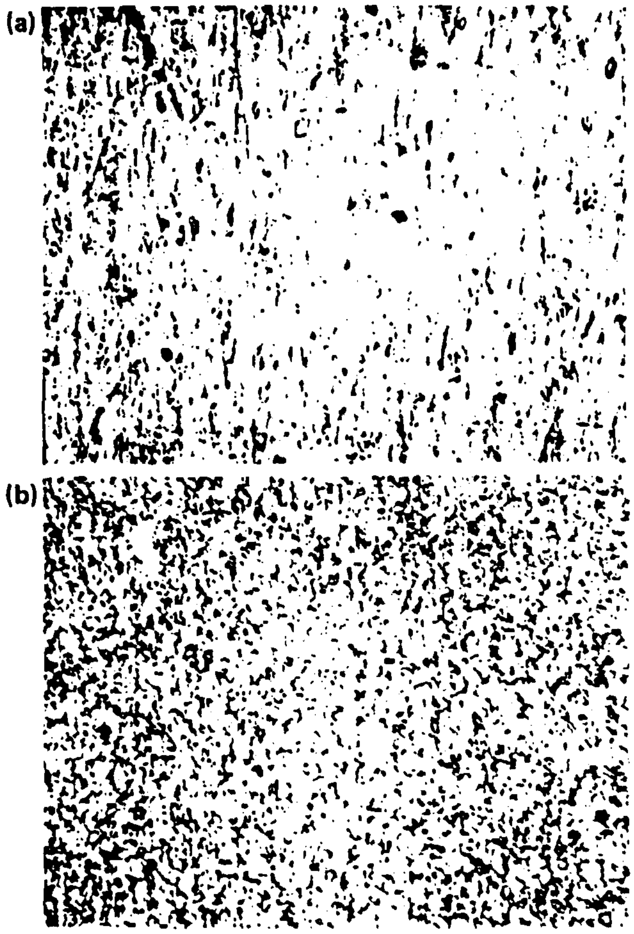

Fig. 2 Optical micrographs of 1.14 mm × 0.889 mm area on turbine blade: (a) substrate, (b) coating.

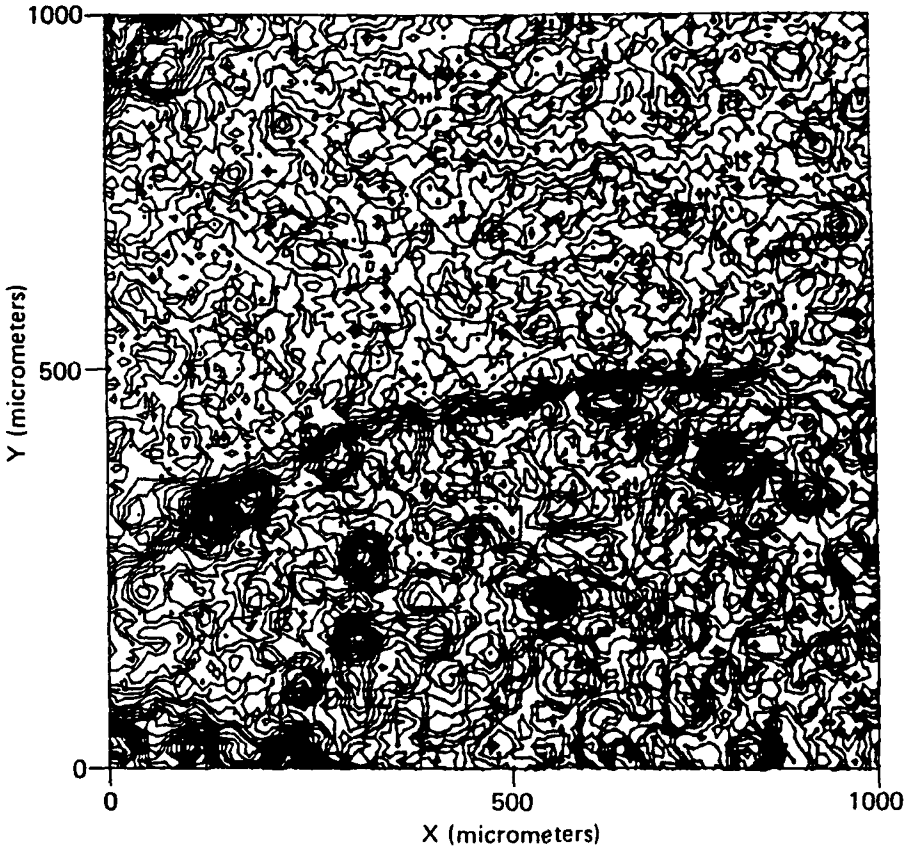

Fig. 3 Transverse PTOBD amplitude contour map of area near substrate-coating interface on turbine blade, f = 2 kHz.

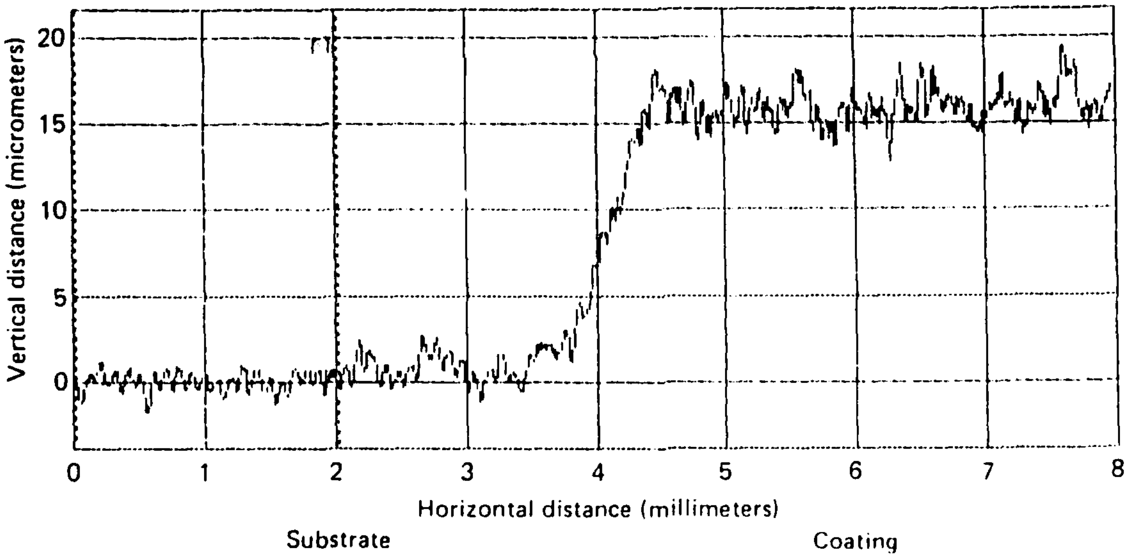

Fig. 4 Profilometer scan across substrate-coating interface on turbine blade.

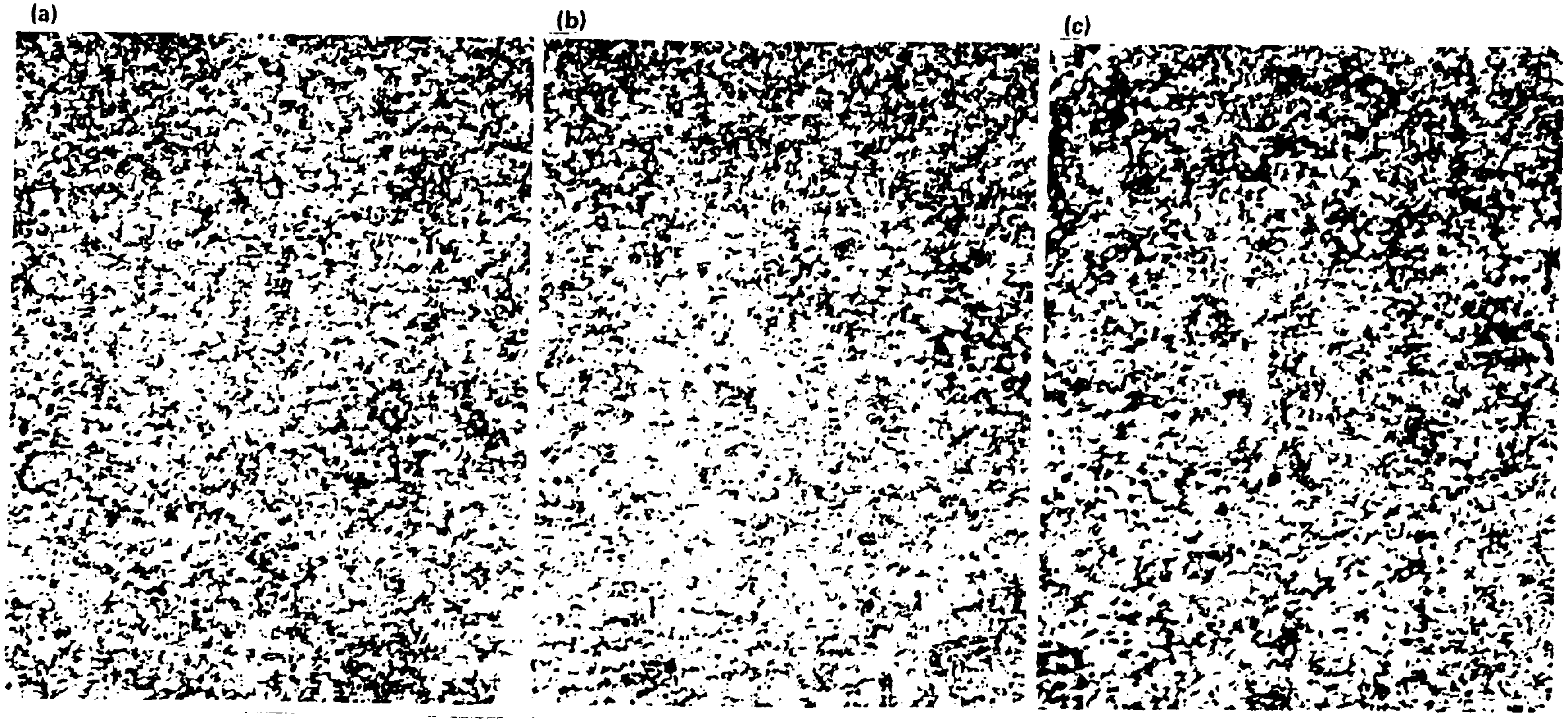

Fig. 5 Optical micrographs of 572 μm × 445 μm area of coating on samples: (a) No. 12, (b) No. 13, (c) No. 15.

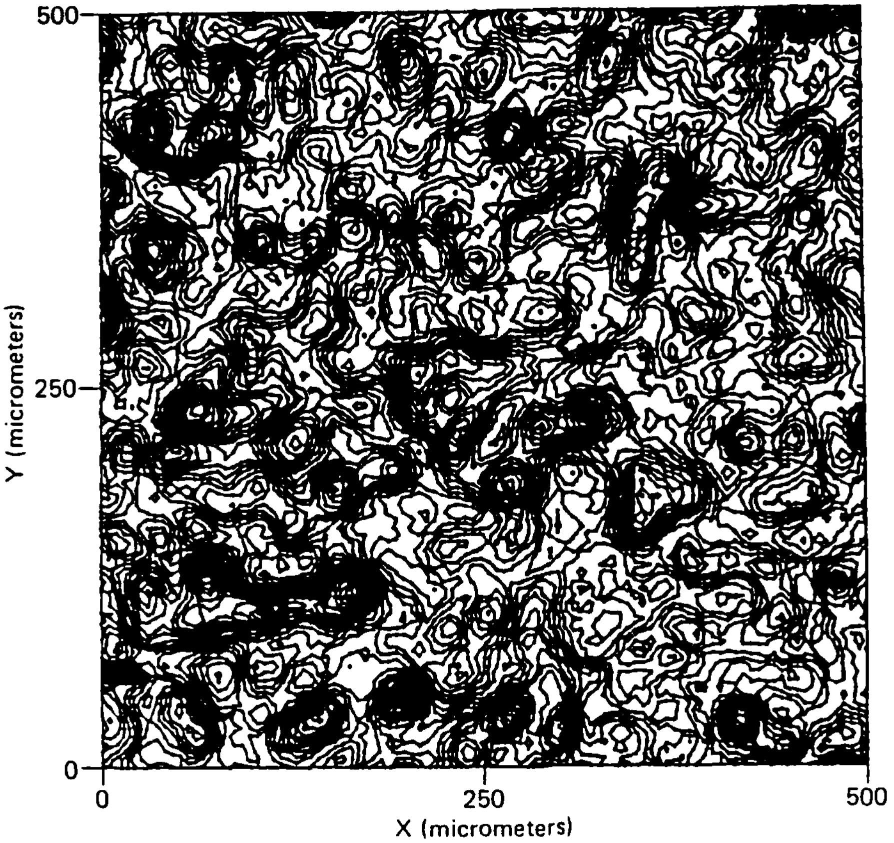

Fig. 6 Normal PTOBD amplitude contour map of 500 μm X 500 μm area of coating on sample No. 12, f = 2 kHz.

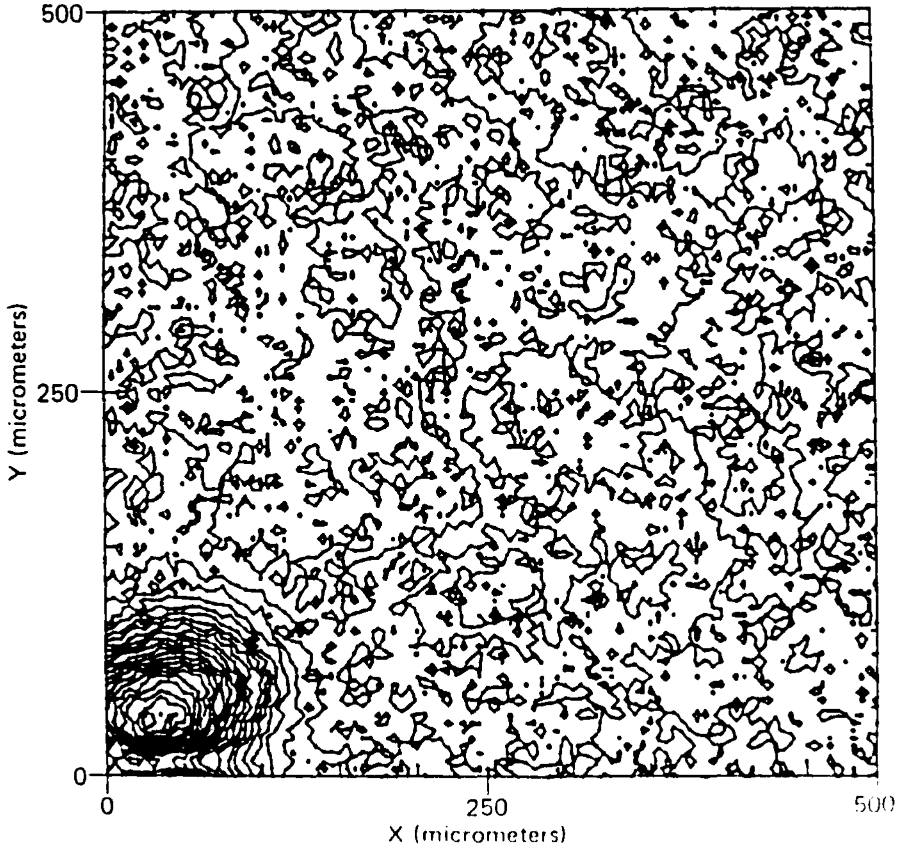

Fig. 7 Transverse PTOBD amplitude contour map of 500 μm × 500 μm area of coating on sample No. 12, f = 2 kHz.

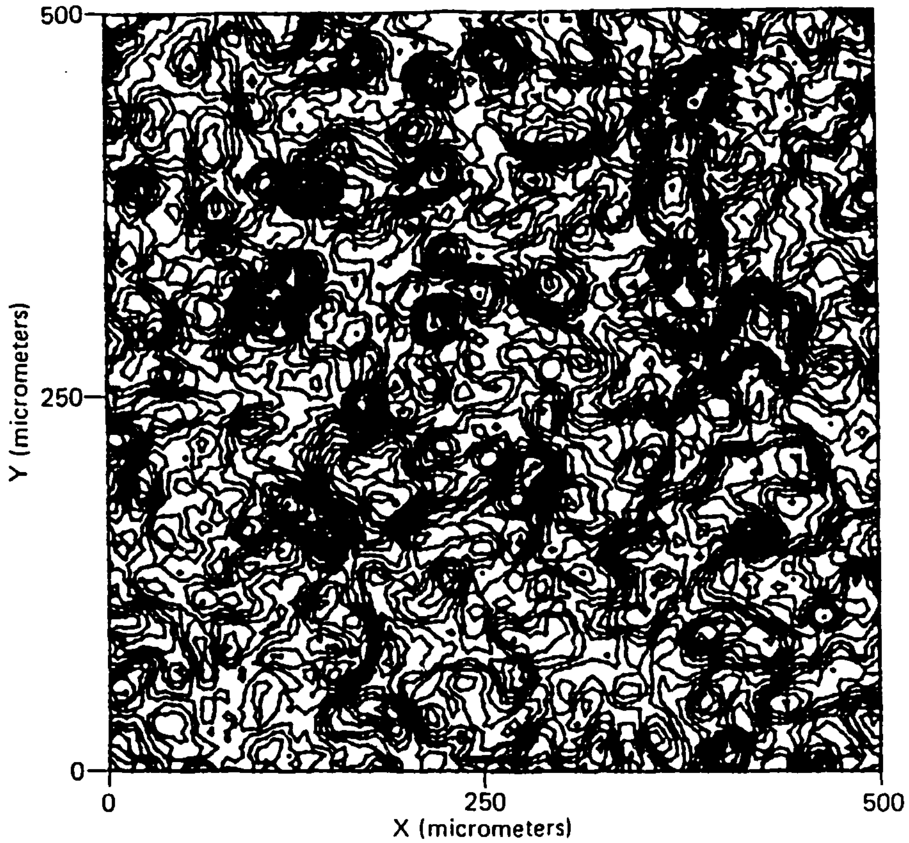

Fig. 8 Normal PTOBD amplitude contour map of 500 μm X 500 μm area of coating on sample No. 13, f = 500 Hz.

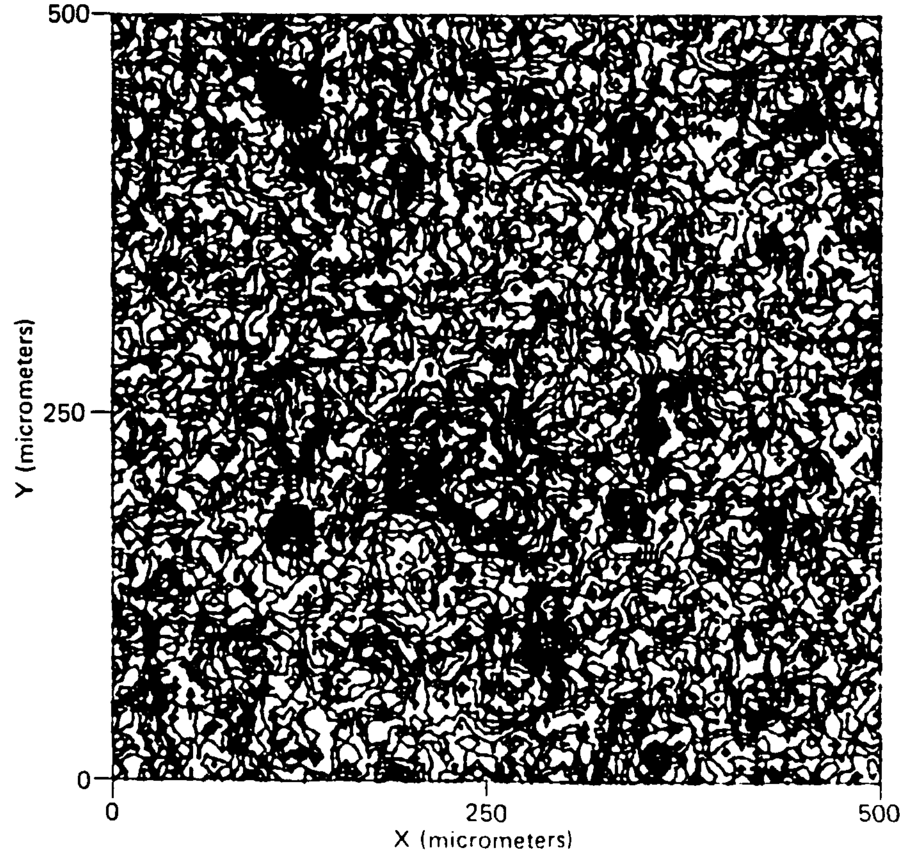

Fig. 9 Normal PTOBD amplitude contour map of 500 μm X 500 μm area of coating on sample No. 15, f = 500 Hz.

APPENDIX

PHOTOTHERMAL IMAGING OF DEFECTS IN METALS AND CERAMICS

15. J. C. Murphy, L.C. Aamodt, and G. C. Wetsel, Jr., "Coating Thickness Determination Using Time Dependent Surface Temperature Measurements," Review of Progress in Quantitative NDE, to be published.

COATING THICKNESS DETERMINATION USING TIME DEPENDENT SURFACE TEMPERATURE MEASUREMENTS

J. C. Murphy, L. C. Aamodt, and G. C. Wetsel, Jr.*

The Johns Hopkins University,
Applied Physics Laboratory
Johns Hopkins Road, Laurel, Md. 20707

INTRODUCTION

Thin film coatings are used to protect metal alloys from oxidation. To be effective they must have adequate thickness and be well bonded to the metal substrate. This is especially important for metals subject to high temperatures or to highly oxidizing environments. As a consequence, there is a need for a non-destructive method for evaluating coating thickness, bonding, and other coating properties.

In this paper we report measurements made on nickel based superalloys (IN 738) coated with an aluminide coatings (AEP 32) using a dynamic thermal method of measurement. In addition, we describe an analysis which could be a convenient means of monitoring the thermal parameters of thin film coatings.

The three samples reported on here were in the form of circular cylinders coated on one end and on the cylinder side. The other end was uncoated. These cylinders were designated as samples DC#12, DC#13, and DC#15 and have the following dimensions: (a) DC#12, 12.1 mm in diameter x 10.5 mm long, with a nominal coating thickness of 38-51 μm; (b) DC#13, 12.1 mm in diameter x 9.6 mm long, with a nominal coating thickness of 25-38 μm; and (c) DC#15, 12.1 mm diameter x 10.5 mm long, with a nominal coating thickness of 56-64 μm. Measurements of the coated and the uncoated ends were made on each sample.

THERMAL MODEL/PHOTOTHERMAL RADIOMETRY

Figure 1 shows the thermal model and terminology that we use. A pulsed light source illuminates the thin coating and is partially reflected. The absorbed light heats the opaque coating surface and heat diffuses into the coating. At the coating-metal interface, a thermal mismatch occurs if the thermal effusivities of the coating and substrate are not identical. [Thermal Effusivity(E) = $\sqrt{(\rho \kappa C)}$ where ρ is the density, κ is the thermal conductivity, and C is the thermal capacity.] When there is no thermal mismatch, heat flows uninterrupted into the sample bulk; otherwise a portion of the heat is reflected back toward the sample surface, while the remainder flows into the metal substrate.

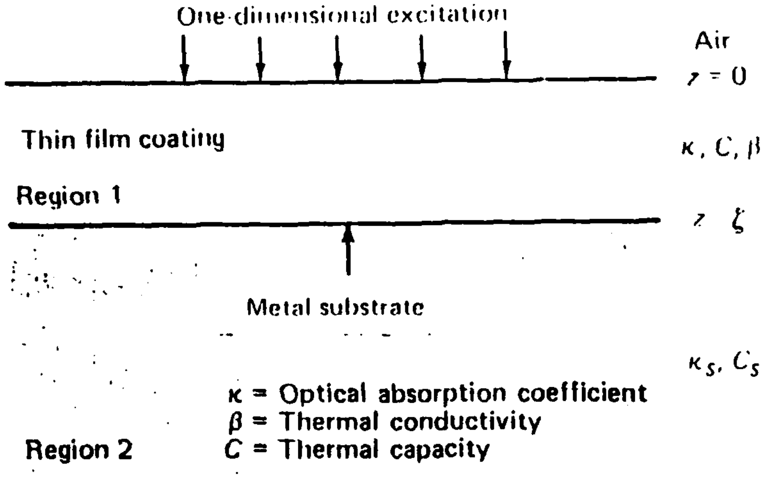

Fig. 1 Thermal model used in this paper - thin coating of thickness ζ on a thermally thick substrate; planer geometry.

If the thermal bonding of the coating to the metal is good, the magnitude of this reflection is determined by the ratio of the thermal effusivities of the coating and the base metal. If the thermal bond is not good, e.g., a void exists, a large heat reflection can be produced by the thermal barrier associated with the disbonding. For partial bonding, the amount of heat reflection lies between these extremes.

The time, τ, that it takes for the reflected heat to return to the sample surface depends upon the thermal diffusivity (= $\kappa/\rho C$) of the coating, the coating thickness, and the distribution of heat generated in the coating (if the coating is not perfectly opaque).

The effect of heat reflection can be seen in Fig. 2. The particular curve identified as $E_b/E_f=1$ is the decay pattern of the surface temperature when there is no thermal mismatch between the coating and the metal substrate (or if the coating were thermally thick). The drop in surface temperature is caused by thermal diffusion into the coating bulk. The initial decay pattern corresponds to diffusion in the coating and is the same for all thermal mismatches. At longer times, the transit time, τ, is approached and the surface temperature decay pattern deviates from the decay pattern of the thick specimen. The direction of the deviation depends upon whether the metal is a better or worse conductor than the coating, while the magnitude of the deviation depends upon the magnitude of the thermal effusivity ratio. Since the temporal surface temperature decay pattern is affected by coating thickness and by bonding quality, a study of this pattern potentially provides a means for determining both of these quantities.

We use photothermal radiometry to measure surface temperature. The general features of this method are seen in Fig. 3. Details of the method can be found in References 1-3 for both CW and pulsed illumination.

IR radiometry theoretically measures the temperature at a point on the sample surface; in actuality, it measures the temperature integrated over a small area on the sample surface determined by the spatial resolution of the detector. The surface radiance of the heated sample (see Fig. 4a) varies with specimen temperature and IR wavelength. The incremental change in radiance with changes in specimen temperature is shown in Fig. 4b. This example corresponds to the experiment reported here where a change in

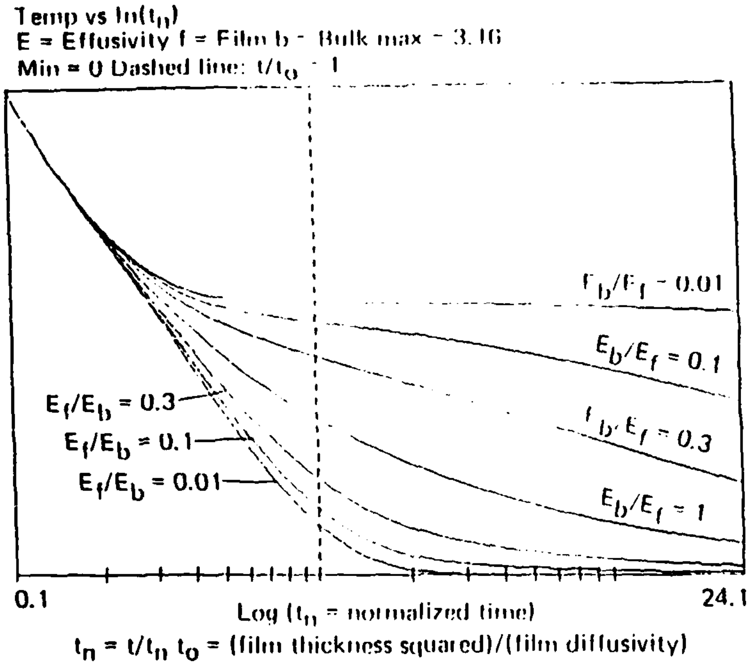

Fig. 2 Theoretical time dependent surface temperature following an instantaneous pulse for several ratios of coating and substrate thermal effusivity.

specimen temperature is induced by modulated laser heating and the resultant change in IR emission is monitored. While the radiance, L(t), is proportional to the fourth power of temperature, $L(t) = \varepsilon(\lambda)\,\sigma\,T^4$, the change in radiance with temperature, $\Delta L(t)$, is linear with the change in surface temperature, ΔT, for small ΔT, i.e., $\Delta I(t) \approx 4\,T^3\,\Delta T$. For homogeneous materials (no coating) the time dependent signal obtained from the IR detector is proportional to the excess surface temperature,

$$T_s(z=0,t) = (\pi\kappa\rho C)^{-1/2} \int_0^\infty \exp[-\beta z - z^2/4\alpha t]\, dz$$

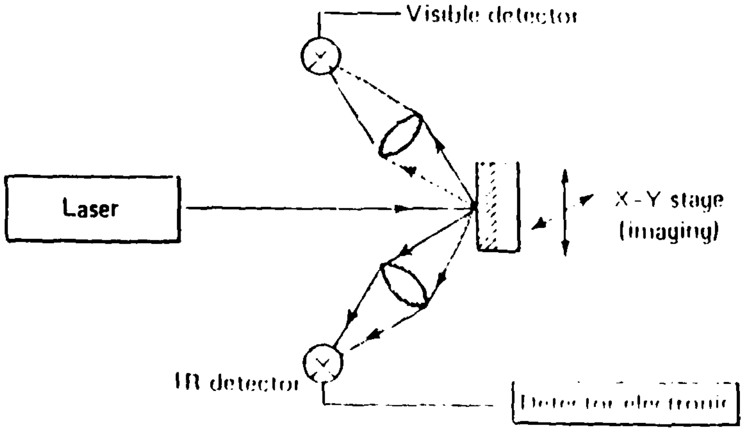

Fig. 3 Experimental IR radiometer arrangement used to obtain temperature data.

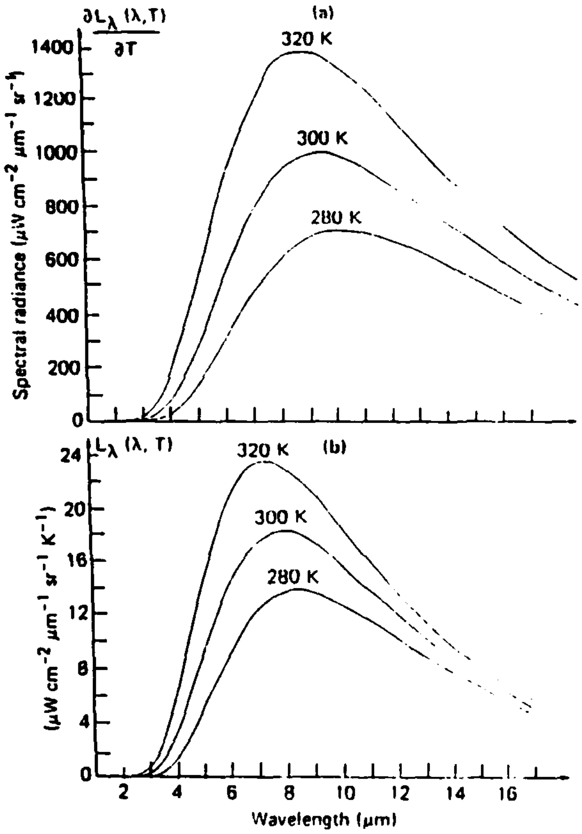

Fig. 4 a) Spectral radiance of a black body. b) First partial derivative of spectral radiance of a blackbody with respect to temperature.

where β is the optical absorption coefficient, α is the thermal diffusivity, and C is the thermal capacity. The first exponential factor is the heat-source profile (with depth) in the sample and the second factor introduces the diffusion time, $z^2/4\alpha$ needed for the heat to flow from a depth z to the sample surface.

EXPERIMENTAL RESULTS

Using the experimental set-up of Fig. 3, we have measured the thermal response under pulsed heating of the three samples described above. The laser was a 30 mJ Nd:Yag laser with a pulse width of approximately $7x10^{-8}$ sec (Fig. 5), which is short compared with the thermal response of the coated and uncoated samples. The IR detector used was a LN_2 cooled HgCdTe detector with a 20 MHz bandwidth and data was stored in a Data Precision Model 6000 transient analyzer with a 100 MHz digitizing rate.

Figure 6 shows the thermal response for the coated ends of the three samples while Fig. 7 shows the corresponding curve for the three uncoated ends. The IR emission from the uncoated samples peak at essentially the same time while the emission from the coated samples shows distinct delays which are correlated with coating thickness. The different response patterns for coated and uncoated samples is also evident in Fig. 8 (for DC#13). This result is typical of the response patterns for the other samples, with the coated sample peaking later than the uncoated sample.

One factor affecting these results is the coating structure and topography which results in non-uniform coating properties and thickness.

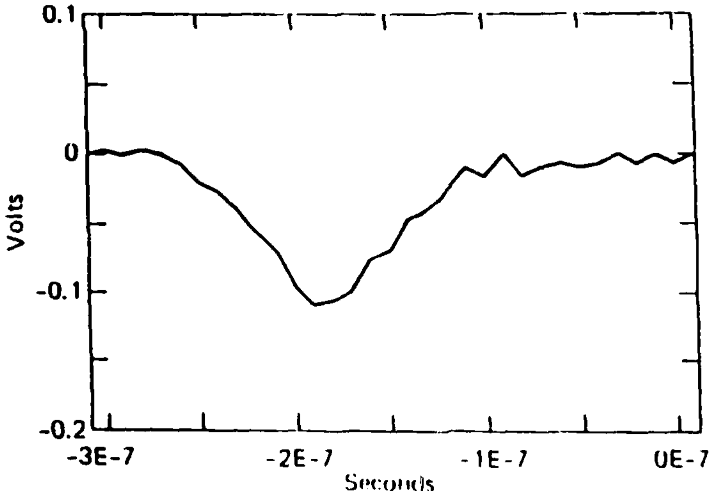

Fig. 5 Intensity of a 30 mJ Nd:Yag laser pulse used to heat samples.

Profilometer scans show variations ranging up to 25% of the nominal coating thickness across the specimen with occasional variations even greater. Coating nonuniformity is evident in Figure 9a,b (for DC#12) which shows an apparent porous, "spongy" texture of the coating surface. These figures are two optical microscope views of the coating surface focused respectively at the top and bottom visible layer of the coating. The estimated texture height from this measurement is 15 microns.

The "porous" appearance of the coating surface suggests that this is the origin of the delay of the thermal peak in the coated samples. Incident radiation is absorbed within the porous structure, and IR emission would emerge from a range of sites. Diffusion processes would also be affected with a more complex process related to the reduced dimensionality of the layers occuring. Quantitative treatment of these issues requires more analysis, which is in progress.

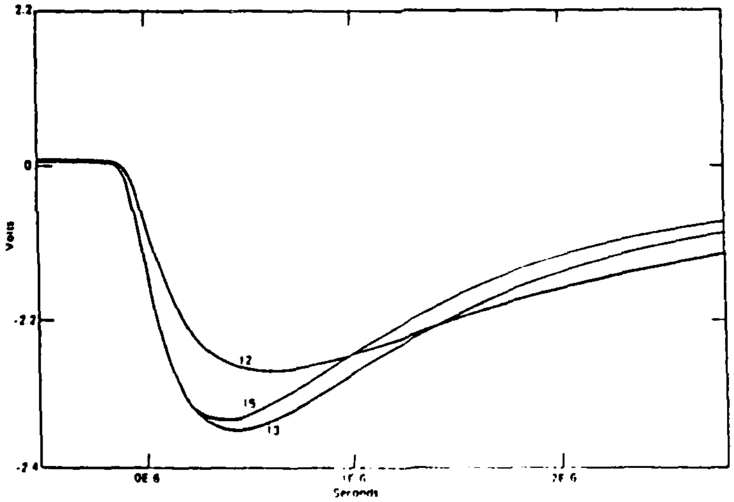

Fig. 6 IR thermal response pattern of three IN 738 specimens DC 12, 13, 15 (Alpak) coating. Nominal thickness 2.0, 1.5, 2.5 mils.

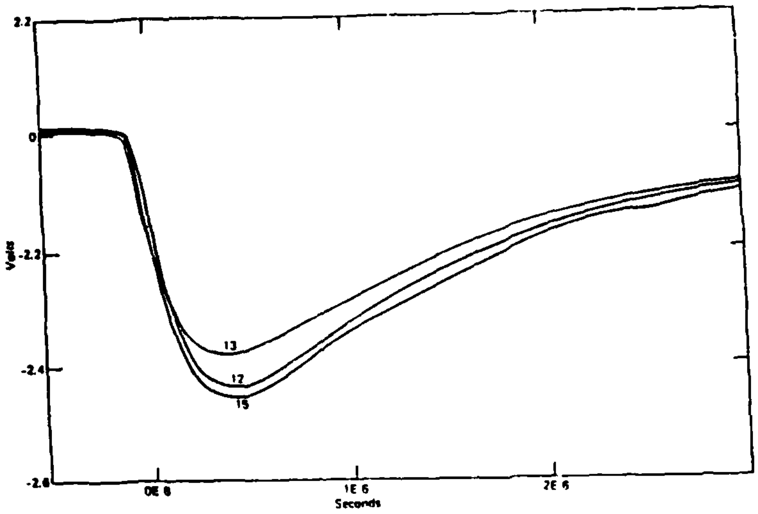

Fig. 7 IR thermal response pattern of three uncoated specimens of IN 738. DC 12, 13, 15.

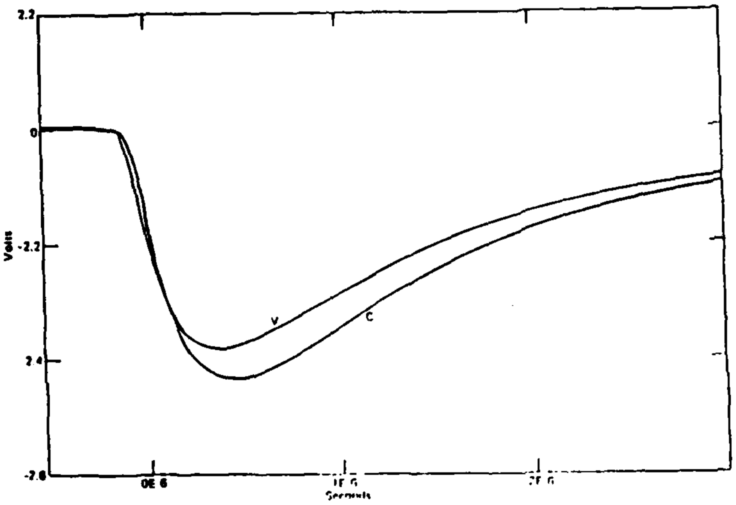

Fig. 8 Thermal response pattern of specimen DC#13 showing coated and uncoated response. This result was typical of the response pattern for the other specimens.

ANALYSIS OF HEAT FLOW IN THIN FILMS

The surface temperature of a homogeneous uncoated material is modified when a thin film coating is applied. If the coating is opaque or near opaque, the optical absorption coefficient of the coating governs the source profile of heat generation rather than the optical absorption coefficient of the sample. If the substrate is thermally thick, its thermal properties affect the thermal mismatch at the coating-substrate interface, however, the time for heat diffusion back to the coating surface is determined by the thermal diffusivity of the coating and not the substrate diffusivity. When the sample is porous and specimen structure need be considered, a statistical approach must replace the deterministic approach used here. The present analysis does not accommodate this case.

The excess surface temperature of an almost opaque coated material heated by a spatially uniform temporal pulse is given by the expression,

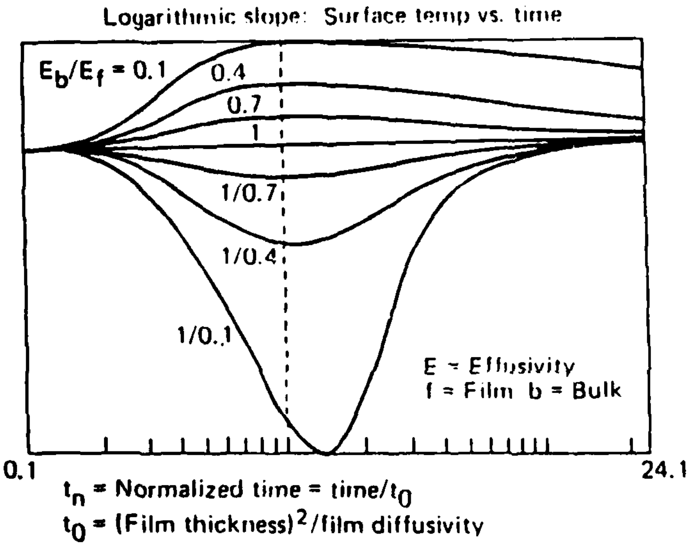

Fig. 9 Two optical microscope views of the coating surface focused at the top and bottom visible layers of the coating, respectively. Estimated texture height, 15 microns.

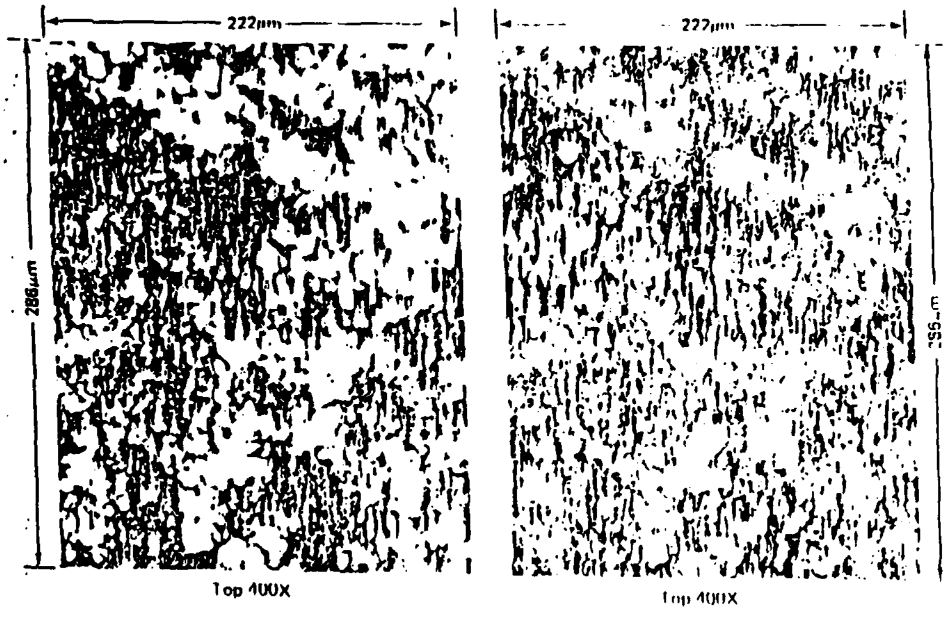

Fig. 10 Logarithmic derivative of the temperature patterns in Figure 1 vs. time. The curves peaks (or troughs) in the vicinity of the time, $t= \zeta^2/\alpha$.

$$T_s(z=0,t) = (\pi\rho\kappa C)^{-1/2} \int_0^{\zeta} \exp[-\beta z] \{\exp(-z^2/4\alpha t) + \sum_{\ell=1}^{\infty} (-\Gamma)^{\ell} [\exp(-z/4\alpha t) + \exp(z^2/4\alpha t)] \exp(\ell\tau_n/t) \} dz$$

where $\tau = \xi^2/\alpha$. ζ is the coating thickness, α, the coating thermal diffusivity, β, the coating optical absorption coefficient, $\Gamma = [1 - E_s/E_c] / [1 + E_s/E_c]$, and E_s and E_c are the sample and coating thermal effusivities, respectively.

The sum in the equation represents successive thermal reflections between the upper and lower coating surfaces. The temperature decay patterns obtained from this expression for a fully opaque coating are shown in Fig. 2. The decay patterns in this figure are different for different thermal mismatches, but to ascertain the coating thickness or thermal mismatch from this pattern would involve a difficult task of curve fitting. A more convenient method way to obtain this information is to measure the logarithmic derivative of this decay (Fig. 10). As seen in this figure, the derivative's peak or trough always occurs close to the time, $t = \tau_u$, from which the sample thickness can be obtained if the coating thermal diffusivity is known. It is also evident from this figure that a thermal approach to characterizing film thickness requires the thermal mismatch between coating and sample to be significant.

This work has been jointly supported by the Army Research Office and the Naval Sea Systems Command under Contract No. N00024-85-C-5301 (ARO Nbr. 21066-MS).

*Permanent address: Department of Physics, Southern Methodist University, Dallas, TX 75275

REFERENCES

1. P. E. Nordal and S. O. Kanstad, Physica Scripta, 20, 659 (1979).
2. G. Busse, Infrared Phys., 20, 419 (1980).
3. P.-E. Nordal and S. O. Kanstad, Infrared Phys., 25, 1/2, 295, (1985).

APPENDIX

PHOTOTHERMAL IMAGING OF DEFECTS IN METALS AND CERAMICS

16. J. C. Murphy, J. W. Maclachlan, and L. C. Aamodt, "Image Contrast Processes in Thermal and Thermoelastic Imaging", IEEE Transactions on Ultrasonics, Ferroelectrics and Frequency Control, Vol. 33, No. 5, pp. 529-541, 1986.

IEEE TRANSACTIONS ON ULTRASONICS, FERROELECTRICS, AND FREQUENCY CONTROL, VOL. UFFC-33, NO. 5, SEPTEMBER 1986 529

Image Contrast Processes in Thermal and Thermoacoustic Imaging

JOHN C. MURPHY, JANE W. MACLACHLAN, AND LEONARD C. AAMODT

Abstract—**Recent developments in thermal wave or more generally modulated source imaging using laser-, electron-, and ion-beam sources are discussed. Thermal wave imaging is further classified on the basis of the type of detection process used, and recent work relating to contrast mechanisms in the several classes of thermal imaging is discussed.**

THERMAL WAVE IMAGING (TWI) is a term that encompasses a family of imaging methods with important applications for materials characterization and for nondestructive evaluation of materials. It has already made contributions to understanding structural materials including metals, ceramics, and composites and electronic materials and devices. In addition, it has application to polymers and related organic systems. A number of review papers have been written covering aspects of the field including recent works by Busse [1], Rosencwaig [2], and Birnbaum and White [3].

Thermal wave imaging techniques are characterized by the use of a modulated excitation source, which produces a change in specimen temperature. Imaging methods may be distinguished by the excitation source used and by the method of detecting temperature changes in the specimen. Image contrast depends on spatial variations in specimen properties and how these variations are converted into a measured signal by the specific detection method chosen. This paper reviews some of the information presently available about image formation and image contrast in TWI. It also summarizes recent experimental studies which contribute to an understanding of the role thermal and thermoelastic contrast mechanisms play in TWI. Images obtained by "thermoelastic" thermal wave methods are compared with those obtained by purely "thermal" methods. Thermal methods are those where the detected signal depends primarily on the surface or bulk temperature of the specimen. Thermoelastic methods are those where the signal depends on specimen temperature through the temperature-dependent elastic properties of the specimen.

SURVEY OF THERMAL WAVE IMAGING TECHNIQUES

Fig. 1 is a composite sketch representing most of the major thermal wave imaging methods. Absent from the figure is the method titled scanning photoacoustic microscopy (SPAM). This was the first of the recent series of TWI methods to be developed [4], [5] and stemmed directly from photoacoustic spectroscopy using the gas microphone. Its use of an enclosed cell makes it inconvenient for many specimens. The sample shown in Fig. 1 is opaque to the incident beam but TWI techniques are also applicable to transparent specimens with modification of the experimental geometry [6]. In Fig. 1 a modulated excitation beam is shown vertically incident on a specimen. This beam would typically be a laser or particle (e.g., electron or ion) beam but could also be a microwave beam [7], [8] or a sound beam [9]. Other modulated heating methods which have been used include a resistively heated source attached to the sample [10] and induction heating [11]. In all cases the beam changes the specimen temperature directly via the beam–specimen interaction and indirectly via thermal or mass diffusion.

Several detection methods are identified in Fig. 1. Optical beam deflection (OBD) or "mirage" detection (Method 1) is represented by the surface skimming probe ray traveling through a gas or liquid in thermal contact with the surface of the sample. This ray is deflected by time-dependent refractive index variations in the fluid caused by heat transfer from the specimen [12], [13], [14]. The deflection is measured by a position-sensitive optical detector, either a sectored quadrant detector, a lateral detector or a conventional optical detector apertured by a knife edge.

Fig. 2 is a representation of the geometry of the OBD process showing in further detail both the excitation and probe laser beams with a relative displacement of the two beam centers. Two deflection components exist, one in the plane defined by the probe ray and the normal to the specimen surface (normal component) and the second orthogonal to that plane (transverse component) [14], [15]. For radially symmetric beams and isotropic specimens the amplitude of the transverse signal is zero for intersecting beams. In this configuration the transverse component is a sensitive monitor of thermal anisotropy in the specimen. For all relative positions of the beams, the normal deflection has been shown to be sensitive to changes in specimen surface temperature, while the transverse component is sensitive to the component of the specimen temperature gradient orthogonal to the probe ray [15]. While this description of the OBD imaging process assumes a localized excitation source, the probe beam detection is localized

---

Manuscript received January 8, 1986; revised March 5, 1986. This work was supported by the U.S. Army Research Office and the U.S. Navy Sea Systems Command under Contract N00024-85-0-5301.

The authors are with The Johns Hopkins University Applied Physics Laboratory Laurel, MD 20707, USA.

IEEE Log Number 8609266.

0885-3010/86/0900-0529$01.00 © 1986 IEEE

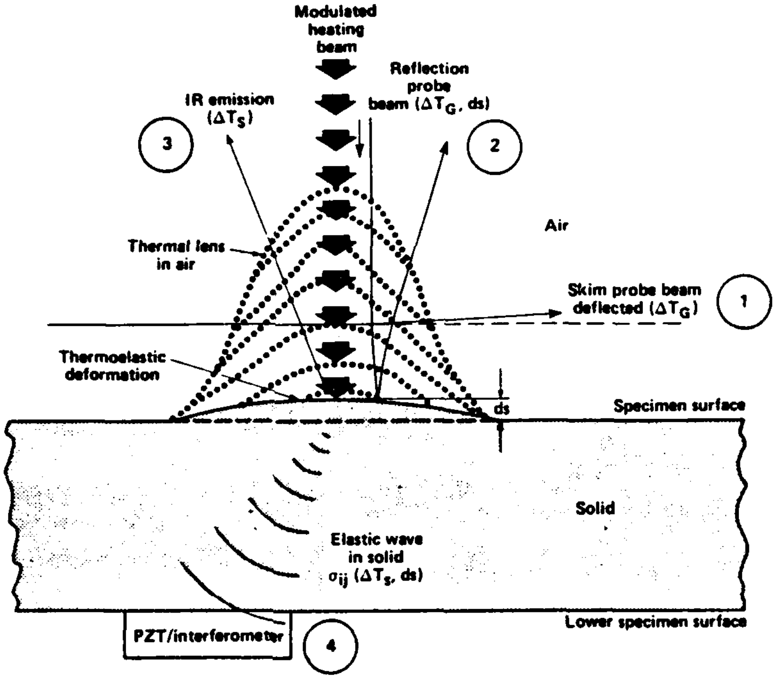

Fig. 1. Composite sketch summarizing several thermal wave imaging methods (1) optical beam deflection; (2) reflective optical beam deflection; (3) IR radiometric; and (4) thermoelastic (transducer or interferometric).

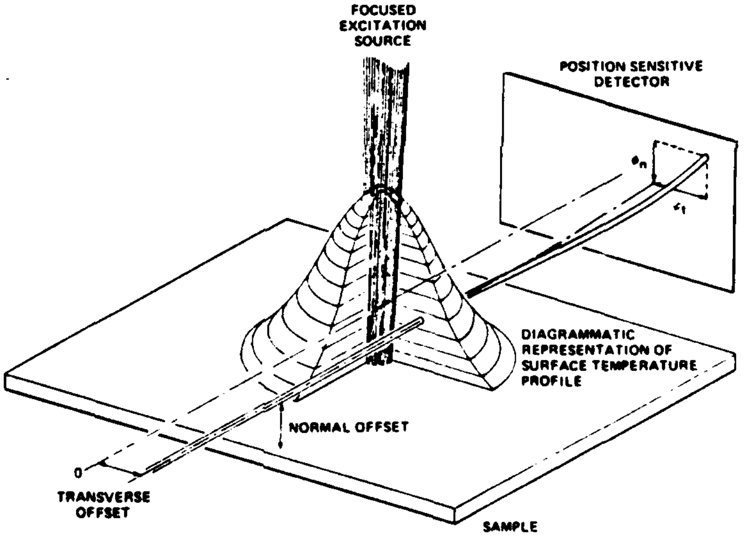

Fig. 2. Schematic of the optical beam deflection imaging method showing the two deflection components mentioned in the text.

as well. The probe signal is an integral of the deflection along the ray path over the sample. While this localization is only in two dimensions, it still allows imaging using a nonlocalized source. Measurement with two probes beams angularly displaced permits reconstruction of the specimen surface temperature distribution by a method somewhat resembling X-ray tomography [16].

Reflective optical beam deflection (method 2) [17], [18], [19] is represented by the vertically oriented probe ray. This ray is shown to be approximately parallel to the excitation beam in the figure and passes through the thermal lens region discussed. The deflection of this ray is detected by a position-sensitive optical detector after reflection from the specimen surface. The figure shows that the position of the reflected beam is affected also by a thermally induced deformation of the specimen produced locally near the region where heating occurs. Image formation may involve 1) thermal modulation of specimen reflectivity (thermoreflectance) [20], 2) deflection associated with surface deformation, or 3) deflection associated with thermal lens formation in the gas (or in the sample in nonopaque materials). The thermoreflectance and thermal lens deflection are viewed as "thermal" methods in the context of this paper; while the surface deflection is viewed as thermoelastic since it involves elastic properties of the solid.

Another method which also monitors thermally induced surface deformation is optical interferometry [21], [22] This method monitors the vertical component of sample surface displacement. It is complementary to the reflective optical beam deflection imaging in that interferometry detects the vertical displacement of the surface deformation of the specimen while the optical beam deflection detects the angular tilt of the surface.

Photothermal radiometry (PTR) (Method 3) is based on the enhanced IR emission of a heated object [23]–[25]. This thermal method has the features of being noncontacting and capable of parallel acquisition of the spatially-resolved surface temperature by using devices such as detector arrays or pyrovidicons. Photothermal radiometry has been applied to a range of topics including measurement of thin-film thickness on refractory metals [26] and studies of thermal structures of layered materials [27]. Infrared detection in a scanning electron microscope has been applied to a study of subsurface structures in silicon [28]. Advances in pyroelectric detector design have been made which employ thin polymer films of β-polyvinylidene difluoride (PVDF) [29]. The low thermal mass of these detectors allows nanosecond range thermal response times to be achieved.

PTR has the potentially important feature of also providing image contrast through spatial variations in emissivity. The dependence of PTR on emissivity effects distinguishes it from other thermal methods such as OBD. Several methods have been developed to make emissivity-independent PTR measurements in order to emphasize subsurface thermal structures. An early work by Green [30], the dual scan technique, minimizes emissivity effects by using the ratio of early-time and late-time measurements of specimen irradiance. A second method by Dallaire and Cielo [31] uses a hemispherical cavity to minimize effects of specimen emissivity. Other methods of minimizing emissivity effects in PTR imaging include dual-wavelength detection [32]. In experimental comparisons of thermal and thermoelastic contrast described later in this paper, the thermal method chosen is OBD. Excluding emissivity effects, the conclusions reached there should apply to PTR imaging as well.

The fourth method shown in Fig. 1 involves detection of the thermoelastic stress using an attached transducer [33]–[36] or an optical interferometer [37], [38] placed at a point on the sample removed from the point of heating. While the detector position shown in the figure is on the side of the sample opposite to that illuminated by the exciting beam, other geometries are possible and may offer some advantages in specific applications. Method 4 is a thermoelastic imaging method since it involves both the temperature field in the sample and the elastic and thermoelastic response of the sample in the signal formation process. A wide range of attached transducers can be applied to thermoelastic imaging. In the discussion of contrast mechanisms later in this paper, data collected using several types of transducers will be presented. These transducers include an NBS conical transducer developed for acoustic emission studies [39], a commercial 0.5 MHz ultrasonic transducer, and a transducer fabricated from a PZT-5A ceramic wafer 1 cm in diameter and in an aluminum housing. The NBS conical transducer has been shown to be a nearly ideal displacement sensor for stiff materials including metals and ceramics. It contacts the specimen over an area of 1 mm in diameter and hence provides localized detection capability. Other transducers with much larger contact area give a response that corresponds to an integration over this larger area. Recently, Kubota and Murai [40] have used an array of transducers fabricated on a single block of piezosensitive material to demonstrate the localization of laser–acoustic response in silicon. Other novel transducers fabricated from PVDF [41] and ZnO [42] allow measurement of thermoelastic response over time scales on the order of nanoseconds. The use of excitation sources such as pulsed lasers and rapidly-blanked electron beams [43] along with such transducers allows time-resolved thermoelastic measurements to be made over significantly shorter times.

The wide range of thermal wave imaging techniques described in this section can be implemented in a number of experimental configurations. Fig. 3 is a block diagram of an experimental setup which can be used for either electron or ion beam excitation and attached transducer detection. Note that the specimen current can be monitored simultaneously. Experiments involving combined detection methods for the purpose of comparing contrast can be carried out with a system such as that shown in Fig. 4, which incorporates both attached-transducer and optical-beam deflection.

There are certain general analytical techniques applicable to all imaging methods. These include Hadamard transform techniques for specimen illumination [44]. Transform techniques were developed for spectroscopic applications in order to improve the signal-to-noise ratio (SNR) and data acquisition time for systems where the system SNR is determined by detector noise. This noise characteristic is a general feature of all thermal detection systems. Hence spatial transform methods offer advantages in throughput and SNR over conventional scanning systems in TWI.

Similarly, transform techniques in the time domain have been shown by Sugitani to offer advantages in determining the frequency response of thermal systems in spectroscopy applications [45], [46]. These methods have been subsequently applied to imaging [47]. These techniques are analogous to the spatial transform methods since wide band spectral excitation is used and the frequency response of the system is extracted by analysis from the broad band response of the system. Analysis of TW images using optical Fourier transform concepts has also been made [48].

THEORETICAL BACKGROUND

Thermal imaging involves production and detection of temperature changes in a specimen in accordance with (1), the three-dimensional thermal diffusion equation with sources, subject to appropriate boundary conditions [49],

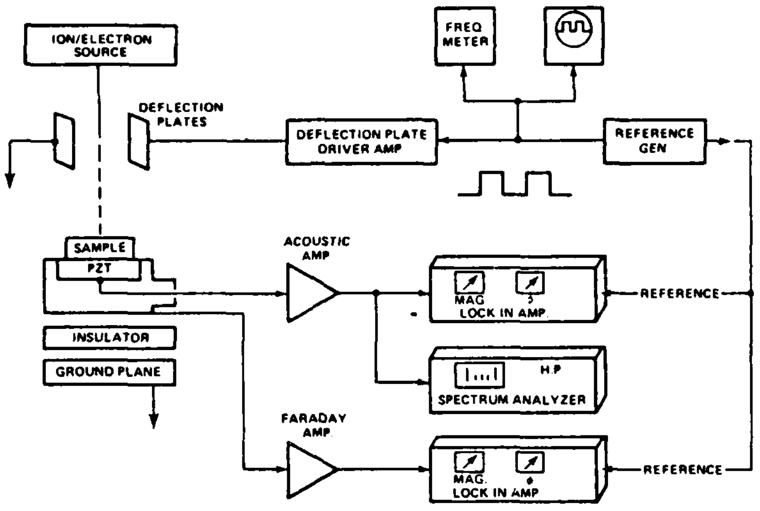

Fig. 3. Block diagram of electron or ion acoustic detection system showing simultaneous detection of specimen current.

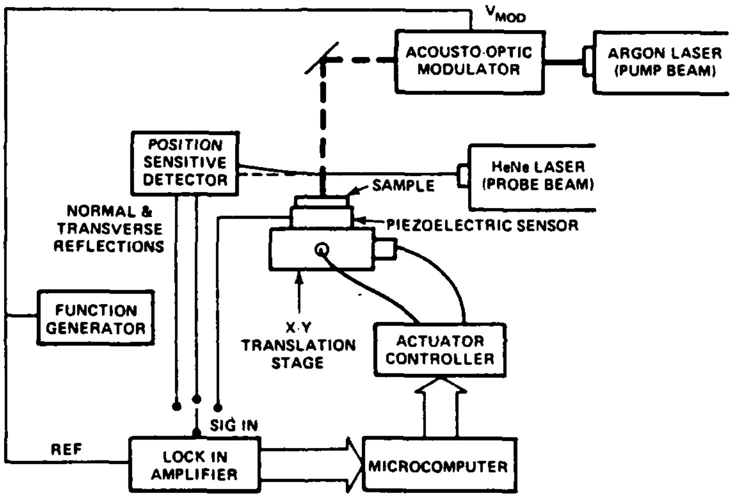

Fig. 4. Block diagram of laser source optical beam deflection and acoustic imaging system.

[50], [51]

$$\nabla^2 T - \alpha^{-1}\frac{\partial T}{\partial t} = -\frac{H(r, t)}{\kappa}. \qquad (1)$$

Here $\alpha = \kappa/\rho C$ is the thermal diffusivity (with the thermal conductivity κ, the density ρ, the specific heat C), and $H(r, t)$ is the energy input from the source. In general, H extends throughout the specimen volume. For strongly absorbing specimens H may only be significant near the specimen surface.

The thermal diffusion equation may be solved for $T_s(x, y)$ and $T_B(x, y, z)$, the surface and bulk specimen temperatures, respectively, for a number of special cases. A partial list of such cases, which have been analyzed from the thermal imaging perspective, includes homogeneous plates of arbitrary thickness [15], vertically layered materials with arbitrary numbers of layers [52], [53], [54], and rectangular parallelpipeds, where the lateral dimensions of the specimen establish thermal boundary conditions for the diffusion process [55]. These boundary conditions have allowed some choice of the degree of thermal isolation assumed. In the majority of cases considered the modulated temperature excursions have been assumed to be small enough that the thermal parameters could be assumed independent of temperature. Recently, some work has been conducted on nonlinear thermal and thermoacoustic imaging [56], [57], [58], where this assumption is not made.

Solutions of (1) have also been obtained in plate samples for thermal wave scattering from sample defects such as voids and cracks [59]. A preliminary nonscattering analysis of a general heterogeneous material with spatially varying thermal characteristics [60] and analysis of granular specimens has been made [61].

These analyses lead to a determination of T_B and T_s as functions of position and time, or for CW modulation, as a function of ω, the angular modulation frequency. For opaque solids most *thermal* imaging techniques depend directly on T_s. In OBD imaging, for example, there is heat transfer from the specimen surface to the adjacent fluid and the specimen parameters are reflected in the image through changes in T_s. This dependence on T_s makes thermal diffusion an integral part of the imaging process if subsurface details of the specimen are of interest and consequently makes the process intrinsically restricted to long observation times or low modulation frequencies.

When thermoelastically produced stress and resulting displacement is detected, however, the analysis is modified [51]. The thermal diffusion and elastic wave equations coupled by thermoelastic interactions are represented by

$$\nabla^2 T - \alpha^{-1} \frac{\partial T}{\partial t} - \eta \operatorname{div} u = -\frac{H(r, t)}{\kappa} \tag{2a}$$

$$\mu \nabla^2 u + (\lambda + \mu) \operatorname{grad} \operatorname{div} u = \rho \ddot{u} + \gamma \operatorname{grad} T \tag{2b}$$

with $\eta = (\gamma/\kappa) T_0$; $\gamma = (3\lambda - 2\mu)\alpha^T$ where α^T is the linear thermal expansion coefficient, u is the particle displacement, λ and μ are the Lamé constants, and T_0 is the reference temperature of the specimen. Equation (2a) differs from (1) by the addition of the term η div u. This term represents heat produced by particle displacements associated with an elastic wave. It can usually be neglected. These equations must be solved subject both to thermal and mechanical boundary conditions and in the extreme near-field limit. That is, for most specimens of interest to thermal wave imaging, the specimen's elastic response is detected within one acoustic wavelength of the place where excitation occurs. No satisfactory solution of this problem is available for the CW case. Some progress has been made for larger specimens under pulsed-laser heating. The analytical development has involved work by Scruby *et al.* [62], [63], Dewhurst *et al.* [64], and a more recent theoretical development by Rose [65]. Kino and Stearns [66] have also presented an analysis of elastic wave generation in solids which is applicable to imaging. Comparison of the calculated surface displacements with experimental results has been made in some cases [62], [63]. Much of this work draws on the theoretical development of elastic wave propagation in plates initiated by mechanical step unloadings [67]–[71]. Also, some developments of one-dimensional models of elastic wave generation have been presented [72]. Preliminary imaging applications of time-domain laser acoustic measurements have included location and sizing of buried, flat-bottomed holes in plates [73], and delaminations in composites [74].

Rose [65] has developed formal solutions for surface stress and displacement for a specimen illuminated by a delta function source. These results are in reasonable agreement with measurements made on laser generated ultrasound. In addition he has obtained some results for a periodic source in the far-field limit. Unfortunately, this is not the limit important for many of the current thermoelastic imaging studies.

It is important to note that for opaque solids where only surface heating exists, the signal depends on an integral over the specimen volume affected by thermal diffusion, i.e., T_B contributes to the image directly and not merely indirectly through its effect on T_s. This result provides the basis for the observation that subsurface features can be detected at greater depths in thermoelastic imaging than in thermal imaging. Since temperature changes in the specimen directly generate stress which is detectable by the transducer, the role of thermal diffusion in the signal generation process is reduced. Some increase in modulation frequency and hence scanning rate may be made.

IMAGE CONTRAST MECHANISMS

A number of potential contrast mechanisms have been identified and some controversy has existed over their relative importance, especially for the thermoelastic case. This issue is further complicated by an apparent contrast mechanism, which is related to visual processing in the brain (Craik–O'Brien effect) [75]. It induces apparent contrast between areas on either side of a visible boundary which is not observed in numerical processing of the image data. This effect is seen in SEAM images of grain structure in aluminum and is presumably a common feature of other images. When viewing TWI images with strong boundary contrast, care must be taken to ensure that this effect does not influence the interpretation of the image.

BEAM–SPECIMEN CONTRAST

Beam–specimen interactions are an important source of image contrast. For optical sources this is manifested by a spatial dependence of the optical absorption or the reflectivity, either of which may be wavelength dependent. For specimens which show photochemical or photocatalytic activity, spatial variations in relaxation rate can contribute to the image.

For electron sources, spatial variations in the fraction of beam energy absorbed is a source of beam-specimen contrast. The volume over which the beam is absorbed is related to the energy distribution of both secondary and backscattered electrons. However, it is the rate of heat deposited in the specimen and its spatial distribution that plays the primary role in thermal wave imaging. Measurement of the specimen, secondary electron, and backscattered electron currents alone does not adequately specify the signal generation process. Many of the details of this interaction have not been established. As an example of electron beam-specimen contrast, Fig. 5 compares secondary electron (SEM) and scanning electron acoustic microscope (SEAM) images of a silicon IC for two beam voltages (5 keV and 30 keV) [76]. The NBS conical transducer was used to detect the acoustic signals. At the lower beam voltage where the interaction depth is of the order of 0.5μ [77], both SEM and SEAM images show similar structure. At the higher beam voltage (interaction depth about 9μ), the SEAM image shows buried structure not observed in the SEM image. In other experiments it was found that an origin of the contrast observed in the SEAM images may be spatial changes in electron absorption associated with doping. Thermal spreading of the image is observed at lower modulation frequencies.

Ion beams can be sources for thermal wave imaging [78], [79]. Ion-specimen interactions have been widely

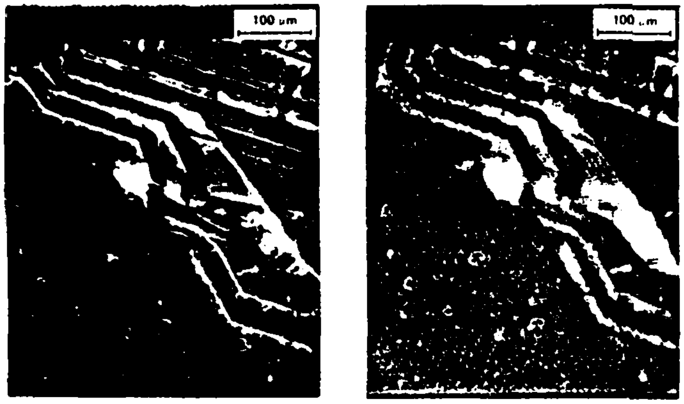

5 keV, S.E. 5 keV, ρ, 480 kHz

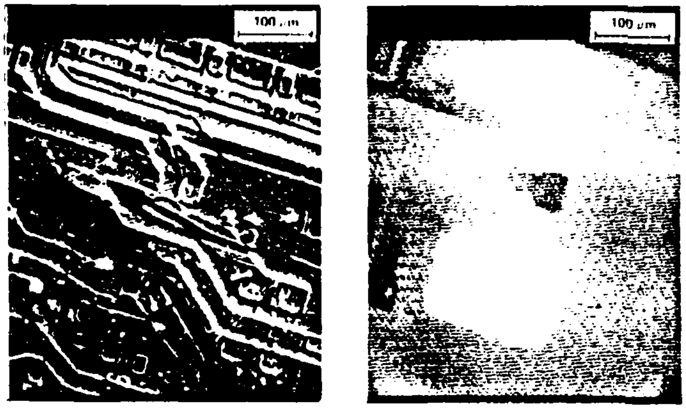

30 keV, S.E. 30 keV, ρ, 480 kHz

Fig. 5. Secondary electron and electron-acoustic images at two primary-beam voltages showing beam-specimen contrast.

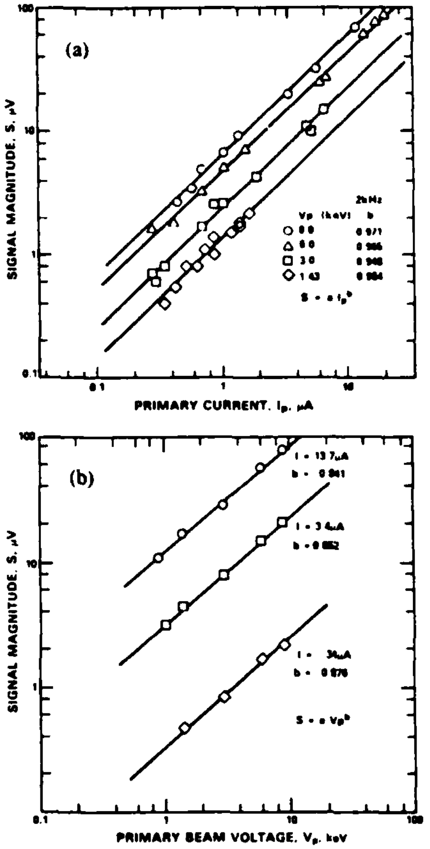

Fig. 6. Ion-acoustic signal dependence on beam current (a) and beam voltage (b). A slope of 1.0 is expected for the voltage dependence if thermal effects dominate and 0.5 if momentum processes dominate.

studied and ion bombardment has become an important tool for semiconductor processing and surface treatment of materials (see for example [80], [81], [82]). In addition, ion beams have been used as analytical tools in sputtering. A literature has developed based on imaging using focused ion beams coupled with sputter-ion detection [83], [84]. In general, the details of the interactions are complex and depend on the ions used for bombardment, on the composition of the target and on the incident ion energy, and total dose, among other parameters [85]. However, a common characteristic of ion sources is the existence of a "range" that defines a depth in the specimen at which a substantial fraction of the energy in the incident beam is selectively deposited. This raises the prospect that ions might be depth-selective probes for materials studies in imaging applications.

In light of the high ion mass (relative to electron mass) and the prospect of ion-specimen interactions specific to some beam-specimen combinations, the question of the role thermal and nonthermal beam-specimen interactions play in ion-acoustic imaging becomes important. One potential mechanism which has been identified is acoustic wave generation caused by ion impact and the related momentum transfer.

Momentum transfer is thought to be responsible for fast-ion beam recrystallization of silicon [80], and here thermal contributions have been shown to be relatively unimportant. Sputtered ion mass spectroscopy (SIMS) mechanisms are also dominated by momentum transfer to the specimen [86]. The relative importance of momentum and thermal mechanisms in ion-acoustic signal generation were investigated experimentally by a study of beam voltage dependence [78]. Figs. 6(a) and (b) show the dependence of the acoustic signal in an aluminum specimen as a function of beam current and voltage, respectively. The relative importance of momentum and thermal processes in acoustic generation should vary with beam voltage V_B since the beam momentum rate, $P_B = N_I(2M_I q V_B)^{1/2}$, where N_I is the ion fluence, q the specific ion charge, M_I the ion mass, and V_B the beam voltage. The resulting total acoustic signal S_T has both momentum and thermal terms:

$$S_T = S_{\text{mom}} + S_{\text{TH}} = K_1\left(1 + \frac{K_2}{V_B^{1/2}}\right)V_B$$

where K_1 and K_2 are constants. For a momentum-only process the slope in Fig. 6(b) would be 0.5 based on this relation. A thermal process would ideally have a slope of 1.0. In Fig. 6(a) the slope of the acoustic signal is linear in beam current (slope ≈ 1). However, in Fig. 6(b), the slope of acoustic signal with beam voltage V_B is approximately equal to 0.8. This suggests that a strong thermal contribution is present. This thermal contribution exceeds that expected from the relative importance of momentum and thermal processes in sputtering.

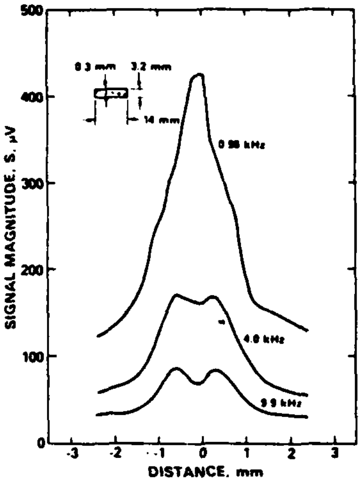

Fig. 7. Ion-acoustic profiles for a sample containing a subsurface slant hole. At low frequencies thermal interaction with the hole causes a signal increase. At high frequencies the signal generation process is still thermal but the contrast interaction is nonthermal.

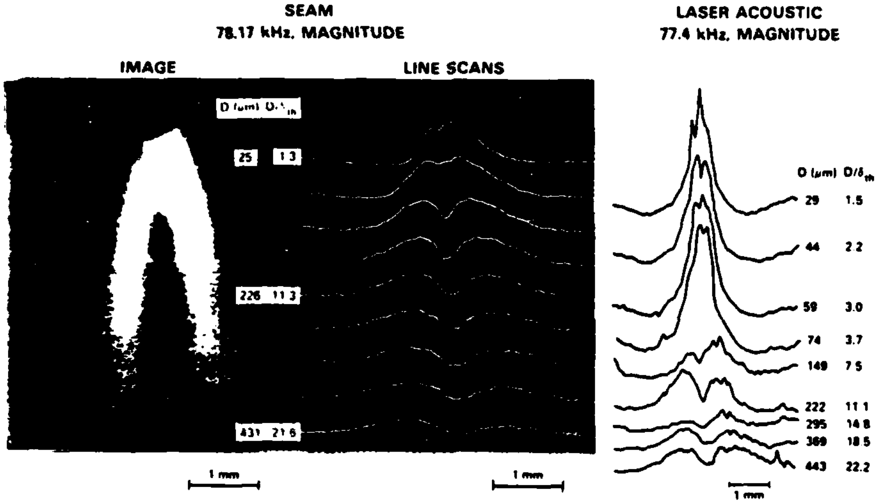

Fig. 8. Electron-acoustic image and line scans of sample of buried slant hole in Al from Fig. 7. Laser acoustic line scans are also seen. While the modulation frequency is much higher than that of Fig. 7, the information is similar. Particle and laser excitation yield similar specimen response.

The dominant role of the thermal contribution under specific experimental conditions is supported by line scan and image data comparing ion, electron, and laser acoustic signal contrast [87]. It is shown that all three sources give equivalent scan images as a function of frequency. The specimen studied was an aluminum disk 1 cm in diameter and 3 mm thick containing a slanted subsurface hole with a diameter of 1 mm. Fig. 7 shows ion line scans at constant slant hole depth for several frequencies. Fig. 8 shows image and line scan data for the same sample using electron and laser sources at higher frequency and for a series of slant hole depths. In all three cases, the signal increases over the hole for $D/\delta_{TH} < 1$, where D is the depth of the slant hole at the scan location and $\delta_{TH} = [2\alpha/\omega]^{1/2}$ is the thermal diffusion length, with $\alpha = \kappa/\rho C$ and $\omega = 2\pi f$ the angular modulation frequency. As the ratio of D/δ_{TH} increases (either by increasing the depth of the hole or decreasing δ by increasing the frequency), the signal over the hole decreases and two lobes develop adjacent to the hole position. The specifics of these particular signal shapes are discussed in a following section on thermoacoustic contrast, but for the purposes of the present discussion on beam-specimen contrast mechanisms, it is important to note that these signal shapes are independent of excitation beam type, indicating a common thermal signal generation mechanism for all sources. Therefore momentum transfer does not play a significant role in ion-acoustic-imaging contrast under the conditions of these experiments.

THERMAL CONTRAST

Thermal contrast mechanisms are widely observed in TWI. They represent a major aspect of current applications of TWI to materials characterization and nondestructive evaluation of materials. In many of these studies the questions of interest are the visualization of specimen

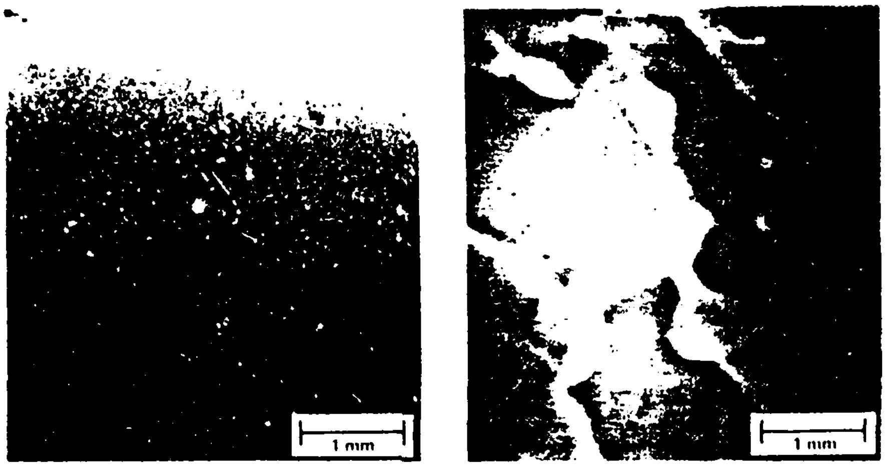

(a) (b)

Fig. 9. Electron-acoustic image of grains in high purity aluminum. Note the presence of contrast at the grain boundaries and between the interiors of grains. Some of the interior contrast is due to the Craik-O'Brien effect. (a) Secondary electron image. (b) Acoustic magnitude image.

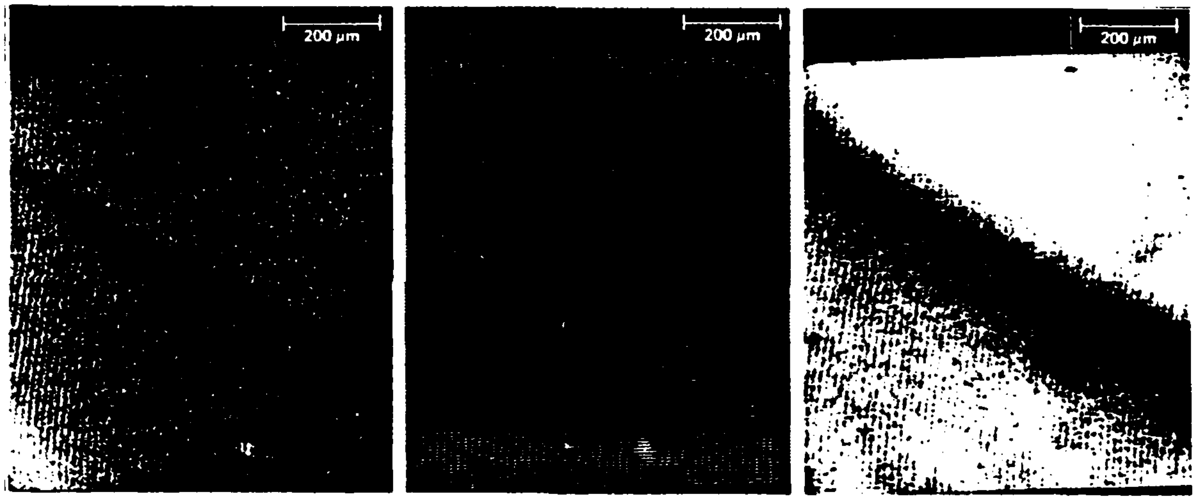

(a) (b) (c)

Fig. 10. Grain-boundary images of aluminum grains as a function of modulation frequency. The width varies as $\omega^{-0.5}$. (a) 205.760 kHz. (b) 89.133 kHz. (c) 15.40 kHz.

microstructure, location, and sizing of buried defects in opaque solids, including cracks and voids, and the determination of the characteristics of films on a variety of substrates including film thickness and bonding. It has been suggested that thermal contrast mechanisms are the principal mechanisms responsible for imaging of microstructure in SEAM applications [2]. The importance of elastic anisotropy and other nonthermal contrast mechanisms in SEAM imaging has been stressed by other authors [88], [89] in part due to the importance of elastic contrast in acoustic microscopy. High contrast images of grain boundaries and specimen microstructure have been observed in SAM and in SEAM. Fig. 9 is an example of SEAM imaging of microstructure obtained on a specimen of polycrystalline aluminum. Contrast between grain interiors and contrast at the grain boundaries are both clearly observed. The dependence of the boundary width observed by SEAM on modulation frequency is shown in Fig. 10. Fig. 11 shows SEM image with superimposed SEAM line scans measured on an aluminum bicrystal where the grain boundary is normal to the plane of the image [90]. The precise position of the grain boundary is identifiable in the SE image due to preferential attack of the grain boundary by a chemical polishing procedure. The physical extent of this attack was much smaller than a thermal diffusion length over the frequency range studied and did not influence the SEAM images. Data of this type were used to construct the dependence of boundary width on modulation frequency and the results are shown in Fig. 12. The solid line indicates the thermal diffusion length in pure aluminum as a function of $\omega^{-0.5}$. The data points indicate the HWHM value for the phase signal on the right-hand side of the boundary for the middle line scan of Fig. 11 for a series of five different frequencies.

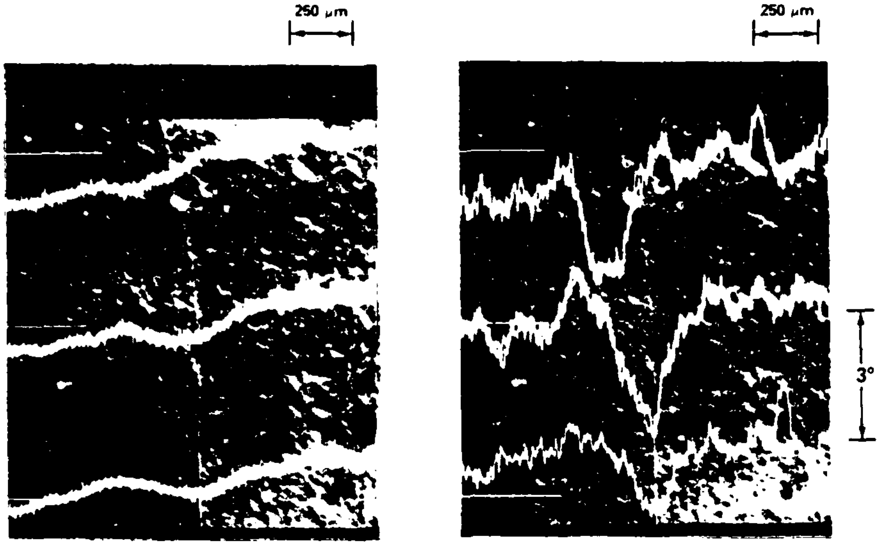

(a) (b)

Fig. 11. Secondary electron image with an overlay of electron-acoustic line scans taken on a large bicrystal of aluminum. (a) Log magnitude. (b) Phase. The crystal was overetched to show the boundary. The position of the scans is indicated by the horizontal lines in the figure. Data for Fig. 12 used the response on the right-hand side of the boundary because of the interfering subsurface structure seen on the left-hand side.

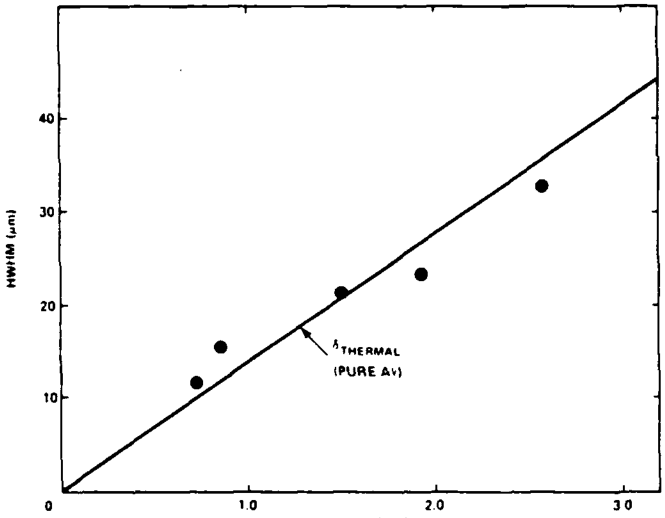

Fig. 12. Plot of grain boundary width vs. $\omega^{-0.5}$. The solid line is the thermal diffusion length of aluminum calculated using a diffusivity $\alpha = 1.0$ $\text{cm}^2\ \text{s}^{-1}$.

This indicates a definite thermal component to the boundary contrast observed in SEAM images of grain structure. Elastic contrast mechanisms are not excluded from a role in microstructural contrast, however.

Thermal contrast can involve spatial variations in the thermal properties of the specimen, κ and ρC and through them, on temperature, composition, doping in the case of semiconductors, and many other parameters. For homogeneous specimens these parameters may be determined using modulated temperature methods through the temporal or frequency response of the specimen temperature. The lateral measurement scale can be small. Thomas *et al.* [91] have shown that OBD measurements of thermal diffusivity can be made on the lateral scale of a focused laser beam. In a modified form this method might be used for spatially imaging the diffusivity of relatively homogeneous specimens. The degree of homogeneity required [60] depends on the thermal detection method selected, on the pump beam diameter, and on the frequency dependent complex thermal diffusion length ($\delta = [j2K/\omega C]^{1/2}$) and thermal effusivity ($Y = [KC]^{1/2}$). The potential spatial resolution of the imaging of the thermal parameters is limited by these considerations.

Thermal contrast also depends on changes in the specimen temperature distribution caused by thermal boundaries [55], [59]. These boundaries can inhibit thermal flow in the specimen and lead to localized increases in specimen temperature [60]. For many metal and ceramic specimens, the macroscopic thermal parameters depend on the microstructure and on the processing history of the material. Thermal wave imaging may be able to help determine the contribution of the intrinsic thermal property values and the thermal boundary impedance to the macroscopic parameter values. However, relating image features to intrinsic and boundary thermal contrast mechanisms is difficult. The difficulty of this problem may be visualized by imagining the grains in Fig. 9 shrinking in size so that the distinction between the contrast of the grain interior and grain boundary disappears. Hence, measurement of the intrinsic material parameters requires measurement within a grain with a temperature resolution smaller than the grain size. This requires that the thermal diffusion length be small enough that grain boundary effects can be ignored when heating occurs at the grain center. In selected cases it may be possible to determine by imaging methods whether internal stresses generated by specimen processing change the thermal parameters within individual grains.

As a final note on thermal contrast effects, when the modulated temperature component is high, the thermal parameters may no longer be independent of temperature. In this case [56]–[58], nonlinear contrast mechanisms may be important. This issue bears further study.

THERMOACOUSTIC CONTRAST

Thermoelastic contrast mechanisms encompass the coupling of potentially anisotropic elastic parameters with the temperature field through the thermal expansion tensor, all in the presence of thermal and elastic boundary conditions. This problem is probably unsolvable except in selected special cases. However, substantial progress has been made in acoustic microscopy in interpreting images in terms of elastic parameters [92]–[94]. Analysis has shown that these images can be interpreted in terms of a surface wave generated by mode conversion of the incident elastic wave and described by the $V(z)$ curve, where z is the distance of the acoustic lens from the specimen. Scanning acoustic microscopy clearly shows the presence of microstructure such as grains and grain boundaries in metals. Briggs [86] has noted the similarity of acoustic images and electron-acoustic images and has suggested that elastic contrast may play a role in SEAM imaging.

The presence of elastic contrast mechanisms in thermal wave imaging using an attached transducer was demonstrated through experiments employing simultaneous optical beam deflection and piezoelectric detection [87], [95] and in SEAM imaging. Laser acoustic and normal deflection component OBD line scans of an aluminum sample containing a buried slant hole are shown in Fig. 13. This sample was used for the comparison of excitation sources described in a previous section. The acoustic detection method senses the hole to greater depths than the purely thermal method. This result is consistent with the previous discussion of the role T_B and T_s play in the two detection methods. The importance of nonthermal contrast mechanisms in thermoelastic imaging is shown by Fig. 8 where a second type of signal shape develops as the hole depth increases. In this figure the hole is observable down to depths reaching to $D/\delta_{TH} > 23$, where D is the depth and δ_{TH} is the thermal diffusion length. Ringermacher [96] has made similar observations. Neither T_B or T_s are affected by the presence of the hole at such large values of D/δ_{TH}. Hence, the contrast mechanism must be nonthermal.

A speculative explanation of these observations is that the angular distribution of the specimen stress response is a cone of approximately 40 degree cone angle peaked on epicenter. If this cone is interrupted by the hole at varied depth, the image of Fig. 8 is produced. The existence of a finite extent to the stress distribution is supported by observations using localized detectors. In our experiments an increase in signal is observed when an excitation beam passes over the region of the specimen directly above the NBS conical transducer. Also, Kubota and Marai [32] have conducted laser-acoustic experiments with a monolithic detector array on a PZT substrate and have found a very strong maximum in PZT signal when the exciting beam was directly above the active detector. Ion-acoustic studies of other slant-hole and partial-hole specimens are consistent with this proposal.

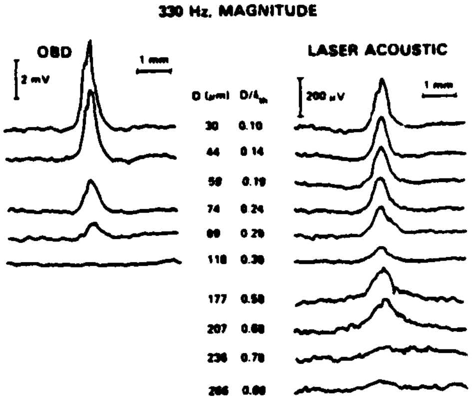

Fig. 13. Laser source-normal OBD and PZT line scans of a slant hole specimen. Thermal interaction with the buried hole is observed at greater depths with attached transducer detection than with OBD detection.

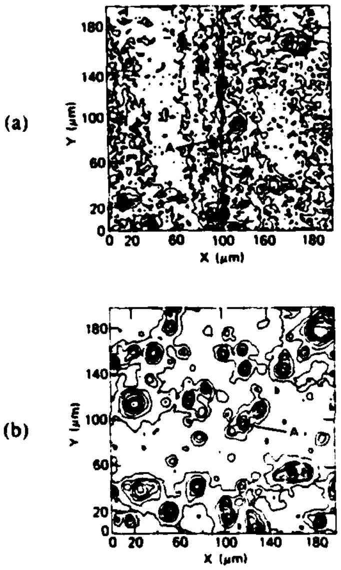

Fig. 14. (a) Transverse deflection component optical beam deflection contour image showing a narrow vertical boundary. (b) Attached transducer image (PZT) of the same region. Points labeled A allow registration. The 2024 aluminum sample consisted of two sections lapped, polished, clamped together with other faces, and then polished.

Both thermal and thermoacoustic contrast mechanisms contribute to thermoelastic imaging of vertical boundaries. Figs. 14(a) and (b) are magnitude images at 1.1 kHz of a portion of a sample containing a fabricated vertical crack for transverse OBD and PZT detection, respectively, and excitation with an Ar^+ laser source. Registration of the figures is possible using the features labeled A in each figure [95]. The local features seen are probably iron and manganese inclusions in the 2024 aluminum alloy.

The interface is not visible in the normal deflection magnitude and phase images but is present in the transverse magnitude and phase images. The transverse phase image shows a 180° phase reversal at the boundary and no signal related to inclusions. The PZT image closely resembled the normal deflection image and gave no indication of the interface.

The measurements were repeated using the electron source with the same specimen-detector combination without disrupting the bond. The frequency dependence observed for the electrons fits an ω^{-1} dependence at low frequencies and shows a frequency corner around 8 kHz. No interface contrast is seen below 4.5 kHz but strong contrast is present above 7 kHz with a transition region between. The absence of interface contrast in the laser source images at 1.1 kHz is consistent with the absence of contrast at low frequencies using the electron beam. The ω^{-1} dependence suggests a thermal signal generation process in this low-frequency regime. The visibility of the interface above 8 kHz, however, suggests that a nonthermal mechanism contributes to the image contrast in this case. This conclusion is further supported by the absence of any frequency dependence of the width of the boundary region ($\sim$200 μm). This width should be compared with the SEM determined width of the interface of 3 μm and with the thermal diffusion length of 70 μm at 7 kHz. The conclusion is that thermal contrast is not important in this case possibly because the width of the apparent boundary (200 μm) is large relative to the thermal diffusion length. Elastic contrast may be important at higher frequencies. No model of these phenomena is presently available.

SUMMARY OF RESULTS REGARDING CONTRAST

Source-modulated thermal imaging continues to develop with progress being made in theory, analytical techniques, and applications. The spatially resolved information extracted from these images is determined by the excitation source and the method of detection. There are a wide range of sources and detection methods in use in the field and the discussion of image contrast must take into account the specific beam-detector combination chosen.

At this time image contrast for purely thermal detection is understood qualitatively. For relatively simple specimen geometries, such as thin films, quantitative information about the specimen may be obtained. For complex, heterogeneous materials such as composites there are both practical and conceptual problems of image analysis on a small geometric scale. However, useful specimen information may be obtained for cases such as layer disbonding where the resolution scale and depth scale required is large relative to the scale of the heterogeneity.

Image contrast in thermoelastic imaging is not yet well understood. However, some progress is being made. This method provides striking image contrast which is qualitatively different from that observed using purely thermal methods and thermoelastic methods may offer advantages in specific applications. These features are incentives to further development of these methods. Both the thermal and elastic properties of the sample contribute to the observed contrast. Additional work is required for these methods to become quantitative tools for materials studies.

Nonthermal beam-specimen interactions and nonlinear contrast mechanisms have also been observed, but are presently not well understood. They offer the prospect of enhancing contrast by their association with specific aspects of the specimen and should find significant applications in future developments of the field.

REFERENCES

[1] G. Busse, "Imaging with optically generated thermal waves," *IEEE Trans. Son. Ultrason.*, vol. SU-32, no. 2, p. 355, 1985.

[2] A. Rosencwaig, "Thermal-wave imaging in a scanning electron microscope," *Ann. Rev. Mater. Sci.*, vol. 15, p. 103, 1985.

[3] G. Birnbaum and G. S. White, "Laser techniques in NDE," in *Research Techniques in Nondestructive Testing* (vol. 7), R. S. Sharpe, Ed., 1984, p. 259, New York: Academic, 1984.

[4] Y. H. Wong, R. L. Thomas, and G. F. Hawkins, "Surface and subsurface structure of solids by laser photoacoustic spectroscopy," *Appl. Phys. Lett.*, vol. 32, p. 538, 1978.

[5] R. L. Thomas, J. J. Pouch, Y. H. Wong, L. D. Favro, P. K. Kuo, and A. Rosencwaig, "Subsurface flaw detection in metals by photoacoustic microscopy," *J. Appl. Phys.*, vol. 51, p. 1152, 1980.

[6] W. B. Jackson, N. Amer, A. C. Boccara, and D. Fournier, "Photothermal deflection spectroscopy and detection," *Appl. Opt.*, vol. 20, p. 1333, 1981.

[7] A. L. Tronconi, M. A. Amato, P. C. Morais, and K. S. Neto, "Simple model for measurements of the photoacoustic signal by a piezoelectric detector in the microwave region," *J. Appl. Phys.*, vol. 56, no. 5, p. 1462, 1984.

[8] R. L. Nasoni, G. A. Evanoff, Jr., P. G. Halverson, and T. Bowen, "Thermoacoustic emission by deeply penetrating microwave radiation," in *Proc. IEEE Ultrason. Symp.*, 1981, p. 633.

[9] J.-P. Monchalin, J. F. Bussiere, and L. Bertrand, "Measurement of ultrasonic absorption in a polycrystalline metal by a photoacoustic-like technique," 4th International Topical Meeting on Photoacoustic, Thermal and Related Sciences, Ville d'Esterel, Quebec, 1985.

[10] D. R. Green, "Thermal surface impedance method for NDT," *Mater. Eval.*, vol. 10, p. 231, Oct. 1967.

[11] J. Saniie, M. Luukkala, A. Lehto, and R. Rajala, "Thermal wave imaging through radio-frequency induction heating," *Electron. Lett.*, vol. 18, p. 651, 1982.

[12] A. C. Boccara, D. Fournier, and J. Badoz, "Thermo-optical spectroscopy: Detection by the mirage effect," *Appl. Phys. Lett.*, vol. 36, p. 136, 1980.

[13] D. Fournier and A. C. Boccara, "The mirage effect in photothermal imaging," in *Scanned Image Microscopy*, E. A. Ash, Ed. London: Academic, 1980, p. 347.

[14] J. C. Murphy and L. C. Aamodt, "Optically detected photothermal imaging," *Appl. Phys. Lett.*, vol. 38, p. 196, 1981.

[15] L. C. Aamodt and J. C. Murphy, "Photothermal measurements using a localized excitation source," *J. Appl. Phys.*, vol. 52, p. 4903, 1981.

[16] D. Fournier, F. Lepoutre, and A. C. Boccara, "Tomographic approach for photothermal imaging using the mirage effect," *J. de Physique*, Colloque C6, p. 479, 1983.

[17] M. A. Olmstead, N. M. Amer, S. Kohn, D. Fournier, and A. C. Boccara, "Photothermal displacement spectroscopy: A new optical probe for solids and surfaces," *Appl. Phys. A*, vol. 32, p. 141, 1983.

[18] A. Rosencwaig, J. Opsal, and D. L. Willenborg, "Thin film thickness measurements with thermal waves," *Appl. Phys. Lett.*, vol. 43, p. 166, 1983.

[19] J. C. Murphy and L. C. Aamodt, "Reflective photothermal imaging," *J. Physique*, Colloque C6, p. 513, 1983.

[20] A. Rosencwaig, J. Opsal, W. L. Smith, and D. L. Willenborg, "Detection of thermal waves through optical reflectance," *Appl. Phys. Lett.*, vol. 46, no. 11, p. 1013, 1985.

[21] S. Ameri, E. A. Ash, V. Neuman, and C. R. Petts, "Photodisplacement imaging," *Electron Lett.*, vol. 17, p. 337, 1981.

[22] C. R. Petts and H. K. Wickramasinghe, "Photothermal spectroscopy on a microscopy scale," in *Proc. IEEE Ultrason. Symp.*, 1981, p. 832.

[23] P.-E. Nordal and S. O. Kanstad, "Photothermal radiometry," *Physica Scripta*, vol. 20, p. 659, 1979.

[24] G. Busse, "Photothermal transmission probing of a metal," *Infrared Phys.*, vol. 20, p. 419, 1980.

[25] P.-E. Nordal and S. O. Kanstad, "New developments in photothermal radiometry," *Infrared Phys.*, vol. 25, no. 1/2, p. 295, 1985.

[26] D. P. Almond, P. M. Patel, I. M. Pickup, and H. Reiter, "An evaluation of the suitability of thermal wave interferometry for the testing of plasma sprayed coatings," *NDT International*, vol. 18, no. 1, p. 17, 1985.

[27] P. Cielo, "Pulsed photothermal evaluation of layered materials," *J. Appl. Phys.*, vol. 56, no. 1, p. 230, 1984.

[28] F. H. Dacol, H. Ermert, and L. Melcher, "Advances in non-contacting thermal wave imaging with infrared detection," *Scan. Elec. Microscopy 1985*, II, p. 627.

[29] H. Coufal, "Photothermal spectroscopy using a pyroelectric thin film detector," *Appl. Phys. Lett.*, vol. 44, no. 1, p. 59, 1984.

[30] D. R. Green, "Principles and applications of emittance—independent infrared nondestructive testing," *Appl. Opt.*, vol. 7, no. 9, p. 1779, 1968.

[31] S. Dallaire and P. Cielo, "Pulsed laser glazing," *Thin Solid Films*, vol. 108, p. 19, 1983.

[32] R. F. Gasparovic and L. D. Tubbs, "Influence of reference source properties on ocean heat flux determination with two-wavelength radiometry," *J. Geophys. Res.*, vol. 380, no. 28, p. 2667, 1975.

[33] A. Hordvik and H. Schlossberg, "Photoacoustic technique for determining optical absorption coefficients in solids," *Appl. Opt.*, vol. 16, no. 1, p. 101, 1977.

[34] A. C. Tam and C. K. N. Patel, "High-resolution optoacoustic spectroscopy of rare-earth oxide powders," *Appl. Phys. Lett.*, vol. 35, p. 843, 1979.

[35] G. Busse and A. Rosencwaig, "Subsurface imaging with photoacoustics," *Appl. Phys. Lett.*, vol. 36, p. 815, 1980.

[36] G. S. Cargill, "Electron-acoustic microscopy," in *Scanned Image Microscopy*, E. A. Ash, Ed. London: Academic Press, p. 319, 1980.

[37] Y. Martin and E. A. Ash, "Imaging of micro-cracks by photo-displacement microscopy," in *Proc. IEEE Ultrason. Symp.*, 1984, p. 647.

[38] P. Cielo, F. Nadeau, and M. Lamontagne, "Laser generation of convergent acoustic waves for materials inspection," *Ultrason.*, p. 53, Mar. 1985.

[39] T. M. Proctor, Jr., "An improved piezoelectric acoustic emission transducer," *J. Acoust. Soc. Amer.*, vol. 71, no. 5, p. 1163, 1982.

[40] K. Kubota and H. Murai, "Photoacoustic spectroscopy of semiconductor heterostructures by piezoelectric transducers II. Space-resolved detection of photoacoustic modes," *J. Appl. Phys.*, vol. 56, no. 3, p. 835, 1984.

[41] A. C. Tam and H. Coufal, "Photoacoustic generation and detection of 10 ns acoustic pulses in solids," *Appl. Phys. Lett.*, vol. 42, no. 1, p. 33, 1983.

[42] A. C. Tam, "Pulsed-laser generation of ultrashort acoustic pulses: Application for thin film ultrasonic measurements," *Appl. Phys. Lett.*, vol. 45, no. 5, p. 510, 1984.

[43] E. Menzel and E. Kubalek, "Electron beam chopping systems in the SEM," *Scan. Elec. Microscopy*, vol. 1, p. 305, 1979.

[44] H. Coufal, U. Moller, and S. Schneider, "Photoacoustic imaging using the Hadamard transform technique," *Appl. Optics*, vol. 21, no. 1, p. 116, 1982.

[45] K. Kato, S. Ishino, and Y. Sugitani, "Correlation photoacoustics," *Chem. Lett.*, p. 783, 1980.

[46] Y. Sugitani, A. Uejima, and K. Kato, "Correlation photoacoustic spectroscopy," *J. Photoacoust.*, vol. 1, p. 217, 1982.

[47] Y. Sugitani and A. Uejina, "Depth resolved thermal wave imaging of layered samples by correlation photoacoustics," 4th International Topical Meeting on Photoacoustic, Thermal and Related Sciences, Ville d'Esterel, Quebec, 1985.

[48] J. J. Cox and C. J. R. Sheppard, "Imaging in a scanning photoacoustic microscope," *J. Acoust. Soc. Amer.*, vol. 76, no. 2, p. 513, 1984.

[49] R. M. White, "Generation of elastic waves by transient surface heating," *J. Appl. Phys.*, vol. 34, no. 12, p. 3559, 1963.

[50] H. S. Carslaw and J. C. Jeager, *Conduction of Heat in Solids*, 2nd ed. Oxford: Clarendon, 1959.

[51] W. Nowacki, *Thermoelasticity*. London: Addison-Wesley, 1962.

[52] J. Opsal and A. Rosencwaig, "Thermal-wave depth profiling: theory," *J. Appl. Phys.*, vol. 53, no. 6, p. 4240, 1982.

[53] M. V. Iravani and H. K. Wickramasinghe, "Scattering matrix approach to thermal wave propagation in layered structures," *J. Appl. Phys.*, vol. 58, p. 122, 1985.

[54] L. C. Aamodt and J. C. Murphy, "A thermal wave approach for heterogeneous materials with continuously varying thermal and optical properties in one dimension," to be published *Can. J. Phys.*

[55] —, "Effect of 3-D heat flow near edges in photothermal measurements," *Appl. Opt.*, vol. 21, no. 1, p. 111, 1982.

[56] Y. N. Rajakarunanayake and H. K. Wickramasinghe, "Nonlinear Photothermal Imaging," *Appl. Phys. Lett.*, vol. 48, no. 3, p. 218, 1986.

[57] G. C. Wetsel, Jr., "Nonlinear photothermal imaging," 4th International Topical Meeting on Photoacoustic, Thermal and Related Sciences, Ville d'Esterel, Quebec, 1985.

[58] L. J. Balk, D. G. Davies, and N. Kultscher, "The dependence of scanning electron acoustic microscopy (SEAM) imaging on chopping and detection frequency for metal samples," *Phys. Stat. Sol. (a)*, vol. 82, p. 23, 1984.

[59] K. R. Grice, L. J. Inglehart, L. D. Favro, P. K. Kuo, and R. L. Thomas, "Thermal-wave imaging of closed cracks in opaque solids," *J. Appl. Phys.*, vol. 54, no. 11, p. 6245, 1983.

[60] L. C. Aamodt and J. C. Murphy, "Thermal effects in photothermal spectroscopy and photothermal imaging," *J. Appl. Phys.*, vol. 54, no. 2, p. 581, 1983.

[61] J. P. Monchalin, L. Bertrand, and G. Rousset, "Photoacoustic spectroscopy of thick powdered or porous samples at low frequency," *J. Appl. Phys.*, vol. 50, p. 190, 1984.

[62] C. B. Scruby, D. J. Dewhurst, D. A. Hutchins, and S. B. Palmer, "Quantitative studies of thermally generated elastic waves in laser-irradiated metals," *J. Appl. Phys.*, vol. 51, no. 12, p. 6210, 1980.

[63] C. B. Scruby, "Studies of laser-generated ultrasonic waveforms at different orientations," *Harwell AERE Report*, R11686, Apr. 1985.

[64] R. J. Dewhurst, D. A. Hutchins, S. Palmer, and C. B. Scruby, "Quantitative measurements of laser generated acoustic waveforms," *J. Appl. Phys.*, vol. 53, no. 6, p. 4064, 1982.

[65] L. R. F. Rose, "Point-source representation for laser generated ultrasound," *J. Acoust. Soc. Amer.*, vol. 75, no. 3, p. 723, 1984.

[66] G. S. Kino and R. G. Stearns, "Acoustic wave generation by thermal excitation of small regions," *Appl. Phys. Lett.*, vol. 47, no. 9, p. 926, 1985.

[67] Y.-H. Pao, R. R. Gajewski, and A. N. Ceranoglu, "Acoustic emission and transient waves in an elastic plate," *J. Acoust. Soc. Amer.*, vol. 65, no. 1, p. 96, 1979.

[68] J. Miklowitz, *The Theory of Elastic Waves and Waveguides*. Amsterdam: North-Holland, 1978.

[69] C. Chang and W. Sachse, "Analysis of elastic wave signals from an extended source in plate," *J. Acoust. Soc. Amer.*, vol. 77, no. 4, p. 1335, 1985.

[70] L. M. Lyamshev and B. I. Chelnokov, "Sound generation in a solid by penetrating radiation," *Sov. Phys. Acoust.*, vol. 29, p. 220, 1983.

[71] N. N. Hsu, J. A. Simmons, and S. C. Hardy, "An approach to acoustic emission signal analysis—Theory and experiment," *Mater. Eval.*, vol. 35, p. 100, 1977.

[72] G. C. Wetsel, Jr., "Ultrasonic wave generation by surface and bulk heating in multimaterial structures," in *Acoustical Imaging* (vol. 12), E. A. Ash and C. R. Hill, Ed. London: Plenum, 1982, p. 137.

[73] A. M. Aindow, R. J. Dewhurst, S. B. Palmer, and C. B. Scruby, "Laser-based nondestructive testing techniques for the ultrasonic characterization of sub-surface flaws," *Harwell AERE Report*, R-11562, Jan. 1985.

[74] G. Rousset, L. Bertrand, and P. Cielo, "A pulsed thermoelastic analysis of photothermal surface displacements in layered materials," *J. Appl. Phys.*, vol. 57, no. 9, p. 4396, 1985.

[75] F. Ratliff, "Contour and contrast," *Amer. Sci.*, June 1972.

[76] J. W. Maclachlan, J. C. Murphy, R. B. Givens, and F. G. Satkiewicz, "Linear thermal wave imaging," in *Proc. 11th World Conf. Nondestructive Testing*. Dallas: Taylor Publishing Co., p. 441, 1985.

[77] J. I. Goldstein, D. E. Newbury, P. Echlin, D. C. Joy, C. Fiori, E. Lifshin, *Scanning Electron Microscopy and X-Ray Microanalysis*. New York: Plenum, 1984, p. 72.

[78] F. G. Satkiewicz, J. C. Murphy, L. C. Aamodt, and J. W. Maclachlan, "Ion-acoustic imaging of subsurface flaws in aluminum," in *Rev. Progr. Quantitative NDE*. New York: Plenum, 1986.

[79] D. N. Rose, H. R. Turner, and K. O. Legg, "Scanning ion acoustic microscopy," 4th International Topical Meeting on Photoacoustic, Thermal and Related Sciences, Ville d'Esterel, Quebec, 1985.

[80] B. Svensson, J. Linros, and G. Holmen, "Ion-beam induced anneal-

ing of radiation damage in silicon on sapphire," *Nucl. Instr. Meth.*, vol. 209, p. 755, 1983.

[81] S. U. Campisano, Chu-Te Chang, A. Lo Giudice, and E. Rimini, "Ion-beam mixing in Au-Al thin film bilayers," *Nucl. Instr. Meth.*, vol. 209, p. 139, 1983.

[82] D. Hoohout and F. W. Saris, "Threshold energy density for pulsed-laser annealing of ion implanted silicon," *J. Appl. Physics*, vol. 194, p. 429, 1982.

[83] R. Levi-Setti and T. R. Fox, "High resolution ion probes: Applications to physics and biology," *Nucl. Instrum. Meth.*, vol. 205, p. 299, 1980.

[84] A. Wagner, "Applications of focused ions beams to microlithography," *Solid State Tech.*, vol. 26, p. 97, 1983.

[85] O. Auciello and R. Kelly, Ed., *Ion Bombardment Modification of Surfaces*. Amsterdam: Elsevier, 1984.

[86] P. Sigmund, "Sputtering by ion bombardment: Theoretical concepts," in *Sputtering by Particle Bombardment I* (Topics in Applied Physics, vol. 47), R. Behrisch, Ed. Berlin: Springer-Verlag, 1981.

[87] J. C. Murphy, J. W. Maclachlan, R. B. Givens, F. G. Satkiewicz, and L. C. Aamodt, "The generation of ultrasound by laser, electron and ion probes and its application to the characterization of materials," in *Proc. Ultrason. Int. 1985*, to be published.

[88] G. A. D. Briggs, "Scanning electron acoustic microscopy and scanning acoustic microscopy: a favorable comparison," *Scan. Elec. Microscopy*, vol. III, p. 1041, 1984.

[89] M. G. Sommekh, G. A. D. Briggs, and C. Ilett, "The effect of elastic anisotropy on contrast in the scanning acoustic microscope," *Phil. Mag. A*, vol. 49, no. 2, p. 179, 1984.

[90] J. W. Maclachlan, R. B. Givens, J. C. Murphy, and L. C. Aamodt, "Contrast mechanisms in scanning electron acoustic imaging of grain boundaries," 4th International Topical Meeting on Photoacoustic, Thermal and Related Sciences, Ville d'Esterel, 1985.

[91] R. L. Thomas, L. J. Inglehart, M. J. Lin, L. D. Favro, and P. K. Kuo, "Thermal diffusivity in pure and coated materials," in *Rev. Progr. in Quantitative NDE* (vol. 48), D. O. Thompson and D. E. Chimenti, Eds. New York: Plenum, p. 859, 1985.

[92] H. K. Wickramasinghe, "Contrast and imaging performance in the scanning acoustic microscope," *J. Appl. Phys.*, vol. 50, no. 2, p. 664, 1979.

[93] C. Ilett, M. G. Somekh, and G. A. D. Briggs, "Acoustic microscopy of elastic discontinuities," in *Proc. R. Soc. Lond. A*, vol. 393, p. 171, 1984.

[94] K. K. Liang, G. S. Kino, and B. T. Khuri-Yakub, "Material characterization by the inversion of $V(Z)$," *IEEE Trans. Sonics Ultrason.*, vol. 32, no. 2, p. 213, 1985.

[95] G. C. Wetsel, J. B. Spicer, J. W. Maclachlan, and J. C. Murphy, "Comparison of photoacoustic and photothermal optical beam deflection imaging of subsurface structure in solids," in *Proc. 1985 IEEE Ultrason. Symp.*

[96] H. I. Ringermacher and L. Jackman, "Deep thermoacoustic imaging using scanning electron acoustic microscopy (SEAM)," in *Rev. Progr. Quantitative NDE*. New York: Plenum, 1986.

John C. Murphy was born in Wilmington, DE, on February 28, 1936. He received the M.S. degree in physics from the University of Notre Dame, South Bend, IN and the B.A. and Ph.D. degrees in physics from Catholic University, Washington, DC.

He has had research interests in the optical and microwave spectroscopy of solids and recently has been involved in studies of materials using thermal wave imaging.

Jane W. Maclachlan was born in Glasgow, Scotland on August 9, 1957. She received the B.Sc. degree in physics and the M.Sc. (Eng.) degree in metallurgy from Queen's University, Kingston, ON, Canada.

She is presently doing research in thermal wave imaging for the Ph.D. degree in the Department of Materials Science and Engineering, The Johns Hopkins University, Baltimore, MD.

Leonard C. Aamodt was born in Salt Lake City, Utah on July 19, 1922. He received the B.S. degree in electrical engineering from the University of Utah, Salt Lake City, UT, and the M.S. and Ph.D. degrees from Columbia University, New York, NY.

He taught briefly at Brigham Young University in Provo, UT. His research interests have been in microwave spectroscopy of solids and gases and more recently in studies of materials using photothermal techniques and thermal wave imaging.

END

2-87

DTIC